FIBRE DIFFRACTION REVIEW

Reports on Progress in Fibre Diffraction

A CCP13 / NCD Publication

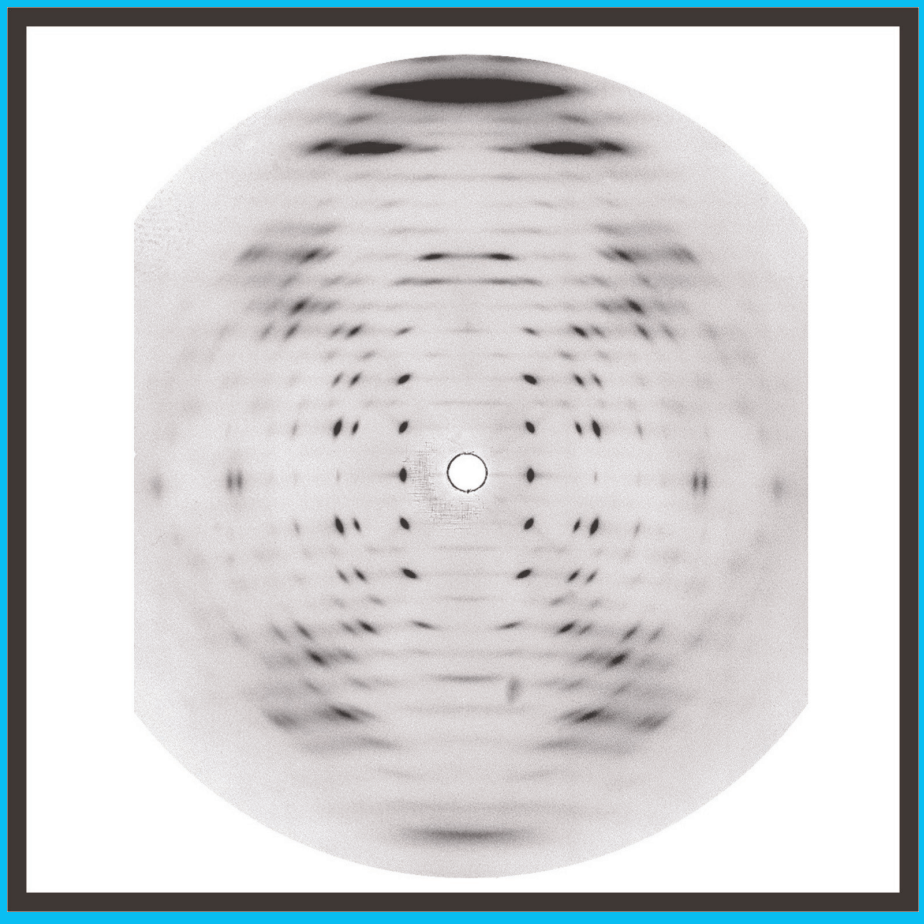

50 Years of The Double Helix - A triumph for Fibre Diffraction

Issue 11

April 2003

12th Annual Fibre Diffraction and Non-Crystalline Diffraction Workshop
2nd - 4th July 2003

Speakers include:

Hind AL-Khayat	Imperial College London
Struther Arnott FRS	Imperial College London
Jane Crawshaw	Cambridge, UK
Athene Donald FRS	Cambridge, UK
Trever Forsyth	ILL, France/ Keele, UK
Kenn Gardner	Dupont, Wilmington, USA
Otto Glatter	Graz, Austria
Simon Hanna	Bristol, UK
Andrew He	Imperial College London
Tom Irving	Illinois, USA
Carlo Knupp	Imperial College London
Tim Lodge	Minnesota, USA
Jianpeng Ma	Houston, USA
Keith Meek	Cardiff, UK
Keiichi Namba	Osaka, Japan
Peter Olmsted	Leeds, UK
Jan Skov Pederson	Aarhus, Denmark
Steve Perkins	UCL, London
Ganeshalingam Rajkumar	Imperial College London
Matthew Rodman	Daresbury Laboratory
Christian Riekel	ESRF, France
Louise Serpell	Cambridge, UK
Tim Wess	Stirling, Scotland
Alan Windle FRS	Cambridge, UK

For further information and registration,
see the web pages at
www.ccp13.ac.uk
or contact Jane Crawshaw (jc10027@hermes.cam.ac.uk)

Supported by CCP13, DARTS and Daresbury Laboratory, with sponsorship from Bruker AXS and Spectra Stable Isotopes.

12th Annual Fibre Diffraction and Non-Crystalline Diffraction Workshop
2nd - 4th July 2003

Speakers include:

Hind AL-Khayat	Imperial College London
Struther Arnott FRS	Imperial College London
Jane Crawshaw	Cambridge, UK
Athene Donald FRS	Cambridge, UK
Trever Forsyth	ILL, France/ Keele, UK
Kenn Gardner	Dupont, Wilmington, USA
Otto Glatter	Graz, Austria
Simon Hanna	Bristol, UK
Andrew He	Imperial College London
Tom Irving	Illinois, USA
Carlo Knupp	Imperial College London
Tim Lodge	Minnesota, USA
Jianpeng Ma	Houston, USA
Keith Meek	Cardiff, UK
Keiichi Namba	Osaka, Japan
Peter Olmsted	Leeds, UK
Jan Skov Pederson	Aarhus, Denmark
Steve Perkins	UCL, London
Ganeshalingam Rajkumar	Imperial College London
Matthew Rodman	Daresbury Laboratory
Christian Riekel	ESRF, France
Louise Serpell	Cambridge, UK
Tim Wess	Stirling, Scotland
Alan Windle FRS	Cambridge, UK

For further information and registration,
see the web pages at
www.ccp13.ac.uk
or contact Jane Crawshaw (jc10027@hermes.cam.ac.uk)

Supported by CCP13, DARTS and Daresbury Laboratory, with sponsorship from Bruker AXS and Spectra Stable Isotopes.

FDR April 2003 Contents Issue 11

Contents, Cover Caption and Production . . . 1
The CCP13 Committee Members . . . 2
Chairman's Message . . . 3
From the Editor . . . 5
CCP13 Research Assistant Profile . . . 5

Meeting Reports

NOBUGS 2002, Steve King . . . 6

Technical Reports

Status of CCP13 Software - overview, John Squire *et al* . . . 7
SRS Station MPW6.2 - A new facility for variable energy SAXS/WAXS at Daresbury Laboratory, Nick Terrill . . . 20

Reviews

Millisecond Time-Resolved Low-angle X-ray Fibre Diffraction: A Powerful, High-Sensitivity Technique for Modelling Real-Time Movements in Biological Macromolecular Assemblies, John Squire *et al.* . . . 28
Small-Angle Scattering Functions of Micelles, V. Castelletto *et al* . . . 36
Synchrotron studies of electric-field effects in smectic liquid crystals, Helen Gleeson . . . 44
Multiscale Modelling in Polymer Science, J. Crawshaw & A.H. Windle . . . 52

Original Articles

The effects of shear and co-surfactants on the evolution of the micro-structure in concentrated di-chain cationic surfactant solutions, J. Penfold *et al*... . . . 68
Preparation of Tunicin Cellulose Iβ Samples for X-ray and Neutron Diffraction, Yoshiharu Nishiyama *et al*.. . . . 75
Cross-beta structure of an amyloid-forming peptide studied by electron nano-crystallography, Ruben Diaz-Avalos *et al* 79
Type-4 bacterial pili: molecular models and their simulated diffraction patterns, D. A. Marvin *et al*... . . . 87
Structural changes of α-crystallin during heating and comparisons with other small heat shock proteins, J. W. Regini & J.G. Grossmann... . . . 95
X-ray fibre diffraction analysis of assemblies formed by prion-related peptides: Polymorphism of the heterodimer interface between PrP^{C} and PrP^{Sc}, Hideyo Inouye & Daniel A. Kirschner . . . 102

Expended Poster-Prize Abstracts

Structure-Property Relationships for Polyisocyanurates with Varied Modulus, A-L. Abbott *et al*.... . . . 113
Analysis of collagen structure in parchment by Small angle X-ray diffraction, C. J. Kennedy.*et al*... . . . 117
X-ray diffraction of rat tail tendon at ambient and cryo-cooled temperatures - a comparison, J. H. Laing *et al*.... . . . 119
A Wide-Angle X-ray Diffraction Study of the Developing Embryonic Chicken. Cornea, C. Boote *et al*.... . . . 123

11th Annual Workshop Abstracts . . . 130
Fibre Diffraction Review: Instructions to Authors . . .

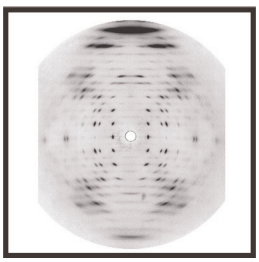

The "E-DNA" pattern was first published by A. G. W. Leslie, Struther Arnott, R. Chandrasekaran, and R. L. Ratliff as part of a report in *J. Mol. Biol.* (1980) **143**, 49-72 on the polymorphism of DNA duplexes with repetitious mono-, di-, and tri-nucleotide sequences. At the time it was casually but accurately described as resulting from a 3_2 molecular helix with a large oligonucleotide duplex as the asymmetric unit. The strong meridional reflexion on the 15th layer line encouraged mistaken support for pentanucleotide units of secondary structure rather than the hexanucleotides that were later found to provide a solution to the diffraction problem as well as being more compatible with the trinucleotide primary structure of this synthetic DNA.

Fibre Diffraction Review Production
Editor: Prof. John Squire, Biological Structure and Function Section, Biomedical Sciences Division, Imperial College, London SW7 2AZ.
Production: Dr Andrew He, Biological Structure and Function Section, Biomedical Sciences Division, Imperial College, London SW7 2AZ.

The CCP13 Committee Members (As at April 2003)

Chairman

Prof John Squire (to 2005)
Biological Structure and Function Section
Biomedical Sciences Division, Imperial College London, London SW7 2AZ, UK
Editor "Fibre Diffraction Review".
Phone 0207 594 3185 **Fax** 0207 594 3169 **Email** j.squire@ic.ac.uk

Vice Chairman

Dr Trevor Forsyth (to 2005)
Institut Laue-Langevin, BP 156 F-38042, Grenoble Cedex 9, France, and Physics Dept, Keele University, Staffordshire ST5 5BG, UK
Phone +33 4 (0) 76207158 **Fax** +33 4 (0) 76483906 **Email** tforsyth@ill.fr

Secretary

Dr. Patrick Fairclough (to 2005)
Department of Chemistry, The University of Sheffield,
Dainton Building, Brookhill, Sheffield, S3 7HF
Phone 0114 222 9411 **Fax** 0114 273 8673 **Email** p.fairclough@sheffield.ac.uk

Research Assistants

Dr Jane Crawshaw
Polymer Group, Department of Materials Science and Metallurgy, University of Cambridge, Pembroke St., Cambridge CB2 3QZ
Phone 01223 334335, **Email** jc10027@hermes.cam.ac.uk

Dr David Dover
Biomedical Sciences Division, Imperial College London, London SW7 2AZ,
Phone 0207 4331071, **Email** sdd@doversoft.co.uk

Dr Andrew He
Biomedical Sciences Division, Imperial College London, London SW7 2AZ,
Email andrew.he@ic.ac.uk

Ganeshalingam Rajkumar
Biomedical Sciences Division, Imperial College London, London SW7 2AZ,
Email g.rajkumar@ic.ac.uk

Dr Matthew Rodman
Daresbury Laboratory, Daresbury, Warrington WA4 4AD,
Phone 01925 603626 , **Email** m.j.rodman@dl.ac.uk

Members

Dr David Blundell (to 2005)
Physics Department, Keele University, Keele, Staffordshire, ST5 5BG,
Phone 01782 583330

Dr Mike Ferenczi (to 2004)
Biomedical Sciences Division, Imperial College London, London SW7 2AZ,
Phone 0207 594 3139, **Fax** 0207 594 3169, **Email** m.ferenczi@ic.ac.uk

Dr Steve King (to 2004)
Rutherford Appleton Laboratory, Chilton, Didcot, OX11 0QX,
Phone 01235 446437, **Fax** 01235 445720, **Email** s.m.king@rl.ac.uk

Dr Tim Wess (to 2005)
Department of Biological and Molecular Sciences, University of Stirling, Stirling, FK9 4LA,
Phone 01786 467775, **Fax** 01786 464994 **Email** tjw3@stir.ac.uk

Prof. Alan Windle FRS (to 2004)
Department of Materials Science and Metallurgy, University of Cambridge, Pembroke Street, Cambridge CB2 3QZ.
Phone 01223 334335 **Fax** 01223 335637, **Email** ahw1@cam.ac.uk

Prof. Struther Arnott FRS (to 2004)
Biomedical Sciences Division, Imperial College London, London SW7 2AZ,
Phone 0207 594 3185, **Fax** 0207 594 3018, **Email** s.arnott@ic.ac.uk

Members (Co-opted)

Dr Greg Diakun
Daresbury Laboratory, Daresbury, Warrington WA4 4AD,
Phone 01925 603343 **Email** g.diakun@dl.ac.uk

Dr Tom Irving
CSRRI, Dept BCPS, Illinois Institute of Technology, 3101 s. Dearborn, Chicago IL. 60616, USA.
Phone (312) 567-3489 **Fax** (312) 567-3494 **Email** irving@biocat1.iit.edu

Dr. K. H. Gardner
DuPont CR&D, P.O. Box 80228, Experimental Station, Wilmington, Delaware, DE 19880-0228, USA
Phone Tel: +1 302 695 2408 **Email** kenn.h.gardner@usa.dupont.com

Dr Geoff Mant
Daresbury Laboratory, Daresbury, Warrington WA4 4AD
Phone 01925 603169 **Email** g.r.mant@dl.ac.uk

Prof. Rick Millane
Dept of Electrical and Computer Engineering, University of Canterbury, Christchurch, New Zealand.
Email rick@elec.canterbury.ac.nz

Dr Keiichi Namba
Matsushita Electric Industrial Co. Ltd., 3-4 Hikaridai, Seika 619-0237, Japan.
Phone 81-774-98-2543 **Fax** 81-774-98-2575 **Email** keiichi@crl.mei.co.jp

Prof. Gerald Stubbs
Dept of Molecular Biology, Vanderbilt University, 2200 West End Avenue, Nashville, TN 37235
Phone (615) 322-7311 **Email** stubbsgj@ctrvax.vanderbilt.edu

Chairman's Message

This year above all others brings to us a palpable reminder of the power of fibre diffraction. Without the excellent X-ray diffraction patterns from DNA fibres produced by Rosalind Franklin in the laboratory of Maurice Wilkins at King's College London, the modelling studies of Francis Crick and Jim Watson at Cambridge 50 years ago would have had nothing concrete about the dimensions of the DNA molecule to go on apart from Astbury's earlier demonstration of the 3.4 Å repeat of the bases. The facts that the structure was helical, based on the helical diffraction theory of Cochran, Crick and Vand (1952: Acta Cryst. 5, 581), theory which also been developed (but not published) by Alec Stokes at King's College London, that the space group contained a dyad axis perpendicular to the fibre axis suggesting a pair of anti-parallel strands of polynucleotide, and that the axial repeat was 34 Å, all came from the fibre diffraction patterns of the King's College group. Without knowledge of these key experimental observations it is hard to see how the Watson-Crick double helix model for DNA could have been developed. Together with Watson's almost mystical discovery of base-pairing, following Jerry Donohue's advice on the correct tautomeric forms of the bases, fibre diffraction led inevitably to the solution of probably the single most important question in biology 'how is the genetic information passed from parent to offspring?' (J.D.Watson & F.H.C. Crick, Nature 171, 737-738, 1953 and other papers in the same issue). An excellent insight into this story and the role of the Cavendish laboratory was recently given by Hugh Huxley (2003: Physics World, March 2003, 29-35), himself a pioneer in the application of fibre diffraction methods, this time to muscle.

Despite this initial flurry of activity on DNA structure, in fact it took the Wilkins group about another 10 years to prove that the Watson-Crick model was essentially correct by providing accurate coordinates of helical, base-paired duplexes that fitted improved fibre diffraction patterns very much better than the first Crick-Watson wire model. Nowadays of course there are many known DNA forms, almost all recognised first from fibre diffraction studies, and there are new structures still being discovered, such as the polyhexanucleotide

DNA duplex whose X-ray diffraction pattern appears on the front cover of this volume.

However, in the excitement about the double helix it is very easy to overlook the fact that fibre diffraction led the way in solving or at least confirming the structures of all of the known regular secondary folds of proteins. The correctness of Pauling and Corey's proposal about the α-helix was confirmed by the fibre diffraction studies by Perutz on keratin and poly-benzyl-glutamate, the β-sheet structure was first demonstrated in diffraction patterns from silks, and the characteristic collagen triple helical structure was first proposed based on diffraction patterns from tendon fibres and their relationship with data from some synthetic polypeptide fibres (e.g. poly-glycine and poly-proline).

Fibre diffraction has had a very long history of success and yet one still hears comments such as 'the structure of DNA was not really confirmed until oligonucleotides were crystallised and their structure solved by the methods of Macromolecular crystallography'. Why were the very good, earlier fibre diffraction results not in themselves compelling? One of the reasons for setting up CCP13 was the need to develop rigorous methods of stripping and modelling fibre diffraction data so that the quality of structural conclusions from fibre diffraction could be objectively assessed and so that the results would be believed by non-practitoners in the field. We are now well on the way to doing this. Excellent data extraction programs such as XFIX, FTOREC and LSQINT can now remap raw fibre patterns into reciprocal space, fit good backgrounds to the observed images and also model either Bragg peaks or continuous layer-lines with robust algorithms. Unfortunately these programs have been non-trivial to use, so a major challenge is to provide both better instruction manuals for their use and in the longer term a friendlier and more intuitive Graphical User Interface in Java (to be portable) from which all of the programs can be run. This Java GUI is currently in preparation. In addition to this we are in the process of developing a number of programs for modelling of either atomic arrangements in fibres based on high resolution fibre diffraction data (e.g. LALS and FX-PLOR), or the organisation of molecular domains based on low-angle fibre diffraction data (e.g. MOVIE). A full description and summary of the available CCP13 software with flow diagrams showing the logic of the processing procedure is given on pages 7-19 of this volume.

The CCP13 website (www.ccp13.ac.uk) is now more informative and active than in the past and there are three live mirror websites; in the UK at Imperial College (www.ccp13.org), in the US at the APS in Chicago (www.bio.aps.anl.gov/biocat/mirror/www.ccp13.ac.uk/), and in France at the ILL (http://www.ill.fr/ccp13). The CCP13 bulletin board (ccp13bb@dl.ac.uk) is becoming more active and is an excellent place to exchange ideas or to get help. It is there for you to use - so please use it! Last year in June we had a memorable Workshop at Keele University and this year the Workshop will be held at Fitzwilliam College, Cambridge from July 2 to 4. In addition to some excellent talks, we plan to hold hands-on demonstrations of various kinds of CCP13 software, so why not come along and find out what can be done with your data.

Finally, I would like to record my thanks, surely reiterating your own feelings, for the enormous contributions to CCP13 that Trevor Forsyth made in his time as Chairman. This was a time when CCP13 saw considerable expansion and consolidation and Trevor's tremendous enthusiasm and ability were central to bringing this about. Fortunately, Trevor retains an active involvement in CCP13 as Vice Chairman of the Steering Committee. He also provides a strong connection to X-ray and neutron fibre diffraction facilities at the ESRF and the ILL in Grenoble - facilities which are of course of major importance to the CCP13 community. My only hope now, as Chairman again, is that I can help to sustain and further develop CCP13 into as good a core activity for a thriving international fibre diffraction community as it can possibly be. However, this can only be done with your help and support. Please come to the Workshop, make your views known, if you are not giving a talk bring a poster on your work, and above all let us know how the existing software can be developed to be more useful for you. CCP13 is there to help you to get the best out of your data, but it requires your input to make it really flourish.

John Squire - Imperial College - March 2003

From the Editor

Fibre Diffraction Review is going from strength to strength. The present issue is a testament to the breadth and interest in the fibre diffraction and non-crystalline diffraction fields and to the excellence of the research being undertaken. As would be expected of a quality Journal, all Reviews, Original Papers and Extended Abstracts are subjected to strict peer review by at least two expert referees. But from now on all the published papers, including papers in back issues, are being made available in PDF format for downloading from the CCP13 website. In addition, the Journal has joined the organisation known as 'CrossRef' so that each paper has a DOI (Digital Object Identifier) for cross-referencing throughout the web. We hope that ***Fibre Diffraction Review*** papers will be listed by abstracting search engines so that both the Journal and also the high quality individual papers in it receive as broad publicity and accessibility as possible.

It has been the custom to invite speakers at the annual CCP13/NCD Workshops to contribute articles to the Journal. We will continue to do this. But the Journal is also an excellent forum for presentation of any piece of fibre diffraction or non-crystalline diffraction research. All colour illustrations are reproduced free of charge, PDF versions of all ***Fibre Diffraction Review*** papers will be downloadable free of charge, and hard copies of the Journal will land on the desks not only of all fibre diffractionists across the world who are on our mailing list, but also of many at research sponsoring bodies such as Research Councils, Science Foundations and Charities. If you would like to receive a copy of ***Fibre Diffraction Review***, but are not on our mailing list, please contact one of the CCP13 RAs or subscribe to the bulletin board (CCP13bb@dl.ac.uk).

John Squire - Imperial College London - March 2003.

New CCP13 Members

Dr David Dover

David Dover graduated in mathematical physics from Cambridge and joined Struther Arnott as his second PhD student at King's College London. Following six years of post-doctoral work in protein crystallography at Oxford and Zurich, he returned to King's where he worked primarily on image processing of electron micrographs. He left King's in 1994 to become a freelance software developer and has a number of non-scientific contracts with small private companies as well as the BBC and NATS (National Air Traffic Services). He continues to work freelance while contributing part-time to CCP13, where his main interests are in implementing LALS (Linked Atom Least Squares), the program he helped to start with Struther Arnott and Alan Wonacott, as part of the CCP13 suite and in developing a JAVA interface as a user-friendly front for current CCP13 programs.

Meeting Reports

NOBUGS 2002 - New Opportunities for Better User Group Software

National Institute of Standards, Gaithersburg MA, USA, November 2002

This was the fourth of the approximately biennial NOBUGS meetings. For the benefit of the uninitiated, NOBUGS provides a forum in which both developers and users of computer software and techniques in those information technology areas relevant to scientific research, especially as employed at large-scale user facilities such as synchrotrons and neutron sources, can come together and present developments, discuss problems and evolve standards. Against a backdrop of rising geopolitical tensions, travel restrictions and increased security there were nonetheless 88 registered delegates present of which a healthy 39% were from Europe plus a few from Japan, Australia and South Africa. CCP13 was indirectly represented by Steve King and Geoff Mant.

Delegates were comfortably accommodated in the Holiday Inn at Gaithersburg, a short ride by NIST shuttle from the main campus. NIST provided a good venue, and thanks are due to the local organising team of John Barnes, Przemek Klosowski and Alan Munter for their hard work behind the scenes.

After a welcome by J Michael Rowe, Director of the NIST Centre for Neutron Research, the meeting kicked off with a keynote address from Roger Pynn (now UCSB, but until recently Director of LANSCE) entitled "Can Software be a Competitive Advantage for User Facilities?". Over the next two and a half days there were 8 oral sessions (2 on experiment control, 1 each on user tracking & remote collaboration, high-throughput crystallography, experiment simulation, data treatment, data formats & software development tools) totalling 43 presentations, and 2 discussion sessions (one on the NeXus data format and the other on issues facing the community). There was also a poster session throughout which attracted 29 contributions, one of them advertising CCP13 programs.

The ongoing development of the NeXus data format was undoubtedly one of the central themes of the meeting. The goal is to create a format that will facilitate the exchange of neutron and synchrotron scattering data between facilities, users and their institutions. It is being developed by an international team of scientists and computer programmers from the principle neutron and X-ray facilities around the world. NeXus uses the Hierarchical Data Format (HDF) which is portable, binary, extensible and self-describing. The NeXus data format defines the structure and contents of these HDF files in order to facilitate the visualisation and analysis of the data. More information can be found through the links below. Specific issues for Small-Angle Scattering are being discussed in the canSAS forum. Contributions from the community are always welcome.

Steve King, ISIS

Useful links:
http://www.ncnr.nist.gov/events/nobugs2002/schedule.php (includes links to abstracts)
http://lns00.psi.ch/nexus/ or
http://www.neutron.anl.gov/nexus/
http://hdf.ncsa.uiuc.edu/
http://www.ill.fr/lss/canSAS/main.html
http://www.isis.rl.ac.uk/LargeScale/LOQ/loq.htm

New CCP13 Software and the Strategy Behind Further Developments: Stripping and Modelling of Fibre Diffraction Data

John Squire[1], Hind AL-Khayat[1], Struther Arnott[1], Jane Crawshaw[3], Richard Denny[1,2], Greg Diakun[2], David Dover[1], Trevor Forsyth[4,5], Andrew He[1], Carlo Knupp[1], Geoff Mant[2], Ganeshalingam Rajkumar[1], Matthew Rodman[1,2], Mark Shotton[1,2] & Alan Windle[3]

[1] Biological Structure & Function Section, Biomedical Sciences Division, Imperial College London, London SW7 2AZ
[2] Synchrotron Division, CLRC Daresbury Laboratory, Warrington, Cheshire WA4 4AD
[3] Department of Materials Science and Metallurgy, University of Cambridge, Pembroke Street, Cambridge CB2 3QZ
[4] Institut Laue Langevin, 6 Rue Jules Horowitz, BP156 F-38042 Grenoble Cedex 9, France
[5] Lennard-Jones Laboratories, School of Chemistry and Physics, Keele University, Staffordshire ST5 5BG, UK

ABSTRACT

The aim of the CCP13 project is to provide easily usable software programs for those doing fibre diffraction or solution scattering studies; in fact any studies using diffraction from non-crystalline materials. Over the last ten years CCP13 project scientists have developed a set of programs for stripping and analysing fibre diffraction patterns and also patterns from solution scattering and other low-angle diffraction methods. The suite is now being updated to keep in step with new developments in beamlines, in detectors and in computing power and, in addition, new programs are being developed to allow for systematic modelling of different kinds of structures. The present report discusses the strategy behind the approach, it describes what has been implemented so far and it outlines new developments that are in the pipeline.

INTRODUCTION

Fibre diffraction has made critical contributions to our understanding of biomolecular and synthetic polymer systems and it will without doubt continue to do so as new resources and instrumentation become available to the scientific community. In the hands of adept practitioners the information content of X-ray and neutron diffraction data from fibres and other less than crystalline systems can be much greater than crystallographers generally concede. However, the problem of carrying out satisfactory data extraction and modelling of fibre diffraction patterns has still not been completely solved (Arnott, 1999). Furthermore, the outstanding success of the high-intensity X-ray beams and excellent area detectors at synchrotron X-ray sources, together with new applications of neutron beam sources has led to an accumulation of high quality experimental data which in the recent past could not be analysed satisfactorily due to a lack of appropriate software. In addition, massively increased computing power allows both biological and synthetic polymer questions to be addressed in a way that was not possible a few years ago. The present report summarises both the approach being taken by CCP13 personnel to consolidate and develop its data stripping software activity (Denny, 1993; 1994; 1995a,b; 1996; Shotton *et al.*, 1998; Shotton & Denny, 1999; Stubbs, 1999) and also the further expansion of its software development into the rigorous modelling of fibre diffraction data. The clear aim is to establish generally accepted objective standards of data stripping and modelling so that, as in the case of protein crystallographers using CCP4 programs, the quality and reliability of our diffraction analysis can be objectively assessed by others, and important scientific problems can be tackled with confidence. The new methods are being applied to key fibrous and non-crystalline targets in biology, medicine and materials science.

DEVELOPMENTS IN DATA ANALYSIS

So far, the major effort in CCP13 has concerned the extraction of useful intensity data from fibre diffraction patterns and from small-angle scattering (SAXS) data. The nature of the patterns from fibres

can be quite diverse, ranging from those which exhibit Bragg sampling from polycrystalline specimens, to patterns where the intensity is continuously distributed along layer-lines, reflecting a complete lack of axial alignment across the sample. Most programs in the CCP13 suite are designed to be as problem independent as possible: XFIX, FTOREC, LSQINT, FDSCALE, FD2BSL and SAMPLE are all dedicated to analysing two-dimensional fibre diffraction patterns. CORFUNC is a collective name for a set of programs for calculating correlation functions from SAXS data. XFIT is a one-dimensional peak-fitting program of general applicability, including its application to the analysis of time-resolved diffraction data. XCONV provides utilities for converting image files in a variety of detector formats to either BSL format (the format used by the NCD group at the CLRC Daresbury SRS) or to TIFF format. Achievements to date include the development of data reduction programs incorporating full mathematical and theoretical rigour, the incorporation of interactive and batch methodology for treatment of time-resolved diffraction data and the treatment of complex background data with low pass filters, roving windows and so on. Background treatment methods can also be applied to separation of crystalline from continuous data.

TYPICAL PROCEDURES IN FIBRE DIFFRACTION ANALYSIS

This Section provides an overview of the processes involved in data analysis and modelling and the CCP13 (or other) programs that can be used at each stage. These programs are then described in more detail in a later section.

Data Extraction

Once a fibre diffraction pattern has been recorded, and nowadays this is usually in digital form from an image plate, CCD or multiwire area detector rather than film, the image needs to be corrected for the particular properties of the detector (e.g. spatial distortion, detector response, etc). This is often most conveniently done using the software associated with the detector. Following this there is often a need to add diffraction patterns (e.g. from multiple short experiments of the same kind to build up enough counts), there may be a need to normalise various exposures according to the intensity of the incoming beam which will vary over time, there may be a need to subtract a camera or solution background and it may be necessary to do this over a whole time-series recorded in a single experiment. How this is done depends on the circumstances. Many of these manipulations can be done in the Daresbury NCD program BSL, once the files have been through XCONV to convert them from detector to BSL format (see Fig. 1), but BSL itself does not display the images and is not associated with a GUI. Alternatively, some operations can be done by the ESRF program FIT2D which instantly displays images and includes many useful manipulations (http://www.esrf.fr/computing/espg/subgroups/data_analysis/FIT2D). For example, FIT2D is very good for looking at 1D profiles across selected regions of the pattern. However, there is a new WINDOWS-based version of BSL called BS developed by Natalia Koubassova (http://jan.imec.msu.ru/~natalia/bs_form.htm) which may also be found useful. A new, improved program for these manipulations is currently being developed as part of the CCP13 suite.

Assuming that these preliminary stages have been completed, the next step is to carry out true fibre diffraction analysis. Figure 1 shows a flow diagram of the procedures that can be followed. The first step requires the determination of the tilt and rotation of the fibre relative to the vertical, finding the centre of the pattern and determining any tilt of the detector that may have been present. Once the files are in BSL format, this process can be done in XFIX (Fig. 1) which displays and analyses these parameters. The values coming out of XFIX can then be used in the program FTOREC to produce a corrected, centred, quadrant-folded image. This consists of intensities correctly mapped to reciprocal space (e.g. initially curved layer-lines from a highly tilted fibre will become straight). The image from FTOREC needs to be viewed in XFIX. Subtraction of a smoothly varying background can also be carried out in XFIX or it can be done in LSQINT, which is the next program in the sequence.

LSQINT is designed either to estimate the integrated intensities within Bragg peaks in patterns from a polycrystalline specimen or to determine smoothly varying intensities along continuous layer-lines. Among other things, account needs to be taken: (i) of the Lorentz correction (outer reflections will spend less time crossing the Ewald sphere and will be under-represented), (ii) of the peak shape and (iii) of the disorientation within the specimen. LSQINT will fit a smoothly varying background using several

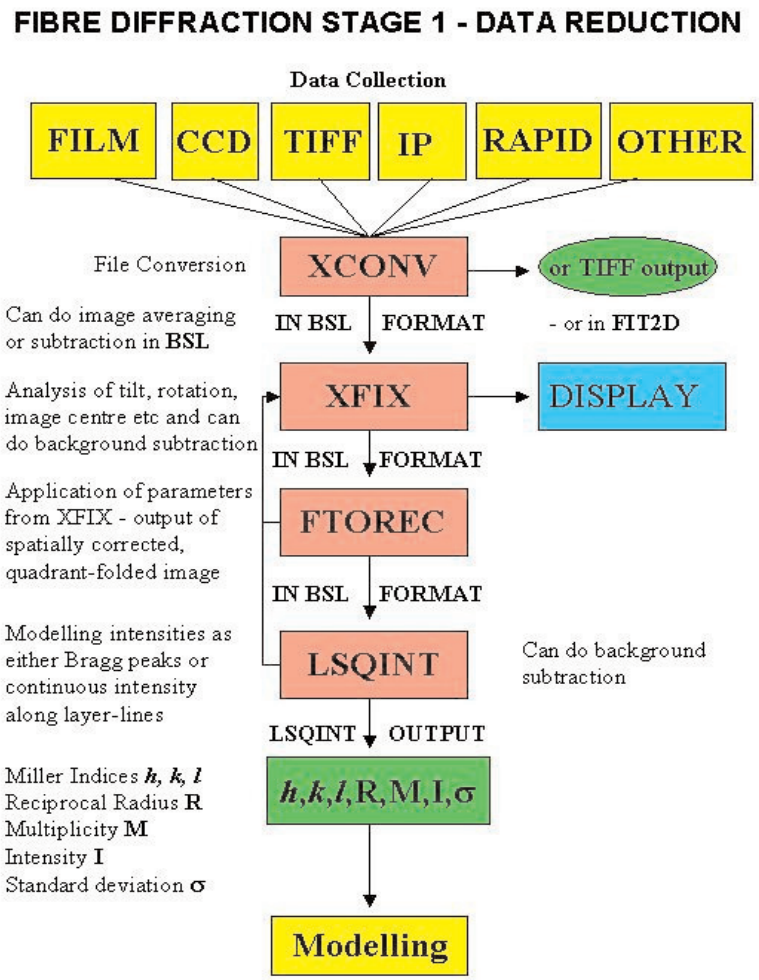

Figure 1: Flow diagram to show the processing procedure for treating a raw fibre diffraction pattern from a variety of detector sources through the file conversion program XCONV, into the analysis and display program XFIX which outputs parameters such as fibre tilt and rotation for input into FTOREC where the pattern is corrected and remapped in reciprocal space. Once again it can be viewed in XFIX. The corrected data from FTOREC can be fitted in LSQINT either as continuous intensities or as Bragg peaks after suitable background removal. Intensities output from LSQINT can then be used in modelling processes outlined in Figure 2.

alternative procedures if this has not been done in FTOREC.

In the case of well-sampled layer-lines (Bragg peaks) the important output parameters from LSQINT (apart from peak shape and disorientation) are:

[1] the ***h***, ***k***, ***l*** values for a particular peak,
[2] the multiplicity **M** of the peak. (The fibre pattern is essentially a section taken through a 3D transform that has been rotated continuously through 360° such that reflections at the same radius along a layer-line are added. The number of such reflections (i.e. the multiplicity) will vary depending on the space group involved and on the values of **h** and **k** for the particular peak and some peaks will be weighted more strongly than others.)
[3] the integrated intensity (**I**) of the peak and the standard deviation (**σ**).

In the case of continuous layer-lines the important features are the layer-line number (***l***), the reciprocal radius along the layer-line (**R**) and the values of **I** and **σ**.

Modelling

Once good intensity values have been determined from LSQINT, the problem is how to determine the associated structure. The strategy to be followed (Fig. 2) depends on the resolution of the information in the diffraction pattern. Patterns containing high resolution diffraction peaks, say from a nucleic acid, polysaccharide or crystalline polymer, need to be fitted at an atomic level, but, unlike protein crystallography where electron density maps are

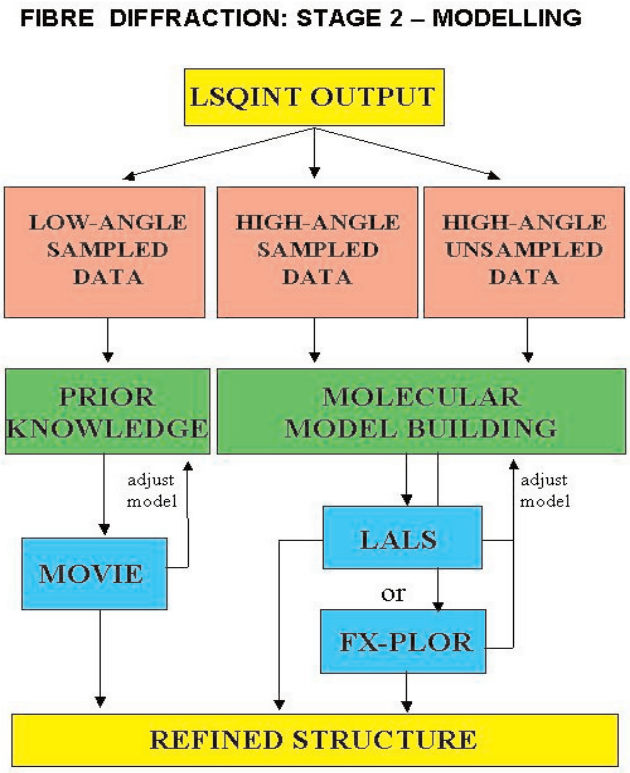

Figure 2: Alternative steps in the modelling procedure depending on whether the analysis is carried out at atomic resolution (high-angle pathways) or at the level of protein sub-domains (low-angle pathway). The programs in blue boxes are still in development.

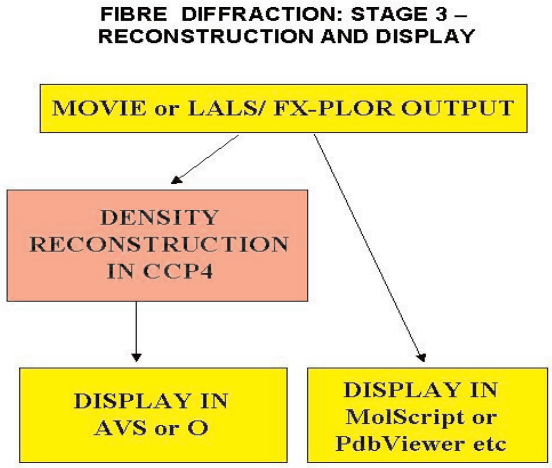

Figure 3: The final steps in the modelling process depend once again on the resolution of the data being processed. Models from high-resolution data can be viewed in conventional molecular graphics programs (e.g. MolScript, PdbViewer). In the case of low-resolution Bragg data the output from MOVIE or another such program can be used as an input to CCP4 programs which can calculate electron density maps at the required resolution that can be displayed in O or on AVS.

computed and fitted, this has to be done by creating a possible model, comparing its computed diffraction pattern with the observations coming from LSQINT, and then refining the model against the data. CCP13 currently uses two alternative programs to do this, LALS and FX-PLOR (see below), each of which also has the facility to minimise the energy of the structure being studied, along with assessing goodness of fit to the X-ray diffraction data using a crystallographic R-factor. Once the best atomic coordinates have been determined, the structures can be displayed using conventional molecular graphics programs (e.g. PdbViewer or MolScript: Fig. 3).

In the case of low-angle X-ray diffraction data, where the resolution is limited, it can be helpful to use protein sub-domains as the repeating units and to parameterize the domain positions, compute the diffraction patterns and vary them to give the optimal fit to the intensities coming from LSQINT (Fig. 2; see Squire *et al.*, 2003 - this volume). However, final testing of any model should be carried out where possible with the full atomic coordinates of the component molecules. In the case of diffraction from muscle, the program MOVIE will take in molecular shapes, change the positions of sub-domains within molecules, and optimise all of these things by simulated annealing against the observed diffraction data as assessed by a computed R-factor (Hudson *et al.*, 1997). MOVIE is currently designed for a specific task, but expansion of these ideas to more general objects (i.e. other than muscle) is under way. Once the best parameters have been determined (Fig. 3), the structure can be transformed or reconstructed using CCP4 programs (http://www.ccp4.ac.uk) and computed density maps can be viewed, for example, in O (Jones *et al.*, 1991) or in AVS.

CCP13 DATA CONVERSION AND STRIPPING PROGRAMS

This section builds on the overview of the last section, it summarises the technical details of the available programs and it also reports on new developments that have already been implemented or are planned. Platforms on which the various programs are implemented are shown in Table 1.

TABLE 1: CCP13 PROGRAM STATUS AND PLATFORMS

Program	Description
XOTOKO	1-D data manipulation
BSL	2-D data manipulation
V2A	vax to unix data conversion
A2V	unix to vax data conversion
OTCON	ascii to otoko data conversion
RECONV	otoko to ascii data conversion
TIFF2BSL	image plate (tiff) to bsl conversion
BSL2TIFF	bsl to tiff conversion
I2A	ieee to ansi data conversion (DEC)
XCONV	file format conversion (GUI-driven)
XFIT	1-D fitting and plotting (GUI-driven)
XFIX	fibre pattern analysis (GUI-driven)
CONV	file format conversion (cmd line)
FTOREC	reciprocal space transformation
LSQINT	2-D integration and background fitting
CORFUNC	correlation function analysis
SAMPLE	Fourier-Bessel smoothing
FDSCALE	scaling and merging of intensities
FD2BSL	intensity to bsl conversion

Program	Solaris 2.7	Irix 6.2	OSF 3.2	Linux	Windows
XOTOKO	31/03/03	30/05/96	29/04/97	31/03/03	-
BSL	31/03/03	21/03/97	27/04/97	31/03/03	-
V2A	19/05/95	-	-	-	-
A2V	19/05/95	-	-	-	-
OTCON	06/06/95	08/07/94	-	08/05/97	-
RECONV	06/06/95	31/10/94	-	08/05/97	-
TIFF2BSL	01/2002	01/2002	-	01/2002	-
BSL2TIFF	21/03/97	-	-	-	-
I2A	n/a	n/a	29/04/97	02/05/97	n/a
XCONV	08/11/02	08/11/02	08/11/02	08/11/02	15/04/03
XFIT	06/12/99	17/08/99	17/08/99	17/08/99	-
XFIX	06/12/99	17/08/99	17/08/99	17/08/99	-
CONV	25/05/99	25/05/99	25/05/99	25/05/99	05/02/03
FTOREC	10/07/99	10/07/99	10/07/99	10/07/99	05/02/03
LSQINT	09/01/03	08/01/03	08/01/03	09/01/03	05/02/03
CORFUNC	25/05/99	22/04/99	-	22/08/99	-
SAMPLE	22/04/99	22/04/99	15/07/99	22/04/99	-
FDSCALE	22/04/99	22/04/99	22/04/99	22/04/99	-
FD2BSL	22/04/99	22/04/99	19/02/02	19/02/02	-

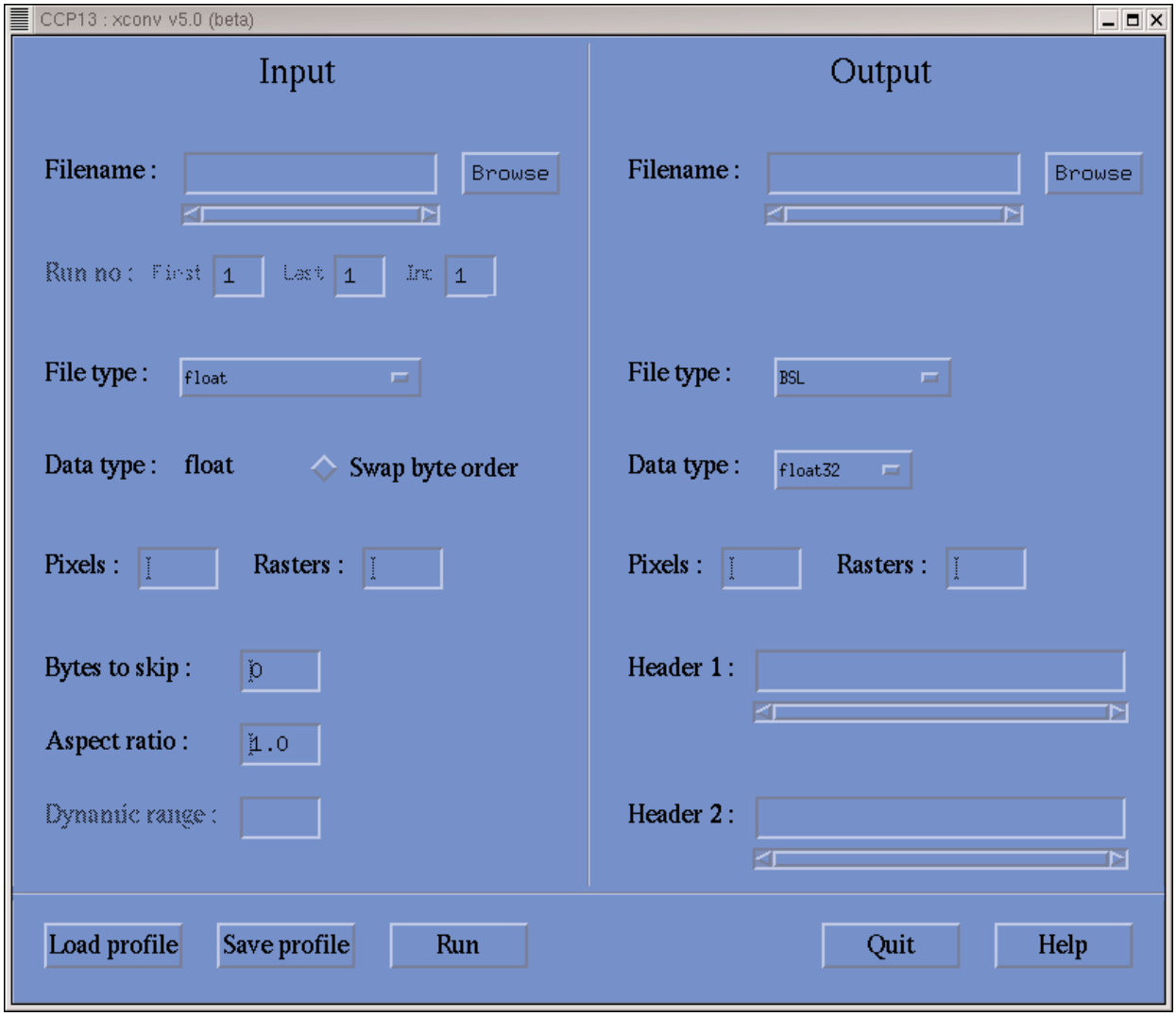

Figure 4: Illustration of the XCONV graphical user interface.

2-D Image Data File Conversion

XCONV *R. Denny (updated Ganeshalingam Rajkumar - December 2002*)

XCONV provides for the conversion of various image data files (e.g. from a variety of detector systems) to either **BSL** or **TIFF** format with the aid of an OSF/Motif-based graphical user interface (GUI). It replaces the CONV program. The XCONV window (Fig. 4) is split into two sections relating to the input image data file(s) and the output BSL file (header file + data file) or TIFF file.
The following input file types are allowed: **float** - float, **int** - unsigned int, **short** - unsigned short, **char** - unsigned char, **smar** - small MAR image plate (1200 x 1200), **bmar** - big MAR image plate (2000 x 2000), **fuji** - Fuji image plate (2048 x 4096), **fuji2500** - BAS2500 Fuji image plate (2000 x 2500), **rax2** - R-Axis II image plate, **rax4** - R-Axis IV image plate, **psci** - Photonics Science CCD, **riso** - RISO file format, **tiff** - TIFF (8,12,16-bit greyscale with all Compression type), **ESRF Id2 (KLORA)** - ESRF Data Format, **LOQ 1D** - one dimensional ASCII data files recorded at LOQ, **LOQ 2D** - two dimensional ASCII data files recorded at LOQ, **SMV** - used by ADSC CCD detectors (8 bit unsigned, 16 bit unsigned, 32 bit signed integer, 32 bit floating), **ESRF Id3** - ESRF Data Format, **BRUKER** - Area detector Frame format Siemens/Bruker file format (8 ,16 or 32 bits per pixel), **Mar345** - MAR345 Image Plate (File extension mar1200, mar1800, mar1600, mar2400, mar2000, mar3000, mar2300, mar3450), **BSL** - the Daresbury NCD BSL file format as described in the BSL manual.

Output formats are: **BSL** - The BSL file format (suitable for input to XFIX, FTOREC and LSQINT), **TIFF8** - 8 bit greyscale tiff image and **TIFF16** - 16 bit greyscale tiff image.

2D Intensity Stripping

XFIX: *R. Denny (updated Mark Shotton - April 99; Ganeshalingam Rajkumar - December 2002*)

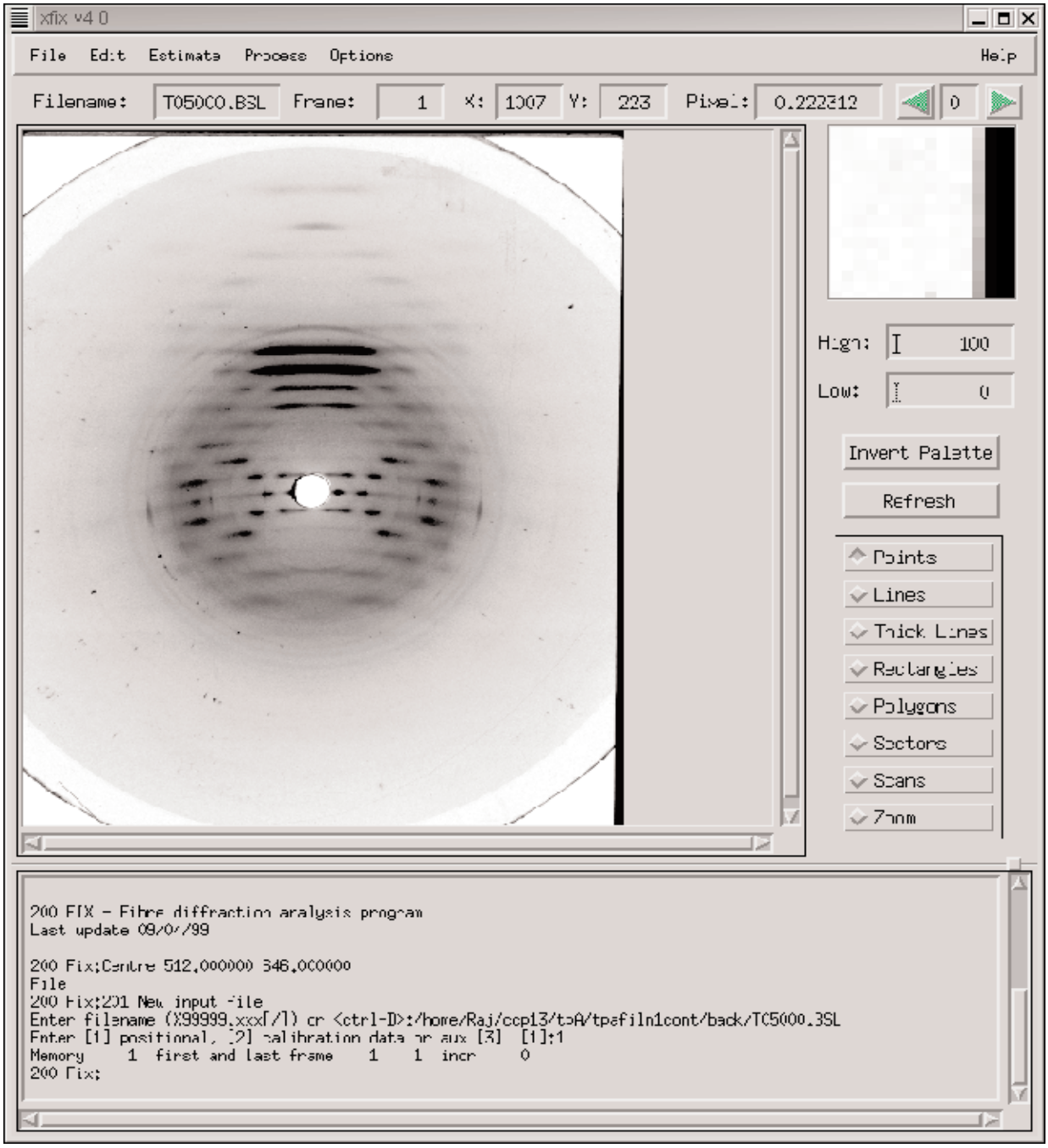

Figure 5: A raw fibre diffraction pattern visualised in XFIX.

XFIX is designed to help ascertain important parameters of a fibre diffraction pattern with the aid of an OSF/ Motif-based graphical user interface (GUI; Fig. 5). The job of the program is to handle the image display, collect information specifying regions of the data and to communicate with the program FIX which performs much of the underlying data-processing. Information such as the pattern centre, detector orientation and fibre tilt can be estimated and refined and putative unit cells can be plotted over the pattern. In addition, more general functions are available such as the capability to plot and fit integrated slices or scans through the pattern. The program also allows the use of three background subtraction tools - the choice of which will depend on the type of data being studied. The background options are: (a) Paul Langan's "roving window" method, (b) a circularly-symmetric background and (c) calculation of a "smoothed" background through iterative low-pass filtering based on the method of Ivanova and Makowski (1998).

FTOREC: *R. Denny (updated Mark Shotton April 99; Ganeshalingam Rajkumar - December 2002*)

This program is designed to take all or part of a diffraction image and transform this portion of the image into reciprocal space, given knowledge of the specimen to film distance, orientation of the image,

XFIX IN ACTION

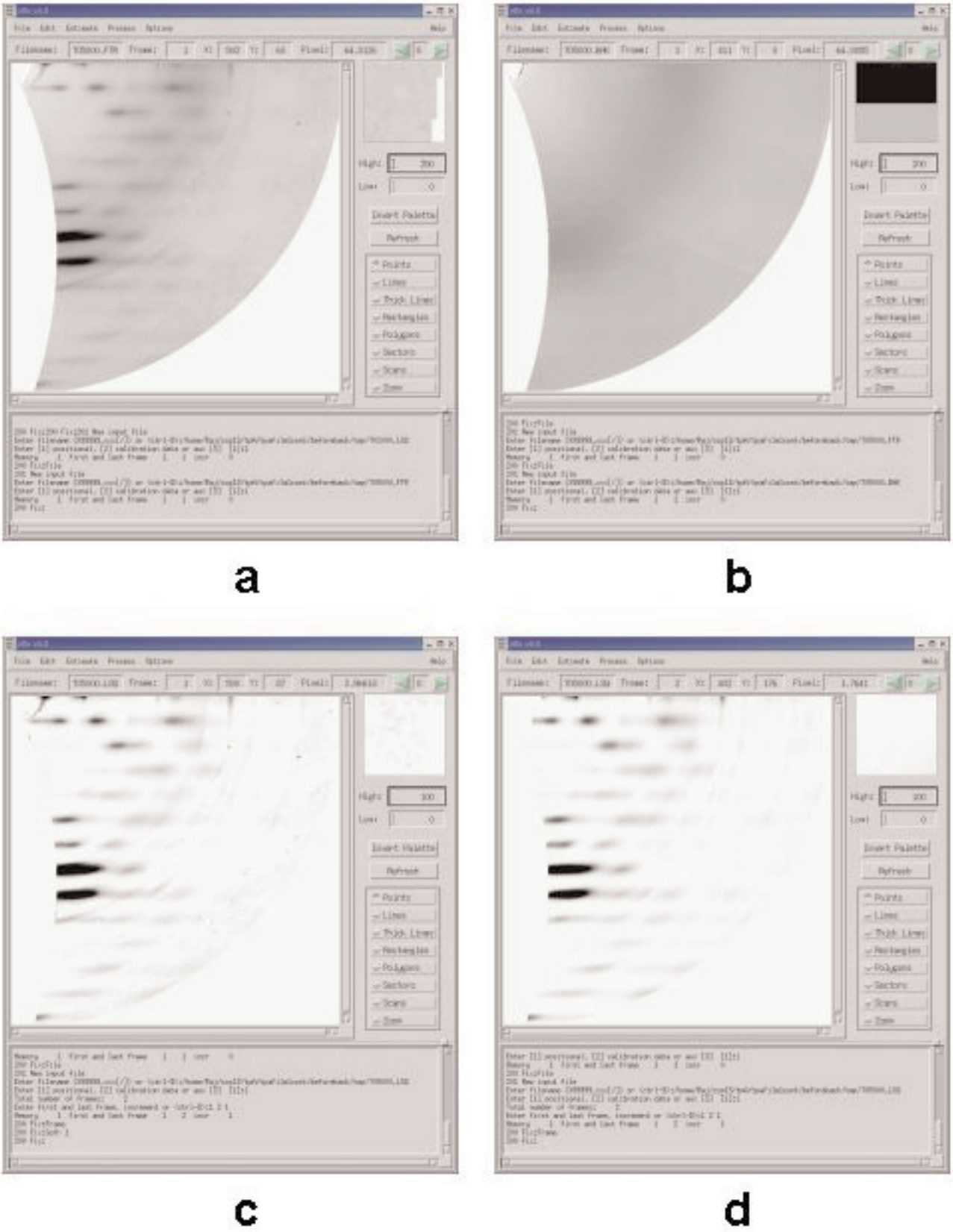

Figure 6: Stages in the processing of the pattern in Figure 5, all displayed using XFIX. **(a)** The spatially-corrected, quadrant-folded version of Figure 5 using parameters determined in XFIX and implemented in FTOREC. **(b)** The estimated background in (a). **(c)** Pattern in (a) after removal of the background in (b). This represents the Bragg diffraction peaks that need to be fitted by LSQINT. **(d)** The best fit to the intensity distribution in (c) as determined using LSQINT, with the LSQINT output redisplayed in XFIX using both the peak intensity values and the estimated peak shapes, fibre disorientation angle etc as needed to get a good fit in LSQINT.

wavelength and tilt of the specimen determined in XFIX. Either polar or Cartesian reciprocal space outputs are available. The effect of this transformation is to straighten out the diffraction pattern and to apply appropriate scaling to detector pixel values as described in Fraser *et al* (1976). The corrected, quadrant-folded image can then be re-displayed in XFIX (Figs. 5, 6)

LSQINT: *R. Denny (updated Mark Shotton - April 99; updated for WINDOWS (DOS) Ganeshalingam Rajkumar - January 2003)*

The purpose of LSQINT is to provide an automatic method for the integration of intensities for fibre diffraction data. The program will handle patterns which are largely crystalline in nature, or patterns which have intensity continuously distributed along layer-lines, with sampling only occurring parallel to the c-axis. More than one lattice can be fitted in a single pattern. The approach used is to generate spot profiles and then to fit these profiles to the observed pixel values by a robust linear least-squares method or using the maximum entropy method of Skilling and Bryan (1984). A typical result is shown in Figure 6. Several background subtraction methods are available: (a) a global background can be fitted simultaneously with the spot profiles, (b) a circularly symmetric background can be fitted, (c) a notional roving aperture and filter can be used to define a background, or (d) a background plane can be fitted in a region of the pattern along with the spot profiles, the background at the centres of the regions being joined by an interpolating surface (Shotton *et al*., 1998). Alternatively, the background subtraction can be done in XFIX (see above) prior to entry into LSQINT. Refinement of the cell and profile parameters is also available by a downhill-simplex method. This can be cycled with the profile fitting to produce an overall refinement procedure.

Figure 6(a) shows an original FTOREC-treated fibre diffraction pattern as viewed in XFIX. Figure 6(b) shows the estimated background. Figure 6(c) shows the pattern in 6(a) minus the background - it represents the Bragg peaks to be fitted by LSQINT. Finally Figure 6(d) shows the LSQINT fit to the peaks when replotted in XFIX with the same peak profiles, disorientation etc parameters that give a good fit in LSQINT.

SAMPLE: *R. Denny*

This program performs Fourier-Bessel smoothing of intensities extracted from continuous layer-line data as produced by LSQINT, using the formula described by Makowski (1982). The data are fitted using singular value decomposition to give intensity values at the specified number of knot points.

FDSCALE: *R. Denny*

FDSCALE provides a means of scaling intensities produced in LSQINT from different data sets.

FD2BSL: *R. Denny*

This converts the ASCII output from LSQINT (or FDSCALE) output files to BSL format, allowing flexibility in the output image dimensions and $I/\sigma(I)$ cut-offs for intensity rejection. The output file has one raster per layer-line and a user-defined number of pixels per raster. For Bragg-sampled data, the intensity of a reflection is divided by its multiplicity so that a representation of the cylindrical average of the squared molecular transform is given.

One-dimensional Peak Fitting

XFIT: *R. Denny (updated Mark Shotton - August 98)*

XFIT provides a flexible means of fitting various peak shapes to 1D intensity data and is particularly suited to fitting a sequence of time-resolved data. A polynomial and/or exponential background can be fitted along with the peaks and simple constraints can be applied between pairs of parameters. Once an initial model has been specified, the program can run through a sequence of data frames refining the previous best parameter set to fit the current frame. If the fit worsens unacceptably between consecutive frames, the user is warned and the starting model for the current frame can be specified interactively. An illustration of XFIT in action is given in Figure 7.

Small-angle Scattering

CORFUNC: *T.W. Nye (updated Richard Denny, Mark Shotton - 1999; updated Matthew Rodman - 2002/3)*

This is a suite of programs for calculating one and three-dimensional correlation functions (Γ_1 and Γ_3) from small-angle scattering (SAXS) data. Operation of the programs can be broken down into three logical steps:

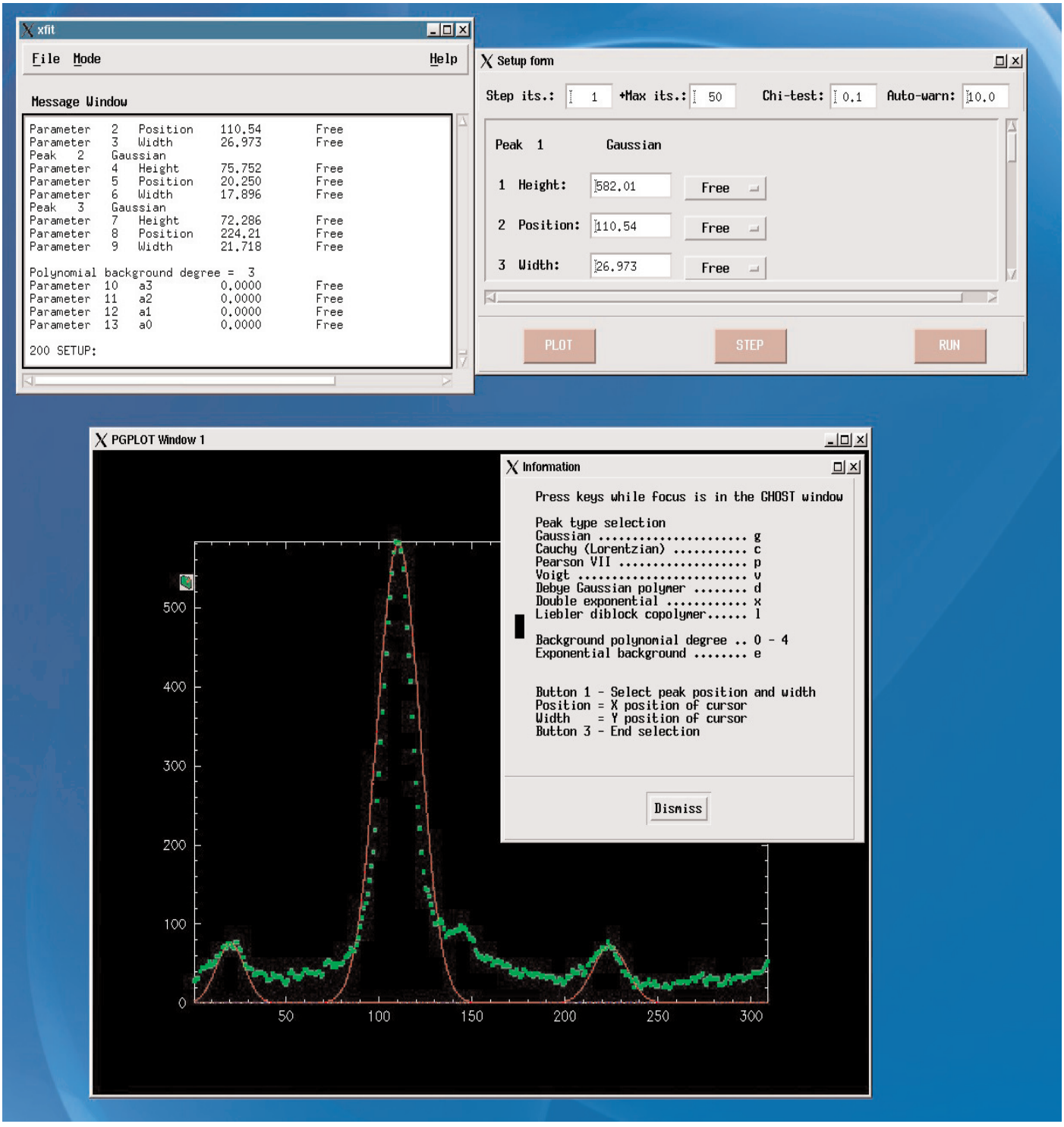

Figure 7: An example of XFIT in action showing modelling peaks roughly in position on a plot of experimental data points (lower window) before any optimisation has been carried out.

(i) Extrapolation of the experimental SAXS curve to $q = \infty$ and $q = 0$ (TAILFIT, TAILJOIN).
(ii) Fourier transformation of the extrapolated data (TRANSFORM).
(iii) Interpretation of Γ_1 based on ideal lamella morphology (EXTRACT).

The individual programs involved are given in brackets; they are run in sequence by the CORFUNC shell script.

CORFUNC has recently been modified so that it is more flexible in handling ASCII input; it is now less strict about numeric format and file termination. Also, the error-handling mechanism in the underlying EXTRAPOLATE.F program has been substantially re-written with the aim of being less ambiguous; the previous mechanism was somewhat degenerate (that is, many diverse error sources mapped to the same error code and message). More

importantly, however, is the change made to CORFUNC's convergence behaviour in the module TRANSFORM.F. Here, the maximum **q**-value permissible has been dramatically extended to enable data processing with larger **q**-ranges. This has led to only a minor increase in transform convergence times, inconsequential when compared to overall process duration.

Future developments planned for Corfunc involve adding the option of employing a Hilbert transform. This type of analysis is used to generate segment density distribution functions of adsorbed polymers from SANS data. Currently there are no public domain programs to do this. The work will thus bring CCP13 to the attention of a new audience and will be undertaken with the kind assistance of Steve King (ISIS).".

A useful tutorial on analysing solution scattering data is given at:
http://www.srs.dl.ac.uk/ncd/Saxs_Training_School_overheads/SoftwareTrainingWorkshop.html

DEVELOPMENTS IN HIGH-RESOLUTION MODELLING

FX-PLOR: *A Patch for X-PLOR: (Richard Denny, Mark Shotton - 1999/2000)*

In full consultation with Prof. A. Brunger, CCP13 has written and developed a patch (Denny *et al.*, 1997) that enables X-PLOR (Brunger *et al.*, 1987) to be used with fibre diffraction data. The CCP13 patch follows that created by Wang & Stubbs (1993) for the use of continuous fibre diffraction data. This allows (a) connectivity between symmetric units of crystallographic or strict non-crystallographic symmetry to be maintained and (b) diffraction data to be treated as composite intensities or overlapping Bessel function contributions. For the poly-crystalline part of the patch where the situation is more likely to require approximate helical symmetry and strict crystallographic symmetry, the symmetry linkage routines were modified so that a continuous chain can be built passing from asymmetric unit to asymmetric unit or through the bottom and top of the unit cell. The target functions were also redefined to take account of reflection overlap and the residual function changed to deal with composite intensities rather than structure factor moduli. The patch is a CCP13 creation and does not work without X-PLOR itself, which must be acquired using the normal routes for academic or commercial users.

LALS - Linked-Atom Least Squares analysis

Linked Atom Least Squares (LALS) has proved to be a very successful method of analysing fibre diffraction data from microcystalline fibres (Arnott & Wonacott, 1966; Arnott *et al.*, 1969). It allows the refinement of a stereochemically valid model against observed diffraction intensities with constraints and restraints to force non-crystallographic repeat geometry and intra- and inter-molecular contacts. A Windows version of LALS has been developed and will be available for incorporation in the CCP13 suite in the coming year. It is our intention to maintain a single distributed executable which runs also under Linux using WINE.

Several support programs are being developed for LALS mainly concerned with display and manipulation of the molecular model. Once these have been further developed in practice they too will be incorporated into the CCP13 suite.

Outputs can be viewed using MolScript or PdbViewer.

DEVELOPMENTS IN MODELLING MACROMOLECULAR ASSEMBLIES

Over the last decade the low-angle diffraction facilities at Daresbury have gradually improved and developed so that lines 2.1, 8.2 and now 14.1 are excellent cameras for low-angle and high-angle fibre diffraction work and line 16.1, with its high intensity, together with the RAPID detector system (see below), currently represents, because of the speed of the detector, the best available beamline worldwide for very fast time-resolved low-angle X-ray diffraction experiments on dynamic processes. Such processes include phase transitions in synthetic polymer systems (seconds) and molecular movements in muscular contraction (milliseconds and less). Other beamlines at third generation sources (e.g. line ID02 at the ESRF and the BioCAT beamline at the APS), because of their superb brilliance, can produce very high quality diffraction patterns on image plates or on CCD detectors, but the readout speed remains relatively slow.

The Daresbury detector group has pioneered the development of very fast 2-dimensional multiwire

proportional counters. The resulting RAPID detector allows previously impossible time-resolved low-angle diffraction studies to be carried out. For example, the whole of the low-angle diffraction pattern from muscle (spacings between, say, 600 Å and 40 Å) can be followed with 1 ms time resolution during typical contraction cycles (Harford & Squire, 1992; 1997; Squire, 1998; 2000). The most intense parts of the pattern can be recorded with 100 µs time resolution (Irving *et al.*, 1992; Lombardi *et al.*, 1995). Now that such experiments can be done, and even more sophisticated experiments are in the offing, it is crucial that the data being recorded so successfully should be rapidly stripped and analysed to produce definitive results about the particular specimen involved.

A key aspect of the on-going CCP13 programme is the development of software to model low-resolution structures (e.g. macromolecular assemblies), to compute their transforms and to refine them against the observed, peak-fitted intensity data. Some highly effective, subject-specific modelling programs are already being developed (e.g. the program MOVIE which carries out simulated annealing modelling of muscle diffraction patterns; Hudson *et al.*, 1997; Squire *et al.*, 1998; Squire 2000), but what is needed is more general modelling software that will be applicable to most kinds of fibrous molecular assemblies. This is a demanding task, but with the advent of much faster computers and parallel processing options, the problem of refining models against observed data is now becoming tractable and is one of the aims of the current CCP13 project.

Future Modelling Strategies

Another approach, complementary to that already used, but possibly more powerful when fibre disorientation causes layer-line overlap at higher radii, is to use the correctly mapped whole diffraction patterns as targets against which to do 'whole pattern fitting' by modelling (e.g. Lorenz *et al.*, 1993). Thus a model, as described above, could also include all the fibre disorder factors as parameters, so that the whole diffraction pattern, including background and overlapping layer-lines, is modelled and refined in one process.

CONCLUSIONS

In summary, good software to extract intensity data from diffraction patterns produced by non-crystalline materials is available as part of the CCP13 package. Although these programs work extremely well, we are currently producing a front end JAVA driven program that will integrate all aspects of the measurement software from raw data to reduced intensities whether they relate to a crystalline system or to continuous diffraction (i.e. it will link XCONV, XFIX, FTOREC and LSQINT into a common program). We believe that this front-end overlay will reduce the "energy barrier" for new users as well as providing addition useful functionality. At the same time existing programs are being modified and updated and new software is being developed to model the observed intensities at high or low resolution in terms of realistic molecular structures.

In the final analysis, a primary objective of CCP13 is to solve structures by fibre X-ray diffraction in as rigorous and objectively tested a manner as is being done, for example, in protein crystallography. We need to define objective assessment procedures that can be demonstrated to be effective and which meet with general acceptance so that structures solved from fibre diffraction patterns are considered to be just as reliable as those of globular proteins treated using CCP4 tools.

Acknowledgements

The work of CCP13 described here is supported by a project grant (#25/B15281) from the BBSRC & EPSRC, and directly employs Jane Crawshaw, David Dover (60%), Andrew He, Ganeshalingam Rajkumar and Matthew Rodman (50% BBSRC/EPSRC, 50% CLRC).

REFERENCES

[1] Arnott, S. (1999) Lessons for today and tomorrow from yesterday. *Fibre Diffraction Review* **8**, 21-27.
[2] Arnott, S. & Wonacott, A.J. (1966) Atomic co-ordinates for an α-helix: refinement of the crystal structure of α-poly-l-alanine. *J. Mol. Biol.* **21**, 371-83.
[3] Arnott, S., Dover, S.D. & Wonacott, A.J. (1969) Least-squares refinement of the crystal and molecular structures of DNA and RNA from X-ray data and standard bond lengths and angles. *Acta Cryst.* **B25**, 2192-2206.
[4] Brunger, A.T., Kuriyan, J. & Karplus, M. (1987) Crystallographic R-factor refinement by molecular dynamics. *Science* **235**, 458-460.
[5] Denny, R.C. (1993) Integration of fibre diffraction patterns. *Fibre Diffraction Review* **2**, 5-8.
[6] Denny, R.C. (1994) CCP13 Program Developments. *Fibre Diffraction Review* **3**, 12-16.
[7] Denny, R.C. (1995a) CCP13 Program Updates. *Fibre*

Diffraction Review **4**, 8-10.
[8] Denny, R.C. (1995b) Assessment of the Torus algorithm for global optimisation. *Fibre Diffraction Review* **4**, 11-14.
[9] Denny, R.C. (1996) Fibre diffraction spot profiles and the Lorentz correction. *Fibre Diffraction Review* **5**, 24-27.
[10] Denny, R.C., Shotton, M.W. & Forsyth, V.T. (1997) X-PLOR for polycrystalline fibre diffraction. *Fibre Diffraction Review* **6**, 30-33.
[11] Fraser R.D.B., Macrae T.P., Miller A. & Rowlands R.J. (1976) Digital processing of fibre diffraction patterns. *J. Appl. Cryst.* **9**, 81-94.
[12] Harford, J.J. & Squire, J.M. (1992) Evidence for structurally different attached states of myosin cross-bridges on actin during contraction of fish muscle. *Biophys. J.* **63**, 387-396.
[13] Harford, J.J. & Squire, J.M. (1997) Time-resolved studies of muscle using synchrotron radiation. *Reps. Progr. Physics* **60**, 1723-1787 (1997).
[14] Hudson, L., Harford, J.J., Denny, R.J. & Squire, J.M. (1997) Myosin head configurations in relaxed fish muscle: resting state myosin heads swing axially by 150Å or turn upside down to reach rigor. *J. Mol. Biol.* **273**, 440-455.
[15] Irving, M., Lombardi, V., Piazzesi, G. & Ferenczi, M.A. (1992) Myosin head movements are synchronous with the elementary force-generating process in muscle. *Nature* **357**, 156-158.
[16] Ivanova, M.I. & Makowski, L. (1998) Iterative low-pass filtering for estimation of the background in fiber diffraction patterns. *Acta Cryst.* **A54**, 626-631.
[17] Jones, T.A., Zou, J.Y., Cowan, S.W. & Kjeldgaard, M. (1991) Improved methods for building protein models in electron density maps and the location of errors in these models. *Acta Cryst.* **47**, 110-119.
[18] Lombardi, V., Piazzesi, G., Ferenczi, M.A., Thirlwell, H., Dobbie, I. & Irving, M. (1995) Elastic distortion of myosin heads and repriming of the working stroke in muscle. *Nature* **374**, 553-555.
[19] Lorenz, M., Popp, D. & Holmes, K.C. (1993) Refinement of the F-actin model against X-ray fiber diffraction data by the use of a directed mutation algorithm. J. Mol. Biol. 234, 826-836
[20] Makowski, L. (1982) The use of continuous diffraction data as a phase constraint. II. Application to fiber diffraction data. *J. Appl. Cryst.* **15**, 546-557.
[21] Shotton, M.W. & Denny, R.C. (1999) CCP13 software development. *Fibre Diffraction Review* **8**, 14-19.
[22] Shotton, M.W., Denny, R.C. & Forsyth, V.T. (1998) CCP13 Software development. *Fibre Diffraction Review* **7**, 40-44.
[23] Skilling, J. & Bryan, R.K. (1984) Maximum entropy in image reconstruction: general algorithm. *Mon. Not. R. Astr. Soc.* **211**, 111-124.
[24] Squire, J.M. (1998) Time-resolved X-ray Diffraction. In '*Current Methods in Muscle Physiology: Advantages, Problems and Limitations' IUPS Commission on Muscle Physiology (H. Sugi, Ed.)* 241-285. Oxford University Press.
[25] Squire, J.M. (2000) Fibre and Muscle Diffraction" in *Structure and Dynamics of Biomolecules (E. Fanchon, Geissler, L-L. Hodeau, J-R. Regnard & P. Timmins, Eds)* pp. 272-301. Oxford University Press, Oxford, UK.
[26] Squire, J.M., Cantino, M., Chew, M., Denny, R., Harford, J.J., Hudson, L. & Luther, P.K. (1998) Myosin rod packing schemes in vertebrate muscle thick filaments. *J. Struct. Biol.* **122**, 128-138.
[27] Squire, J.M., Knupp, C., AL-Khayat, H.A. & Harford, J.J. (2003). Millisecond Time-Resolved Low-angle X-ray Fibre Diffraction: A Powerful, High-Sensitivity Technique for Modelling Real-Time Movements in Biological Macromolecular Assemblies. *Fibre Diffraction Review* **11**, 28-35.
[28] Stubbs, G. (1999) Developments in fiber diffraction. *Curr. Opin. Struct. Biol.* **9**, 15-619.
[29] Wang, H. & Stubbs, G. (1993) Molecular dynamics in refinement against fiber diffraction data. *Acta Cryst* **A49**, 504-513.

SRS Station MPW6.2 - A New Facility for variable energy SAXS/WAXS at the Daresbury Laboratory

N. J. Terrill[1], G. Bushnell-Wye[1], R. J. Cernik[1,2,3], A. J. Dent[1], G. P. Diakun[1], C. J. V. Flaherty[1], J. Kay[1], C. Tang[1], P. Barnes[2], G. N. Greaves[4], T. Rayment[5] and A. Ryan[6]

[1] Daresbury Laboratory, Warrington WA4 4AD, UK
[2] Department of Crystallography, Birkbeck College, London WC1E 7HX
[3] Manchester Materials Science Centre, University of Manchester and UMIST, Grosvenor St, Manchester M1 7HS
[4] Department of Physics, The University of Wales, Aberystwyth, Penglais, Aberystwyth, Ceredigion, SY23 3BZ
[5] Department of Chemistry, University of Cambridge, Cambridge CB2 1TN, UK
[6] Department of Chemistry, University of Sheffield, Western Bank, Sheffield S10 2TN, UK

ABSTRACT

Station 6.2 has entered its commissioning phase having taken "first light" in November 2001 (Fig. 1). A team comprising elements from SRD, ID and ED departments at Daresbury Laboratory (Fig. 2) built the beamline. The project has also benefited from the scientific direction given by four University Partners: Dr. Trevor Rayment - Department of Chemistry, University of Cambridge; Prof. Neville Greaves - Department of Physics, University of Aberystwyth; Prof. Tony Ryan - Department of Chemistry, University of Sheffield and Prof. Paul Barnes - Department of Crystallography, Birkbeck College London. The project, funded by the EPSRC, forms part of the SRS upgrade which began in 1998. The commissioning phase is due to be completed in December 2002 and the Station should be handed over for user operations in the spring of 2003.

Introduction

Significant advances in technology over recent years have resulted in scientists who use the SRS requiring sample cells that mimic the real world ever more closely. As a result they require facilities that can collect data faster and on smaller or more dilute systems. Pressure, temperature, pH, humidity and the presence of corrosive atmospheres are all part of the current experimental trend. The new beamline is capable of taking full advantage of the high flux generated by MPW 6 to deliver high quality research in all of the above areas with unprecedented accuracy and at millisecond timescales.

Figure 1: First light in the MPW 6.2 Experimental Hutch.

X-ray delivery and Optics

A ten-pole wiggler, identical in design to that installed on beamline 14 and described by Duke *et al.* (1998) has been installed in straight section 6 (Fig. 3) of the SRS. The characteristics for the source can be found in Appendix A.

The X-ray flux output of the device reaches a peak at approximately 8 keV. The practical photon energy range (5 to 18 keV) is defined by beryllium window absorption at low energy and the high-energy flux limit from the 2T magnetic poles of the insertion device. The total radiation fan from the multipole wiggler on beamline 6 has been split into two sections 9.8 m from the tangent point. A plane mirror deflects 7.5 mrad of beam in the UV energy range for use in station MPW6.1 (Bowler *et al.*, 2002). The first beamline element on MPW6.2 is a water-cooled defining aperture at 12.88m that defines an X-ray beam of 4.5 mrad (horizontal) and 1.4 mrad (vertical). This is followed by a set of

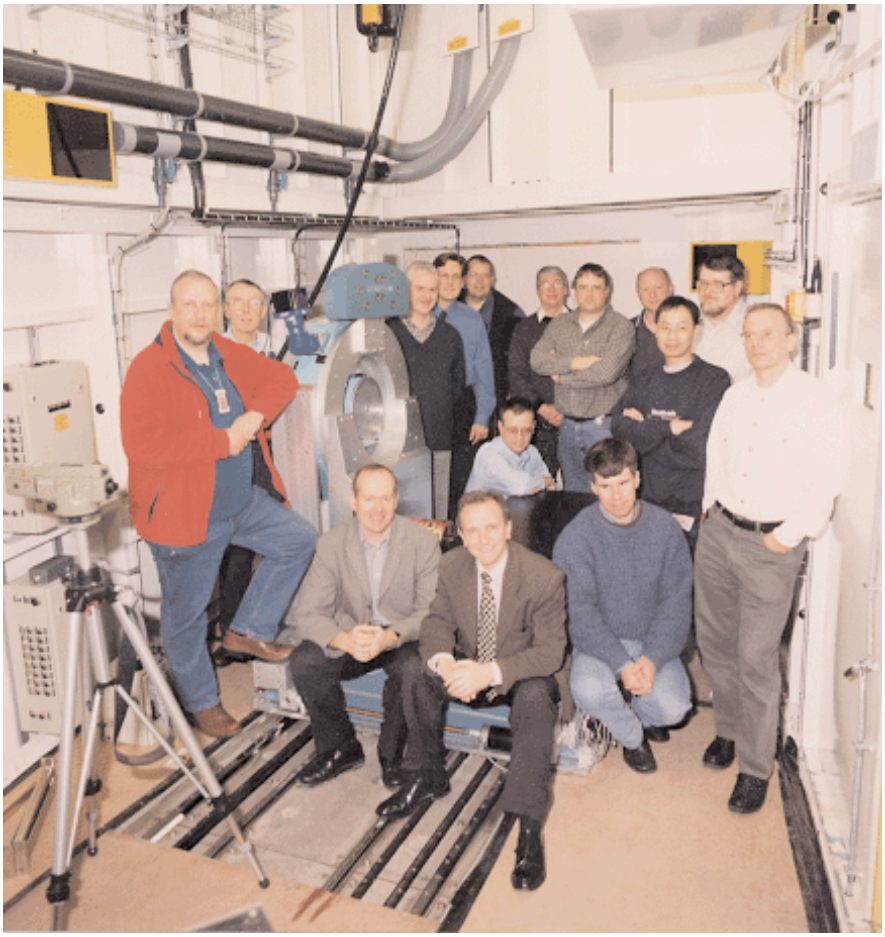

Figure 2: The DL team responsible for the project.

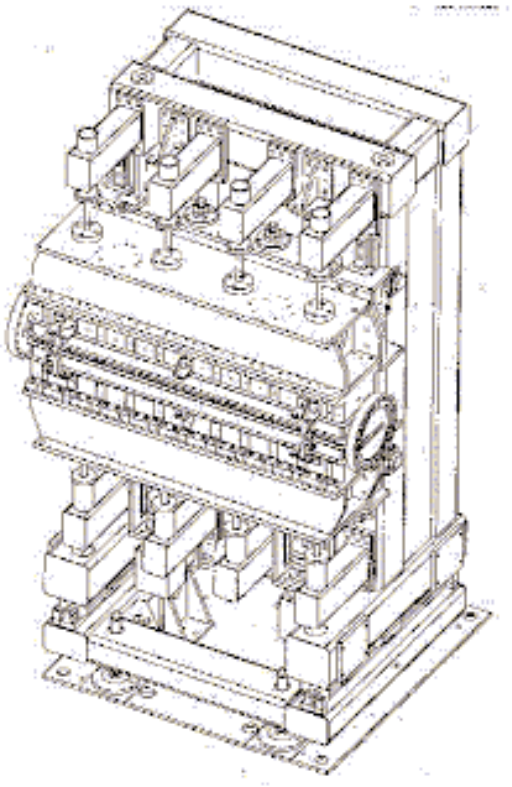

Figure 3: A schematic of the MPW insertion device from which Station 6.2 will obtain its X-rays.

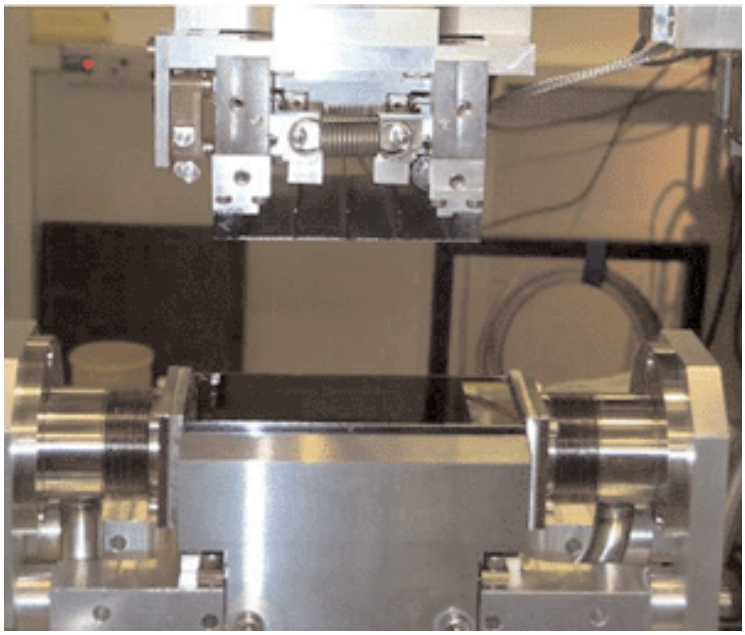

Figure 4: Sagittal Monochromator showing ribs of top crystal.

water-cooled slits. The beam is then collimated by the first of two identical planar, cylindrically bent, Si mirrors (1200 x 120 x 50 mm with a 500 Å rhodium coating). The sagittal-crystal monochromator, designed by Bilsborrow *et al.* (in preparation) and shown in Figure 4, gives both energy selection and horizontal focussing. The monochromator has a flat, water-cooled, first crystal cut along the [111] direction. The second Si crystal, also cut along the [111] direction, is sagittally bent and collects the entire available horizontal aperture. It has 4 ribs to prevent anticlastic bending. The focal point of the second crystal can be adjusted to any point in the experimental area over a range of 5 m.

A second set of slits, immediately after the monochromator, provides further beam definition. These slits directly precede a second mirror, which provides vertical focussing for the beamline. A third set of slits has been installed after the mirror and is in turn followed by the station stop. The monochromator and mirror systems are all contained within a separate optics hutch in order to reduce parasitic scattering. Two further sets of slits are accommodated in the experimental hutch to reduce parasitic scatter still further for SAXS experiments. The overall beamline layout is shown in Figure 5.

Experimental Station

The experimental station is designed on a modular basis for complete flexibility. Unlike other NCD stations at the SRS, the station does not have an optical bench so experiments can be built up from the floor of the hutch giving extra versatility in sample environment design. A system of rails has been incorporated into the floor of the hutch to aid alignment. The two options in Figure 6 are representative of what is possible, but are by no means exhaustive. SAXS cameras can be built to any length between 1m and 4m with 25cm intervals. Coupled to the energy capabilities, this leads to a very adaptable station environment indeed.

Detectors

The beamline has been built to take advantage of recent developments in detector technology. The centrepiece of the new station, and its most significant development, is the SAXS/WAXS gas multiwire detector combination based on RAPID technology (Helsby *et al.*, 2002). The SAXS detector system, whose funds were included in the project costs, has a 60° quadrant with radius 200mm. The detector is capable of global count rates in excess of 10MHz, with peak resolutions (FWHM) of about 400 μm using 1024 pixels. The curved position sensitive detector for measuring WAXS spectra, also funded by the EPSRC in a separate grant, has a complex and rapid way of interpolating the diffraction peaks (Fig. 7). This enables the detector to obtain a peak resolution of better than 0.06° and data to be collected in milliseconds. This timescale and statistical precision will be a much better match for the complementary small-angle scattering and spectroscopy techniques also available on the station. The detector is capable of collecting 60° in 2θ at a global count rate of at least 10MHz.

Early Commissioning Tests

Initial tests of the station/detector combination have been promising. To give some idea of the quality of data from the WAXS detector, Figure 8 shows a comparison of data collected on HDPE with the INEL detector from Station 8.2. Data are clearly visible at 100μs using the new detector system whereas with the INEL information is difficult to resolve below 1s. A collagen standard sample collected in 120sec is shown to illustrate the quality of data available from the quadrant detector and to give some idea of **q**-range at 10keV with a 3m camera (Fig. 9). Commissioning is still ongoing with both detectors to establish a better understanding of end effects and energy response.

Tests of the SAXS/WAXS combination were carried out by analysing a 0.5 wt% high-density polymer (E76B38) in hexane. Scientifically, this experiment was designed to examine crystallisation in constrained geometries. The block copolymer chains have two hydrophobic amorphous ends and a crystallisable centre. When the ethylene oxide crystallises, the micelle ends up with exposed hydrophilic sides. In a previous study on station 8.2, data from a 10 wt% solution were collected. However, the data contained both structure and form factor information. On station MPW 6.2 using the 0.5 wt% solution, the form factor could be isolated giving information on the shape of individual micelles (Fig. 10(a)). The corresponding wide-angle scattering data are shown in Figure 10(b), crystallisation can be clearly seen taking place within the micellar rafts at $2\theta \approx 19.1$ and 23.4° respectively. Crystallisation at these low concentrations has not previously been observed.

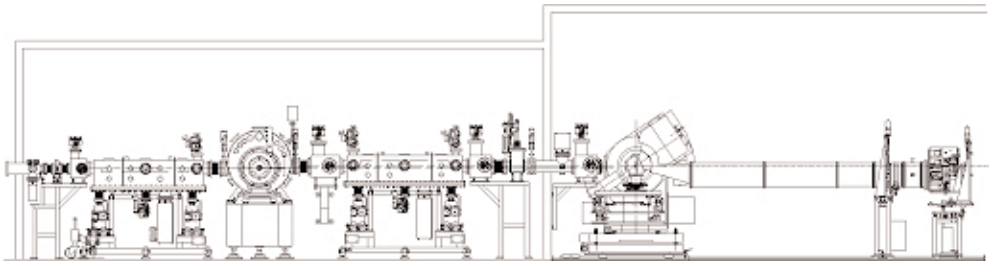

Figure 5: Beamline layout showing optics and experimental hutches.

a)

b)

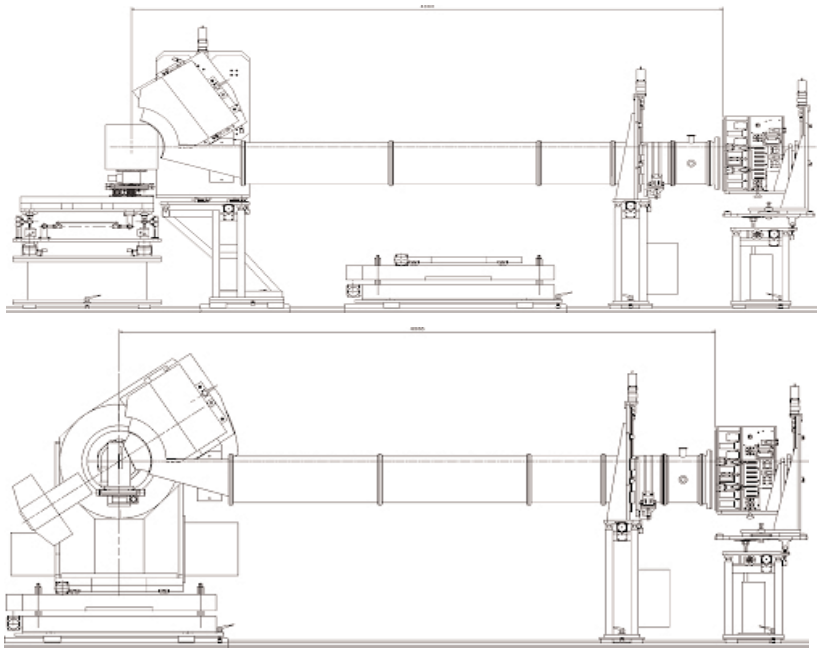

Figure 6: Station configuration options a) with 7-axis sample table and b) with 2-circle diffractometer with 3 axis sample mount.

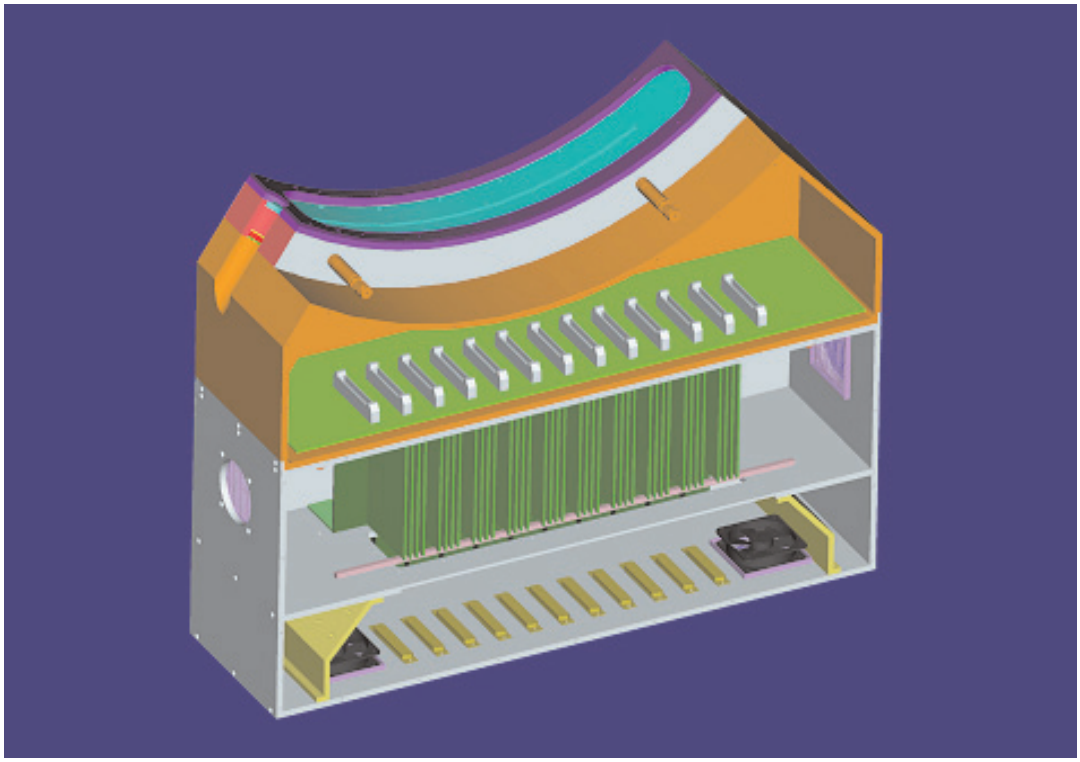

Figure 7: Schematic of the RAPID II Detector body showing basic arrangement of electrical components and connections.

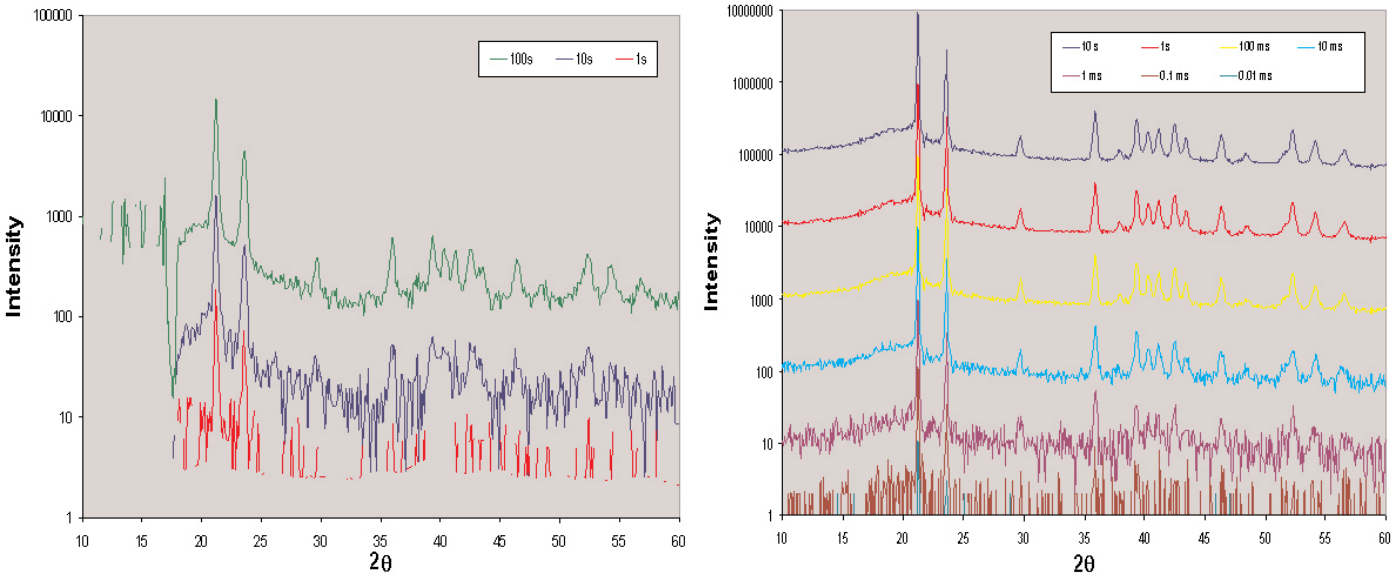

Figure 8: Spectra of the same HDPE sample collected by the INEL detector (left) and RAPID II (right).

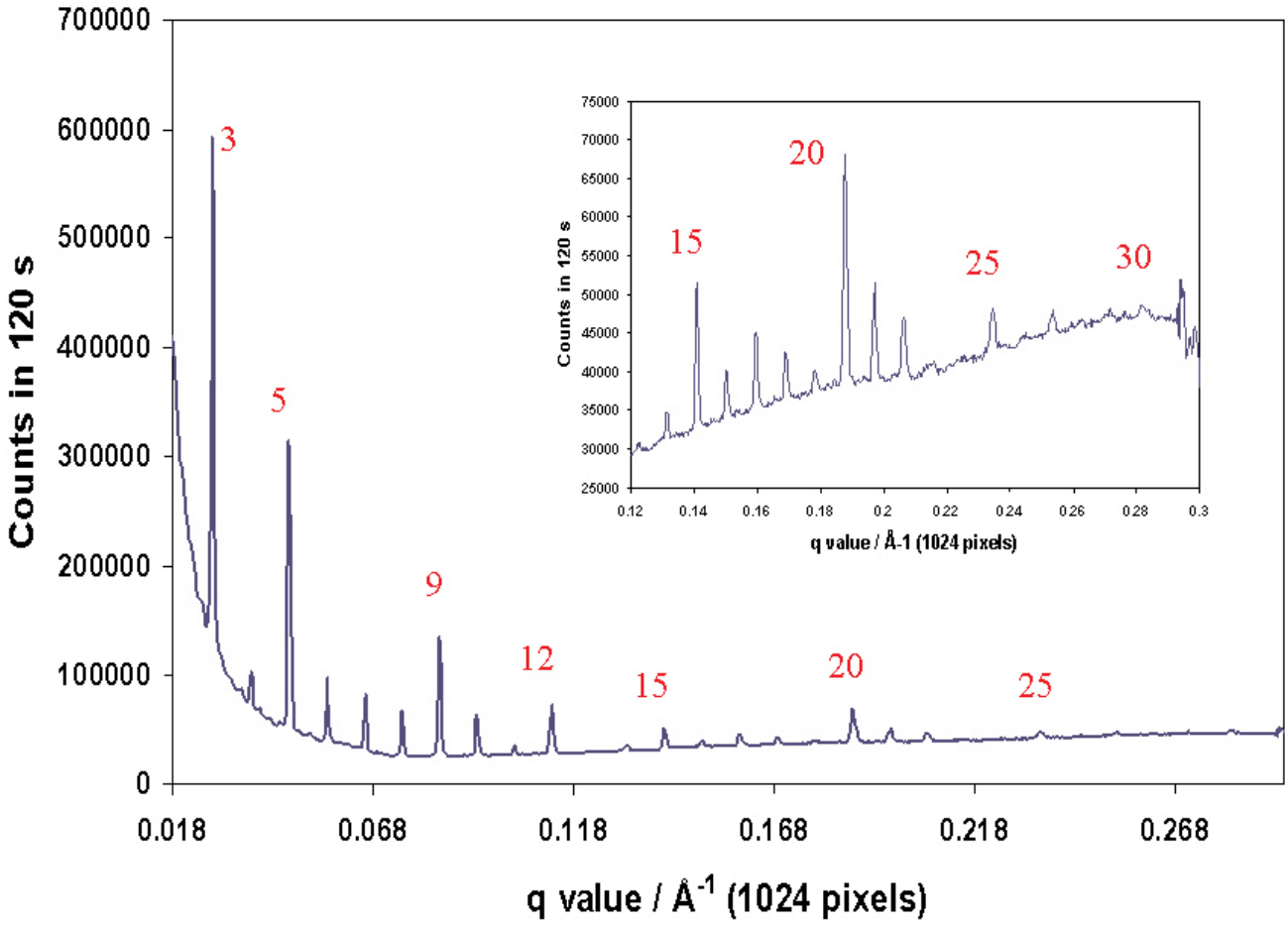

Figure 9: Collagen pattern collected at 3m and 10keV

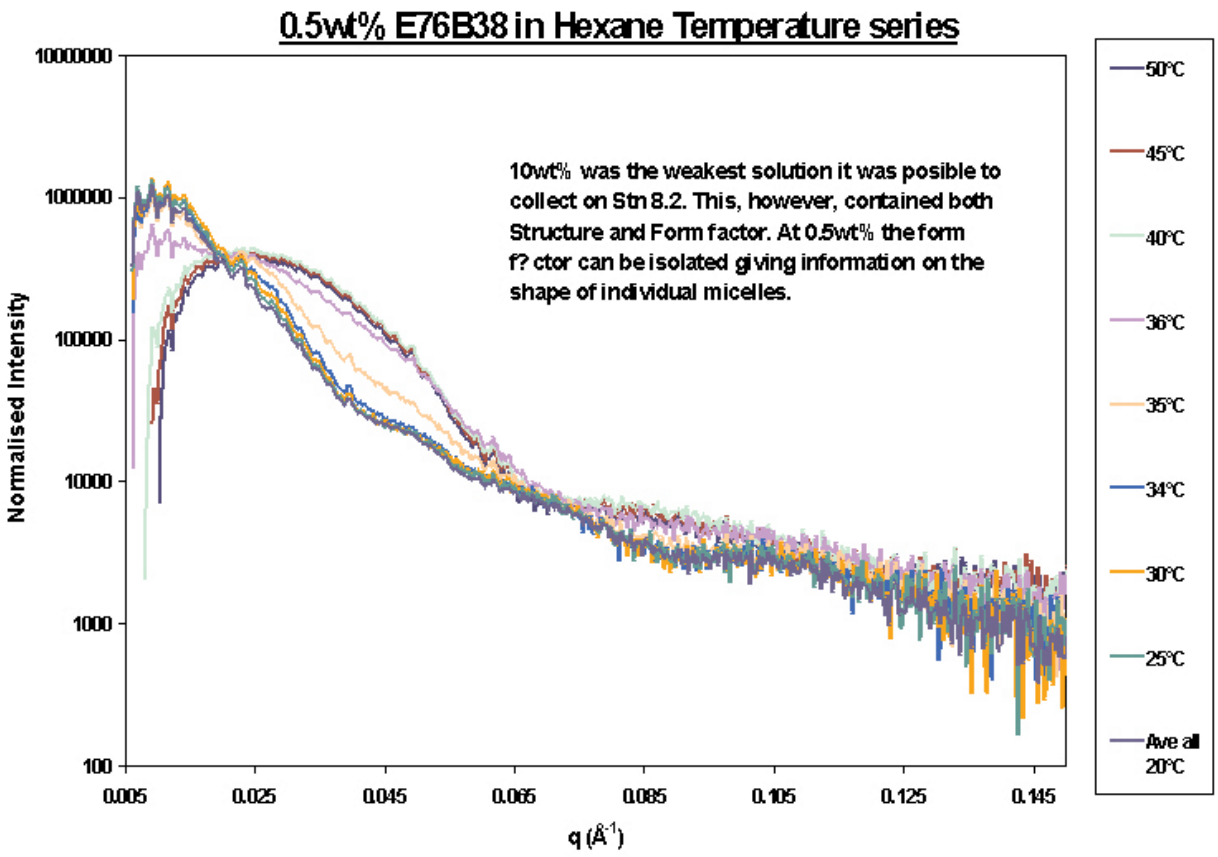

(a)

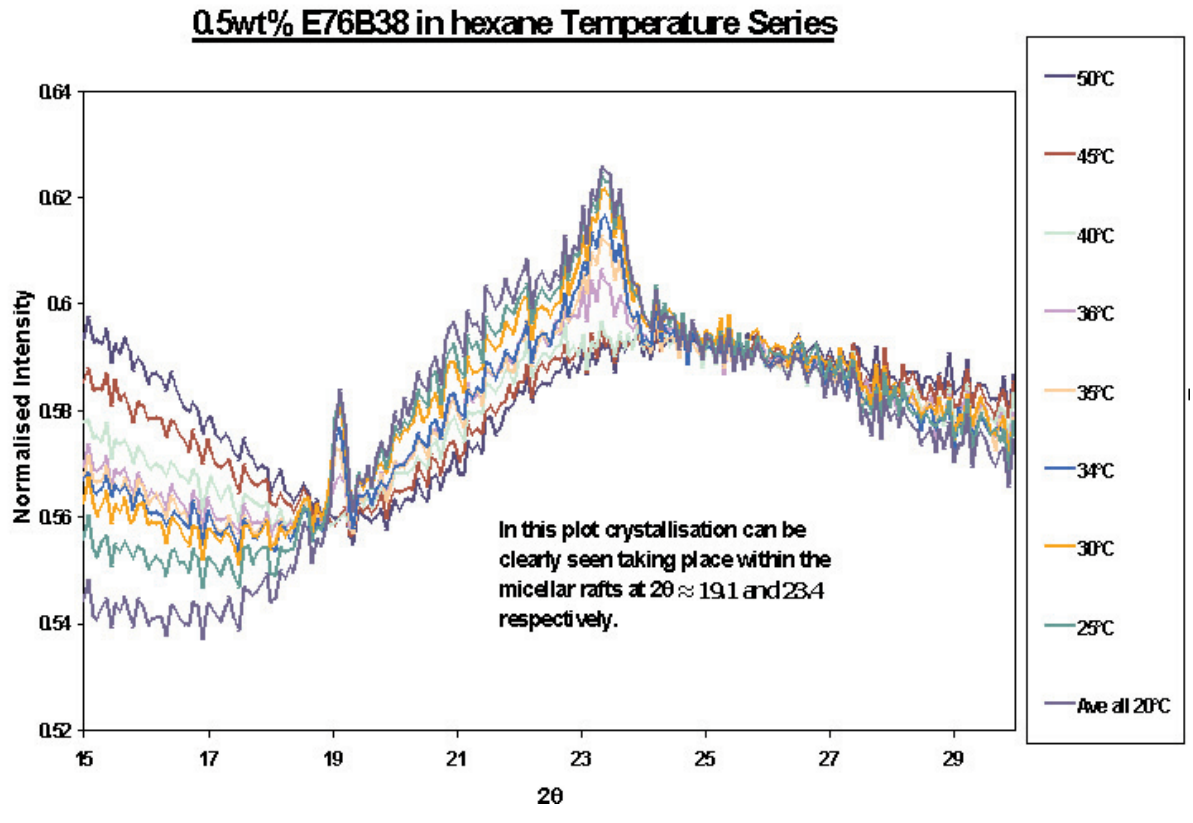

(b)

Figure 10 (a) and (b): Data taken with SAXS and RAPID II

The RAPID 2 wide-angle detector shows at least 3 orders of magnitude improvement over the INEL PSD previously used to collect diffraction data. However, the comparison with the INEL detector is perhaps less relevant, since there are much better detector systems available to users today. For example, the Dutch-Belgian beamline DUBBLE at ESRF (Borsbroom *et al.*, 1998) has an excellent user facility for SAXS/WAXS. The wide-angle component is based on gas-glass microstrip technology. This has inherently higher count rates than RAPID 2, but at present poorer angular resolution. Data collected recently by Ellen Heeley (Manchester Univ.) and Tony Ryan (Sheffield Univ.) demonstrate this point. Figure 11 shows the same polymer data set (Daplen iPP) collected (a) on DUBBLE and (b) on RAPID2 in approximately one hour. The rather poor appearance of the background in (b) is due to incomplete determination of the RAPID 2 instrumental resolution function. However, the count rate, peak height statistics and angular resolution are superior to the ESRF bending magnet beamline.

Future Developments

Closely associated with the project is the development of new data acquisition software. This forms part of the generic data acquisition project at the Daresbury Laboratory. A modular design has been adopted using a JAVA interface and a point and click approach to motor control. Data acquisition is also modular. It will be capable of taking sample environment modules written in a number of common equipment controls languages. Scripting is also a feature. It should be possible to build scripts from the GUI.

References

[1] Duke, E.M.H., Kehoe, R.C., Rizkallah, P.J., Clarke, J.A. & Nave, C. (1998) Beamline 14: a new multipole wiggler beamline for protein crystallography on the SRS. *J.Synch.Rad.* **5**, 497-499.

[2] Bowler, M., West, J.B., Quinn, F.M., Holland, D.M.P., Fell, B., Hatherly, P.A., Humphrey, I., Flavell, W.R. & Hamilton, B. (2002) A new XUV beamline on a multi-pole wiggler in the *SRS. Surface Review and Letters* **9(1)**, 577-581 .

[3] Bilsborrow, R.L., Dobson, B.R., Cheung, K.C., Dent, A.J., Murphy, L.M., Stephenson, P.C., Hindley, P., Atkinson, P., Bliss, N. & Fell, B. The Daresbury design Sagittal Monochromator, In preparation.

[4] Helsby, W.I., Berry, A., Buksh, P.A., Hall, C.J. & Lewis, R.A. The RAPID2 interpolating system. Presented at SAMBA 2, Trieste May 2002, and Submitted to *NIMS-A as conference proceeding*, in press.

[5] Borsboom, M., Bras, W., Cerjak, I., Detollenaere, D., van Loon, D.G., Goedtkindt, P., Konijnenburg, M., Lassing, P., Levine, Y.K., Munneke, B., Oversluizen, M., van Tol, R. & Vlieg, E. (1998) The Dutch-Belgian beamline at the *ESRF. J.Synch.Rad.* **5**, 518-520

Figure 11: The figure shows a comparison of the same polymer sample collected on the DUBBLE beamline at ESRF (left) and on MPW6.2 (right). It can be seen that the Daresbury data have a higher count rate and better angular resolution but are, at present, slightly noisier.

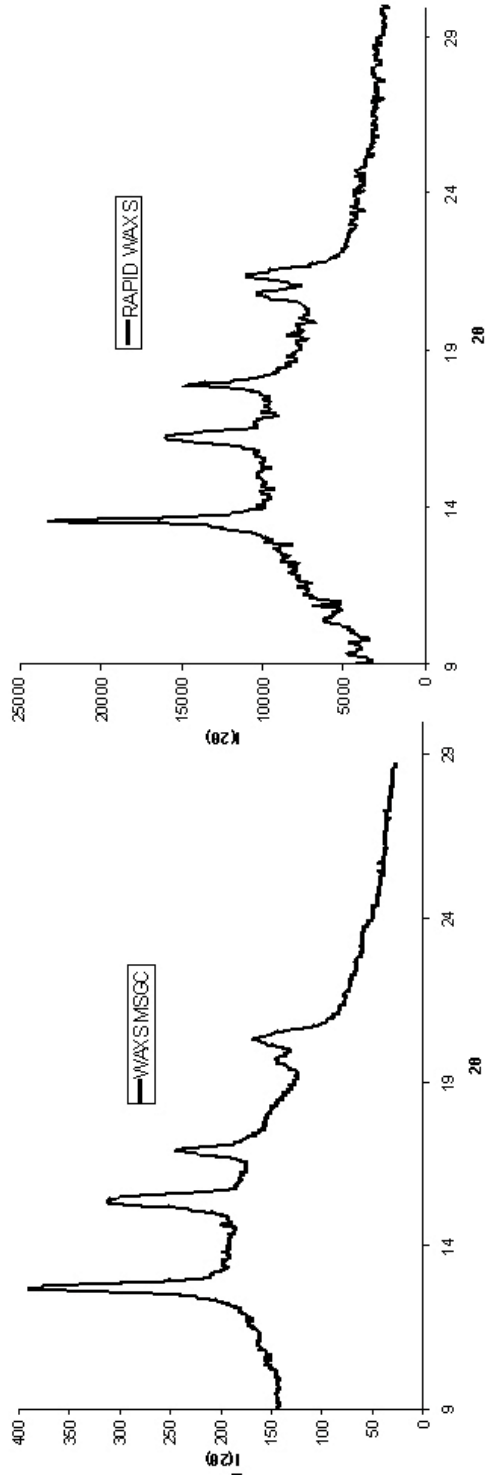

Appendix A

1·	**Source Type**	Multipole Wiggler Insertion Device
2·	**Operating Gap**	19.2 mm
3·	**K value**	37.4
4·	**Period**	200 mm
5·	**No of Poles**	9 Full Poles + 2 End Poles
6·	**Peak on axis Field**	2 T
7·	**Peak Flux @ 1.2Å**	4.4 x 1013 (photons/s/mrad/0.1% bw/300mA)
8·	**Critical Wavelength**	2.33 Å @ 0 mR
9·	**Total Power**	2.4 kW @ 300 mA
10·	**Line Power density**	220 W/mrad @ 300 mA
11·	**Peak Power density**	1130 W/mrad2 @ 300 mA

Camera Length		MIN 100 mm = 0				MAX 400 mm = 0			
Limits of useful detector / mm		min =	8.27	max =	195.23	min =	8.27 ±	max =	195.23
Energy / keV	Wavelength / Å	d_{max} / Å	±	d_{min} / Å	±	d_{max} / Å		d_{min} / Å	±
5	2.48	300	14	12.88	0.02	1200	56	51	0.10
8	1.55	188	9	8.05	0.02	750	35	32	0.06
10	1.24	150	7	6.44	0.01	600	28	25	0.05
12	1.03	125	6	5.37	0.01	500	23	21	0.04
15	0.83	100	5	4.29	0.01	400	19	17	0.03
18	0.69	83	4	3.58	0.01	333	15	14	0.03

Table A - An illustration of the working range of the station.

Millisecond Time-Resolved Low-angle X-ray Fibre Diffraction: A Powerful, High-Sensitivity Technique for Modelling Real-Time Movements in Biological Macromolecular Assemblies

John M. Squire, Carlo Knupp, Hind A. AL-Khayat & Jeffrey J. Harford*

Biological Structure & Function Section, Biomedical Sciences Division and *Biological Sciences Department, Imperial College London, London SW7 2AZ, UK.

ABSTRACT

The modern post-Genomic era heralds the elucidation of many thousands of protein and nucleic acid structures by X-ray crystallography and other techniques. But knowledge of individual macromolecular structures is often not enough. In some cases such macromolecules function as components of much larger molecular assemblies, some of which are filamentous in nature. Striated muscle is a particularly well-ordered example of an organised macromolecular assembly and, in addition, it is dynamic; it functions as a mechanical motor using molecular movements which occur in a millisecond timescale. It, therefore, provides a good test case for the development of structural methods. Here we show that time-resolved, low-angle, X-ray fibre diffraction can be used to follow the molecular movements in contracting muscle in real time and with high spatial sensitivity. More generally, the techniques discussed here can be applied to any uniaxially ordered macromolecular assembly.

INTRODUCTION

One of the current aims of structural biologists is not just to determine the atomic arrangements in proteins, nucleic acids and other biological macromolecules, but also to see how these molecules move or change their shape as they carry out their normal biological functions. Ways to attempt to do this with, for example, a typical enzyme involve following structural changes by protein crystallography in a time-resolved mode (Helliwell & Rentzepis, 1997; Helliwell, 2002). For example Laue diffraction or instantaneous monochromatic diffraction methods can be used to take rapid X-ray diffraction 'snapshots' of a protein crystal at a prescribed time after reaction initiation (Hajdu & Johnson, 1990; Duke *et al.*, 1991; Helliwell & Rentzepis, 1997; Helliwell, 2002). Alternatively, by 'snap-freezing' the enzyme-substrate complex at various times during a reaction, the structure can be determined at leisure by conventional crystallographic methods (Taubes, 1994). However, these approaches not only require synchronous initiation of reactions by, for example, photolysis of caged compounds (e.g. Kaplan *et al*, 1978), they also demand the maintenance of good 3-D crystalline order giving diffraction to high resolution throughout the process. Systems amenable to these approaches are, as yet, few in number (see Helliwell & Rentzepis, 1997). Even so, these techniques generally apply only to single molecules, or small molecular aggregates, whereas *in vivo* many functional proteins are parts of large macromolecular assemblies that may carry out their normal function in a concerted or cooperative manner. In many cases these assemblies are not such that crystallisation and X-ray crystallography is a realistic approach. How can the structures of such assemblies be solved and how can changes in such large assemblies be followed in a dynamic way? If protein crystallography cannot do it, are there other approaches that can be tried? If so, do these other approaches have a spatial sensitivity that approaches that of conventional crystallography?

A few years ago a 'Ways and Means' article by Holmes (1994) presented the powerful case for combining structures determined by protein

crystallography with results from aggregates studied by cryo-electron microscopy or by high-angle fibre diffraction. In the case of electron microscopy, this is now a common approach (e.g. Wriggers *et al.*, 1999). However, this approach is never likely to be a method for studying dynamic changes in macromolecular assemblies other than as a time series of instantaneous 'snapshots' processed individually from separate experiments. Here we present the case for a dynamic, high sensitivity, X-ray diffraction approach to studying macromolecular assemblies, namely that of using time-resolved low-angle X-ray diffraction from fibres or other assemblies, as a means of following structural changes in biological systems with a time-resolution of microseconds to milliseconds and a spatial sensitivity (not resolution) of a few Å.

Many important biological systems occur naturally as extended aggregates, some of which are regularly organised as filaments. Actin filaments, myosin filaments, collagen fibrils, microtubules, intermediate filaments and some viruses represent obvious examples. Some of these, such as actin, myosin and microtubules, clearly have a dynamic role in basic cellular processes; cell division, organelle movement, muscle contraction and so on. Provided that such filaments can be obtained in sufficiently large quantities, preferably with good axial alignment, they can give enormously rich fibre X-ray diffraction patterns. Such patterns rarely extend to the kinds of resolution that X-ray crystallographers are used to, but, even so, diffraction in the low to medium-angle region can be extremely informative. Here we use the examples of actin and myosin filaments that occur in abundance and excellent alignment in skeletal muscle tissue to illustrate the power of the low-angle time-resolved X-ray diffraction technique. Note that the arguments also apply, but with less sensitivity, to low-angle scattering from solutions of macromolecular aggregates when the structures of the individual macromolecules are known (Perkins *et al.*, 1993; 2001; Sugimoto *et al.*, 1995; Maruta *et al.*, 2000; Svergun and Koch, 2002). However, in this case only rotationally averaged data are obtainable and there is more ambiguity in the modelling.

LOW-ANGLE X-RAY DIFFRACTION FROM RESTING MUSCLE

Figure 1 shows a low to medium-angle X-ray diffraction pattern from a bony fish muscle (sculpin)

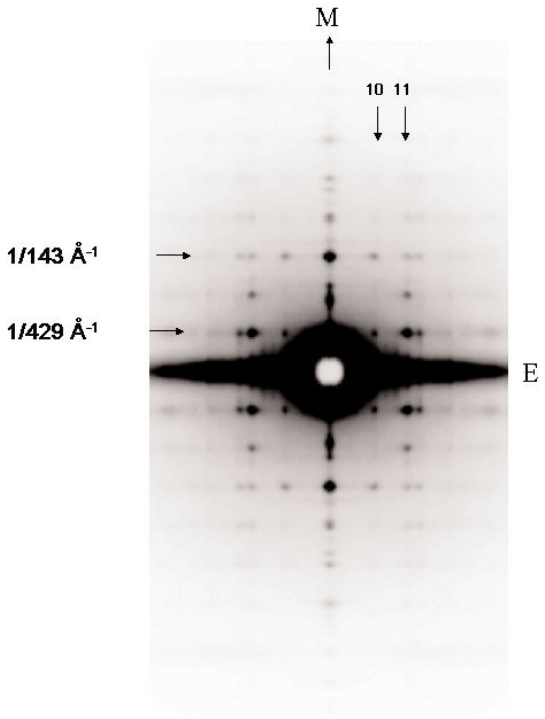

Figure 1. Low-angle X-ray diffraction pattern from the myotomal muscle of the sculpin fish in the resting state recorded at SPring-8. The fibre axis was vertical (M). The layer-line intensities are largely from the quasi-helical arrangement of myosin heads around the muscle myosin filaments which have a 429 Å repeat. The 10 and 11 row-lines (vertical) that arise from the high degree of lateral and axial order in the hexagonal A-band array of myosin and actin filaments are also indicated.

in the relaxed state and recorded at the Spring-8 synchrotron in Japan. The pattern shows the beautifully sampled low-angle layer-lines typical of diffraction from fish muscles (Harford & Squire, 1986), including the characteristic set of layer-lines, orders of an axial repeat of 429 Å, which are due to the quasi-helical arrangement of the globular heads of the myosin molecules in the muscle myosin filaments. Such patterns cannot usually be used in direct Fourier synthesis by solving the phase problem as in protein crystallography. But what if one already knows from protein crystallography the structures of the principal protein components - in this case myosin and actin molecules? We have found that the observed low-angle diffraction patterns from muscle are sensitive not only to the position and orientations of such molecules, but also to the relative positions of their sub-domains. Whole molecule or sub-domain movements of only a few Å can have a marked effect on the low-angle diffraction patterns.

In previous work (Hudson *et al.*, 1997; Squire *et al.*, 1998) we have modelled the array of myosin heads in resting bony fish muscle based on diffraction

patterns such as that in Figure 1 and the result is shown in Figure 2(a). Note that here the filament long axis has been turned 90° relative to Figure 1. It is these myosin heads that interact with actin filaments to produce muscular force and movement. The current working model for muscle action involves the so-called crossbridge cycle. The myosin heads (crossbridges) start off loaded with the molecule adenosine triphosphate (ATP) that has been hydrolysed to adenosine diphosphate (ADP) and inorganic phosphate (Pi). In this state the heads can bind to actin, provided that the muscle machinery has been switched on by Ca^{2+} (Squire and Morris, 1998). Actin then activates the attached myosin heads to release the 'products' Pi and ADP during which the heads undergo a structural change on actin thus generating force and movement (sliding) of the actin filaments relative to the myosin filaments (see Squire, 1997; Harford *et al.*, 1998). An attached myosin head (crossbridge) remains attached to actin until a fresh ATP molecule binds to the head and releases it from actin. The detached head can then hydrolyse the bound ATP to ADP and Pi and reset itself ready for another crossbridge cycle further along the actin filament.

This mechanism is a working model. The key structural question here is 'how can one actually see and monitor the structural events that take place in the crossbridge cycle?'. It should also be noted that in typical muscles each head goes through several attachment/ detachment cycles on actin in a second; interesting events are in fact taking place in muscle on a millisecond timescale. A technique is needed to monitor changes in muscle structure with very fast time resolution and with considerable structural sensitivity.

LOW-ANGLE X-RAY DIFFRACTION FROM ACTIVE MUSCLE

That very big intensity changes occur in the low-angle diffraction patterns from muscle in different physiological states is illustrated in Figure 3. This shows a **difference** diffraction pattern obtained by subtracting a pattern from fully relaxed muscle (as in Figure 1) from a pattern from fully active muscle. In this case the muscle being used was the fin muscle of plaice (*Pleuronectes platessa*) and the patterns were recorded with a camera length of about 2.5 m on the high intensity beamline 16.1 at the CLRC Daresbury Synchrotron (Bliss *et al*, 1995).

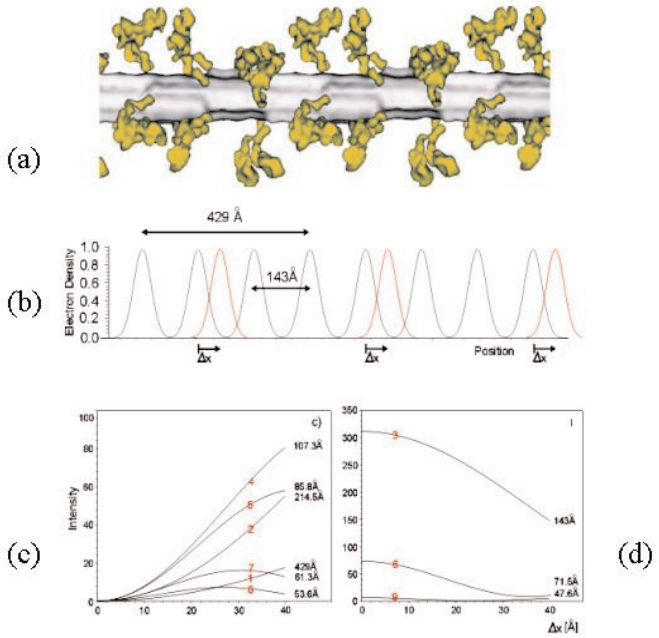

Figure 2. (a) The crossbridge array on myosin filaments in relaxed bony fish muscle determined by Hudson *et al* (1997). (b) Example of an axial shift by Dx of every third level of heads in (a) and the effect of this on various low-angle meridional X-ray reflections from muscle (c,d), all orders of 429 Å. The usual strong meridional orders of M3 (labelled 3) at 143 Å are shown in (d) and the so-called 'forbidden' reflections in (c) are meridional reflections that become apparent when a true 429 Å repeat is established.

The myosin layer-lines in Figure 1, based on the 429 Å repeat, largely disappear when the muscle is activated and this shows up in the difference diffraction pattern (Figure 3) as black regions. In addition various parts of the pattern increase in intensity (green and yellow regions). In particular, layer-lines which come from the actin filaments and have spacings which are orders of about 360 Å generally become stronger. This is partly due to activation-related changes produced by Ca^{2+} within the actin filaments themselves and partly due to the increased mass on actin produced by the attaching myosin heads. The reflection A2 indicated in Figure 3 is the second order layer-line of the 360 Å actin repeat that occurs at a spacing of about 2/360 $Å^{-1}$. It changes intensity as a function of muscle Ca^{2+}-activation (Squire & Morris, 1998). These actin layer-lines will be discussed more in a later Section.

We show below that intensity changes of the kind in Figure 3 are sensitive to rather small movements of the myosin heads or actin sub-domains. Modelling

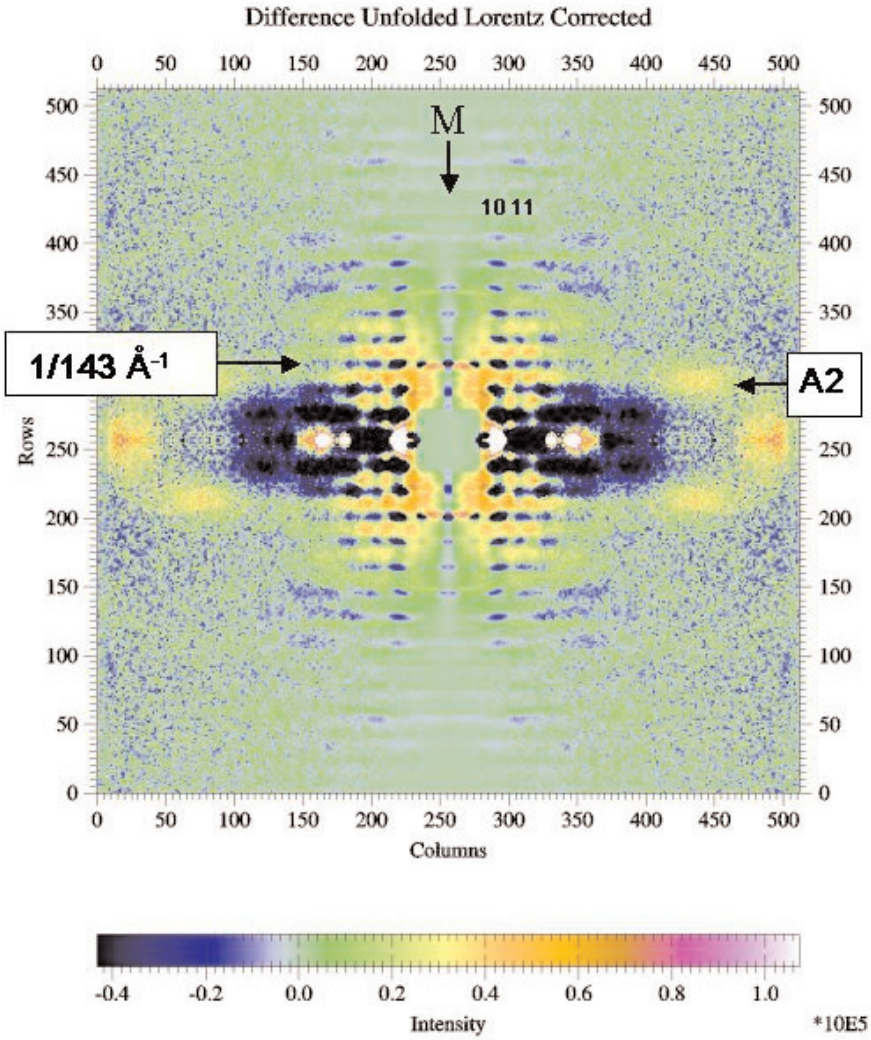

Figure 3. Difference diffraction pattern between resting and active plaice fin muscle (active-resting) recorded using the RAPID detector on beamline 16.1 at the Daresbury SRS (muscle long axis vertical). For details see text.

with known protein structures the intensity changes observed in time-resolved low-angle X-ray diffraction patterns is in fact very sensitive to quite subtle molecular changes.

MONITORING AXIAL MOVEMENTS OF MYOSIN HEADS.

We have tested the sensitivity of the myosin filament low-angle diffraction pattern in two ways. In one case (Figure 2) we have represented the axial positions of myosin heads as a 1-dimensional array of Gaussian density profiles and have tried moving some of the elements of this array. In the other case (Figure 4) we have used the whole modelled diffraction pattern and have tested the layer-line sensitivity to head position by Fourier difference synthesis.

Figure 2(b) is a simple approximation to what is seen in Figure 2(a). The myosin head arrangement in Figure 2(a) has a true axial repeat of 429 Å and a near sub-repeat of this at 143 Å. What has been done in Figure 2(b) is to start with an array of myosin head levels with a true 143 Å repeat and then move every third of these levels by a small distance (Δx; Fig. 2(b)). The resulting Fourier transform has been computed as a function of Δx for the first few orders of the 429 Å repeat (Figure 2(c)). It can be seen that very large intensity changes in these very low-angle reflections occur even when Δx is only 10 or 20 Å. The spacings of the layer-lines themselves are clearly 'low' resolution in the crystallographic sense, but

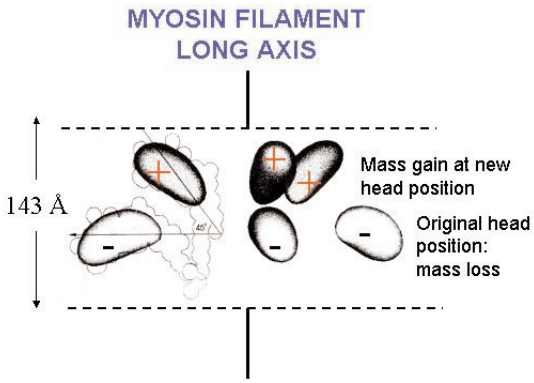

Figure 4. Illustration of the sensitivity of the low-angle X-ray diffraction method to single head movements in one of each of the three myosin head pairs in only one crown out of three myosin head crowns in a 429 Å repeat as in Fig. 1(a). A very clear shift of mass is observed from the lower densities (mass loss: -ve peaks) to the upper densities (mass gain: +ve peaks) using Fourier difference synthesis. The peaks coincide exactly with the original and new positions of the heads (fine outlines).

they are nevertheless sensitive to movements measured in a few Å.

The second test, illustrated in Figure 4, is to take one level of the myosin heads in Figure 2(a), a so-called 'crown' of heads in which there are three pairs of heads separated by 120° around the filament backbone, and then within each head pair in the crown move one of the heads by tilting it axially to a new position, as might occur in a putative crossbridge cycle. We computed Fourier transforms based on either the 'original' model in Figure 2(a) or on the 'modified' model in which one head in each pair was moved only in one of the three crowns separated axially by 429 Å. The amplitudes in the two Fourier transforms were then subtracted and this difference was used with the model phases from the original structure to give a Fourier difference electron density map (Figure 4). Only the affected crown level is shown in Figure 4, which represents the density difference between the modified and original structures computed using layer-lines of spacings ranging from the first order at 429 Å to the highest order used, the 6th, at 72 Å. Fourier difference maps show peaks of negative density where an object has moved away from and peaks of positive density where objects have moved to. Figure 4 is no exception; there are clear negative densities where the myosin heads originally were and there are clear positive densities at the positions to which the heads were moved in the modified model. Clearly the low-angle diffraction pattern, despite its apparently low-resolution, can be used to monitor myosin head movements such as those that might occur between different muscle states.

MONITORING MOVEMENTS OF THE SMALLEST SUB-DOMAIN OF ACTIN

The sensitivity of the low-angle region of the muscle diffraction pattern can also be illustrated by changes in actin filament structure that may be involved in Ca^{2+} regulation of muscular activity. Figure 5 illustrates the principle.

As proposed by Holmes *et al.* (1990), the actin monomer, with its four sub-domain structure (Kabsch *et al.*, 1990) can be positioned and oriented with appropriate helical symmetry to give a sensible model for the actin filament (Figure 5(a)). Although this model has been subsequently refined (Lorenz *et al*, 1993), it appears to be substantially correct. Our own analysis supports this conclusion (AL-Khayat *et al.*, 1995). On the whole, the remaining uncertainties in the structure have been to do with the position of the smallest of the four sub-domains, namely sub-domain 2. This is because its small mass will make only a relatively small contribution either to observed X-ray diffraction patterns or to helical reconstructions from electron micrographs of actin filaments. The position of sub-domain 2 will therefore be relatively difficult to determine.

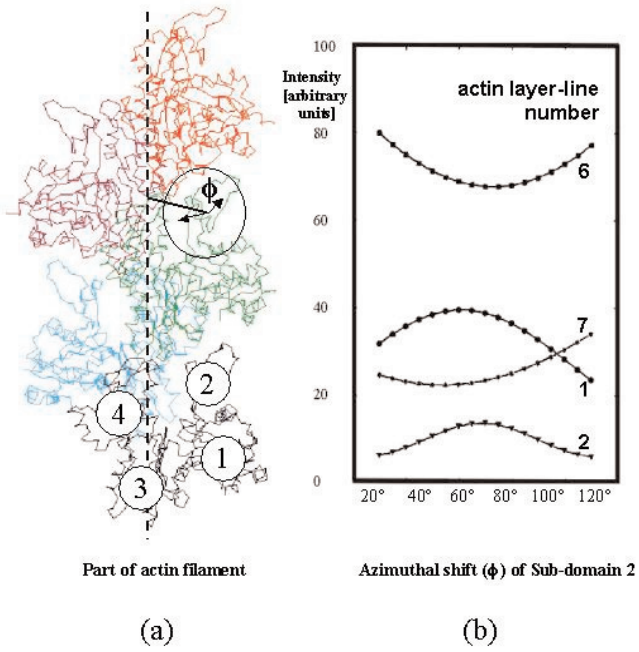

Figure 5. (a) Representation of the actin filament structure proposed by Holmes *et al* (1990), where each actin monomer is shown as a ribbon diagram through the α-carbon atoms in the G-actin crystal structure of Kabsch *et al* (1990). The lowest subunit has the actin sub-domains numbered and above it shows the azimuthal movement of sub-domain 2 used in (b) and discussed in the text. The myosin binding site on actin is mainly located on sub-domain 1. (b) The computed peak intensities on some of the low order actin layer-lines (1 at 1/360 $Å^{-1}$; 2 at 1/180 $Å^{-1}$; 6 at 1/59 $Å^{-1}$ and 7 at 1/51 $Å^{-1}$) shown as a function of the azimuthal position of the smallest actin sub-domain, sub-domain 2. The azimuthal angle is measured around the actin filament axis as in (a), where the 70° position is that in the Holmes *et al* (1990) structure of the actin filament.

Here we have tested this idea by using a four sphere model of the actin monomer, where each actin subdomain is represented by a uniform sphere of appropriate volume (AL-Khayat *et al.*, 1995). The diffraction pattern on the first few layer-lines (orders 1, 2, 6 and 7 of a 360 Å repeat) has then been computed for various models in which the only structural change introduced is in the azimuthal position of sub-domain 2 around the actin filament axis. Compared with the Holmes structure, sub-

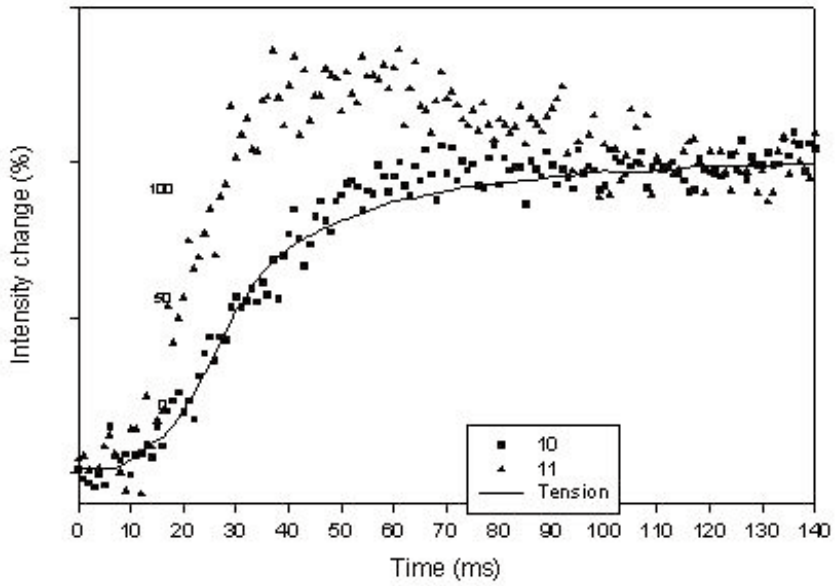

Figure 6. Time-courses of the change in intensity and spacing of the equatorial 10 and 11 reflections from plaice fin muscle during tetanic contractions and recorded on a 1 ms timescale using the fast multiwire "RAPID" area detector (Lewis *et al*, 1996) on beamline 16.1 (Bliss *et al*, 1995) at the CLRC Daresbury Laboratory. The continuous line shows the recorded tension in the muscle (arbitrary scale).

domain 2 has been moved azimuthally by up to a maximum of ±40º around the actin filament axis. Figure 5(b) shows the result. Very marked changes of relative intensity occur on the computed low-angle layer-lines (spacings 1/360 $Å^{-1}$ for l = 1, 2/360 $Å^{-1}$ for l = 2, 6/360 $Å^{-1}$ for l = 6, 7/360 $Å^{-1}$ for l = 7) as sub-domain 2 alone is moved away from the Holmes position. The azimuthal movements may appear to be quite large, but the helical radius of sub-domain 2 from the actin filament axis in the Holmes model is only about 21 Å. Azimuthal swings of up to 30º therefore correspond to shifts in the centre of mass of the sub-domain of only up to 7 Å; the pattern is very sensitive to quite small movements. Compared with the Holmes structure (Ø = 70º), which has I_6/I_2 equal to about 5, the structure with sub-domain 2 at Ø = 100º (i.e. 7 Å away) has this same ratio equal to about 13; well over twice the Holmes value.

It is instructive to note that the 2nd actin layer-line has an axial spacing in reciprocal space of about 1/180 $Å^{-1}$ and the peak is at a radial position of about 1/50 $Å^{-1}$. Layer-line 6 has an axial spacing of about 1/59 $Å^{-1}$ and peaks at a radial position of about 1/110 $Å^{-1}$. Clearly the 'resolution' of the data in the conventional crystallographic sense is very limited and the structure cannot be solved to high resolution. But these same layer-lines are remarkably sensitive to sub-domain movements of only a few Å once the structures of the component domains in the molecule have been solved crystallographically. This represents an excellent example of two apparently disparate techniques, protein crystallography and low-angle X-ray fibre diffraction, coming together to provide useful insights that each technique on its own cannot provide. In conclusion, rather subtle relative movements of the centres of mass of protein sub-domains can be defined quite well by low-angle X-ray fibre diffraction.

DYNAMIC EXPERIMENTS WITH FAST TIME RESOLUTION

Time-resolved low-angle diffraction studies, which are now carried out routinely at Daresbury and elsewhere, can provide information about continuous structural changes in macromolecular assemblies at millisecond time resolution or better (Harford and Squire, 1992; Irving *et al.*, 1992; Martin-Fernandez *et al.*, 1994; Squire *et al.*, 1994; Lombardi *et al.*, 1995 and many others). As an example, Figure 6 illustrates results from dynamic studies of contracting fish muscle on beam line 16.1 at the CLRC Daresbury Laboratory. These were obtained using the very fast multiwire area detector known as RAPID. RAPID was developed by the Daresbury detector group (Lewis *et al.*, 1996) and is still the fastest readout area detector for time-resolved low-angle X-ray diffraction studies at any synchrotron. The traces in Figure 6 show the intensity changes of the innermost 10 and 11 equatorial reflections (d-spacing about 420 Å and 364 Å respectively) from the hexagonal lattice of myosin and actin filaments in the muscle A-band as they change when the

muscle is activated to develop its maximum tension (in an isometric tetanus). These reflections lie on the equator (E) of the diffraction pattern in Figure 1 and on the vertical 10 and 11 row-lines indicated there, but they are overexposed in this particular pattern. Usually in experiments of this kind it has been necessary to subject the muscle to a series of similar contractions and to pool the results in appropriate time bins after the initiation of contraction. However, in most previous studies it was also necessary to pool results from several different muscles in order to accumulate sufficient counts. Unfortunately this leads to degradation in the signal; there is variability between different muscles. With new technical developments it is now possible to acquire enough signal from a few contractions of a single muscle recorded in 1 ms time bins. What is seen in Figure 6 confirms previously reported 'pooled' results from several contractions of several different muscles at lower time resolution (Harford and Squire, 1992). Of particular note is that the timecourses of the 10 and 11 intensity changes are clearly different. Changes in the 10 intensity (actually a drop shown inverted in Fig. 6) are roughly in step with the tension, whereas the 11 reflection changes much faster than tension, overshoots and then returns to a steady level at the tension plateau. This behaviour would not be produced by a single attached conformation of myosin heads on actin. Something much more complicated involving at least two structurally different actin-attached states must be involved.

CONCLUSIONS

We have shown that, although small atomic movements cannot be studied this way, modelling from low-angle X-ray diffraction patterns can provide an indication of mass movements of a few Å within and between proteins and protein domains and can be monitored on a millisecond timescale. These movements can be modelled provided that there is not a total structural reorganisation within the protein. Small changes in the relative atomic positions within a sub-domain cannot be determined by this method. The example of the actin filament shown above has used simple spherical shapes to model the actin sub-domains. We have shown elsewhere (Squire *et al.*, 1994; AL-Khayat *et al.*, 1995) that, at the resolution being considered, the computed diffraction pattern from such a model compares well with patterns computed using all the atomic positions. The subtleties of the changing interactions at the atomic level can be studied by other approaches, including molecular graphics and modelling, in some cases based on the sub-domain movements determined from low-angle diffraction data.

Protein crystallography is an immensely powerful method in structural biology. Time-resolved low-angle X-ray fibre diffraction can build on and complement this technique to show the general arrangement of proteins in oriented macromolecular assemblies and can reveal molecular and sub-molecular movements on a microsecond or millisecond timescale. Improving facilities at synchrotron radiation sources (e.g. the ESRF at Grenoble, France; SPring-8 in Japan; the APS in the USA, etc.) are now opening up even greater opportunities to capitalise on the complementary powers of the macromolecular crystallography and time-resolved low-angle X-ray diffraction methods. The biggest single need at these 3rd generation sources is to have very fast readout detectors such as RAPID (Lewis *et al.*, 1996) which can cope with high fluxes, have a high dynamic range and can be read out on a timescale, milliseconds or better, at which interesting biological events occur. Without such detectors the high brilliance of the new low-angle beamlines, which potentially renders them ideal for time-resolved X-ray diffraction studies of muscle such as those described here, will never be fully exploited.

Acknowledgements

The work described here was supported by project grants from the BBSRC and the Wellcome Trust (#061729) and the data analysis made use of CCP13 programs (BBSRC/ EPSRC grant #25/B15281). We acknowledge the help of Ngai-Shing Mok in preparing Figure 3 and of Dr. Liam Hudson in preparing Figure 4.

REFERENCES

[1] AL-Khayat, H.A., Yagi, N. & Squire, J.M. (1995) Structural changes in actin-tropomyosin during muscle regulation: computer modelling of low-angle X-ray diffraction data. *J. Mol. Biol.* **252**, 611-632.

[2] Bliss, N., Bordas, J., Fell, B.D., Harris, N.W.,Helsby, W.I., Mant, G.R., Smith, W. & Towns-Andrews, E. (1995) W16.1: A new fixed wavelength diffraction station at the SRS Daresbury. *Rev. Sci. Instrum.* **66**, 1311-1313.

[3] Duke, E.M., Hadfield, A., Martin, J.L., Clifton, I.J., Hajdu, J., Johnson, L.N., Reid, G.P., Trentham, D.R., Bruce, I. & Fleet, G.W. (1991) Towards time-resolved diffraction studies

with glycogen phosphorylase. *CIBA Foundation Symp.* **161**, 75-86 (& 86-90).
[4] Harford, J.J. & Squire, J.M.(1986) "Crystalline" myosin cross-bridge array in relaxed bony fish muscle: low-angle X-ray diffraction from plaice fin muscle and its interpretation. *Biophys. J.*, **50**, 145-155.
[5] Harford, J.J. & Squire, J.M. (1992) Evidence for structurally different attached states of myosin cross-bridges on actin during contraction of fish muscle. *Biophys. J.*, **63**, 387-396.
[6] Harford, J.J., Denny, R.C., Hudson, L., Mendelson, R., Morris, E.P. & Squire, J.M. (1998) Myosin head configurations in relaxed, active, rigor and S1-labelled fish muscle: Evidence for characteristically distinct states. *Fibre Diffraction Review* **7**, 45-50.
[7] Hajdu, J. & Johnson, L.N. (1990) Progress with Laue diffraction studies on protein and virus crystals. *Biochemistry* **29**,1669-1678.
[8] Helliwell, J.R. (2002) New opportunities in biological and chemical crystallography. *J. Synchrotron Radiation* **9**, 1-8.
Helliwell, J.R. & Rentzepis, P.M. (1997) *Time-Resolved Diffraction*. (Pp. 454). Clarendon Press.
[9] Holmes, K.C. (1994) Solving the structures of macro-molecular complexes. *Structure* **2**, 589-593.
[10] Holmes, K.C., Popp, D., Gebhard, W. and Kabsch, W.(1990) Atomic model of the actin filament. *Nature* **347**, 44-49.
[11] Hudson, L., Harford, J.J., Denny, R.J. & Squire, J.M. (1997) Myosin head configurations in relaxed fish muscle: resting state myosin heads swing axially by 150Å or turn upside down to reach rigor. *J. Mol. Biol.* **273**, 440-455.
[12] Irving, M., Lombardi, V., Piazzesi, G. & Ferenczi, M.A. (1992) Myosin head movements are synchronous with the elementary force-generating process in muscle. *Nature* **357**, 156-158.
[13] Kabsch, W., Mannherz, H.G., Suck, D., Pai, E.F. & Holmes, K.C. (1990) Atomic structure of the actin: DNaseI complex. *Nature* **347**, 37-44.
[14] Kaplan, J.H., Forbush, B. III & Hoffman, J.F. (1978) Rapid photolytic release of adenosing 5'-triphosphate from a protected analogue: utilization by the Na:K pump of human red blood cell ghosts. *Biochemistry* **17**, 1929-1935.
[15] Lewis, R.A., Hall, C., Parker, B. Jones, A., Helsby, W, Sheldon, J, Clifford, P., Hillen, M. & Fore, N. (1996) The "RAPID" high rate area X-ray Detector System. *Fibre Diffraction Review* **5**, 30-34.
[16] Lombardi, V., Piazzesi, G., Ferenczi, M.A., Thirlwell, H., Dobbie, I. & Irving, M. (1995) Elastic distortion of myosin heads and repriming of the working stroke in muscle. *Nature* **374**, 553-555.
[17] Lorenz, M., Popp, D. & Holmes, K.C. (1993) Refinement of the F-actin model against X-ray fiber diffraction data by the use of a directed mutation algorithm. *J. Mol. Biol.*, **234**, 826-836.
[18] Martin-Fernandez, M.L., Bordas, J., Diakun, G., Harries, J., Lowy, J., Mant, G.R., Svennson, A. & Townes-Andrews, E. (1994) Time-resolved X-ray diffraction studies of myosin head movements in live frog sartorius muscle during isometric and isotonic contractions. *J. Mus. Res. Cell Motil.* **15**, 319-348.
[19] Maruta, S., Aihara, T., Uyehara, Y., Homma, K., Sugimoto, Y. & Wakabayashi K. (2000) Solution structure of myosin-ADP-MgFn ternary complex by fluorescent probes and small-angle synchrotron X-ray scattering. J. Biochem. 128, 687-94.
[20] Perkins, S.J., Gilbert, H.E., Aslam, M., Hannan, J., Holers, V.M. & Goodship, T.H. (2001) Solution structures of complement components by X-ray and neutron scattering and analytical ultracentrifugation. *Biochem Soc Trans.* **30**, 996-1006.
[21] Perkins, S.J., Smith, K.F. & Sim, R.B. (1993) Molecular modelling of the domain structure of Factor I of human complement by X-ray and neutron solution scattering. *Biochem. J.* **295**, 101-108.
[22] Squire, J.M. (1997) Architecture and function in the muscle sarcomere. *Curr. Opin. Struct. Biol.* **7**, (1997) 247-257.
[23] Squire, J.M. & Morris, E.P. (1998) A new look at thin filament regulation in vertebrate skeletal muscle. *FASEB J.* **12**, 761-771.
[24] Squire, J.M., Harford, J.J. & AL-Khayat, H.A. (1994) Molecular movements in contracting muscle: towards Muscle - The Movie. *Biophys.Chem.*, **50**, 87-96.
[25] Squire, J.M., Cantino, M., Chew, M., Denny, R., Harford, J.J., Hudson, L. & Luther, P.K. (1998) Myosin rod packing schemes in vertebrate muscle thick filaments. *J. Struct. Biol.* **122**, 128-138.
[26] Sugimoto, Y., Tokunaga, M., Takezawa, Y., Ikebe, M. & Wakabayashi, K. (1995) Conformational changes of the myosin heads during hydrolysis of ATP as analyzed by X-ray solution scattering. *Biophys. J.* **68** (4 suppl) 29s-34s.
[27] Svergun, D.I. & Koch, M.H.J. (2002) Advances in structure analysis using small-angle scattering in solution. *Curr. Op. Struct. Biol. 12*, 654-660.
[28] Taubes, G. (1994) X-ray movies start to capture enzyme molecules in action. *Science* **266**, 364-365.
[29] Wriggers, W., Milligan, R.A. & McCammon, J.A. (1999) Situs: A package for docking crystal structures into low-resolution maps from electron microscopy. *J. Struct. Biol.* **125**, 185-195.

Small-Angle Scattering Functions of Micelles

V. Castelletto* and I. W. Hamley

Department of Chemistry, University of Leeds, Leeds LS2 9JT, UK.

** Author for correspondence*

ABSTRACT

Models for small-angle scattering of spherical micelles are briefly reviewed, considering both the intra-molecular form factor and the inter-molecular structure factor. Recent examples from the literature, where such approaches have been used to extract information on micellar structure and ordering, are then discussed. A particular emphasis is on micelles formed by block copolymers in solution.

1. Introduction

Micelles are stable aggregates formed by the self-assembly of amphiphiles or copolymers. They exist in thermodynamic equilibrium with unassociated molecules above the critical micelle concentration (at a fixed temperature) or critical micelle temperature (at a fixed concentration). They can adopt a variety of shapes - the most common being spherical, although if the packing of the molecules favours it, anisotropic ellipsoidal, worm-like or rod-like micelles are possible.

The present review is focussed on the analysis of the structure in solutions of spherical micelles via small-angle scattering methods. Although the examples we present are primarily for micelles of block copolymers, the models described can be applied in many cases to other systems such as microemulsion droplets.

Small-angle scattering methods are well suited to investigate the structure of micelles because their size is typically ~5-100 nm, which leads to scattering at small angles. Both Small-Angle X-ray Scattering (SAXS) and Small-Angle Neutron Scattering (SANS) techniques may be employed. X-ray scattering has the advantage that it can be performed in the lab, whereas neutron scattering requires access to central facilities. However, in neutron scattering it is possible to probe details of micellar structure by contrast variation experiments, using mixtures of selectively deuterated amphiphiles or solvents [1]. In very dilute solution, it is possible to measure only intra-micellar scattering, the so-called form factor. However, in most cases the inter-micellar scattering contributes to the scattering, especially at low wave vector q, and increasingly as concentration is increased.

A number of reviews of scattering from micellar systems have appeared recently. Pedersen has presented useful compendia of form factors and structure factors for particulate systems, including micelles[2]. The focus of the latter article was on free-form fitting methods to determine intra-micellar structure. The present review, where the emphasis is on modelling the form factor and structure factor (it is particularly difficult to obtain these together by free-form techniques), complements nicely ref [2]. Scattering studies on block copolymer micelles have been mentioned as part of a review of scattering from polymer systems [3].

2. General Theory

The small angle scattering intensity *I(q)* of an isotropic solution of polydisperse spherical micelles can be written within the "decoupling approximation" as [4]:

$$I(q) = n_p \overline{P}(q) S'(q) \qquad (1)$$

where n_p is the average number density of micelles and $\overline{P}(q)$ is the average of the form factor *P(q,R)* over the distribution *f(R)* of micellar radius:

$$\overline{P}(q) = \int_0^\infty P(q,R)\, f(R) dR \qquad (2)$$

S'(q) in Eq. 1 is the effective structure factor, given

by:

$$S'(q) = 1 + \beta(q)[S(q) - 1] \qquad (3)$$

where $S(q)$ is the structure factor of the system and $\beta(q)$ is defined by

$$\beta(q) = |< F(q,R) >|^2 / \overline{P}(q) \ .$$

$F(q,R)$ is the amplitude factor [4,5], which is related to the form factor through:

$$P(q,R) = F(q,R)^2 \qquad (4)$$

An alternative model for the scattering from polydisperse spherical particles was proposed by Pedersen [5]. In contrast to the decoupling approximation, where the positions of particles are independent of their size, the particle position is completely correlated to its size, i.e. the system is approximated as a series of subsystems in which the particles are monodisperse. The corresponding expression for the scattered intensity in this so-called monodisperse approximation is:

$$I(q) = n_p \int_0^\infty P(q,R) S(q, R_{eff}) f(R) dR \qquad (5)$$

where R_{eff} is the effective radius of interaction between the micelles. R_{eff} is a function of R, and therefore is included in the integral in Eq. 5.

Pedersen has shown that the local monodisperse approximation works better than the decoupling approximation for high volume fractions and large polydispersity, in that it is able to reproduce average micellar radii and size distributions when fitting simulated data for spherical particles such as micelles [5].

In a very dilute system only the form factor needs to be considered. Intermolecular interferences are manifested by the increasing contribution of the structure factor as concentration is increased.

Here, we review recent attempts to model small angle scattering data from micellar systems. First we give expressions for model form factors and structure factors and then discuss their application to micellar systems, taking examples from the recent literature.

2a. Form Factors

The simplest model for scattering from a spherical micelle is based on a uniform sphere (radius R_o and volume V_o) with excess electron density $\Delta\rho$. The corresponding well-known equation for the form factor was derived by Lord Rayleigh [6]:

$$P(q) = (\Delta\rho)^2 V_o^2 \left[3 \frac{\sin(qR_o) - qR_o \cos(qR_o)}{(qR_o)^3} \right]^2 \qquad (6)$$

Generalizing to the case of a micelle with a uniform core of radius R_c and shell of thickness R_s (with different density) leads to a core-shell model, the corresponding form factor being [7]:

$$P(q) = [\frac{4}{3}\pi(\rho_s - \rho_m)(R_s + R_c)^3 F(q,(R_s + R_c)) + \frac{4}{3}\pi(\rho_c - \rho_s) R_c^3 F(q, R_c)]^2 \qquad (7)$$

where $F(q,R_i) = 3\{[\sin(qR_i) - (qR_i)\cos(qR_i)]/(qR_i)^3\}$ is the amplitude factor for a sphere of radius R_i, ρ_i is the scattering length density, and $i=c,s,m$ label core, shell and solvent medium respectively.

Other models consider that the core scattering amplitude is that of a homogeneous sphere, but the density profile of the shell is a function of the radial distance r, for example the density profile of the shell is given by [8]:

$$n(r) = r^{-x}/(1 + \exp[(r - R_M)/\sigma_F]) \qquad (8)$$

where the Fermi function exhibits a smooth density decay up to $R_M = R_c + R_s$ (here again R_c refers to the micellar core radius and R_s to the width of the shell), σ_F being the width of the Fermi function. For $x \sim 4/3$ a density profile similar to that for a star-like polymer [9] is obtained.

A related model is the so-called "cap and gown" model, with uniform core (cap) and a shell with a decaying density profile (gown) of width σ, described by [10]:

$$n(r) = k \exp(-r^2/\sigma^2) \qquad (9)$$

where k is a constant proportional to the excess scattering length density. This model is also known as a box Gaussian model [11].

Recently, Pedersen and Gerstenberg introduced a new model for the form factor of block copolymer micelles, which also considers a homogeneous spherical micelle core, but with attached Gaussian

chains. The Pedersen and Gerstenberg (PG) monodisperse micellar form factor is written [12,13]:

$$P(q) = N^2 \Delta\rho_c^2 P_c(q, R_c) + N\Delta\rho_s^2 P_s(q, R_g) + N(N-1)\Delta\rho_s^2 S_{ss}(q) + 2N^2 \Delta\rho_s \Delta\rho_c S_{cs}(q) \quad (10)$$

where the subscripts *c* and *s* refer to uniform spherical micelle cores (radius *Rc*) and attached Gaussian chains (R_g: radius of gyration of the Gaussian chain), and *N* is the micelle association number. $\Delta\rho_x$ is the total excess scattering density of a chain in the core ($x=c$) or in the corona ($x=s$). The term $P_c(q,R_c)$ in Eq. 10 is the normalised self-correlation term for a uniform sphere and $P_g(q,R_g)$ is the self-correlation term for Gaussian chains. $S_{cs}(q)$ corresponds to the interference cross term between the sphere and the Gaussian chain starting at the surface of the sphere and $S_{ss}(q)$ is the interference term between the Gaussian chains attached to the surface of a sphere. Data from Monte Carlo simulations of an individual block copolymer micelle consisting of a hard core with attached semiflexible chains have recently been analysed and fitted with box-Gaussian profiles for the corona radial density, and profiles derived from a maximum entropy distribution [11].

It should be mentioned that Eq. 10 is reduced to the Gaussian star form factor in the limit of R_c=0 [13]. The Gaussian star form factor, which describes the scattering profile of highly diluted solutions of star-like micelles with only one level of electronic density, is given by [14]:

$$P(q) = \frac{2}{fv^4}\left[v^2 - \left(1-\exp(-v^2)\right)\right] + \frac{f-1}{2}\left[1-\exp(-v^2)\right]^2 \quad (11)$$

where $v = \sqrt{\frac{f}{3f-2}} qR_G$,

f is the number of arms and R_G is the radius of gyration of the whole star, which is related to that of one arm, $R_{G,arm}$, by [15]

$$R_G^2 = \frac{(3f-2)}{f} R_{G,arm}^2 \quad .$$

Within the Gaussian approximation, the radius of the Gaussian star, R_{star}, can be estimated by $R_{star} = R_G$, since for a Gaussian chain the radius of the chain can be taken as the radius of gyration.

Finally, Pedersen has also recently developed another model for *P(q)*, which is based on Monte Carlo results, and corresponds to micelles with a spherical core and self avoiding chains [16]. This model relies on the detailed modelling of the corona density profile which is then used to model the form factor. Within this model *P(q)* is given by[16]:

$$P(q) = N^2 \beta_c^2 F_c(q) + N\beta_s^2 F_s'(q) + 2N^2 \beta_c \beta_s S_{cs}'(q) + N(N - F_s'(q=0))\beta_s^2 S_{ss}'(q) \quad (12)$$

where $F'_s(q)$ in Eq. 12 is the effective-single chain form factor of self avoiding chains [17]. Both $S'_{cs}(q)$, which is the interference cross term between the sphere and the chains in the corona, and $S_{cc}(q)$, which corresponds to the interference term between chains in the corona, in Eq. 12 are expressed as a function of $A_s(q)$, which is the Fourier transform of the configurationally averaged radial density distribution $\rho_s(r)$ of the chains in the corona [16].

As an alternative to model fitting, so-called "free form" methods are frequently used to analyse small angle scattering data in the absence of structure factor effects. For a brief discussion of these methods, the reader is referred to a recent review [18]. Briefly, *P(q)* is fitted to obtain the pair distance distribution function *p(r)*, which is represented by a set of basis functions such as splines. The excess scattering density can then be obtained from *p(r)* by the so-called square-root deconvolution method. The first "free-form" method, the indirect Fourier transformation (IFT), was introduced by Glatter [19] and other methods, which essentially give the same result as Glatter's IFT method, have also been described [20-22].

2b. Structure Factors

Liquid theory gives methods by which the structure factor *S(q)* of a system of interacting particles can be determined for a given interparticle interaction potential. For example, it is well known that the most accurate approximation for *S(q)* able to describe a system of interacting hard spheres is that obtained by Percus and Yevick (PY) [23].

It should be mentioned that the analytical expressions for structure factors found in the literature are limited to interacting spherical or weakly anisotropic particles [24-26]. Hayter and Penfold gave the analytical solution of the structure factor for a system of particles interacting via a repulsive screened Coulomb potential [24,25]. The

repulsive potential is represented by a Yukawa potential, which has a 'soft' tail at large separations of the particles. The repulsive potential becomes hard sphere-like at short distances between them. This formalism uses the mean spherical approximation as closure for the pair distribution function, and leads to the same result as PY when the micellar surface charge is zero.

In some micellar systems there is an effective intermicellar attraction that has the form of surface adhesion, in addition to the excluded volume effect represented by the finite size hard core. This interaction has been described by Baxter in his sticky hard sphere model (SHSM), within which the PY approximation is used to solve the Ornstein-Zernike (OZ) equation analytically to first order for an adhesive hard sphere potential [26].

In all of the structure factors mentioned above it is assumed that the interaction between the micelles is dominated by the shape of the micelles as a whole and not the characteristics of the molecules that make the micelles. But in the case of some polymeric systems this approximation breaks down because not only the interaction potential between micelles, but also the surface density of the polymer chains themselves, influence *S(q)*. For example, in contrast to star-like polymers, a thin polymer layer tethered to a large spherical micellar core has highly extended chains resembling a polymer brush. A theoretical investigation of the transition between the polymer brush profile and the star like density profile was undertaken some years ago by Lin and Gast [27-29]. The work focused on polymeric chains tethered to a surface in a curvature regime between the limiting cases of a star polymer and a planar interface, i.e. polymer micelles mimicking polymer brushes. Each tethered polymer was described as a freely jointed chain with *n* statistical segments of length *b*. The chains were modelled as random walks within a mean field potential. In contrast to star polymers or planar polymer brushes mentioned above, the total interaction potential depended upon the polymer segment distribution and was determined numerically from self-consistent field (SCF) calculations. In this model the radial distribution function is calculated from the interaction potential using integral equations from liquid theory and the OZ equation is solved within the Rogers-Young closure, which is a hybrid approach mixing the PY and Hypernetted Chain (HNC) approximations. The calculations were used to model the structure factor of PS-PI micelles in decane [27-29]. The regime of intermediate surface coverage (between mushrooms and brushes), applicable to block copolymer micelles, was also examined in the Monte Carlo simulations of Svaneborg and Pedersen [11].

3. Recent Applications

The modelling of small-angle scattering data is a useful tool for the analysis of the structure in solutions of spherical micelles. For example, the phase behaviour of a Poly(ethylene oxide)-Poly(propylene oxide)-Poly(ethylene oxide) (PEO_{25}-PPO_{40}-PEO_{25}, the subscripts denote the number of repeats) triblock copolymer in aqueous solution has been studied by SANS, and the structural properties have been determined by fitting the SANS curves with the form factor of a homogeneous sphere in combination with a hard sphere potential of interaction [30]. Another recent SANS study on tertiary amine methacrylate-based diblock copolymer micelles modelled the micelle structure using a core-shell form factor and a polydisperse hard sphere structure factor [31].

In addition to its use to describe interactions between polymeric micelles, the hard sphere structure factor has been used to fit SAXS data obtained for solutions of zwitterionic lipid micelles in the study of the liquid-solid phase transition [32]. The uniform sphere micellar form factor has also been used for other lyotropic systems. For example, the influence of urea on Aerosol-OT/n-hexane/water reversed micelles has been probed by SAXS [33]. In this case, the percolation process occurring in the system was analysed using the structure factor for the SHSM model for the attractive interaction.

The core-shell micellar form factor was used to fit SANS data from reverse micelles of PEO_y-PPO_z-PEO_y, where y= 10, 13, 19, 27 and x= 23, 30, 43, 61. The reversed micelles were formed by controlled addition of oil to the block copolymer/water solutions [34]. Scattering curves from reversed micelles formed by the surfactant perfluoroalkylpoly (ethylene oxide) in supercritical carbon dioxide have also been successfully modelled with a core-shell model [35]. This model has further been used to fit SANS data for polystyrene-poly(ethylene oxide) (PS-PEO) micelles, while a repulsive screened Coulomb potential was used to describe the corresponding structure factor [36]. For the PEO_y-

PPO_z-PEO_y micelles (*x*, *y*= 23, 34 and 26, 40 respectively), also the unimer-to-micelle transition region was studied by modelling SANS curves with a core-shell micellar form factor [37,38]. More recently, the core-shell form factor has also been used to model SANS data from poly(lactic acid)-poly(ethylene glycol) micelles in H_2O/D_2O mixtures [39].

The core-shell model was applied to describe the form factor in a SANS study of the percolation process in PEO_{19}-PPO_{43}-PEO_{19} micelles in aqueous solution, where micellar interactions were described by the SHMS model for the attractive interaction potential [40]. The same authors improved the quality of model fits to SANS data from a related block copolymer solution that exhibits a percolation transition due to intermicellar interactions, by fitting the 'cap-and-gown' form factor to scattering curves from micelles of PEO_{13}-PPO_{30}-PEO_{13} [10,41,42].

A systematic study of the influence of the length of the soluble PEO block on the structural micellar properties was undertaken for poly(ethylene-co-propylene)-PEO micelles modelling SANS curves using Eq. 7 to describe the density profile of the shell [8,43]. A density profile with a power-law derived from scaling theory for star-like polymers has been used in the shell component of the form factor of spherical polymer brushes [44].

The form factor of block copolymer micelles in water has successfully been described by the PG model, for a number of systems, including PS_{10}-PEO_{68} [45], PEO_{25}-PPO_{40}-PEO_{25}, PS-polyisoprene (PI) [12,13] PEO_m-PBO_n (PBO=poly(butylene oxide), *m*,*n*= 86, 10 and 87, 18 respectively) [46-48]. In particular, this form factor was used in combination with the hard sphere structure factor to study the liquid-solid phase transition observed in aqueous micellar solutions of diblocks $PEO_{86}PBO_{10}$ and $PEO_{87}PBO_{18}$. Representative fits are shown in Figure 1.

SANS studies have been performed on more complex micellar structures, such as onion-type block copolymer micelles, prepared from PS-P2VP (P2VP=poly(2-vinylpyridine)) combined with P2VP-PEO to produce a PS-P2VP-PEO three-shell structure with a PS core and PEO corona [49]. Despite the complexity of the onion micelles the scattering data could be fitted using simple models

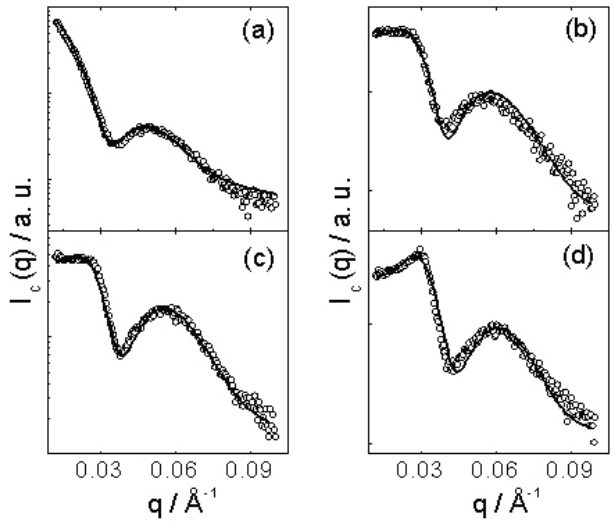

Figure 1. SAXS data and fits using the hard sphere model in combination with the PG model (solid line) for $PEO_{87}PBO_{18}$ at 70º C for: (a) 2, (b) 10, (c) 11 and (d) 12 wt % $E_{87}B_{18}$. (Figure extracted from reference [47])

for the form factor: either that for polydisperse uniform spheres (so-called "bare core" approximation) or the PG model. These models have been used to analyse SANS data from a variety of multi-shell block copolymer nanoparticles, for example three-layer nanoparticles prepared by gamma-radiation-induced polymerization of methyl methacrylate (MMA) around the PS core of PS-poly(methacrylic acid) micelles in aqueous solution [50,51]. The distribution of MMA before polymerization and the structure of nanoparticles containing polymerized MMA were elucidated by modelling the scattering data using the bare-core approximation for a two-component core and also considering a hard micellar core with attached Gaussian chains. The structure of micelles of an ABC triblock, poly(2-ethylhexyl acrylate)-block-poly(methyl methacrylate)-block-poly(acrylic acid) (PEHA-PMMA-PAAc), in H_2O/ D_2O mixtures have been studied via SANS using contrast variation by a selective swelling of PEHA blocks with *d*-cyclohexane [52]. Modelling of the scattering curve with the bare-core approximation showed that the three blocks are segregated in a micelle, PEHA forming the inner and PMMA the outer layer of the core. Solutions in D_2O of other charged micelles, formed by PMMA-PAAc copolymers neutralized to various degrees with Li, Na, or K counterions, were studied by SANS [53]. The bare-core approximation for the form factor was used to study the influence of degree of neutralization on the solubilization of organic substances, such as chloroform or chlorobenzene, in the PMMA core.

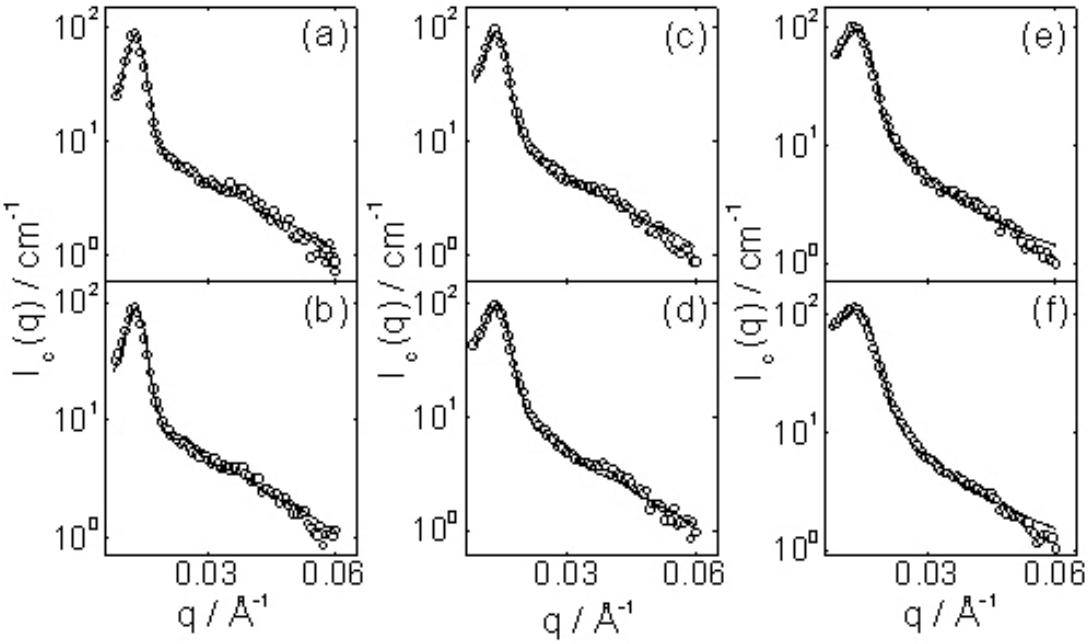

Figure 2. SANS data and fits using the hard sphere model in combination with the form factor with self avoiding chains (solid line) at 45 °C for: (a) 3 and (b) 3.6 wt % $PEO_{398}PBO_{19}$. (Figure extracted from reference [54])

Figure 3. SAXS data and fits using the hard sphere model in combination with the form factor for Gaussian stars (solid line) for 2 wt % MMA_{10}-b-$DMAEMA_{10}$-b-$HEGMA_{10}$ at (a) 25 and (b) 66 °C, for 2 wt % MMA_{10}-b-$HEGMA_{10}$-b-$DMAEMA_{10}$ at (c) 25 and (d) 66 °C and for 2 wt % $DMAEMA_{10}$-b-$HEGMA_{10}$-b-MMA_{10} at (e) 25 and (f) 66 °C (DMAEMA: 2-(dimethylamino)ethyl methacrylate; HEGMA: hexa(ethylene glycol)methacrylate; MMA: methyl methacrylate; the subcripts are the number-average block lengths in repeat units) The SAXS patterns have been shifted by multiplying by an arbitrary constant. (Figure extracted from reference [58])

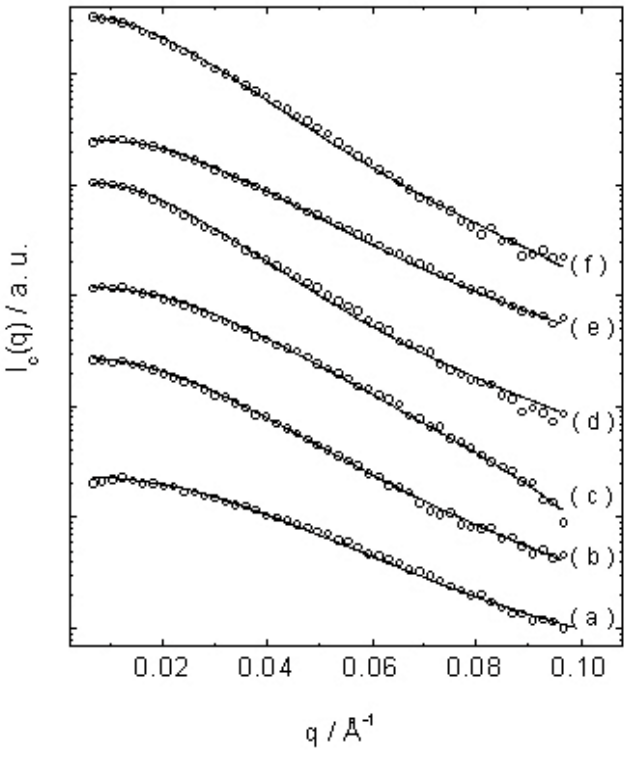

The form factor of highly swollen block copolymer micelles, including PS-PI and $PEO_{398}PBO_{19}$ systems [16,54], has been successfully described by the model reported by Pedersen for micelles with a spherical core and self avoiding chains [16] Representative fits showing the results obtained using this form factor in combination with the hard sphere structure factor to study the liquid phase of $PEO_{398}PBO_{19}$ aqueous micellar solutions, are shown in Figure 2 [54].

The Gaussian star model has been used to analyze results from neutron spin-echo experiments on PI stars which determined for the first time the internal relaxation modes of such polymers [55]. A

systematic structural investigation of star polymers in solution by SANS has been undertaken on a series of PI or polybutadiene star polymers using the Gaussian star model to fit the scattering curves [56]. In a SANS study of the dilute solution behaviour of a series of star-branched PEO molecules, the modelling of the scattering curves using the Gaussian star model has also been reported [57]. Recently, the Gaussian star model has been successfully used in SAXS studies of ABC triblock stars thermopolymers, in order to provide an alternative simplified picture of the system (representatives fittings are shown in Figure 3) [58].

4. Conclusions

Analysis of small-angle scattering data from micellar solutions consisting of lyotropic or polymeric materials has been discussed. The most common analytical expressions for model form factors and structure factors for spherical micelles have been presented.

Despite the alternative 'free-form' methods often used to interpret small-angle scattering data from micellar systems [18], modelling is still an important procedure for analysing small angle scattering data, in particular because it can account for the structure factor contribution and because it facilitates comparison with theoretical density profiles or structure factors. It is expected that during the next few years computer simulations and integral equation theories will play an increasing role in data analysis, supplementing existing analytical and numerical methods.

References

[1] Hamley, I. W. *Introduction to Soft Matter*; John Wiley: Chichester, 2000.

[2] Pedersen, J. S. (1997) Analysis of small-angle scattering data from colloids and polymer solutions: modeling and least-squares fitting. *Advances in Colloid and Interface Science* **70**, 171-210.

[3] Fairclough, J. P. A.; Hamley, I. W.; Terrill, N. (1999) Application of scattering techniques to polymers, block copolymers and micellar systems. *Radiation Physics and Chemistry* **56**, 159-173.

[4] Kotlarchyk, M.; Chen, S.-H. (1983) Analysis of small-angle scattering spectra from polydisperse interacting colloids. *Journal of Chemical Physics* **79**, 2461-2469.

[5] Pedersen, J. S. (1994) Determination of size distributions from small-angle scattering data for systems with effective hard-sphere potential. *Journal of Applied Crystallography* **27**, 595-608.

[6] Rayleigh, L. (1911) *Proceedings of the Royal Society (London)* **A-84**, 25.

(7) Cabane, B. *Colloïdes et Interfaces:* Les Ulis, France, 1984.

[8] Willner, L.; Poppe, A.; Allgaier, J.; Monkenbusch, M.; Lindner, P.; Richter, D. (2000) Micellization of amphiphilic diblock copolymers: Corona shape and mean-field to scaling crossover. *Europhysics Letters* **51**, 628-634.

[9] Halperin, A. (1987) Polymeric micelles: A star model. *Macromolecules* **20**, 2943-2943.

[10] Lobry, L.; Micali, N.; Mallamace, F.; Liao, C.; Chen, S.-H. (1999) Interaction and percolation in the L64 triblock copolymer micellar system. *Physical Review E* **60**, 7076-7087.

[11] Svaneborg, C.; Pedersen, J. S. (2002) Form factors of block copolymer micelles with excluded-volume interactions of the corona chains determined by Monte Carlo simulations. *Macromolecules* **35**, 1028-1037.

[12] Pedersen, J. S.; Gerstenberg, M. C. (1996) Scattering form factor of block copolymer micelles. *Macromolecules* **29**, 1363-1365.

[13] Pedersen, J. S. (2001) Structure factor effects in small-angle scattering from block copolymer micelles and star polymers. *Journal of Chemical Physics* **114**, 2839-2846.

[14] Benoit, H. (1953) On the effect of branching and polydispersity on the angular distribution of the light scattered by Gaussian chains. *Journal of Polymer Science* **11**, 507.

[15] Zimm, B. H.; Stockmayer, W. H. (1949) The dimensions of chain molecules containing branches and rings. *Journal of Chemical Physics* **17**, 1301.

[16] Pedersen, J. S.; Svaneborg, C.; Almdal, K.; Hamley, I. W.; Young, R. N. (2002) A small-angle neutron and X-ray contrast variation scattering study of the structure of block copolymers micelles: corona shape and excluded volume interactions. *Macromolecules*, submitted.

[17] Pedersen, J. S.; Schurtenberger, P. (1996) Scattering functions of semiflexible polymers with and without excluded volume effects. *Macromolecules* **29**, 7602-7612.

[18] Pedersen, J. S. (1999) Analysis of small-angle scattering data from micelles and microemulsions: free-form approaches and model fitting. *Current Opinion in Colloid and Interface Science* **4**, 190-196.

[19] Glatter, O. (1977) A new method for the evaluation of small-angle scattering data. *Journal of Applied Crystallography* **10**, 415-421.

[20] Svergun, D. I.; Semenyuk, A. V.; Feijin, L. A. (1988) Small-angle-scattering data treatment by the regularization technique. *Acta Crystallographica* **A44**, 244-250.

[21] Hansen, S.; Pedersen, J. S. (1991) A comparison of three different methods for analyzing small-angle scattering data. *Journal of Applied Crystallography* **24**, 541-548.

[22] Svergun, D. I.; Pedersen, J. S. (1994) Propagating errors in small-angle scattering data treatment. *Journal of Applied Crystallography* **27**, 241-248.

[23] Percus, J. K.; Yevick, G. J. (1958) Analysis of classical statistical mechanics by means of collective coordinates. *Physical Review* **110**, 1-13.

[24] Hayter, J. B.; Penfold, J. (1981) An analytical structure factor for macroion solutions. *Molecular Physics* **42**, 109-118.

[25] Hansen, J. P.; Hayter, J. B. (1982)Rescaled MSA structure factor for macroion solutions. *Molecular Physics* **6**, 651-656.

[26] Baxter, R. J. (1968) Percus-Yevick equation for hard spheres with surface adhesion. *Journal of Chemical Physics* **49**, 2770-2774.

[27] Lin, E. K.; Gast, A. P. (1996) Self consistent field

calculations of interactions between chains tethered to spherical interfaces. *Macromolecules* **29**, 390-397.
[28] Gast, A. P. (1996) Structure, interactions and dynamics in tethered chain systems. *Langmuir* **12**, 4060-4067.
[29] Lin, E. K.; Gast, A. P. (1996) Semicrystalline diblock copolymer platelets in dilute solution. *Macromolecules* **29**, 4432-4441.
[30] Mortensen, K.; Pedersen, J. S. (1993) Structural study on the micelle formation of poly(ethylene oxide)-poly(propylene oxide)-poly(ethylene oxide) triblock copolymer in aqueous solution. *Macromolecules* **26**, 805-812.
[31] Bütün, V.; Armes, S. P.; Billingham, N. C.; Tuzar, Z.; Rankin, A.; Eastoe, J.; Heenan, R. K. (2001) The remarkable "flip-flop" self-assembly of a diblock copolymer in aqueous solution. *Macromolecules* **34**, 1503-1511.
[32] Castelletto, V.; Itri, R.; Amaral, L. Q. (1997) Micellar aggregates near the isotropic-cubic liquid crystal phase transition. *Journal of Chemical Physics* **107**, 638-644.
[33] Itri, R.; Amaral, C. L. C.; Politi, M. J. (1999) Interactive forces on Aerosol-OT/n-hexane/water/urea reversed micelles by small angle X-ray scattering. *Journal of Chemical Physics* **111**, 7668-7674.
[34] Svensson, B.; Olsson, U.; Alexandridis, P.; Mortensen, K. (1999) A SANS investigation of reverse (water-in-oil) micelles of amphiphilic block copolymers. *Macromolecules* **32**, 6725-6733.
[35] Fulton, J. L.; Pfund, D. M.; McClain, J. B.; Romack, T. J.; Maury, E. E.; Combes, J. R.; Samulski, E. T.; DeSimone, J. M.; Capel, M. (1995) Aggregation of amphiphilic molecules in supercritical carbon dioxide: A small-angle X-ray scattering study. *Langmuir* **11**, 4241-4249.
[36] Brown, G. J.; Richards, R. W.; Heenan, R. K. (2001) Organisation and interactions in aqueous dispersions of polystyrene-polyethylene oxide block copolymer micelles. *Polymer* **42**, 7663-7673.
[37] Goldmints, I.; von Gottberg, F. K.; Smith, K. A.; Hatton, T. A. (1997) Small-angle neutron scattering study of PEO-PPO-PEO micelle structure in the unimer-to-micelle transition region. *Langmuir* **13**, 3659-3664.
[38] Goldmints, I.; Yu, G.-E.; Booth, C.; Smith, K. A.; Hatton, T. A. (1999) Structure of (deuterated PEO)-(PPO)-(deuterated PEO) block copolymer micelles as determined by small angle neutron scattering. *Langmuir* **15**, 1651-1656.
[39] Heenan , R. K.; Eastoe, J. (2000) Droplet interfacial structure studied by SANS contrast variations. *Journal of Applied Crystallogaphy* **33**, 749-752.
[40] Liu, Y. C.; Chen, S. H.; Huang, J. S. (1996) Relationship between the microstructure and rheology of micellar solutions formed by a triblock copolymer surfactant. *Physical Review E* **54**, 1698-1708.
[41] Liu, Y.; Chen, S.-H.; Huang, J. S. (1998) Small-angle neutron scattering analysis of the structure and interaction of triblock copolymer micelles in aqueous solution. *Macromolecules* **31**, 2236-2244.
[42] Chen, S.-H.; Liao, C.; Fratini, E.; Baglioni, P.; Mallamace, F. (2001) Interaction, critical, percolation and kinetic glass transitions in pluronic L-64 micellar solutions. *Colloids and Surfaces A* **183-185**, 95-111.
[43] Poppe, A.; Willner, L.; Allgaier, J.; Stellbrink, J.; Richter, D. (1997) Structural investigation of micelles formed by an amphiphilic PEP-PEO block copolymer in water. *Macromolecules* **30**, 7462-7471.
[44] Förster, S.; Wenz, E.; Lindner, P. (1996) Density profile of spherical polymer brushes. *Physical Review Letters* **77**, 95-98.
[45] Mortensen, K.; Brown, W.; Almdal, K.; Alami, E.; Jada, A. (1997) Structure of PS-PEO diblock copolymers in solution and the bulk state probed using dynamic light-scattering and small-angle neutron scattering and dynamic mechanical measurements. *Langmuir* **13**, 3635-3645.
[46] Castelletto, V.; Caillet, C.; Hamley, I. W.; Yang, Z. (2002) The liquid-solid transition in a model hard sphere system of diblock copolymer micelles. *Physical Review E* **65**, 050601(R).
[47] Castelletto, V.; Caillet, C.; Fundin, J.; Hamley, I. W.; Yang, Z.; Kelarakis, A. (2002) The liquid-solid transition in a micellar solution of a diblock copolymer in water. *Journal of Chemical Physics* **116**, 10947-10958.
[48] Derici, L.; Ledger, S.; Mai, S.-M.; Booth, C.; Hamley, I. W.; Pedersen, J. S. (1999) Micelles and gels of oxyethylene-oxybutylene diblock copolymers in aqueous solution: The effect of oxyethylene-block length. *Physical Chemistry, Chemical Physics* **1**, 2773-2785.
[49] Plestil, J.; Krí , J.; Tuzar, Z.; Prochazka, K.; Melnichenko, Y.; Wignall, G.; Talingting, M.; Munk, P.; Webber, S. (2001) Small-angle neutron scattering study of onion-type micelles. *Macromolecular Chemistry and Physics* **202**, 553-563.
[50] Plestil, J.; Pospíšil, H.; Kadlec, P.; Tuzar, Z.; Krí , J.; Gordeliy, V. (2001) SANS study of multilayer nanoparticles based on block copolymer micelles. *Polymer* **42**, 2941-2946.
[51] Plestil, J.; Pospíšil, H.; Krí , J.; Kadlec, P.; Tuzar, Z.; Cubitt, R. (2001) Characterization of nanoparticles based on block copolymer micelles. *Langmuir* **17**, 6699-6704.
[52] Krí , J.; Masar, B.; Plestil, J.; Tuzar, Z.; Pospíšil, H.; Doskocilová, D. (1998) Three-layer micelles of an ABC block copolymer: NMR, SANS, and LS study of a poly(2-ethylhexylacrylate)-block- poly(methylmethacrylate)-block poly(acrylic acid) copolymer in D2O. *Macromolecules* **31**, 41-51.
[53] Krí , J.; Masar, B.; Pospíšil, H.; Plestil, J.; Tuzar, Z.; Kiselev, M. (1996) NMR and SANS study of poly(methyl methacrylate)-block-poly(acrylic acid) micelles and their solubilization interactions with organic solubilizates in D_2O. *Macromolecules* **29**, 7853-7858.
[54] Castelletto, V.; Hamley, I. W.; Pedersen, J. S. (2002) A SANS investigation of the structure of highly swollen block copolymer micelles. *Journal of Chemical Physics* **117**, 8124-8129.
[55] Richter, D.; Stuhn, B.; Ewen, B.; Nerger, D. (1987) Collective Relaxation of Star Polymers - A neutron Spin Echo Study. *Physical Review Letters* **58**, 2462-2465.
[56] Willner, L.; Jucknischke, O.; Richter, D.; Roovers, J.; Zhou, L.-L.; Toporowski, P. M.; Fetters, L. J.; Huang, J. S.; Lin, M. Y.; Hadjichristidis, N. (1994) Structural investigation of star polymers in solution by small angle neutron scattering. *Macromolecules* **27**, 3821-3829.
[57] Boothroyd, A. T.; Squires, G. L.; Fetters, L. J.; Rennie, A. R.; Horton, J. C.; de Vallera, A. M. B. G. (1989) Small-angle neutron scattering from star-branched polymers in dilute solution. *Macromolecules* **22**, 3130-3137.
[58] Castelletto, V.; Hamley, I. W.; Triftaridou, A. I.; Patrickios, C. S.; Staurouli, N.; Tsitsilianis, N. (2002) A SAXS investigation of ABC triblock star polymers. *Journal of Macromolecular Sciences: Physics*, submitted.

Synchrotron studies of electric-field effects in smectic liquid crystals

Helen F. Gleeson

Department of Physics and Astronomy, Manchester University, Manchester M13 9PL
e-mail: helen.gleeson@man.ac.uk

ABSTRACT

X-ray studies of liquid crystals can reveal a variety of information regarding their physical properties including structures, order parameters, configurations within devices and switching mechanisms. This Review describes the use of synchrotron radiation to examine electric-field effects in ferroelectric and antiferroelectric liquid crystal devices. Three general types of experiment are described. Firstly, static studies in which either no electric field is applied to the device of interest, or the field is changed sufficiently slowly to ensure that the equilibrium response is measured. Secondly, time-resolved studies are described, in which layer deformations are followed on a 10 μs time scale, providing detailed information about the switching mechanisms in ferroelectric devices. Finally, resonant X-ray scattering experiments are described in which the influence of electric fields on interlayer structure within devices containing antiferroelectric and intermediate (ferrielectric) phases is considered.

Introduction

X-rays provide an ideal probe of smectic liquid crystals. In such materials, molecules typically around 40Å in length are organised in layers that are more correctly considered as density waves. The layer spacing is usually close to the molecular length. The ordering of the molecules within the layers is determined by the phase type, as indicated in Figure 1. The simplest smectic phase is the smectic-A phase (SmA), in which the orientational order of the molecules (defined by a director, **n**) is coincident with the layer normal, **k**. In smectic-C (SmC) liquid crystals, the director adopts a temperature dependent tilt angle, θ, with respect to **k** and molecules in consecutive layers are oriented in the same direction (synclinic ordering). The chiral form of the SmC phase (chirality is indicated by an asterix, SmC*) is of particular interest as it has the potential to exhibit ferroelectricity [1] in surface-stabilised devices [2]. The details of this phenomenon are discussed in many excellent texts [3]. Antiferroelectricity was first observed in liquid crystals in 1989 [4] in a system closely related to the SmC* phase. In the SmC^*_{AF} phase, the molecules in consecutive layers adopt an anticlinic arrangement, modified by a macroscopic helix induced by the chirality which has a pitch typically several hundred smectic layers in length. Two final modifications of the tilted, chiral, smectic phases should be introduced; the

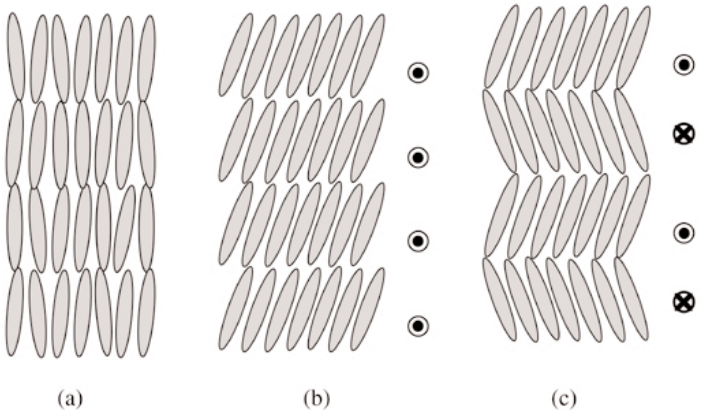

Figure 1. Representations of the several types of smectic liquid crystals: (a) smectic-A, (b) smectic-C* and (c) smectic-C^*_{AF}

intermediate SmC^*_{FI1} and SmC^*_{FI2} phases. These occur between the ferroelectric SmC* phase and the antiferroelectric SmC^*_{AF} phase and were originally described as ferrielectric, though this is now known not to be strictly true. The structure of these phases has been elucidated recently by resonant scattering X-ray [5,6,7] and optical [8] experiments. It is the higher temperature SmC^*_{FI2} phase, which has a 4-layer repeat, that is of interest in this Review.

Ferroelectric and antiferroelectric liquid crystals are of significant interest, not just because they are the only known fluids that exhibit such properties (all

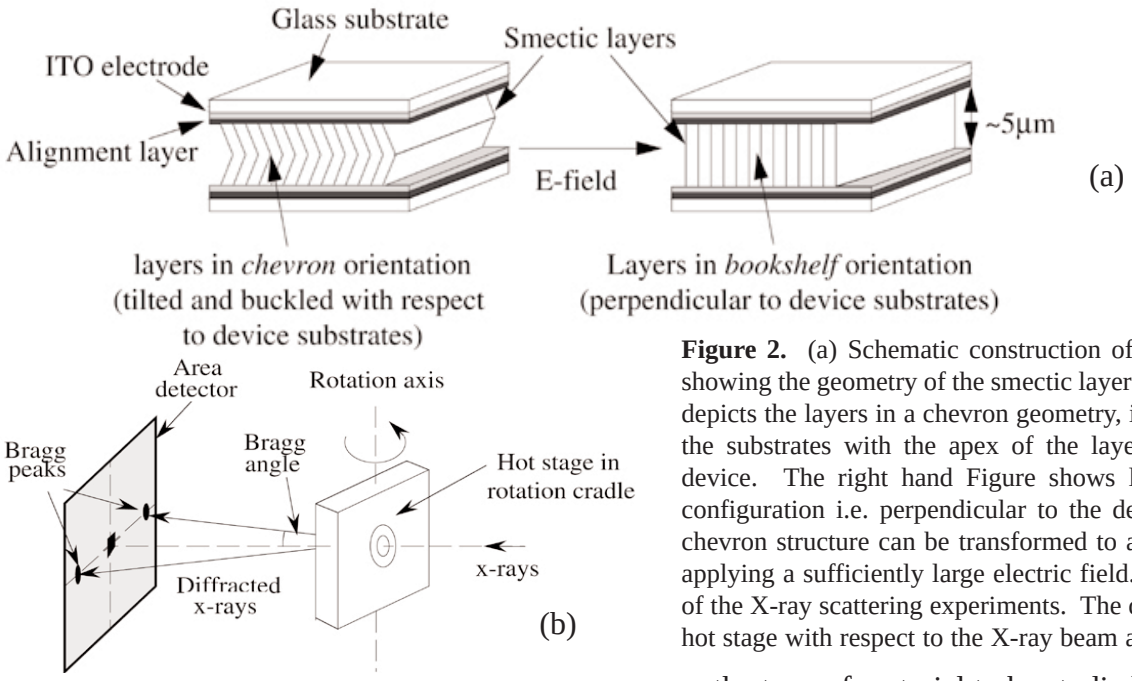

Figure 2. (a) Schematic construction of a liquid crystal device showing the geometry of the smectic layers. The left hand Figure depicts the layers in a chevron geometry, i.e. tilted with respect to the substrates with the apex of the layers in the centre of the device. The right hand Figure shows layers in the bookshelf configuration i.e. perpendicular to the device substrates. The chevron structure can be transformed to a bookshelf structure by applying a sufficiently large electric field. (b) The arrangement of the X-ray scattering experiments. The device is held within the hot stage with respect to the X-ray beam as depicted in Figure 3.

other materials in this class are solids), but because of their potential in electro-optic devices. Ferroelectric liquid crystal devices are characterised by bistability and switching that is a factor of 10^2-10^3 times faster than the millisecond switching exhibited by conventional (nematic) devices such as those used in lap-top computers. Antiferroelectric liquid crystal devices have the potential for tri-state switching and also exhibit rapid switching times of around 10^{-5}-10^{-6} seconds. Despite their clear advantages over nematic liquid crystals, ferroelectric and antiferroelectric liquid crystal devices are only just appearing in the market place, primarily because of the added complexity that the smectic layer structure adds to the device geometry and electric-field switching mechanisms. Synchrotron radiation has proven to be a powerful tool in studying these phenomena. This Review paper highlights some of the ways in which synchrotrons can be used to investigate the layer structure in devices and the ways in which electric-fields deform this layer structure.

Experimental

All of the conventional X-ray scattering experiments described within this Review were carried out at station 2.1 of the SLS at Daresbury Laboratory. The resonant scattering experiments were carried out at the Advanced Photon Source (APS) at Argonne National Laboratories, Il.. The liquid crystal devices were constructed as indicated in Figure 2(a). Parallel glass plates of thickness 150µs were used to encapsulate a thin layer of liquid crystalline material, usually between 3µs and 25µs thick, depending on the type of material to be studied. The glass had a conductive Indium Tin Oxide (ITO) coating on the inner surfaces to allow fields to be applied perpendicular to the glass plates. An alignment layer (usually rubbed nylon) was also added to the inner surfaces to ensure good, uniform alignment of the liquid crystal film.

The liquid crystal devices were held in a temperature-controlled environment in a cradle as shown in Figure 2(b). The liquid crystal phases of interest were exhibited at well-defined temperatures. Rotation of the sample about an axis perpendicular to the direction of incident X-rays allowed the layer structure within the device to be deduced; diffraction maxima occur when the geometry is such that the smectic layers satisfy the Bragg condition. Electric fields were applied to the samples via the transparent electrodes and the electrical signal was synchronised with the detector where necessary. The time-resolved facility at station 2.1 of the SRS allows a minimum time frame of 10µs to be selected which provides reasonably good time resolution in the study of switching mechanisms for ferroelectric liquid crystals.

Smectic layer structures in ferroelectric and antiferroelectric devices and static field effects.

The structure adopted by smectic layers within a device depends on many features, but most significantly the phase sequence of the material studied, the way in which the layer spacing changes with temperature, the alignment layers used within the device and the electric-field history. Most

commonly, ferroelectric and antiferroelectric liquid crystals adopt a so-called chevron structure, first observed by Reiker *et al* [9] (see Fig. 3). The chevron structure is a consequence of the layer shrinkage that occurs as the material cools from an untilted SmA phase to the tilted SmC* phase and the chevron angle is around 0.85 of the tilt angle, θ [3]. Chevron structures have also been observed in devices containing achiral SmC [10] and SmA [11] materials where there is also layer shrinkage, but in which the geometrical considerations differ from the ferroelectric case.

The electric torque produced when a sufficiently large field is applied to the device can cause the chevron structure to transform irreversibly to a so-called bookshelf structure in which the layers are largely perpendicular to the device substrates. This transition is usually accompanied by the formation of a chevron structure in the plane of the device, a consequence of geometric considerations. Figure 3 indicates how the diffraction pattern and experimental geometry can facilitate the study of the layer structure within a device, defining the chevron angle for both types of chevron. The chevron to book-shelf transition has been studied extensively within ferroelectric liquid crystals [12,13]. For conventional, surface-stabilised devices it occurs at relatively high fields (typically between 5 and 10 $V\mu m^{-1}$) and usually has a distinct threshold. The response time of the transition depends on the field applied, but it is slow compared to the ferroelectric switching, occurring over seconds rather than microseconds [13]. This is as expected since the transition is associated with gross reorganisation of the layer structure, rather than switching of the molecular directions within the layers. If the field is removed before the reorganisation is complete, a distorted bookshelf structure results, indicating that the transition is both field- and time-dependent.

There are rather few studies of the chevron structure within antiferroelectric devices [14], or of the nature of the chevron to bookshelf transition [15,16,17, 18,19]. It is important to note that such devices are generally not surface-stabilised in contrast to those discussed above, since the helicoidal pitch of materials that exhibit antiferroelectric phases is generally too small to allow surface stabilisation. Further, the chevron angle differs significantly from the tilt angle θ deduced optically with ratios of around 0.6 quoted for some materials [20]. The chevron to bookshelf transition takes a different form

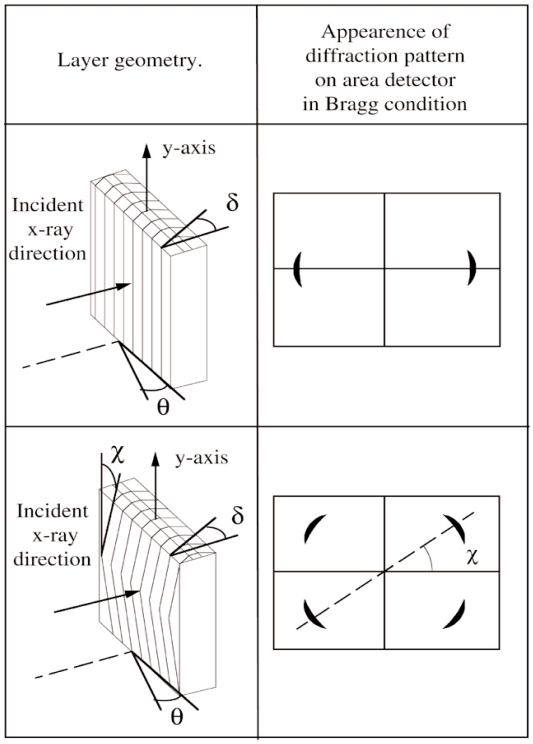

Figure 3. Idealised layer structures adopted within smectic devices and the associated idealised diffraction patterns observed in the Bragg condition. The devices on the left depict the geometry of the smectic layers. In both cases the layers adopt a configuration that combines a chevron structure adjacent to the substrates with bookshelf layers in the centre of the device. The chevron angle is defined as the angle subtended at the glass substrate,δ, so in the bookshelf geometry δ= 0. In the lower diagram, the layers have also buckled in the plane of the device, forming a so-called 'in-plane' chevron at an angle χ to the rotation axis.

in the SmC^*_{AF}, intermediate and SmC* phases, as can be seen from the data shown in Figure 4. In this experiment, an initial rocking curve (inset) shows the original chevron structure adopted within the device, in each case with some residual bookshelf layers, probably situated at the apex of the chevron. The device was held at specific rocking angles and the electric field incremented gradually. The Bragg peak intensity indicates the presence or absence of layers at a specific rocking angle for a particular value of applied field. Once the layers were deformed irreversibly (at voltages higher than around 40 Vrms, 100Hz), the device was subjected to a heating and cooling cycle to ensure that the original layer structure was reformed prior to changing angle and repeating the electric-field experiment. The data show that the chevron to bookshelf transition occurs differently in each phase. In the SmC^*_{AF} phase, a distinct threshold is observed and this has been noted in separate experiments to occur at fields higher than are required to induce an antiferroelectric to ferroelectric transition. Such a result is unsurprising

(a)

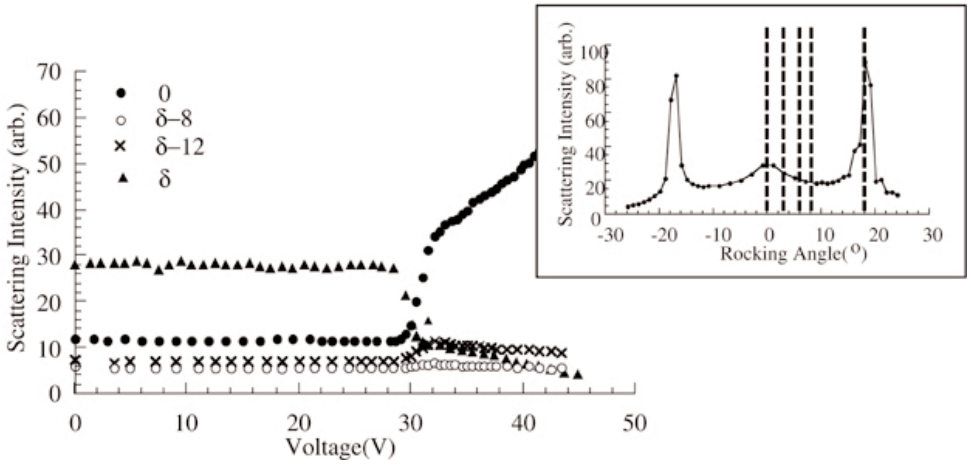

(b)

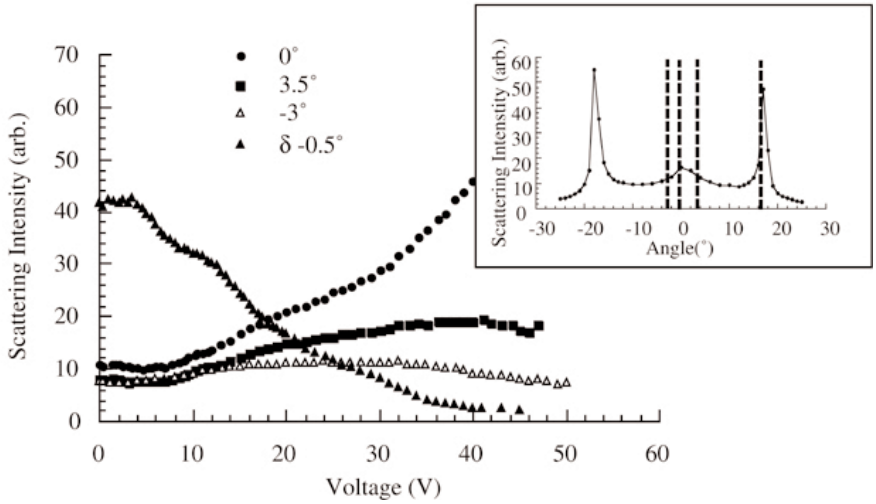

(c)

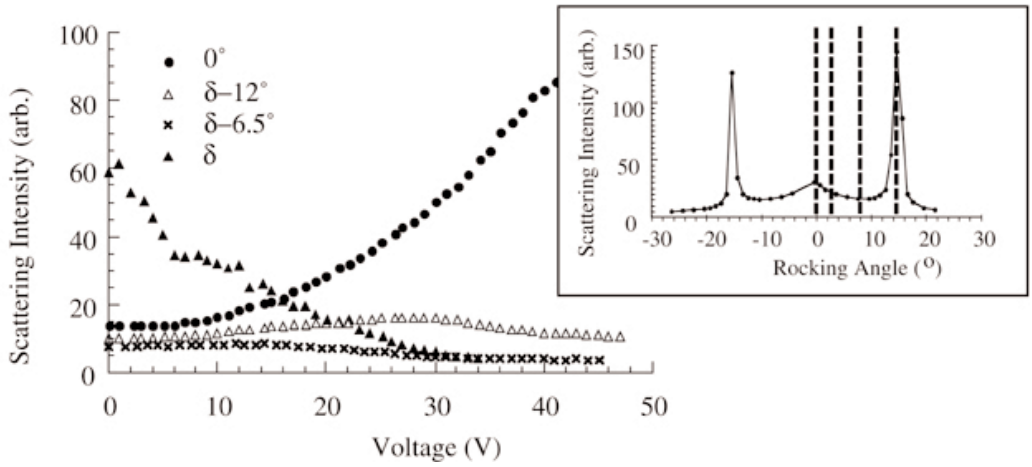

Figure 4. Bragg peak intensities as a function of applied voltage for specific rocking angles in a device containing material exhibiting **(a)** antiferroelectric, **(b)** intermediate and **(c)** ferroelectric phases. The inserts show the field-free rocking curves with distinct peaks at around ±20° indicating that the majority of the original structure was in a chevron configuration. Each of the inserts also shows a broad peak around a rocking angle of 0°, indicating that a small proportion of the layers were in a bookshelf configuration. The angles at which the intensity of the Bragg peak was monitored as a function of applied voltage (main Figures) are indicated by lines on the inserts.

since in the antiferroelectric phase there is no electric torque and the system must thus be switched to a ferroelectric structure before an electric field can influence the layer structure. In the intermediate phases, the threshold is low and there is evidence of layer curvature just above threshold (Bragg scattering is observed for all rocking angles). This is a surprising result and theoreticians are currently

examining possible mechanisms for this type of deformation [21]. Finally, in the ferroelectric phase, there is a continuous growth of the residual bookshelf structure at the expense of the chevron layers and no threshold. Again, theoreticians are currently developing models that explain this feature [22].

Time-resolved X-ray studies of ferroelectric switching mechanisms.

The layer structure and field-evolution of the chevron to bookshelf structure are important features of antiferroelectric and ferroelectric devices. The layer structure has a huge influence on the optical properties of a device [3] and it is advantageous to operate a device below the chevron to bookshelf transition since an in-plane chevron causes large degrees of scattering (and hence loss in contrast and light transmission) in a device. However, a key question that challenged the liquid crystal community for some years was how the layer structure facilitated normal ferroelectric switching. The problem is simple; during switching of a ferroelectric device, the molecules move from one stable state at, say, $+\theta$, to the other at $-\theta$. In doing so, either the layer spacing must change (as the molecules go through $\theta = 0$) or they must flex to accommodate the switching. There are considerable technological difficulties in studying this directly via X-ray scattering since the weakly scattering liquid crystal layer is extremely thin (~ 5μs) and the switching occurs on a microsecond time scale. Station 2.1 at the SRS can be used to study time-dependent scattering on such a time scale and has been used to provide direct evidence of layer flexing during switching [23,24].

The experiment is carefully timed with the field applied to the ferroelectric liquid crystal device triggered by the detector system. The detection is arranged so that the X-ray scattering pattern is recorded at different times along the bipolar switching pulse, with an extremely short integration time of 30μs. The temperature and switching voltages are selected so that the device has an optical response time of around 150μs, ensuring that sufficient detail is obtained across the switching cycle. Naturally, 10μs time frames are of insufficient length to obtain any reliable signal, so the experiment was gated and repeated until the equivalent of 2 seconds of data collection time was accumulated in each diffraction pattern recorded. An area detector was used which afforded two distinct advantages. Firstly, it was possible to obtain information on any layer motion in the *plane* of the device through the switching cycle that might occur concurrently with layer flex through the depth of the device. The former would be apparent through an angular shift in the position in the Bragg peak on the detector, while the latter can be deduced from a change in the Bragg scattering intensity during switching which indicates that the layers have moved from the Bragg position. Further, any change in layer spacing would be apparent through a radial change in the position of the Bragg peak. Secondly, the area detector allowed both of the Bragg peaks in a Friedel pair to be measured at the same time, providing information on the layers at the angle of investigation and at a lower angle, shifted by

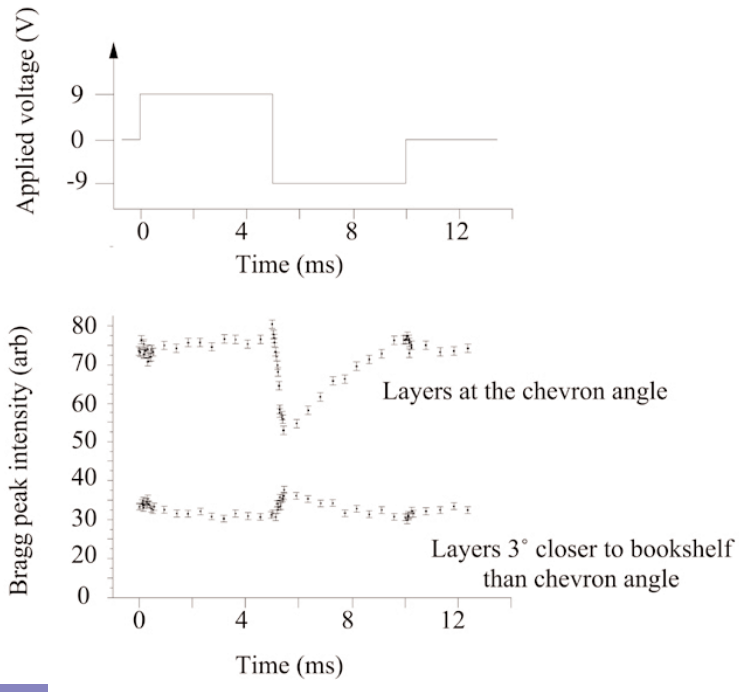

Figure 5. Time resolved data showing the intensity of the Bragg peak at different times along a bipolar switching pulse. Data are shown for an angle corresponding to the chevron angle and one approximately 3° lower. The Bragg peak intensity is a measure of the layers at a particular angle within a device.

twice the Bragg angle.

Typical time-resolved data are shown in Figure 5. It can be seen that as the field is reversed, the intensity of the Bragg peak reduces for layers at the original chevron angle, with a concurrent increase in scattering intensity at lower angles. Thus, layer flexing occurs on a ms time scale and towards lower angles, agreeing with the predictions of Gieβelmann and Zugenmaier [25]. No change in layer spacing was observed throughout the switching cycle in any of the experiments so far reported. The observation of in-plane motion is somewhat inconclusive but appears [23] to be small (around 1°) if indeed it occurs. It appears that switching between the two stable ferroelectric states is mediated in some cases at least by flexing of the layers to lower angles. It is of course interesting to consider whether the layers always flex by the same amount, whether this is a mechanism that is particularly easy relatively close to the SmC* to SmA transition (where our experiments were conducted to allow all the conditions required by the apparatus at station 2.1 to be met) or indeed whether similar phenomena occur in other phases. To date, no further information has been published, probably due to the technical difficulty associated with the experiments. However, preliminary data obtained in very recent experiments indicate that reversible, rapid, layer flexing also occurs to some extent in switching in the antiferroelectric phase [26] . Certainly future experiments will investigate this further.

Resonant X-ray studies of liquid crystal devices.

The previous Sections have indicated the value of X-ray scattering to the study of layer structures and switching mechanisms in ferroelectric and antiferroelectric devices. However, the experiments described can provide no information on the inter-layer structures in the SmC*, SmC*$_{AF}$ and intermediate phases, how they might be modified within devices, or indeed in what way they are influenced by electric fields. Resonant scattering experiments present a powerful probe of interlayer structure in smectic liquid crystals. Briefly, the X-ray energy is tuned to the absorption edge of one of the atoms contained within the liquid crystal molecule, typically either sulphur or selenium. In the resonant scattering experiments, forbidden reflections occur at positions corresponding to:

$$\frac{Q_z}{Q_o} = l + m\left(\frac{1}{\nu} + \varepsilon\right)$$

where l is an integer, m can take integer values between ±2, ν is the super-lattice periodicity and ε is the ratio of the smectic layer spacing to the helicoidal pitch of the structure. The super-lattice periodicity takes values of 1, 2, 3 and 4 in the SmC*, SmC*$_{AF}$, SmC*$_{FI1}$ and SmC*$_{FI2}$ phases respectively. The SmC* phases were first studied using this technique by Mach *et al* [5,27] in free-standing films (the sample is suspended across a hole with no glass substrates), confirming details of the interlayer structures. The technique has been used extensively on films [7] and was later adapted to study devices, though it is has so far proven possible only to examine materials containing a selenium atom in such a geometry since glass is insufficiently transparent at the energies corresponding to the sulphur absorption edge.

Resonant scattering peaks have been obtained for all the SmC* related phases in a device configuration apart from the 3-layer SmC*$_{FI1}$ phase. The resonant scattering signal obtained from a device containing an antiferroelectric liquid crystal [28, 29] , is shown in Figure 6. The resonant peaks are positioned around Q_z/Q_o = 0.5 and the splitting corresponds to the helicoidal pitch adopted by the material at the temperature of the experiment. Application of an electric field leaves the spacing of the resonant peaks largely unchanged until they effectively disappear at the field-induced transition from the antiferroelectric to ferroelectric state, indicating that the pitch is unaffected by the field prior to that transition. The chevron to bookshelf transition occurs almost coincident with the loss of the resonant peaks characteristic of the SmC*$_{AF}$ phase, in agreement with the discussion above. Resonant peaks associated with the 4-layer SmC*$_{FI2}$ phase [29] are shown in Figure 7 at the Q_z/Q_o = 0.75 position. Interestingly, these peaks remain on application of fields beyond that necessary to induce the chevron to bookshelf transition. Since the SmC*$_{FI2}$ phase is strictly antiferroelectric in the absence of a field, it can be concluded that there must be some field-induced deformation of the structure prior to the chevron to bookshelf transition, allowing an electrical torque to be experienced by the layers. It is possible to speculate that this low-field induced

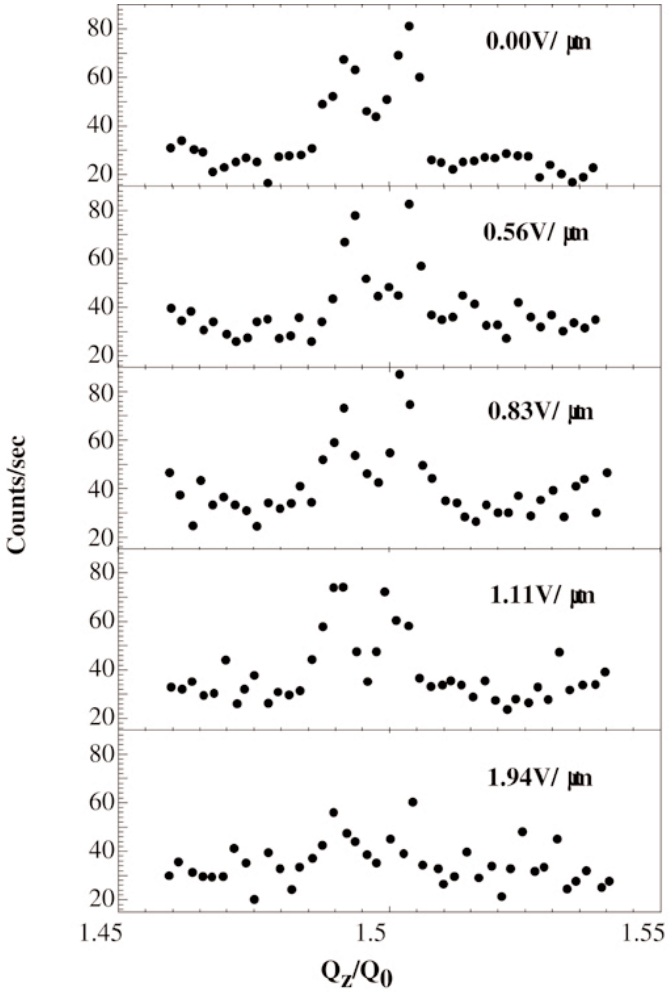

Figure 6. Resonant scattering data for the antiferroelectric phase showing the dependence of the resonant peaks on applied field. It can be seen that the peaks become indistinct for the highest voltage applied, indicating a loss of the 2-layer structure.

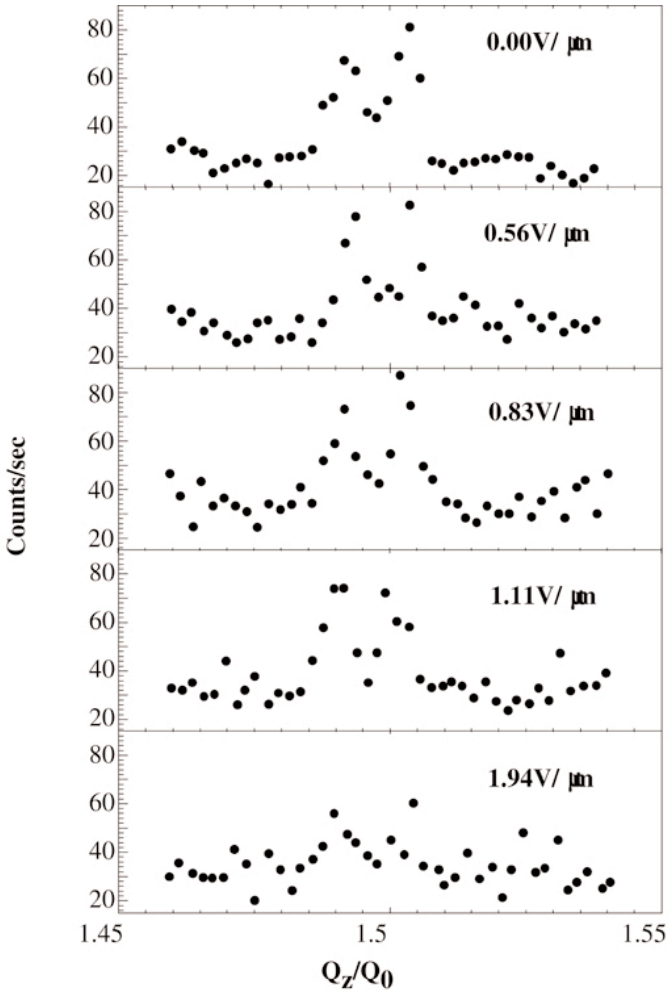

Figure 7. Resonant scattering data for the 4-layer intermediate phase showing the dependence of the resonant peaks on applied field. The resonant peak associated with the 4-layer structure persists for all applied fields, indicating that it is stable with respect to applied field.

deformation is linked to the layer curvature observed at the chevron to bookshelf transition in other experiments. Unfortunately, to date, the resonant scattering data are insufficiently clear to allow detailed study of the 4-layer structure, they are sufficient only to indicate that such a repeat exists.

Summary

It is clear from this Review that a wealth of information can be obtained via synchrotron studies of smectic liquid crystal devices. The value of such experiments lies in the fact that they study layers *directly*. X-ray scattering is an invaluable tool in the study of liquid crystals and liquid crystal devices. It is certain, as synchrotron sources improve, providing microbeam sources, higher flux etc. that more sophisticated experiments will be carried out, providing yet more information about these systems.

Acknowledgements

The work described in this Review was largely funded by the EPSRC with support in the form of CASE awards from GEC, DERA and Lucent Technologies. Many graduate students and postdoctoral researchers at Manchester have been heavily involved in the work at Daresbury and other synchrotron sources over the past few years. The resonant scattering work could not have been carried out without the valued collaboration of colleagues from the USA and France.

REFERENCES

[1] Meyer, R. B., Liebert, L., Strzelecki L. & Keller, P. (1975) Ferroelectric liquid crystals. *J. Phys (Paris), Lett.* **36**, L-69-71.

[2] Clark, N. A. & Lagerwall, S. T. (1980) Submicro-second

bistable electro-optic switching in liquid crystals. *Applied Physics Letters*, **36** 889-901.
[3] See, for example, "Ferroelectric Liquid Crystals. *Principles, Properties & Applications*" by Goodby J. W., *et al*, Gordon & Breach (1991).
[4] Chandani, A. D. L., Gorecka, E., Ouchi, Y., Takezoe, H. & Fukuda, A. (1989), Antiferroelectric chiral smectic phases responsible for the tristable switching in MHPOBC. *pn. J. Appl. Phys.* **28**, 1265-1268.
[5] Mach, P., Pindak, R., Levelut, A-M., Barois, P., Nguyen, H. T., Huang, C. C. & Furenlid, L. 1998) Structural characterization of various chiral smectic-C phases by resonant X-ray scattering. *Phys. Rev. Lett.*, **81**, 1015-1018.
[6] Cady, A., Pitney, J. A., Pindak, R., Matkin, L. S., Watson, S. J., Gleeson, H. F., Cluzeau, P., Barois, P., Levelut, A-M., Caliebe, W., Goodby , J. W., Hird M. & Huang, C .C. (2001) Orientational ordering in the chiral SmC*FI2 liquid crystal phase determined by resonant polarised X-ray diffraction. *Phys. Rev. E., Rapid Communications*, **64**, 050702/ 1-4.
[7] Hirst, L.S., Watson, S.J., Gleeson, H.F., Cluzeau, P., Pindak, R., Pitney, J., Cady, A., Johnson, P., Huang, C.C., Levelut, A-M., Barois, P., Srajer, G., Pollmann, J., Caleibe, W., Seed, A., Herbert, M.R., Goodby, J.W. & Hird, M. (2002) The interlayer structures of the chiral smectic liquid crystal phases revealed by resonant X-ray scattering. *Phys.cRev. E* **65(4)**, 041705/ 1-10
[8] Johnson, P.M., Olson, D.A., Pankratz, S., Nguyen, T., Goodby, J.W., Hird, M. & Huang C.C. (2000) Structure of the liquid-crystal ferrielectric phases as determined by ellipsometry. *Phys. Rev. Lett*. **84**, 4870-4873
[9] Rieker, T.R. & Clark, N.A., (1988) Smectic-C `chevron', a planar liquid-crystal defect: implications for the surface-stabilized ferroelectric liquid-crystal geometry. *Phys. Rev. A*, **37(3)**, 1053-1056.
[10 Findon, A., Gleeson, H.F. & Lydon, J.E. (1998) The realignment of an achiral smectic-C chevron structure with applied field. *Liquid Crystals* **25**, 631-638.
[11] Morse, A.S. & Gleeson, H.F. (1997) Observation of a chevron hybrid structure in the smectic-A phase of a liquid crystal device. *Liquid Crystals* **23(4)**. 531-535.
[12] Patel, J., Lee, S., & Goodby J.W. (1989) Electric-field-induced layer reorientation in ferroelectric liquid crystals. *Phys. Rev. A.*, **40**, 2854-2856.
[13] Bryant, G.K. & Gleeson, H.F. (1998) Evolution of irreversible layer deformations in FLC devices caused by high electric field treatment. *Ferroelectrics* **214**, 709-716 and references therein.
[14] Cluzeau, P., Barois, P., Nguyen, H.T., & Destrade, C. (1998) Polymorphism and chevron layer structure of an antiferroelectric liquid crystal studied by X-ray diffraction. *Eur. Phys. J*. **3**, 73-82.
[15] Matkin, L.S., Gleeson, H.F., Watson, S.J., Baylis, L., Bowring, N., Goodby, J.W., Hird, M. & Seed, A. (2000) Electric field induced layer deformations in the subphases of an antiferroelectric, liquid crystal device. *App. Phys. Lett*. **77(3)**, 340-342.
[16] Watson, S.J., Gleeson, H.F., Matkin, L. & Baylis, L. (2002) Influence of electric fields on the smectic layer structure of ferroelectric and antiferroelectric liquid crystal devices. *Phys. Rev. E* **65(3)**, 031705/ 1-9.
[17] Itoh, K., Johno, M., Ouchi, Y., Takezoe, H. & Fukuda, A. (1991) Self-recovery from alignment damage under AC fields in antiferroelectric and ferroelectric liquid crystal cells. *Jap. J. Appl. Phys.* **30**, 735-740.
[18] Johno, M., Chandani, A.D.L., Ouchi, Y., Takezoe, H., Fukuda, A., Ichihashi, M. & Furukawa, K. (1989) Smectic layer switching by an electric field in ferroelectric liquid crystal cells. Jap. J. Appl. Phys, 28, L119-20; Johno, M., Ouchi, Y., Takezoe, H., Fukuda, A., Terashima, K. & Furukawa, K. (1990) Correspondence between smectic layer switching and DC hysteresis of apparent tilt angle in an antiferroelectric liquid crystal mixture. *Jap. J. Appl. Phys*. **29**, L111-114.
[19] Cluzeau, P., Barois, P. & Nguyen, H. T. (2002) X-ray scattering study of the electric-field-induced layer deformations of an antiferroelectric liquid crystal. *European Physical Journal E*. **7(1)**, 23-29.
[20] Mills, J.T., Gleeson, H.F., Hird, M., Styring, P. & Goodby, J.W. (1998) X-ray and optical studies of the tilted phases of materials exhibiting antiferroelectric, ferrielectric and ferroelectric mesophases. *J. Material Chem*. **8(11)**, 2385-2390.
[21] Taylor, P.L., Case Western Reserve University, Private Communciation.
[22] Mottram, N., Strathclyde University, Private Communication.
[23] Gleeson, H.F. & Morse, A.S. (1996) Microsecond studies of layer motion in a ferroelectric liquid crystal device. *Liquid Crystals Preliminary Communications* **21(5)**, 755-758.
[24] Gleeson, H.F., Bryant, G.K. & Morse, A.S. (2001) Time resolved X-ray scattering studies of reversible layer flexing in surface stabilised ferroelectric liquid crystal devices. Invited paper, *Mol. Cryst. Liq.Cryst*. **362**, 203-215.
[25] Giebelmann, F. & Zugenmaier, P. (1993) Coupled director and layer reorientation in layer tilted ferroelectric smectic liquid crystal cells. *Mol. Cryst. Liq. Cryst*. **237**, 121-143.
[26] Wang, W., Gleeson, H.F., Conn, J. & Roberts, N. Unpublished data (2002)
[27] Mach, P., Pindak, R., Levelut. A.M., Barois, P., Nguyen, H.T., Baltes, H., Hird, M., Toyne, K., Seed, A., Goodby, J.W., Huang, C.C., & Furenlid, L. (1999) Structures of chiral smectic-C mesophases revealed by polarization-analyzed resonant X-ray scattering. *Phys. Rev. E* **60**, 6793-6802.
[28] Matkin, L.S., Gleeson, H.F., Mach, P., Huang, C.C., Pindak, R., Srajer, G., Pollmann J., Goodby, J.W., Hird, M. & Seed, A. (2000) Resonant X-ray Scattering at the Se Edge in Liquid Crystal Free Standing Films and Devices. *Appl. Phys. Lett*. **76(14)**, 1863-1865.
[29] Matkin, L.S., Gleeson, H.F., Watson S.J., *et al*, (2001) Resonant X-ray scattering study of the antiferroelectric and ferrielectric phases in liquid crystal devices. *Phys. Rev. E* **64**, 021705/ 1-6.

Multiscale Modelling in Polymer Science

J. Crawshaw and A. H. Windle

Department of Materials Science and Metallurgy, University of Cambridge, Pembroke Street, Cambridge, CB2 3QZ, UK

ABSTRACT

We present a brief survey of techniques for modelling polymers, with particular emphasis on the multiscale approach as applied in our laboratory. The measurable properties of polymers depend on a structural hierarchy which ranges from chemical detail, to single chains, to aggregates of chains and up to continuum phenomena. Therefore, complete description of a polymer requires a model encompassing a wide range of length- and time-scales. This would take large amounts of computing resources and also produce redundant detailed information. In practice, coarse-grained models are used in place of fully atomistic representations to extend the time- and length-scales accessible to simulation within reasonable computing times. A process of reverse mapping may then be used to recover fully atomistic detail from the coarse-grained model, bridging the gap between modelling large-scale processes and chemical detail. This survey includes a number of examples of polymer modelling at various levels of detail, and illustrates the application of the reverse mapping process.

1. Introduction

Multiscale modelling is a valuable tool in polymer science for exploring the structure and dynamic behaviour of these materials, allowing a wide range of length and time scales to be probed by mutually interlocking models. Our purpose here is to demonstrate the multiscale approach in action, but by drawing on examples predominantly from the work of the Cambridge group. It has been applied to a wide variety of problems including polymer welding, block copolymer morphologies, and the evolution of liquid crystalline polymer textures. The prediction of an X-ray diffraction pattern from a model structure as part of a process of structure refinement is a widely used aspect of computer simulation. An example from the Cambridge group and collaborators is its application by Welsh and Windle [1] and Welsh, Blundell and Windle [2, 3] to the investigation of structural ordering in random copolyesters: Figure 1 shows an example of experimental and predicted X-ray patterns from their work. The simulation of diffraction patterns and methodology of structure refinement is already a very familiar topic to the fibre diffraction community. Therefore, our aim here is to concentrate on some techniques involved in the modelling of polymers and, in particular, on what a multiscale approach has to offer.

2. Hierarchical Models in Polymer Science

The observable properties of any polymer depend on a hierarchy of structure including: chemical detail at the atomistic level, individual chains, microscopic features involving aggregates of chains such as lamellae and spherulites, up to continuum phenomena at the macroscale. Therefore, the complete description of a polymer typically requires a wide range of length scales from the chemical bond, at around one Angstrom in length, up to chain aggregates extending for many hundreds of Angstroms and beyond. There is also a wide range of timescales, with chemical bond vibrations occurring over tens of femtoseconds and, at the other extreme, collective motions of many chains taking seconds, or much longer. Computer simulation of the macroscopic behaviour of a polymer system in principle could include all chemical detail. However, this would take an inordinate amount of computer resources for anything other than small models over short times. Furthermore, it can also introduce a degree of redundancy, as some of the detailed information is irrelevant to macroscopic phenomena. In practice, models therefore concentrate on a narrow length scale by simplifying the picture to isolate a particular structure or process. Coarse-grained models are used in place of fully atomistic representations to extend the time and length scales

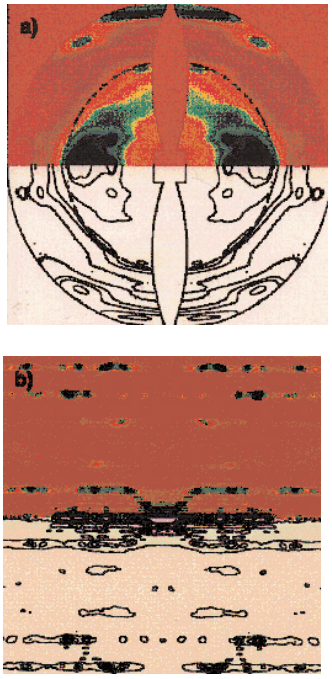

Figure 1: Diffraction patterns from 50% PET/PEN random copolymer: a) experimental pattern mapped into reciprocal space; b) pattern from 3D model. Data extend to 0.5Å^{-1} in both the vertical and horizontal.

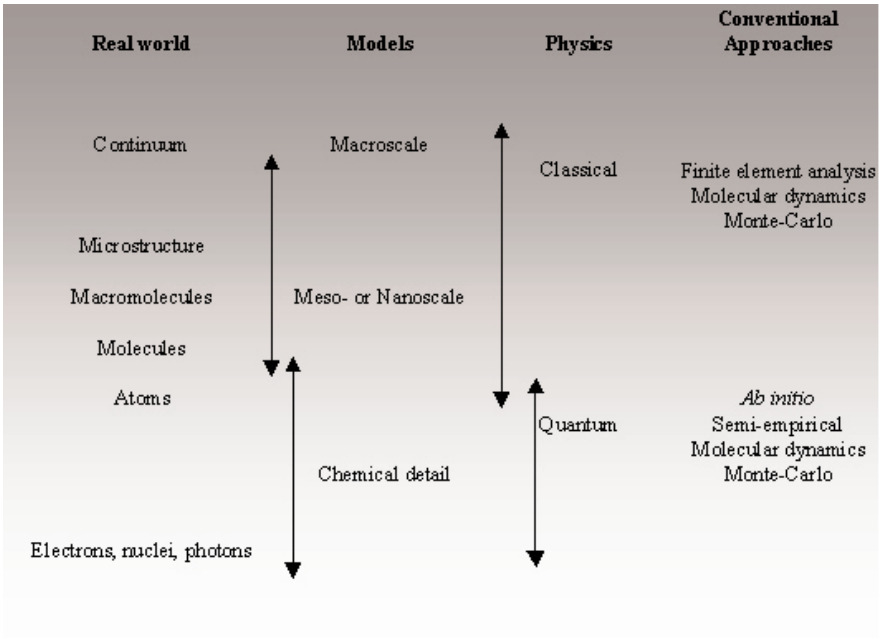

Figure 2: Relationship between modelling and structural hierarchies.

accessible to simulation within reasonable computing times. A process of *reverse mapping* can then be used to recover fully atomistic detail from coarse-grained models generated during a simulation. In this way the gap between modelling large scale processes and chemical detail may be bridged. Figure 2 summarises the relationship between the hierarchy of structures of interest in the study of polymers and the associated modelling hierarchy.

We will begin this survey with an example of modelling at the atomistic level to predict the persistence lengths of polymer chains having specific chemistries, later seeing how the results from this are required as input parameters for microscale models of liquid crystalline polymers.

3. Modelling at the Atomistic Level

Monte Carlo on Chains with Chemical Detail

In the development of synthetic liquid crystalline polymers, the aim is to design molecules that while being sufficiently stiff to form an ordered mesophase, also possess enough chain flexibility for the melting point to lie within the range of practical processing temperatures. Typical means of achieving these properties include the use of flexible alkyl spacers, random copolymerisation to disrupt chain periodicity, or the substitution of bulky side groups onto aromatic rings.

Bedford, Yu and Windle [4] set out to find a simple yet effective parameter for predicting the tendency of a molecule to form a liquid crystalline phase, its *mesogenicity*. A parameter was required that could be derived from a chemically detailed molecular model so that it could potentially be used to target suitable molecules for synthesis of liquid crystalline polymers. Precedents observed in the choice of a candidate parameter were the lattice model of Flory and co-workers [5] which predicts liquid crystallinity for short rigid rods on the basis of their axial ratio, and the use by Kratky and Porod [6] of the persistence length[a] (q), illustrated in Figure 3, as a key parameter for describing semi-flexible worm-like chains. Accordingly, the first parameter to be assessed was the persistence length ratio[b](q/d).

Bedford *et al.* [4] restricted the model to a single isolated chain in order that full chemical detail could

[a] *Persistence length* (q) is the end-to-end distance of the chain projected onto the first bond vector, averaged over all chain configurations, illustrated in figure 3.

[b] *Persistence length ratio* or *persistence ratio* is the ratio of persistence length (q) to chain diameter (d), where d is defined as the largest diameter cylinder that can be accommodated inside the unit cell of the polymer in question.

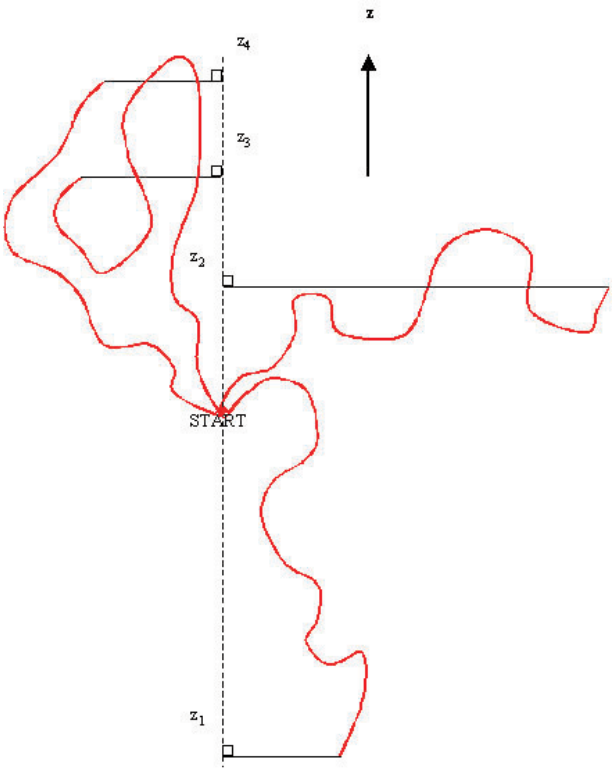

Figure 3: A set of worm-like chains drawn with a common starting direction, showing the persistence length defined as the mean displacement of the chain ends in the direction of the first bond, i.e. $q = \langle z_1 + z_2 + z_3 + z_4 + ... \rangle$.

be considered, thus ignoring the orientating effects of neighbouring molecules, and thereby underestimating the persistence length in a condensed phase. Isolated chains were simulated in a three-step process: first, the polymer chain was built using mean monomer geometries from the Cambridge Crystallographic Data Bank, or from published *ab initio* calculations on fragments and experimental data; next, the structure was optimised using the CERIUS molecular mechanics software to assign rotational energy profiles to all non-ring backbone bonds; finally, a Monte Carlo simulation was used to assign rotational angles to the bonds at a given temperature and thus generate many possible examples of the molecular trajectory from which the average persistence length ratio (q/d) could be determined.

The model was applied to a series of thermotropic aromatic polyesters (PES, HBA/HNA, HBA/IA/HQ, and B-ET) of known nematic to isotopic phase transition temperature. Simulations of these polyesters revealed that those in the liquid crystalline phase had a persistence length ratio exceeding five, pointing to this as an approximate critical value for isolated chains. In a further investigation, with a set of liquid crystalline polymers based on random copolymers of chlorohydroquinone, terephthalic acid and kinked meta-substituted Ph-X-Ph units, where X is $C(CH_3)_2$, SO_2, S, CH_2, or O, liquid crystallinity was again found to coincide with a predicted persistence length ratio exceeding five.

Very stiff polymers will have a nematic to isotropic transition temperature exceeding the degradation temperature. However, if a critical persistence length ratio for mesogenicity is known for the type of polymer in question, the atomistic Monte Carlo simulation can be used to predict the nematic to isotropic phase transition temperature. This predictive aspect of the model has applications in the generation of phase diagrams and in forecasting the nematic to isotropic phase transition temperature in candidate molecules for synthesis.

The persistence length ratio was used in the previous example as a measure of straightness in the context of a semi-flexible worm-like chain model. However, when considering a Kuhn chain model, *i.e.* a series of rods separated by flexible spacers, problems are encountered in the use of persistence length ratio as a predictor of mesogenicity. Completely flexible links would allow the rigid units to double back on themselves, giving rise to a very small persistence length ratio despite this arrangement providing an effective contribution to mesogenicity. With this problem in mind, Bedford *et al.* [4] looked at the turn-round length[c] as an alternative predictor of mesogenicity for Kuhn-like chains. In the case of a smooth worm-like chain, the turn-round length (L_{tr}) is equal to the persistence length.

Bedford *et al.* [4] modelled a series of main chain liquid crystalline polymers containing flexible sequences of $(CH_2)_n$ in an otherwise rigid backbone. Both q/d and L_{tr}/d were measured for isolated chain models built at the transition temperature. Critical q/d was found to drop below five as the length of the flexible spacers increased, despite liquid crystallinity being observed under these conditions. However, L_{tr}/d was found to be much less dependent on the length of the flexible spacers, remaining at around five as the number of CH_2 groups increased. Therefore, it appears that L_{tr}/d is a better measure of mesogenicity across a range of real molecules that lie between worm-like and freely-jointed extremes.

[c] Distance to the first reversal in the direction of an isolated chain with respect to the first link.

In further work, He and Windle [7] applied the Monte Carlo simulation described above to the calculation of persistence lengths in aromatic polyamides. A variety of experimental methods may be used to determine persistence length including light scattering, flow birefringence, viscosity, optical anisotropy and SANS, but the result depends on the method of measurement. Furthermore, interaction between solvent and polymer alters persistence length. Resonance effects in the central C-N bond of the amide group in polyamides, together with partial charges due to protonation by the solvent result in a straightening of the chain, giving higher persistence lengths in solution than in the condensed phase. For this reason lower and upper bound persistence lengths were simulated: the lower bound corresponding to chains in the isotropic melt, and upper bound to those in a strongly interacting solvent.

Atomistic simulation of polymers is limited by the currently available computer resources to small models involving only a few chains over, at most, a nanosecond timescale. However, dense polymer systems exhibit a wide range of structure from the atomistic up to the macroscale, and intermediate levels but full atomistic simulation of dynamic processes involving nanoscale structures and above would require excessive amounts of computing resources. To overcome this problem, a suitable coarse-grained model can be constructed, which disregards atomistic detail and instead, represents the polymer by units corresponding to groups of atoms, monomers or chains, depending on the scale of the model. The structural units are chosen to represent essential collective features of the polymer in question; for example a persistence length or a chain coil diameter in nanoscale modelling, or, at the microscale, groups of chains in for example liquid crystalline polymer domains. The latter case will be discussed in section 5 of this paper, where we will look in detail at the modelling of nematic liquid crystalline polymers. First, we will concentrate on amorphous polymers with a look at a further level of simplification to aid simulating dense polymer systems, in which the coarse-grained modelled units are restricted to lie on a lattice in the *lattice chain model*.

4. Moving up a Level to the Nanoscale

The lattice chain model

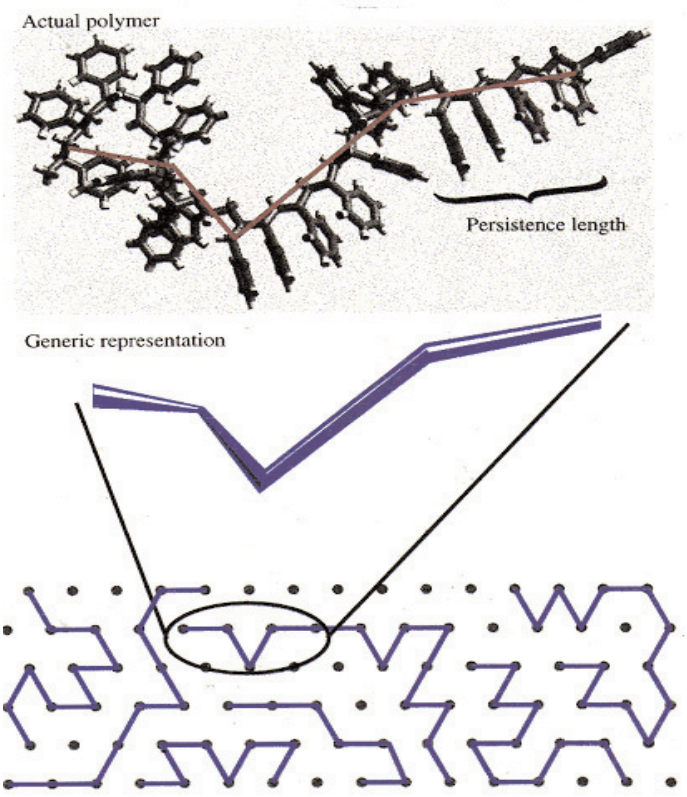

Figure 4: Lattice chain model with the persistence length as the modelled unit.

The scope of a computer simulation may be extended by increasing its efficiency, allowing longer length scales to be probed for greater times. One way of realising this is by restricting the modelled units to lie on a lattice so that self-avoidance is achieved in a straightforward manner. This is the so-called *lattice model* and for polymers, the modelled units can represent atoms, monomers, entire molecules, or assemblies of molecules. The lattice points may be separate, as in for example the modelling of microstructures in nematics, and these will be described in section 5. Alternatively, a polymer chain can be modelled as a set of interaction centres occupying the vertices of the lattice. At the next level of complexity, the polymer chain may be modelled by a set of connected beads, each occupying a lattice site, with the distance between neighbouring beads set, for example, at the persistence length as demonstrated in Figure 4. A bead may represent either a single atom or groups of atoms interacting with bonded and non-bonded neighbours: examples of this applied to polymer welding and microstructures in block copolymers appear in sections 4.2 and 4.3 respectively.

Lattice models can be used to simulate static and dynamic properties. In the static model, the polymer is 'grown' on the lattice according to specified rules, for example by a self-avoiding random walk.

Dynamic behaviour may then be studied by defining rules permitting moves that are physically possible in the real polymer system. The simplicity of the lattice model allows rapid examination of a large number of possible configurations. Alternative chain conformations are created by incorporating vacant lattice sites into the model and allowing these to exchange position with adjacent occupied sites, without breaking chain connectivity. A variety of algorithms has been used in defining sets of rules governing permitted moves to generate new conformations. Simulation is carried out by picking out a lattice site and one of its neighbours at random. If the chosen pair of sites contains a lattice point and a vacancy then a move is attempted, otherwise the attempt is considered to have failed.

In the multiscale approach, lattice model simulations are calibrated so that the timescale of moves on the lattice is proportional to that of a fully atomistic model of the same system. The calibration is done by running an equivalent molecular dynamics simulation on an atomistic model and comparing dynamic properties over the short times accessible to the more detailed model. Additionally, the length scale of the lattice model may be calibrated against the fully atomistic model so that, in principle, a fully atomistic version in continuous space can be recovered from the discrete lattice model. An example of this reverse mapping process is described in the next section where it is applied to the time calibration of a model of chain diffusion in polymer melts.

4.1 Monte Carlo Lattice Model with Reverse Mapping Using Molecular Dynamics

Haire, Carver and Windle [8] showed how a coarse-grained Monte Carlo lattice chain model, applicable to dense polymer systems and previously applied solely to static processes, is valid for studying longer-range dynamic processes such as phase segregation, and welding. Furthermore, they showed that the correct scaling behaviour for the diffusion coefficient, mean square displacement of both the central atom of each chain and of the centres of mass of the chains, and relaxation in orientation can be obtained for both isolated chain and dense polymer melt models. Haire *et al*. [8] calibrated the motions of the *on lattice* chains by interlocking the coarse-grained approach with a fully atomistic molecular dynamics model. This enabled a modelling range from atomistic detail up to the mesoscale to be covered and corresponds to a range of timescales covering six orders of magnitude from picoseconds up to microseconds.

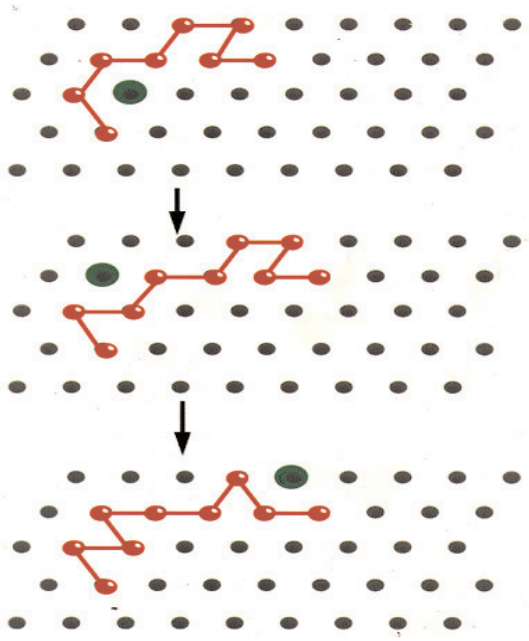

Figure 5: A example of multiple segment movements allowed by a set of chain self-avoidance rules.

The system was modelled according to the FCC lattice chain model in which each polymer is represented by a set of connected beads on 3D, cubic F lattice. The cubic F lattice was chosen because it has a coordination number of 12, higher than that of either the primitive or body centred cubic lattice, allowing the greatest number of possible conformations with the least coarse quantization of the bond angles. The unit of time used was the Monte Carlo *step*, defined by the average number of moves required to visit each lattice site once. The Monte Carlo steps can be correlated to real time in systems with physical move sets. The set of self-avoidance rules governing the movements of the beads on the lattice accommodate multiple chain segment movements as illustrated in Figure 5. Haire *et al*. [8] examined the suitability of this model for studying long-range dynamic processes in both isolated chains and dense polymer melts. In the single isolated chain case the centre of mass diffusivity (D) and the relaxation time of the chain end-to-end vector (τ_R) were calculated from simulations for a range of chain lengths (L). The model was found to agree well with predicted dependence of D and τ_R on chain lengths, *i.e.* the power laws applicable to Rouse dynamics under conditions of excluded volume were obeyed, *i.e.* $D \propto 1/L$.

In the case of a dense multiple chain system, equivalent to a polymer melt, the motion of any one chain is restricted by those around it. As the chain lengths are increased, each chain becomes more confined and the dynamic behaviour is expected to move from Rousian to reptative. Haire *et al.* [8] studied the dynamic motion of individual beads as a function of simulation time in terms of the mean square displacement of the central atom of each chain ($g_1(t)$) and the mean square displacement of the centre of mass of a chain ($g_3(t)$). Reptation theory predicts that in dense melts of polymers exceeding the critical entanglement length, $g_1(t)$ should exhibit five different power laws. These correspond to five different dynamic regimes ranging from very short times where individual chain beads move independently of the rest of the chain, to very long times involved in centre of mass diffusion. The simulated motions of individual beads were found to agree with the predictions of reptation theory within the limitation imposed by the model that the beads can only move in discrete steps between lattice sites. Smaller steps are inaccessible to the model and correspond to timescales where each bead is not influenced by its connection to the rest of the chain. Reptation theory predicts three power law regimes for the centre of mass motions. As with the single bead motion, the centre of mass motions were found to deviate from those predicted by reptation theory at short times due to insufficient time resolution. Centre of mass diffusivity was calculated for a range of chain lengths and was found to obey the predictions of reptation theory for chains over 150 repeat units long i.e. $D \propto 1/L^2$.

Having ascertained the suitability of this lattice chain model for studying long range dynamic processes, Haire *et al.* [8] calibrated it using an atomistic molecular dynamics simulation. The lattice model chain dynamics are described in terms of Monte Carlo time steps, which enables trends in dynamic properties to be studied at the mesoscale level, but does not give quantitative results for any particular polymer. Calibration of length and timescales may be done by running equivalent lattice model and atomistic molecular dynamics simulations for the short period of time the latter can simulate. Haire *et al.* [8] gave an example of this calibration for polyethylene (PE). First, a lattice model was generated with realistic PE chain packing density and characteristic ratio while keeping the number of backbone atoms per lattice point to a minimum to achieve the most realistic match between the lattice

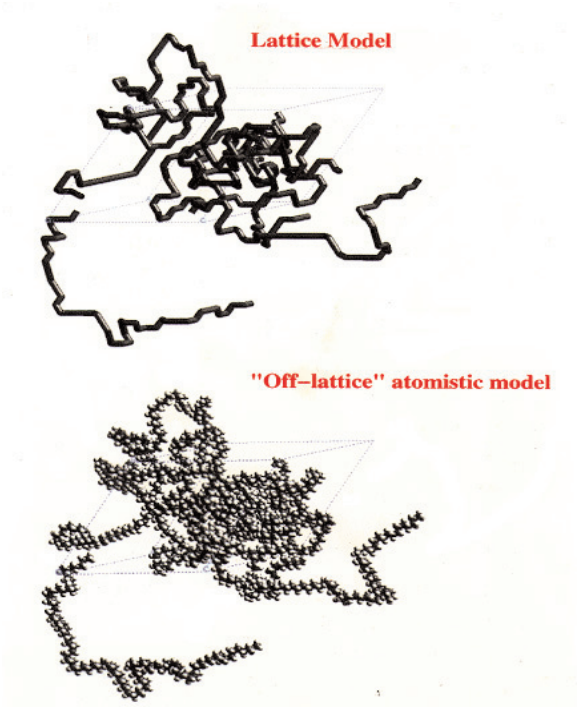

Figure 6: Reverse mapping.

model and the atomistic molecular dynamics. Optimisation of these parameters gave a spatial calibration of one lattice spacing equal to 5Å. The size and chain dimensions of the lattice model were chosen so that the equivalent simulation run in molecular dynamics would not be prohibitively long. An equivalent off-lattice model was then generated from an equilibrated lattice model configuration as illustrated in Figure 6. The lattice sites were used to map an atomistic fragment, composed of two monomer units of PE, onto the atomistic chain model. The mean square displacement of the chain ends and centre of mass motions were then calculated as a function of time in the molecular dynamics simulation, and as a function of Monte Carlo steps in the lattice model simulation. The chain motion parameters from both simulations were then plotted on the same graph and those from the Monte Carlo lattice chain model were shifted along the time axis to give the best fit to the molecular dynamics data. In this way, a time calibration of one Monte Carlo time step was found to be equivalent to 3.0ps of real time, which compared to a typical molecular dynamics times step of 2fs is an increase by a factor of 1500.

4.2 Application of the Monte Carlo Lattice Model to Polymer Welding

The Monte Carlo lattice chain model, verified by Haire *et al*. [8] for application to long-range dynamic processes, was applied by Haire and Windle [9] to

the simulation of welding of linear polymer chains. The process of polymer welding can be described as the diffusion of chains across the interface formed when two hard planar surfaces are brought together. The welding process is deemed complete when the region of the weld has all the characteristics of the bulk polymer. A model was constructed with a mono disperse polymer system having no interaction energies, which corresponds to the welding of compatible polymers well above the glass transition temperature. Time calibration of the model allowed prediction of the intrinsic weld time. The progress of the simulated weld was monitored by the total number of beads (B_{tot}) to have crossed unit area of the original interface. A weld was considered complete when B_{tot} reached a constant value, and the time taken for this to occur was referred to as the *intrinsic weld time*. An example of the behaviour of B_{tot} is shown in Figure 7 with a plot of B_{tot} versus time for two welds, one formed between two homopolymers composed of chains 50 beads long and the other formed between 200 bead chain homopolymers. In both cases, B_{tot} can be seen to increase until a plateau is reached. In the region between 10^2 and 10^5 Monte Carlo steps, B_{tot} obeys a $t^{1/4}$ power law predicted by reptation theory to be characteristic of the welding process.

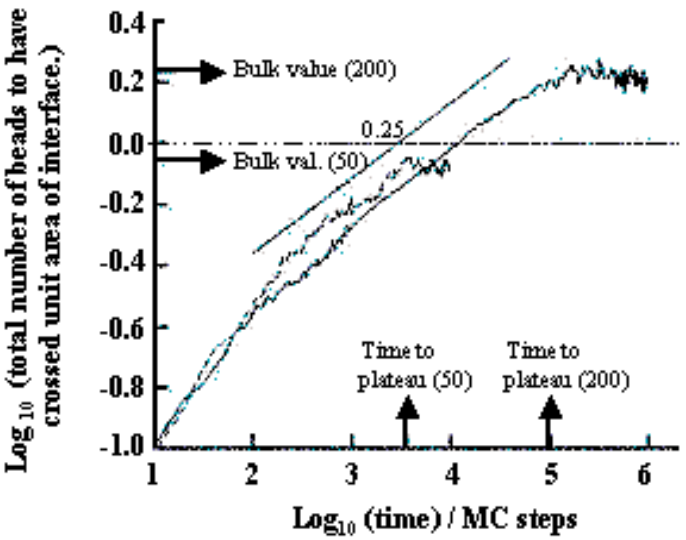

Figure 7: Characteristics of a weld: the total number of beads to have crossed the interface as a function of weld time (redrawn from [9]).

Haire *et al*. [9] also used these simulations to study the shapes of the polymer coils and their distortions at the weld interface. This was done by considering the distribution of beads in the chains. Welding is initially driven by the relaxation of chain coil distortions at the interface imposed by the surface before contact. As welding proceeds, the chain coils relax back towards their equilibrium shapes and orientations. The intrinsic weld time was compared to the end-end relaxation time in the bulk polymer, and the two values were found to be very similar. From this it was concluded that the intrinsic weld time is the relaxation time of the end to end vectors in the bulk polymer, agreeing with the suggestion of Wool *et al*. [10] that weld time is that time taken for a chain to completely renew its conformation.

4.3 Application of the Monte Carlo Lattice Model to Modelling Block Copolymers

If the two components of a diblock copolymer are incompatible then phase separation is favoured, but cannot occur due to chain connectivity. Instead, microphase separation takes place producing microdomains, which in many cases are highly ordered. This is typical of self-organizing phenomena and can lead to lyotropic liquid crystalline phases when there is a rigid rod polymer chain architecture. The trajectories of chains during the formation of domain structure in diblock copolymers are very difficult to determine experimentally. Computer simulation techniques are an excellent complementary approach, but have been limited in that they are unable to analyse the full size range of interest from chain conformation up to microdomain morphology. Molecular dynamics is useful for studying processes in atomistic detail, but at the much larger microdomain scale the computing time required for atomistic modelling is prohibitively long.

Ding, Carver and Windle [11] addressed this problem using the Monte Carlo lattice model incorporating self-avoiding, diffusive chain motions. An FCC lattice was used with periodic boundary conditions. A generic diblock copolymer with components *A* and *B*. was considered. An occupied lattice site contained a bead representing an A or B type block and solvent molecules were represented by vacancies to be referred to as *V*. Figure 8 shows the stages in modelling phase separation of a block copolymer composed of hydrophilic and hydrophobic blocks in an aqueous solvent. Hydrophobic A blocks and hydrophilic B blocks were modelled by setting a negative AA interaction energy, and zero BB, VV, AV, BV, and AB interaction energies. This leads to a

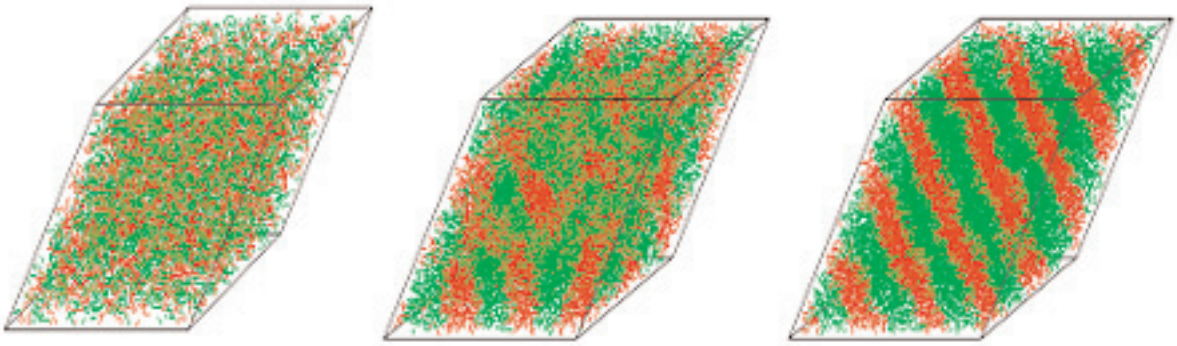

a) t=0
Homogeneous initial state

b)t=50000
Intermediate state

c)t=600000
Lamellar morphology, almost equilibrium state

Block A - red - hydrophobic
Block B - green - hydrophilic

t is in terms of Monte Carlo steps

Figure 8: Phase separation in a hydrophilic/hydrophobic block copolymer (redrawn from [11]).

significantly higher vacancy concentration in the B phase after separation as can be see by the thicker lamellar phase for the B blocks in Figure 8c.

Temperature induced order-disorder transitions were also successfully simulated for this example system. Furthermore, Ding *et al.* [11] showed that the simulation method is capable of predicting different diblock copolymer morphologies. Micelle, hexagonal cylinder, and lamellae were obtained at different diblock compositions. Micellar gel formation was simulated by using long ($A_{16}B_{16}$) blocks as this gave rise to a structure in which B blocks entangles with those of neighbouring micelles.

4.4 Application of the Lattice Chain Model to Polymer Surfaces

In the previous two examples, we have seen how the lattice model can be applied to the prediction of behaviour and morphology in dense polymer systems. The next example shows the use of Monte Carlo lattice model simulation in conjunction with microscopy to provide information at length scales below the resolution of the microscope in addition to aiding the elucidation of structure. Goldbeck-Wood *et al.* [12] investigated the structural organization at the surface of a typical amorphous polymer, atactic polystyrene (aPS), with a combination of high resolution scanning force microscopy (SFM) and coarse-grained lattice simulation techniques. Theory [13] and diffraction experiments predict relatively short-range interactions, of one or two monomer lengths, operating within the bulk of an amorphous polymer as entanglements screen longer range interactions. The screening at the surface is different due to the asymmetry of the chains near the air interface. Long-range interactions, of the order of the radius of gyration of the chains, are expected corresponding to the dimensions of the macromolecular coils, in addition to the short-range bulk interactions and intermediates associated with several monomers. Grazing incidence X-ray diffraction and electron diffraction, used to study crystalline surfaces, are not very informative when applied to amorphous surfaces. However, SFM is a powerful technique now available for examining the surface morphology and properties of amorphous polymers. Goldbeck-Wood *et al.* [12] operated the SFM in tapping mode to scan over surface areas between 300 x 300 nm^2 and 5 x 5 μm^2. The surface features of interest are nanoscale structures as they are of the order of the radius of gyration of the chains. These are of an impractically large size, in terms of computing resources, to simulate using

classical atomistic methods. Therefore, Goldbeck-Wood *et al*. [12] used the coarse-grained FCC lattice chain simulation method, shown by Haire *et al.* [8] to be a valid for studying dense amorphous polymers. The correct representation of the polymer chemistry was obtained, as described in section 4.1, by setting the parameters of the model to achieve the correct density and end-to-end distance for the polymer in question, aPS in this case. The specific environment, *i.e.* a surface in this case, was set by specifying polymer-air and polymer-substrate interactions. To do this, air was represented by vacancies, and cohesive-energy terms in the form of polymer-vacancy interaction parameters were introduced such that the bulk retained the correct density (occupancy) in a simulation box with a polymer surface. This was achieved by a pair-wise interaction energy between nearest neighbour polymer-vacancy sites of $\varepsilon = +36k_BT$, and an attractive interaction energy of $\varepsilon = -36k_BT$ between the surface polymer and substrate (bulk) to ensure that the polymer/substrate surface remained intact.

A similar mathematical analysis was applied to both the SFM and simulation results, allowing direct comparison of the findings. The polymer surface topology in the SFM images was characterised quantitatively with an autocorrelation function analysis. This indicates the average distance from an arbitrary point in the sample beyond which the correlation in the arrangement of the structural units is lost. A set of aPS samples was chosen to cover a range of molecular weights from 3900 up to 9 x 10^6. Likewise, independent simulations were run for different chain lengths selected to overlap with the range of molecular weights used for the SFM. Long relaxation times, associated with long chains, drain computer resources and this limits the simulations to relatively short chain systems, inaccessible to for SFM due to resolution limits. The SFM is able to access the longer chain lengths than simulation, but there is an intermediate region accessible to both, which allows comparison of experimental and simulation results.

Cross section (height profiles) of the SFM images demonstrated a presence of at least two characteristic length scales within the scanned area which, by analogy with more ordered latex particle crystal systems (Bliznyuk *et al.* [14]), was ascribed to two different levels of molecular organization within the system. Autocorrelation function analysis of the SFM images produced curves with an initial exponential decay followed by a series of peaks of decaying amplitude, as shown in Figure 9, suggesting at least two levels of structural organization. Direct inspection of the modelled structures, shown in Figure 10a, revealed roughness at the level of individual chains and on a larger scale. The effect of the surface on chain orientation can be seen in Figure 10b, where the divergence of the lateral and perpendicular components close to the surface means that the chain envelope is effectively flattened close to the surface, in agreement with previous evidence about chains at weld interfaces in the work by Haire *et al.* [9]. Two characteristic length scales can be extracted from the autocorrelation function curves for the simulated surfaces. Comparison of experimental autocorrelation lengths with simulated results suggests that simulated polymer surfaces have a resolution that is at least five times higher than that seen in SFM experiments. Better comparison of SFM and simulation results requires development of a mathematical procedure for deconvolution of the SFM tip shape from the surface relief. Moreover, the current trend of ever increasing computing sources will allow simulation of longer chain systems, allowing more points for comparison with experiment. Combination of the evidence of simulation and experimental results indicates that a characteristic feature of the surface autocorrelation function has a length scale close to the radius of gyration of the chains (calculated theoretically) over several decades of molecular weight. The calculated values of the radii of gyration are plotted in Figure 11 and show rather good agreement with the larger correlation length of height distribution found in both SFM experiments and independently from simulations.

This work provided new insights into the surface topography of amorphous polymer systems and validated coarse-grained simulation techniques for investigating nanoscale polymer surface features.

Now we move up in scale again from the nanoscale to the microscale with a look at how we can predict the evolution of microstructure in nematic liquid crystalline polymers. Our representation of the structure is coarsened with our modelled unit will now representing groups of chains sharing a common direction.

5 Modelling Nematic Liquid Crystalline Polymers

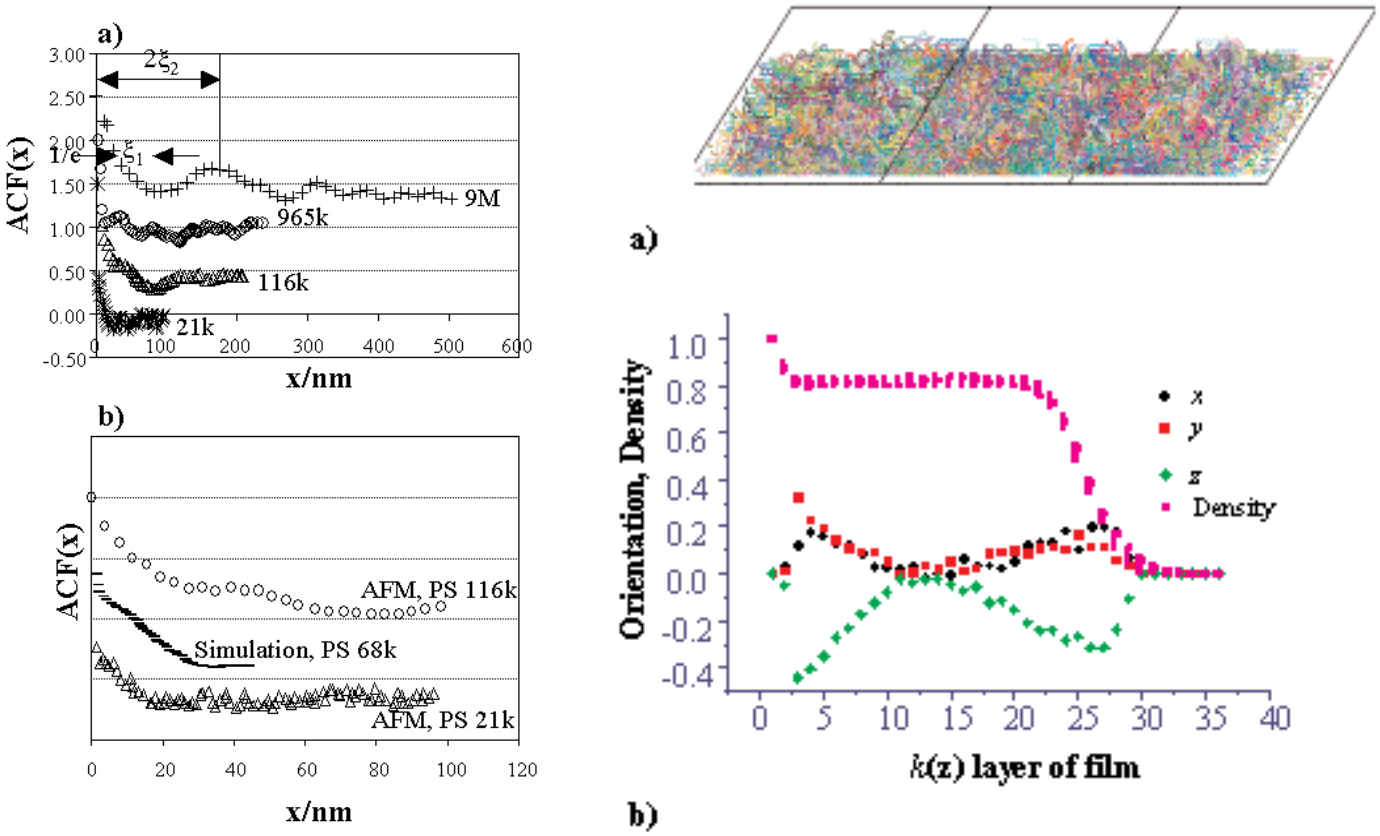

Figure 9: a) Autocorrelation functions calculated from the SFM images for different molecular weight PS samples (the curves have been shifted vertically for clarity.) The principle of the correlation length estimation as 1/*e* level of the exponential decay corresponding to the initial (steep) part of the ACF curve and to the first-order maximum of characteristic oscillations is shown. These two approximations give two different levels of quantitative description of the system: the correlation lengths ξ_1 and long-range correlation parameter ξ_2. b) The initial parts for some of the experimentally determined ACF curves plotted in a), compared with the ACF calculated for a simulated PS surface of *M*n = 68K. (Redrawn from [12]).

Figure 10: (a) The side view of a simulated surface. Note the roughness, and the chain ends protruding from the bulk. (b) Components of the orientation distribution along the surface (x,y) and perpendicular to the surface (z), throughout the simulated PS film. Note, the flattening of the chain envelope close to the surface (modified from [12]).

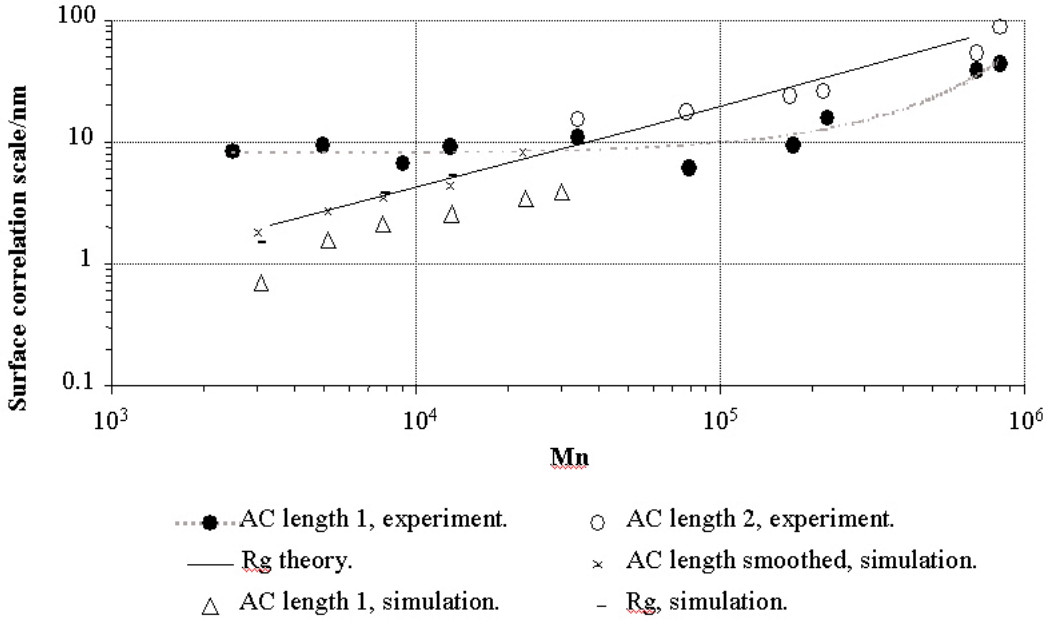

Figure 11: A summary graph of characteristic length scale parameters vs. molecular weight found for amorphous polymer surface. The correlation lengths 1 and 2 are ξ_1 and ξ_2 introduced in figure 9. 'Rg' curves are the theoretically calculated values of radius of gyration for polymer chains in an ideal random coil approximation. (modified from [12]).

The liquid crystalline or *mesogenic* phase is an intermediate between liquid and solid that is possible to achieve with certain molecular architectures. A few concepts associated with liquid crystals, particularly the polymeric variety, will be introduced here but the reader is referred to Donald and Windle [15] for comprehensive coverage of this subject. Liquid crystals flow like liquids but retain some degree of orientational order. Friedel classified liquid crystalline phases as *nematic*, *cholesteric*, and s*mectic* and, although this was originally applied to small molecule liquid crystals, these classes are appropriate for liquid crystalline polymers. The modelling work described here is concerned with the nematic *Friedelian* class defined as showing long-range orientational order with only short-range positional order. Two types of liquid crystalline polymer architecture are found: *main chain* in which the mesogenic units arise from a rigid, or more usually, semi-rigid backbone, or side chain which derive their mesogenicity from stiff side-chain units. The microstructure of a liquid crystal is usually described in terms of a unit vectors, known as *directors*, representing the average locally favoured orientations. Liquid crystalline materials exhibit a rich variety of microstructures and liquid crystalline polymers are no exception demonstrating an enormously varied range of textures. This microstructure is a result of spatial variation in the director field arising due to boundaries and defects. Defects in the form of discontinuities in the director field are known as *disclinations*, and may be point or line defects. Optical micrographs of nematic liquid crystalline materials frequently reveal characteristic lines or *threads*, demonstrated in Figure 12a with MBBA in shear flow. These threads are the cores of disclination lines, which scatter light. Another characteristic of the nematic phase is the Schlieren texture, which is seen between crossed polars and showing point singularities as illustrated in Figure 12b.

Continuous distortion of the director field is described in terms of three possible types elastic orientational distortions namely *splay*, *twist*, and *bend*. Three elastic constants, referred to as the Frank constants, K_{11}, K_{22}, and K_{33} respectively, quantify the reluctance of the material to distort in each of these ways. The splay constant varies with the contour length of the macromolecule, while the bend and twist constants vary with persistence length. As chain length is increased the persistence length reaches a limiting value therefore becoming

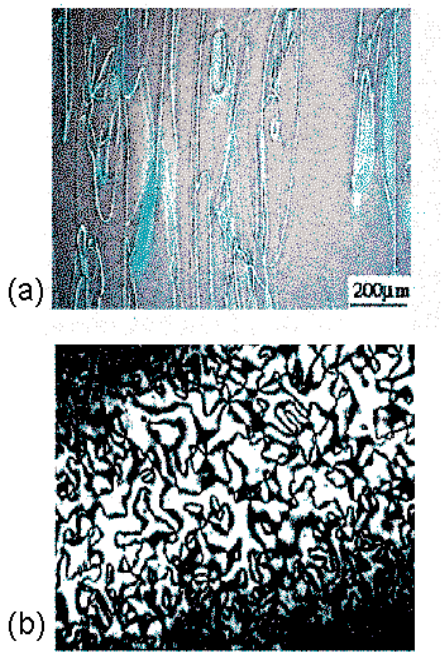

Figure 12: Microstructures in nematics: a) thread texture of MBBA in shear flow under crossed polars and a tint plate; b) Schlieren texture in the polymeric nematic state under crossed polars.

independent of molecular weight. The contour length, and hence the splay constant, increases with molecular weight, leading to significant anisotropy in the elastic constants in main chain liquid crystalline polymers. The splay constant is usually larger than twist or bend in main chain thermotropic polymers, while bend tends to be the largest in lyotropic main chain and smectic side chain polymers. Splay is entropically unfavourable in main chain thermotropic polymers because it requires chain ends to diffuse to regions of high distortion to maintain constant density and this becomes increasingly unlikely as the chain length increases.

Thermotropic liquid crystalline polymers are widely used in high precision mouldings and can also be drawn to produce very stiff and strong fibres. However, their use is hampered by the presence of defects in the microstructure. Simulation plays a valuable role in understanding how and why these defects arise during processing. An hierarchical modelling approach has been adopted by the Cambridge group for studies designed to the predict microstructures observed in main chain thermotropic liquid crystalline polymers as this method can provide considerable insight into the relationships between molecular architecture and microstructure. The simulations typically begin with the system in the isotropic phase, and then relax structure either by minimising the total free energy of the system (*refs*

[17,19-27]), or the overall elastic torque (*refs* [29-32]) thereby aligning directors and reducing the number of defects, coarsening the texture until in some cases a monodomain configuration is reached. We have already introduced atomistic modelling with the prediction of persistence lengths using Monte Carlo simulation by Bedford, Yu, and Windle [4] as described in section 3 of this paper. Moving up one level takes us to the nanoscale where the modelled unit is an entire molecule as adopted by the Lebwohl and Lasher [16] model developed to study the nematic to isotropic phase transition. This is a lattice model containing one molecule per cell, described only by its direction in space. The distribution of molecular orientations is determined by a balance between the randomising influence of the thermal motions and the restoring force defined by the distortion constants. The next level up in scale is the microstructural regime where the modelled unit represents large groups of molecules. At this scale the effect of thermal fluctuations on the interaction energies is reduced, approaching the continuum limit where the thermal fluctuations are considered negligible. Atomistic modelling can provide crucial input parameters for the coarse-grained nano- and microscale models. For example, the elastic constants provide the structural input for coarse-grained simulations of liquid crystalline polymers, but are difficult to obtain from experiment. However, the bend and twist elastic constants vary with persistence length which, as we have shown, can be calculated from atomistic Monte Carlo simulation. This hierarchy of structure involved in the prediction of liquid crystalline polymer microstructure is summarised in Figure 9 and has been discussed in detail by Hobdell, Lavine and Windle [17], and Goldbeck-Wood *et al.* [18] .

5.1 Monte Carlo Modelling of Nematic Liquid Crystalline Polymers

The lattice model has been developed in the Cambridge over the last few years to simulate and predict the director fields and textures in nematic liquid crystalline polymers at the microscale. In the first instance, Bedford, Nicholson and Windle [19] used a simple two-dimensional numerical model to simulate the evolution of liquid crystalline texture during isothermal annealing of the isotropic material. The liquid crystal was modelled by a 2D array of directors, represented by unit vectors, each centred on the lattice point of a primitive square lattice. The orientation of a director was free to vary continuously in two dimensions. Each director represented the average orientation of an assembly of molecules within a domain. This initial model was further simplified by assuming the three elastic constants to be equal and setting them arbitrarily to unity. A sine squared function was chosen to define the interaction energy between adjacent directors so that it is a minimum when they are parallel and a maximum when they are perpendicular. This is shown in equation (1) where θ_i and ϕ_i are the angles of the directors to a reference direction in two adjacent cells.

$$E \propto \sum Sin^2(\theta_i - \varphi_i) \qquad (1)$$

Assender and Windle [20] investigated the choice of energy function in the two-dimensional lattice model and found the sine squared function to be the most successful. Bedford *et al.* [19] used a Monte Carlo algorithm to pick a cell at random. Its energy was calculated by summing individual contributions due to disorder in orientation between the director in the picked cell (θ_i) and those in its four nearest neighbours (ϕ_i). The angle ϕ that minimises the energy was found. The process of picking a cell and minimising the energy was repeated many times until there was no further reduction in the energy of the lattice as a whole. This approach successfully simulated the evolution of a director field from multi- to monodomain via the annihilation of opposite signed strength ½ disclinations.

Bedford *et al.* [19] extended this approach to three dimensions by placing the directors on a simple cubic lattice and allowing them to move in three dimensions, minimising the energy of each director with respect to its six nearest neighbours. In three dimensions, this was done by changing the orientation of the central director until an energy minimum was found. As a single elastic constant approximation was used, this model is only valid for small molecule liquid crystals.

In a further study, Bedford and Windle [21] refined the three dimensional model to allow simulation of liquid crystalline polymers by using unequal elastic constants. A sine squared function was still used, but weighted according to the amount of splay, twist and bend distortion between directors. This led to a novel prediction of layering in liquid crystalline polymers resulting from a high splay constant. Windle, Assender, and Lavine [22] made a further adaptation in order that the model could be applied to the dynamic simulation of disclination processes in

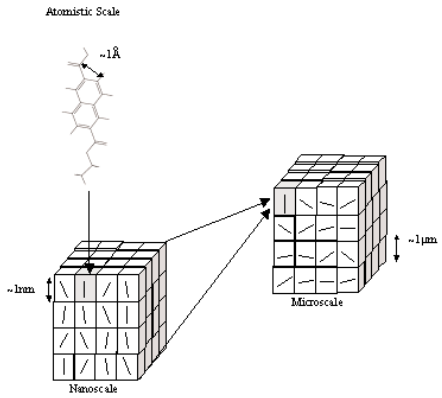

Figure 13: Hierarchy of size-scales used in the prediction of liquid crystalline polymer microstructure.

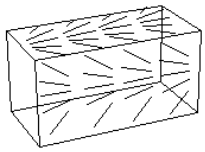

Figure 14: Splay-splay compensation.

liquid crystalline phases. Cells were picked at random, as before, but the orientation of the director was changed by a small amount down the path of steepest energy gradient.

Processes such as injection moulding and extrusion generate shear fields that alter the microstructure of liquid crystalline materials, often producing large numbers of defects. Lavine and Windle [23] modelled the influence of shear on disclination loops in thermotropic liquid crystals by incorporating flow in the Bedford and Windle [19] lattice model.

A significant limitation of the Bedford and Windle [19,21] model was that it could not completely distinguish between splay and bend distortions, assigning bend to some pure splay situations and vice versa. This problem was tackled Hobdell and Windle [24,25,26,27] who developed a technique for simulating microstructure in liquid crystalline polymers that would distinguish between splay, twist, and bend, identify situations of splay-splay compensation, and also allow non-equilibrium states to be probed. The microstructures observed in polymeric nematics are different from those observed in their small molecule counterparts, a typical example being the swirling patterns observed in thermotropic liquid crystalline polymers. Hobdell *et al*. [24-27] proposed that the origin of these unique microstructures lies in the anisotropy of the Frank elastic constants. In particular, they proposed that the swirling microstructure arises as it is a texture involving bend and twist distortion which are preferred over those involving splay owing to the high splay energy of thermotropic liquid crystalline polymers.

Hobdell *et al.* [24-27] used the Frank continuum theory [28] to predict the director fields in liquid crystals. Frank's equation gives the total free energy of a liquid crystal with a general distortion of the director field as the sum of the splay, twist and bend components. Using this equation, it is possible to separate the contributions from splay, twist and bend distortions. Minimisation of the Frank free energy is very complicated when the elastic constants are all different; therefore, Hobdell *et al.* [24-27] applied a simple numerical algorithm to find minimum energy director fields. An additional consideration was that the microstructures observed in liquid crystalline polymers are often far from the equilibrium state and so unlikely to be in a minimum energy state. Therefore, a technique was required that follows the evolution of microstructure, and hence includes non-equilibrium director fields.

Hobdell *et al.* [24-27] divided the mesophase into an array of identical cubic cells, each storing a director representing the local orientation. The model was initialised either to simulate a monodomain by aligning all the directors, or giving them random orientations to simulate the isotropic case. Specific boundary conditions were chosen by setting the directors forming the boundaries at particular orientations. The system was then annealed to reduce the total energy of the system by using a Monte Carlo algorithm to pick a cell at random and then assigning the director a random trial orientation. The energy was calculated for the chosen cell by breaking it down into eight corners and at each corner using the three neighbours to calculate the splay, twist and bend distortions. These were calculated for all eight corners, and the average found. If the interaction energy of the trial orientation was lower than that or the original then the trial was accepted. Otherwise, the trial was accepted with a probability that depends on the difference in energy between the original and trial orientations. One complication is that vectors are incapable of representing nematic symmetry of a director field where $\mathbf{d} = -\mathbf{d}$. Hobdell *et al.* [24-27] solved this problem by checking the angle between pairs of vectors and, if it is found to be greater than 90º, flipping one of the neighbours through 180º.

Splay-splay compensation, illustrated in Figure 14, is where the splay distortion in one plane is the equal

and opposite of that in a perpendicular plane. These opposing distortions compensate, eliminating the density variation resulting from the two individual splay distortions. Therefore, although splay distortions tend to be unfavourable in large polymer molecule systems, the situation of splay compensation alleviates this. Bedford and Windle [19] model, using the sine squared energy function, does not identify splay compensation, giving the splay-splay compensated region the equivalent energy to a pure splay region. However, in Frank's equation, splay distortion is described by a divergence term, so the method of Hobdell *et al.* [24-27] correctly deals with situations of splay-splay compensation.

The decomposition of + or -1 line defects into a series of point singularities is known as *escape into the third dimension*. Hobdell *et al.* [26] were able to show that strength +1 disclination lines in liquid crystalline polymers will be of the twist escaped strength +1 variety. Experimental observations of fracture surfaces by Windle *et al.* [20] have revealed fractures, which are consistent with twist-escaped strength +1 lines.

One problem associated vectorial form of the Frank elastic free energy used by Hobdell *et al.* [24-27], is that it requires ad hoc director-flipping moves to preserve the nematic symmetry. In the following section, we introduce a different approach using a tensor expression for the elastic torque that automatically conserves nematic symmetry.

5.2 Deterministic Approach to Modelling of Nematic Liquid Crystalline Polymers

The mesoscale lattice models of nematic polymers described in the previous section use a Monte Carlo method for the relaxation algorithm. This has two drawbacks, firstly it is difficult to relate Monte Carlo time evolution to that in a real system, and secondly it does not lend itself readily to the inclusion of external fields, particularly flow fields. In response, Tu, Goldbeck-Wood and Windle [29] took a deterministic approach to the simulation of the evolution of texture in liquid crystalline polymers. They adopted a lattice model as before, but this time they calculated the relaxation in the director field using the Ericksen-Leslie equation which describes the process in terms of a torque due to the curvature in the elasticity and the rotational viscosity of the system. In this way, minimisation of the overall elastic torque is the driving force behind the relaxation of the director field, rather than the total free energy used in the previous simulations [19-27]. The Ericksen-Leslie relation is an equation of motion for relaxation of the directors, providing the basis for a molecular dynamics approach to the problem.
In the absence of an external field the Ericksen-Leslie equation takes the form shown in (2), where n is the director field, h the texture field, and their cross product the torque per unit volume due to the curvature of the elasticity. γ_1 is the torsional viscosity coefficient.

$$\frac{\partial \mathbf{n}}{\partial t} = \frac{1}{\gamma_1}(\mathbf{n}\times\mathbf{h})\times\mathbf{n} \qquad (2)$$

Externally applied torques can be included easily in this equation, making it a more amenable method for modelling the effects of external fields. The texture field is generated by the spatial inhomogeneity of the director field and can be obtained from the Frank elastic free energy. Tu *et al.* [29] treated the Frank elastic constants separately to allow for the elastic anisotropy that is typical of polymeric nematics. The equilibrium state is where the director is parallel to the texture field at each point. Tu *et al.* [29] used the Frank elastic free energy equation in tensorial form as this automatically conserves nematic symmetry, and for this reason their model will be referred to as the *tensor model* when brevity is required. They demonstrated the effectiveness of this model at differentiating splay, twist and bend distortions by successfully reproducing the Fréedericksz transitions, which also have analytic solutions. These occur when an electric or magnetic field is applied to a liquid crystal cell constrained by fixed boundary conditions at two parallel plates.

Tu, Goldbeck-Wood and Windle [30,32] proceeded to apply the tensor model to the simulation of both static and dynamic behaviour of liquid crystalline polymers. In the static case, Tu *et al.* [30] simulated diclination processes in a range of elastically anisotropic two and three dimensional structures. In the two dimensional treatment, used to model thin films, the directors are constrained to lie in a plane so the elastic distortions are restricted to splay and bend. These two dimensional distortions, demonstrated in Figure 15 [31] correspond to the Schlieren textures observed in thin specimens between crossed polars as shown in Figure 12b. The two dimensional version of the tensor model was used to explore the effect of splay and bend

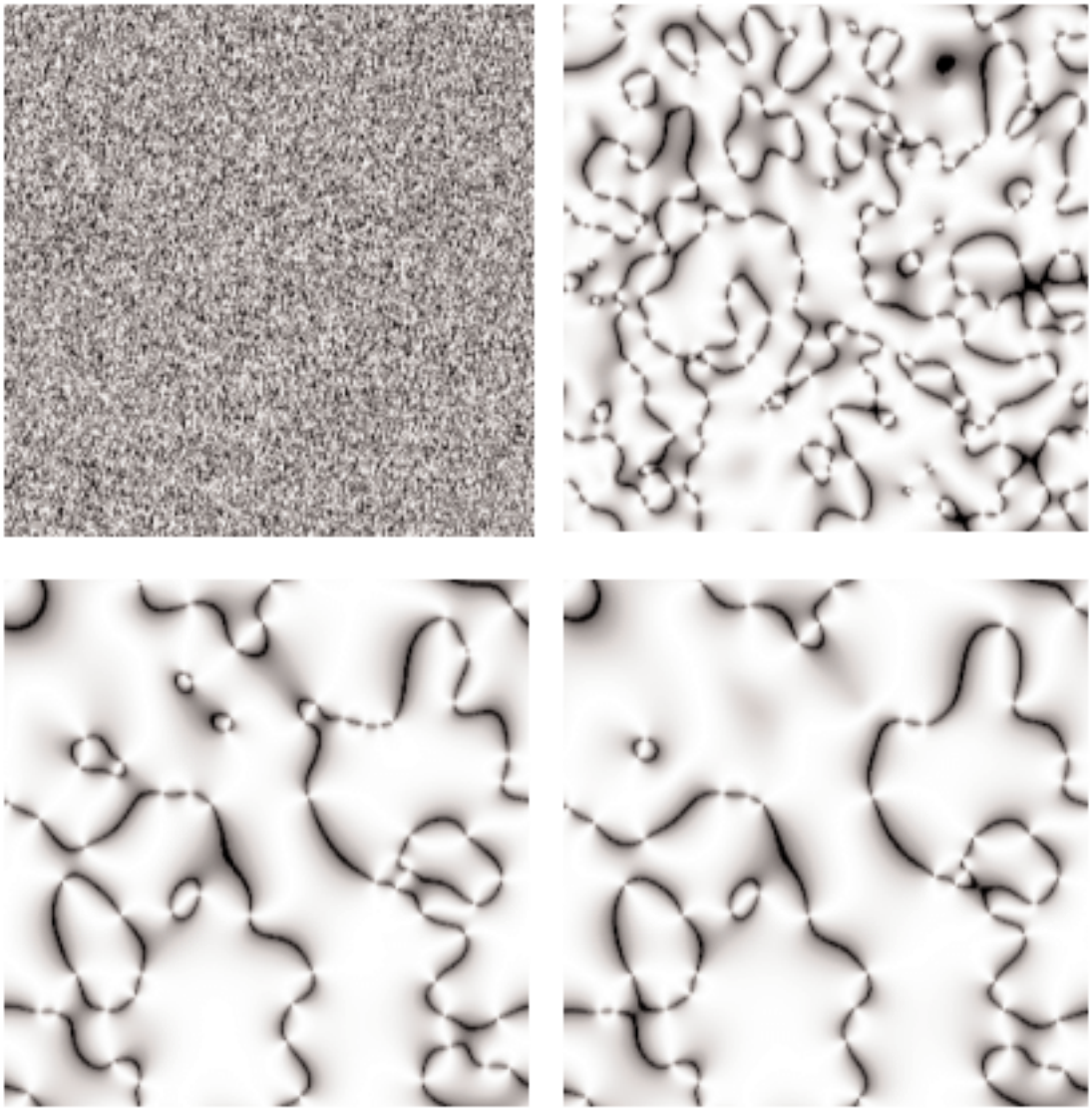

Figure 15: Model structures, presented as their corresponding polarised light intensity profiles, at different time steps: (a) 0s, (b) 600s, (c) 1800s and (d) 2400s .

anisotropy on these structures. A three dimensional version of the tensor model was applied to the investigation of disclination lines and loops in bulk samples. This is particularly valuable as it is as it is difficult to obtain this information using currently available experimental techniques. In their application of the tensor model to dynamic behaviour, Tu *et al*. [32] simulated texture evolution of nematics under shear flow. Defects can be generated and multiplied in liquid crystalline polymers under shear flow and understanding the mechanisms behind these processes is useful in applications like extrusion and injection moulding. The Ericksen -Leslie theory predicts director tumbling and flow aligning behaviours in nematics under shear. Tu *et al*. [32] examined the effect of simple shear flow on polymeric nematics. They compared cases of no elasticity, equal elastic constants, small splay constant, small bend constant and small twist constant respectively. "Log rolling" was predicted to be a consequence of tumbling when the twist constant is smaller than the others as is the case in typical thermotropic liquid crystalline nematics.

6. Concluding Remarks

We began this brief survey with an example of the application of modelling to the prediction of X-ray diffraction patterns in the familiar process of structure refinement. This paper provides a brief insight into how computer modelling can be used proactively as a predictive tool rather than simply as a means to refine diffraction structures. The first example we gave was the prediction of mesogenicity in thermotropic aromatic co-polyesters, showing how simulation can be used to identify suitable candidate molecules for synthetic liquid crystalline

polymers. We then moved up in scale to show how coarse-graining, used in conjunction with a the lattice chain model, is a valuable technique for predicting the behaviour of dense amorphous polymer systems particularly where we wish to examine long range dynamic processes, such as polymer welding. Finally, we moved up to the mesoscale where we looked at how the lattice model was used to show that the origin of the textures observed in thermotropic liquid crystalline polymers lies in the anisotropy of the Frank elastic constants in polymeric nematics. This work was developed further with a deterministic modelling approach using a tensorial model well suited to including the effects of external fields on polymeric nematics in order to model the effect of shear flow on these materials.

References

[1] Welsh, G.E., Windle, A.H. (2001) Levels of Structural Order in Crystals of PET/PEN Random Copolymers. *Polymer*, **42**, 5727-5735.

[2] Welsh, G.E., Blundell, D.J., Windle, A.H. (2000) A Transient Mesophase on Drawing Polymers Based on Polyethylene Terephthalate (PET) and Polyethylene Naphthoate (PEN). *J Mater Sci*., **35**,5225-5240.

[3] Welsh, G.E., Blundell, D.J., Windle, A.H. (1998) A Transient Liquid Crystalline Phase as a Precursor for Crystallization in Random Co-polyester Fibers. *Macromolecules*, **31**,7562-7565.

[4] Bedford, S.E., Yu, K., Windle, A.H. (1992) Influence of Chain Flexibility on Polymer Mesogenicity. *J. Chem. Soc. Fara. Trans*, **88(13)**, 1765-1773.

[5] Flory, P.J. (1956), *Proceedings of the Royal Society of London*, **234**, 60.

[6] Kratky, O., Porod, G.F. (1949) *Recl. Trav. Chim.*, Pays-Bas, **68**, 1106.

[7] He, C., Windle, A.H. (1995) Persistence Lengths of Aromatic Polyamides: a Computer Simulation Approach. *Macromol. Theory Simul.*, **4**, 289-304.

[8] Haire, K.R., Carver, T.J., Windle, A.H. (2001) A Monte Carlo Lattice Model for Chain Diffusuion in Dense Polymer Systems and its Interlocking with Molecular Dynamics Simulation. *Computational and Theoretical Polymer Science*, **11**, 17-28.

[9] Haire, K.R., and Windle, A.H. (2001) Monte Carlo Simulation of Polymer Welding *Computational and Theoretical Polymer Science*, **11**, 227-240.

[10] Wool, R.P., Yuan, B.L., McGarel, O.J. (1989) Welding of Polymer Interfaces. *Polymer Engineering and Science*, **29**, 1340.

[11] Ding, J., Carver, T.J. and Windle, A.H. (2001) Self-assembled Structures of Block Copolymers in Selective Solvents Reproduced by Lattice Monte Carlo Simulation. *Computational and Theoretical Polymer Science*, **11**, 483-490.

[12] Goldbeck-Wood, G., Bliznyuk, V. N., Burlakov, V., Assender, H. E., Briggs, G. A. D., Tsukahara, Y., Anderson, K. L., and Windle, A. H. (2002) Surface Structure of Amorphous Polystyrene : Comparison of SFM Imaging and Lattice Chain Simulations. *Macromolecules*, **35**, 5283-5289.

[13] Strobl, G.R., (1997) *The Physics of Polymers : Concepts for Understanding Their Structures and Behavior*. 2nd Edition. Berlin : Springer-Verlag.

[14] Bliznyuk, V. N., Burlakov, V., Assender, H. E., Briggs, G. A. D, Tsukahara, Y. (2001) Surface Structure of Amorphous PMMA from SPM: Auto-correlation Function and Fractal Analysis. *Macromol. Symp*, **167**, 89-100.

[15] Donald, A.M., and Windle, A.H. (1992) *Liquid Crystalline Polymers*. Cambridge University Press.

[16] Lebwohl, P.A., and Lasher, G. (1972) *Phys. Rev. A*, **6**, 426.

[17] Hobdell, J.R, Lavine, M.S., and Windle, A.H. (1996) Hierarchical Approach to Modelling of Liquid Crystalline Polymers. *Journal of Computer Aided Materials Design*, **3**, 359-368.

[18] Goldbeck-Wood, G., Coulter, P., Hobdell, J.R., Lavine, M.S., Yonetake, K. and Windle, A.H. (1998) Modelling of Liquid Crystal Polymers at Different Length Scales. *Molecular Simulation*, **21**, 143-160.

[19] Bedford, S.E., Nicholson, T.M., and Windle A.H. (1991) A Supra Molecular Approach to the Modelling of Textures in Liquid Crystals. *Liquid Crystals*, **10**, 63-71.

[20] Assender, H.E., and Windle, A.H. (1994) Two-dimensional Lattice Model of Disclinations in Liquid Crystals: Choice of Energy Function. *Macromolecules*¸ **27**, 3439-3441.

[21] Bedford, S.E., and Windle, A.H. (1993) Modelling of Microstructures in Mesophases. *Liquid Crystals* **15**, 31-63.

[22] Windle, A.H., Assender, H.E., Lavine, M.S. (1994) Modelling of Form in Thermotropic Polymers. *Philosophical Transactions of the Royal Society of London*, **348**, 73-94.

[23] Lavine, M.S., and Windle, A.H. (1997) Computational Modelling of Disclination Loops Under Shear Flow. *Macromolecular Symposia*, **124**, 35-47.

[24] Hobdell, J.R. (1997) PhD Thesis, Cambridge University.

[25] Hobdell, J.R., and Windle, A.H. (1996) A Microstructural Model for Liquid Crystalline Polymers. *Mat. Res. Soc. Symp. Proc.*, **425**, 131-136.

[26]Hobdell, J.R., and Windle, A.H. (1997) A Numerical Technique for Predicting Microstructure in Liquid Crystalline Polymers. *Liquid Crystals*, **23**, 157-173.

[27]Hobdell, J.R., and Windle, A.H. (1995) Prediction of Microstructure in Liquid-crystalline Polymers. *J. Chem. Soc. Faraday Trans.*, **91**, 2497-2505.

[28] Frank, F.C. (1958) *Discussions of the Faraday Society*, **25**, 19.

[29] Tu, H., Goldbeck-Wood, G., Windle, A.H. (2001) Deterministic Numerical Model for Treating the Three Elastic Constants in Nematic Liquid-Crystalline Polymers. *Physical Review E*, **64**, 1704.

[30] Tu, H., Goldbeck-Wood, G., Windle, A.H. (2002) A Tensor Model of Liquid Crystalline Polymers: Application to Basic Disclination Processes. *Liquid Crystals*, **29**, 325-334.

[31] Tu, H., Goldbeck-Wood, G., Windle, A.H. (2001) Numerical Simulation of Elastic Anisotropy in Nematic Liquid Crystalline Polymers. *Defects in Liquid Crystals: Computer Simulations, Theory and Experiments*, 201-228, Kluwer Academic Publishers, Netherlands.

[32] Tu, H., Goldbeck-Wood, G., Windle, A.H. (2002) Simulation of Texture Evolution for Nematic Liquid Crystalline Polymers Under Shear Flow. *Liquid Crystals*, **29**, 335-345.

The effects of shear and co-surfactants on the evolution of the micro-structure in concentrated di-chain cationic surfactant solutions

J. Penfold[1], E. Staples[1], I. Tucker[2], J. Hubbard[2], L. Soubiran[2] & A. Creeth[2]

[1] ISIS Facility, CLRC, Rutherford Appleton Laboratory, Chilton, Didcot, Oxon.
[2] Unilever Research, Port Sunlight Laboratory, Quarry Road East, Bebington, Wirral.

ABSTRACT

We have previously reported the use of small-angle neutron scattering, SANS, rheology, and conductivity to characterise the shear thickening transition from an aligned lamellar phase to liposomes [1]. The SANS and conductivity measurements indicate an inhomogeneous distribution of order across the Couette flow cell gap. We present Small-Angle X-ray Scattering, SAXS, data using a micro-focus X-ray beam, which demonstrates the same inhomogeneity. Polarised light scattering measurements in the region of the shear thickening transition show a marked increase in texture. Both measurements provide evidence which is consistent with common stress and common strain 'banding' [2].

Preliminary results on the effects of temperature and the addition of co-surfactants are discussed. Both the addition of co-surfactant and the temperature relative to the L_α / L_β transition temperature are shown to have a profound effect on the solution micro-structure. For solutions which are a mixture of the di-chain cationic and a non-ionic surfactant, rich in the di-chain cationic surfactant, increasing temperature results in a more ordered lamellar structure. For solutions richer in the non-ionic co-surfactant, increasing temperature induces the formation of mixed micelles.

Introduction

Shear induced transitions in surfactant systems have been extensively studied and reported; and include isotropic to nematic transitions [3], growth of elongated micelles [4], lamellar to vesicle transitions [1,5], and variations in orientational order in lamellar phase systems [6,7]. More specifically we have recently reported the characterisation of the shear-thickening transition from an aligned lamellar phase to multi-lamellar vesicles in the di-chain cationic surfactant system, di-octadecyl dimethyl ammonium chloride, 2HT [1]. We compared the behaviour of this charge- stabilised system under shear with those stabilised by ' Helfrich fluctuations' [5]. Such fluctuations are stabilised by a long range repulsive force arising from thermal fluctuations in the lamellar bi-layer. As part of that study, the SANS and conductivity data gave results that were indicative of an inhomogeneous distribution of orientational order across the Couette flow cell gap. It is this aspect that will be pursued in more detail in the first part of the present paper. We have previously shown, in a different lamellar phase system, that changes in orientational order in lamellar phase dispersions are observed as a function of shear [6,7]. In related studies, Berghausen *et al.* [8] have shown that this can be associated with changes in distribution across the Couette flow cell gap in the shear gradient direction.

The original SANS and conductivity data [1] indicate an inhomogeneous distribution of order for the 2HT dispersions, and further SANS data and SAXS data, using a micro-focus beam-line, were used to investigate the distribution in orientational order. Shear-induced phase separation has been the subject of much recent theoretical interest [2,9,10]. Shear-induced phase separation, or 'shear banding', associated with a discontinuity in the stress-strain relationship, is predicted for common stress (in the shear gradient direction), and for common strain (in the vorticity direction). This has now been well-established for a variety of different systems, and we discuss our data in the context of 'shear banding'.

Temperature and the addition of a co-surfactant can both have a profound effect on the macroscopic behaviour and on the micro-structure of lamellar phase dispersions. In many practical applications and formulations non-ionic surfactants are used to manipulate (reduce) the dispersion viscosity. Reductions in lamellar fragment size, where the non-ionic surfactant adsorbs to the fragment edge hence stabilising smaller fragments, are observed [11]. Temperature is also important, as the temperature relative to the L_α / L_β transition temperature dictates its macroscopic behaviour and its micro-structure. In the second part of the paper we report preliminary results on the effects of co-surfactant and temperature on the dispersion micro-structure.

Experimental Details

The SANS measurements were made on the LOQ diffractometer at ISIS [12], using the white beam time-of-flight method, in the scattering vector, Q, range of 0.008 to 0.25 $Å^{-1}$. A quartz Couette flow cell, described previously by Penfold *et al.* [13]; with a 50 mm diameter, a 0.5 mm gap, a fixed inner stator, and a rotating outer cup was used. Measurements were made for shear rates from 0 to 1000 s^{-1}, and for temperatures in the range 25 to 60 °C. The SAXS measurements were made on the ID13 X-ray micro-focus beam-line at the ESRF [14]. SAXS data were recorded using a 20 x 20 micron beam at a wavelength of 0.96 Å, in the Q range 0.002 to 0.3$Å^{-1}$. A poly-carbonate Couette flow cell with an outer diameter of 20 mm and a gap of 1mm was used to establish flow rates up to 4 s^{-1} [8]. The use of an outer rotating cup, a sealed cell, and conical geometry in the cell base [13] provided a wider range of accessible shear rates for the neutron scattering measurements. Both the SANS and SAXS data were corrected and normalised using standard procedures [12,14].

Conductivity measurements were made using a customised cell, and have been described in detail elsewhere [1]. Light scattering measurements were made in the neutron Couette flow cell; which was illuminated with white light, viewed through crossed polarizers, and recorded using a digital camera.

Inhomogeneous Distributions

The shear-thickening transition observed in the rheological response of the concentrated 2HT dispersions (Fig. 1) was characterised by SANS and conductivity measurements to produce a 'shear diagram' (Fig. 2). This shows the shear-rate dependence of the transition from the aligned lamellar phase to multi-lamellar vesicles.

The 'shear diagram' is the out-of-equilibrium equivalent of an equilibrium phase diagram, and has been discussed in detail elsewhere [1]. The SANS data, measured in both the radial (neutron beam incident normal to the flow-vorticity plane) and tangential (neutron beam incident normal to the gradient-vorticity plane) scattering geometries, for the aligned lamellar phase reveal an apparent inconsistency (Fig. 3).

The orientational order observed in Figure 3(b), measured in the tangential scattering geometry, is consistent with lamellae oriented in the flow-vorticity plane, as previously reported [6]. For such orientational order there should be little or no scattering when measured in the radial scattering geometry, and this has been previously observed for other lamellar phase dispersions [6]. The pronounced scattering observed here (Fig. 3(a)), when measured in the radial scattering geometry, is, however, consistent with lamellae ordered in the flow-shear gradient plane. This has been observed previously in the lamellar phase of monohexadecyl hexaethylene glycol, C16E6 [6], and sodium dodecyl sulphate, SDS / dodecane / pentanol [7,8] at higher shear rates. However, in such cases the same scattering was observed in both the radial and tangential scattering geometries, and this is not the case for the 2HT data presented here in Figure 3. At intermediate shear rates, scattering in both the vorticity and shear flow directions has also been observed in C16E6 [6], and SDS / dodecane / pentanol [7], and was attributed to a bi-modal distribution of orientations. Subsequent measurements on SDS / dodecane / pentanol [8] showed that this was consistent with an inhomogeneous distribution across the Couette flow cell gap.

The results reported here for 2HT are not entirely consistent with those reported by Berghausen *et al.* [8], and require a slightly different explanation. On the basis of the SANS data the implication is that the lamellae close to the outer surface of the Couette flow cell gap are aligned parallel to the flow-vorticity plane, and that there is a distribution of orientations across the gap. The scattering in the tangential

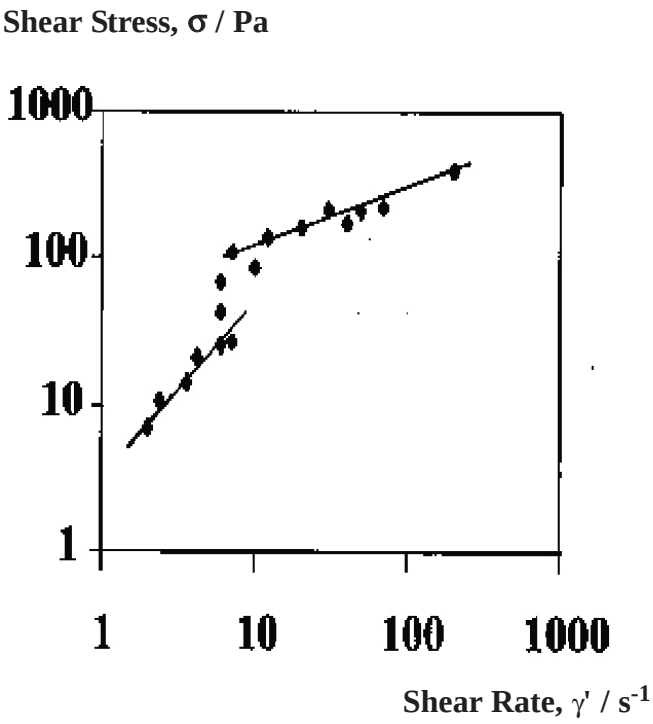

Figure 1. Shear stress, σ, as a function of shear rate, γ', for 45 wt % 2HT.

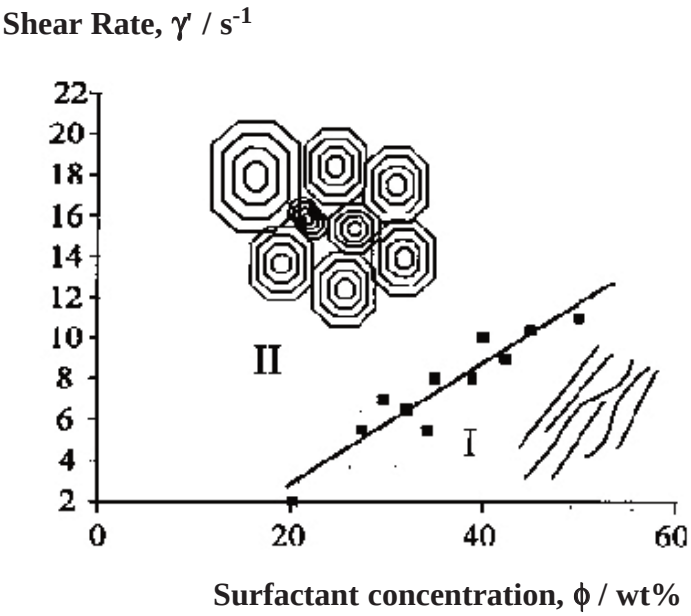

Figure 2. 'Shear diagram' for 2HT, shear rate, γ', as a function of surfactant concentration, ϕ, (in wt %), showing the stability regions of the two time invariant states as a function of shear rate

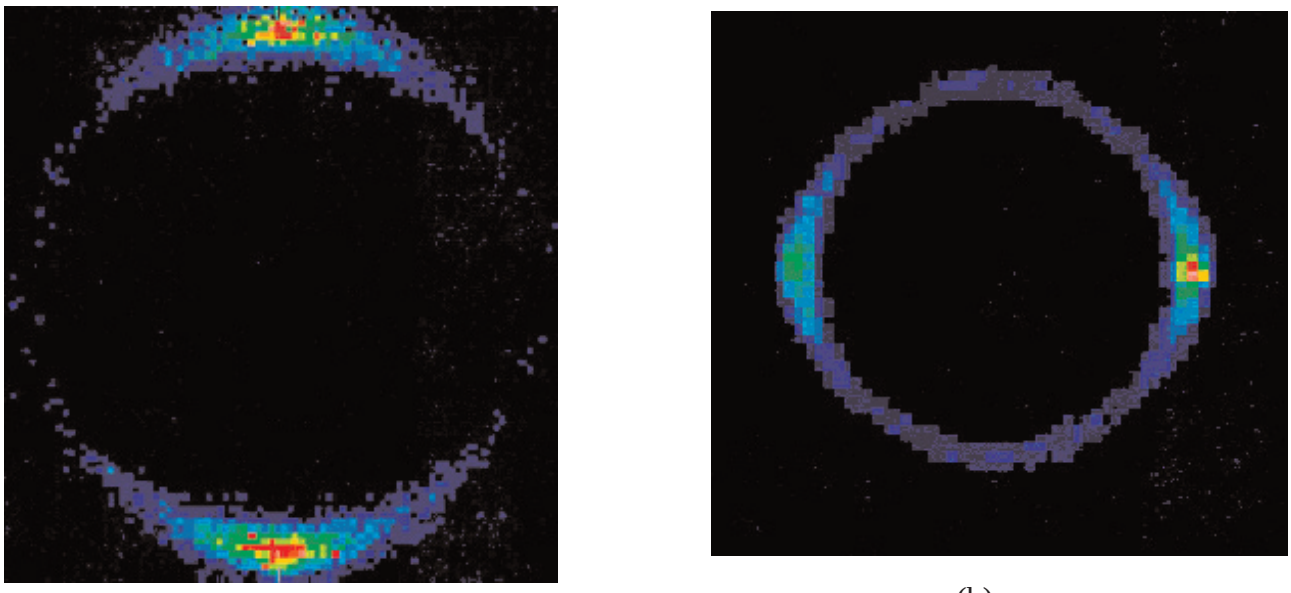

(a) (b)

Figure 3. Two-dimensional SANS pattern for 45 wt% 2HT at a shear rate of 6 sec^{-1}, (a) radial scattering geometry, (b) tangential scattering geometry

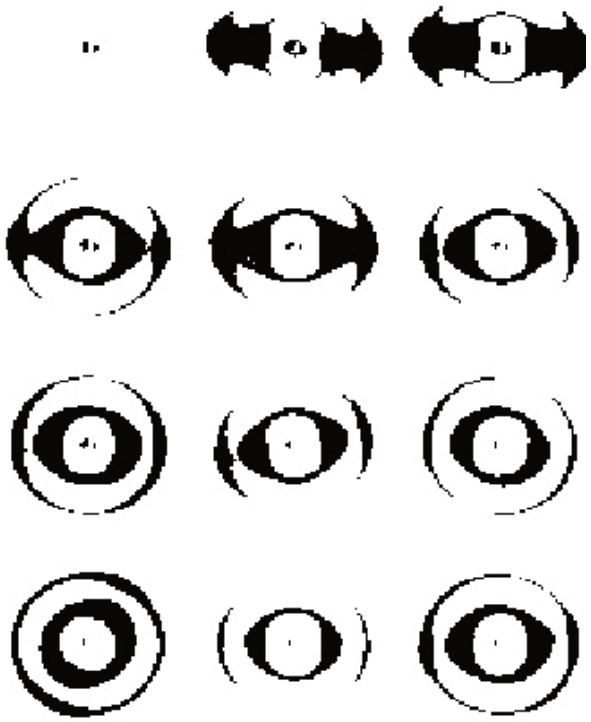

Figure 4. Two-dimensional SAXS scattering patterns for 45 wt% 2HT at a shear rate of 0.4 s^{-1}, from the outer surface towards the centre in 0.1mm steps (starting form the top left hand corner and increasing row by row)

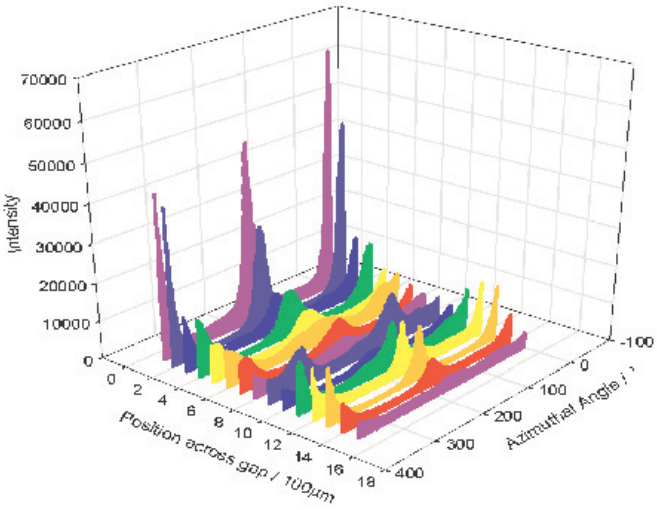

Figure 5. Scattered x-ray intensity as a function of azimuthal angle, from the outer surface towards the centre of the cell in 0.1mm steps, corresponding to the two-dimensional images in figure 4.

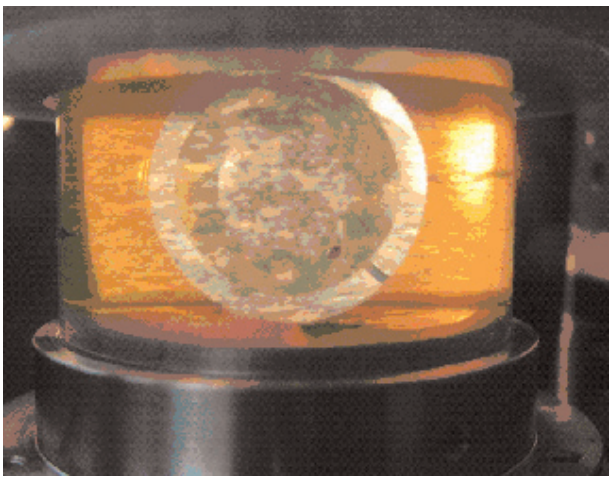

(a)

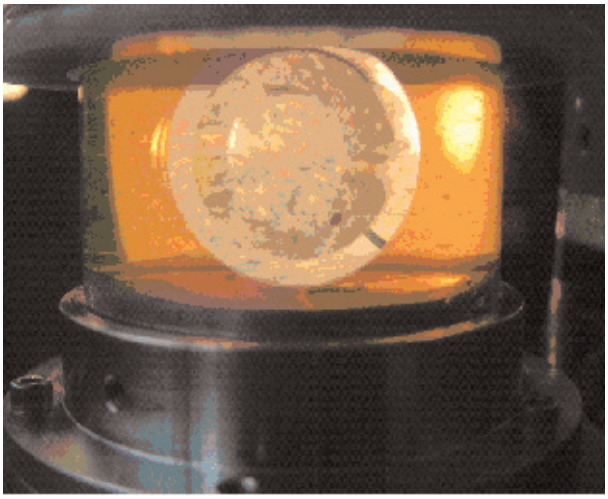

(b)

Figure 6. Polarised light scattering from 45 wt% 2HT at a shear rate of (a) $8s^{-1}$, (b) $2s^{-1}$

geometry will be dominated by the fraction aligned close to the outer surface, whereas the greater neutron path length towards the cell centre will effectively attenuate the scattering from the inner regions of the gap. (Note: At 0.05 mm from the outer surface the mean path length is 4.4mm, whereas at 0.9mm it is 19.1mm. Assuming that a 1mm thick sample has a transmission ~0.8, then the change in mean transmission moving from 0.05 to 0.9 mm from the outer surface of the cell is ~ 40.) In the radial geometry there is no such preferential adsorption, and all regions of the gap will equally contribute to the observed scattering.

To confirm that the SANS scattering observed in the radial and tangential scattering geometries is consistent with an inhomogeneous distribution of orientations across the beam [14], as described in the experimental details section, two-dimensional SAXS scattering patterns are shown in Figure 4, for a series of positions at 0.1mm intervals across the Couette cell gap from the outer surface towards the inner surface.

Figure 5 shows the variation in scattered intensity as a function of azimuthal angle at a Q value corresponding to the second order Bragg peak arising from the ordered lamellar structure. There is a distribution of orientations across the flow cell gap. The lamellae closest to the outer surface are highly aligned in the flow-vorticity direction. There is a lower degree of orientational order further into the cell, and there are regions where the orientation is predominantly in the flow-shear gradient direction. The reduction in orientational order is partly due to averaging over the Couette cell curvature, but the changes in the direction of the orientational order are real. The distinct regions of orthogonal order raise the question of whether this distribution of orientational order is consistent with 'shear banding' [9,10].

'Shear banding' occurs in the proximity of a discontinuity in the stress-strain curve, and can be associated with a phase transition, with different micro-structures, with different orientational ordering, or with concentration changes (de-mixing). For both shear-thickening and shear-thinning systems, common strain 'banding' (in the vorticity direction) and common stress 'banding' (in the shear gradient direction) are possible. If the applied strain rate forces the system into the unstable part of the flow curve, then it can separate into regions (or bands) with high and low strain rates, whilst maintaining the applied strain rate. The radial separation in common stress 'banding' imposes a uniform shear stress and different strain rates, whereas the axial separation in common strain 'banding' results in the same strain rate but different shear stresses.

It was not possible to make the SAXS measurements at a shear rate close to the discontinuity shown in Figure 1, and the rheology measurements are not sufficiently detailed at the lower shear rates to correlate the SAXS data measured at 0.4 s^{-1} directly with a specific rheological response. Further rheology measurements are required to confirm whether the micro-focus SAXS data are consistent with common stress 'banding'.

To explore the possibility of common stress 'banding' in this system, some polarised light scattering measurements were made in the region of the stress / strain discontinuity (Fig. 1) in the neutron Couette flow cell. The results are shown in Figure 6. There is a pronounced increase in the texture of the light scattering in the region of the rheological discontinuity. However, there is no marked development of macroscopic bands. The evolution of banding in the vorticity direction is controlled by 1-D diffusion, and is hence slow. Further measurements at longer incubation times (the measurements in Figure 6 were made after ~ 5 to 10 minutes) will be made. The measurements will also be made at constant stress, rather than constant strain. Common stress and common strain 'banding' has been observed in related lamellar phase systems [15], and in worm-like or elongated micellar structures [16-18]. The measurements made so far for the 2HT system show a distribution of orientational order in the shear gradient direction, and demonstrate the possibility of shear 'banding'.

Effects of temperature and co-surfactant

In the previous section we have highlighted some aspects of the effects of shear on concentrated surfactant dispersions, and the relationship between the micro-structure and the macroscopic rheological response. For the di-chain cationic surfactants, which are used extensively in a variety of formulations, temperature and the addition of a co-surfactant can have a profound effect on the micro-structure of these lamellar phase dispersions. The L_α / L_β transition, the transition from an ordered

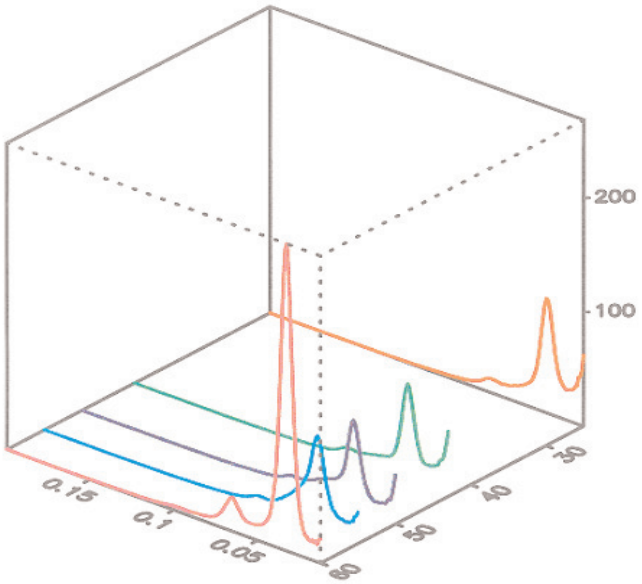

Figure 7. Scattered Intensity, I(Q), as a function of temperature for 12 wt% HEQ / 4 wt % C12E12

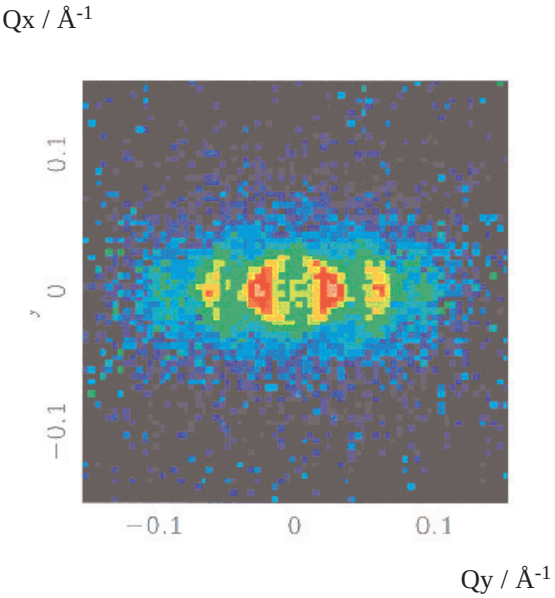

Figure 8. 2-D Intensity contour pattern for 12 wt % HEQ / 4 wt % C12E12 at 55°C and a shear rate of 10 s^{-1}.

'solid-like' phase to fluid bilayers, has a significant impact on the dispersion micro-structure. The addition of co-surfactants will modify (lower) that transition temperature. The non-ionic co-surfactant will adsorb to the edge of lamellar fragments, stabilise smaller fragments, and reduce the dispersion viscosity. We present here some preliminary SANS data on the effects of temperature and the composition of di-chain cationic / non-ionic surfactant mixtures, which complement and extend the results which highlight the role of shear.

A series of SANS measurements for a mixture of the di-chain cationic and non-ionic surfactants, 2,3-di-heptadecyl ester ethoxy-n-propyl-1,1,1-trimethyl ammonium chloride, HEQ and dodecaethylene glycol monododecyl ether, C12E12, rich in the cationic surfactant and as a function of temperature are shown in Figure 7. At all temperatures the data are consistent with lamellar fragments. Increasing the temperature above the L_α / L_β transition temperature (~ 50°C) results in a more ordered lamellar structure. Applying modest shear (≤ 10 s^{-1}) produces pronounced anisotropy (see Fig. 8). The scattering at 55°C shows 4 to 5 orders of diffraction, and is consistent with a highly ordered and oriented lamellar phase. Reducing the cationic / non-ionic composition of the dispersion results in a rather different structural response with increasing temperature (see Fig. 9), and evolution of a different

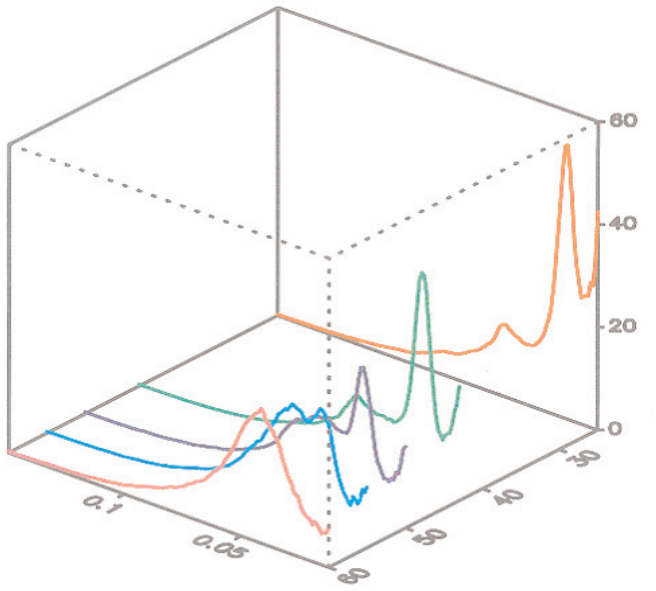

Figure 9. Scattered Intensity, I(Q), as a function of temperature for 4 wt% HEQ / 4 wt% C12E12

sequence of micro-structures.

With increasing temperature the scattering evolves from that corresponding to lamellar fragments to mixed surfactant micelles. At intermediate temperatures micelles and lamellar fragments co-exist. Increasing the temperature has induced the formation of mixed micelles from the lamellar dispersion, such that above the L_α / L_β transition temperature the solution is entirely micellar. Further measurements exploring more completely the phase

behaviour, micro-structure and rheology of such mixtures are now underway.

Summary

We have used a combination of scattering techniques and rheological measurements to understand the micro-structure of complex concentrated di-chain cationic lamellar phase dispersions, and the effects of shear, temperature and the addition of co-surfactants on such dispersions. We have provided evidence of the inhomogeneities in orientational order arising in Couette flow, and we have discussed the data in relationship to the possibilities of 'shear banding'. We have presented preliminary results showing the evolution of order and structure with temperature and with the addition of a co-surfactant. The data show an increase in lamellar order with temperature and the development of mixed micelles.

References

[1] Soubiran, L., Staples, E., Tucker, I. & Penfold, J. (2001) Effects of shear on the lamellar phase of a di-chain cationic surfactant. *Langmuir* **17**, 7988-7994.

[2] Olmsted, P.D. (1999) Two-state shear diagram for complex fluids in shear flow. *Europhys Lett* **48**, 339-345.

[3] Berret, J.F., Roux, D.C., Porte, G. & Lindner, P. (1994) Shear-induced isotropic to nematic transition in equilibrium polymers. *Europhys Lett* **25**, 521-

[4] Berret, J.F., Gamez-Corrales, R., Serero, Y., Molino, F. & Lindner, P. (2001) Shear induced micellar growth in dilute surfactant solutions. *Europhys Lett.* **54**, 605-611.

[5] Diat, O., Roux, D.C. & Nallet, F. (1993) Effect of shear on lyotropic lamellar phas.e J. Phys. II 3,1427-1452: (1995) Layering effect in a sheared lyptropic lamellar phase. *Phys. Rev. E.* **51**, 3296-3299.

[6] Penfold, J., Staples, E., Tucker, I., Tiddy, G.J.T. & Khan Lodi, A. (1997) Shear induced transformation in the lamellar phase of C16E6. J. Phys. Chem. B 101, 66-72: (1997) Shear induced structures in concentrated micellar phases. *J. Appl. Cryst.* **30**, 744-749.

[7] Zipfel, J., Berghausen, J., Lindner, P. & Richtering, W. (1999) Influence of shear on lyotropic lamellar phases with different membrane defects. *J. Phys. Chem. B* **103**, 2841-2849.

[8] Berghausen, J., Zipfel, J., Diat, O., Narayaran, T. & Richtering, W. (2002) Lamellar phases under shear: variation of the layer oreintation across the Couette gap. *PCCP* **2**, 3623-3626.

[9] Olmsted, P.D. & Lu, C.Y.D. (1997) Coexistence and phase separation in sheared complex fluids. Phys. Rev. E 56, R55-R58; (1999) Phase coexistence of complex fluids in shear flow. *Faraday Disc.* **112**, 183-194.

[10] Goveas, J.L. & Olmsted, P.D. (2001) A minimal model for vorticity and gradient banding in complex fluids. *Eur. Phys. J. E* **6**, 79-89.

[11] Partal, P., Kowalski, A.J., Machin, P., Kiratzis, N., Berni, M.G. & Lawrence, C.J. (2001) Rheology and microstructure transition in the lamellar phase of a cationic surfactant. *Langmuir* **17**, 1331-1337.

[12] Heenan, R.K., King, S.M. & Penfold, J. (1997) SANS at a pulsed neutron source. Present and future prospects. *J Appl Cryst* **30**, 1140-1147.

[13] Cummins, P.G., Staples, E., Millen, B. & Penfold, J. (1990) A Couette flow cell for small-angle scattering studies. *Meas. Sci. Technol.* **1**, 179-183.

[14] Engstrom, P., Fielder, S. & Riekel, C. (1995) Microdiffraction instrumentation and experiments with the microfocus beamline at the *ESRF. Rev. Sci. Instrum*. **66**, 1348-1350.

[15] Bonn, D., Meunier, J., (1998) Bi-stability in non-Newtonian flow: rheology of lyotropic liquid crystals. *Phys. Rev. B* **58**, 2115-2118.

[16] Lerouge, S., Decruppe, J.P. & Berret, J.F. (2000) Correlations between rheology and optical properties of a micellar solution under shear banding flow. *Langmuir* **16**, 6464-6474.

[17] Fischer, E. & Callaghan, P.T. (2001) Shear banding and the isotropic to nematic transition in worm-like micelles. *Phys. Rev. E* **64**, 011501-011510.

[18] Decruppe, J.P., Cressely, R., Makhloufi, R. & Cappelaere, E. (1995) Flow birefringence experiments showing a shear banding structure in a CTAB solution. *Coll. Polym. Sci.* **273**, 346-351.

Preparation of Tunicin Cellulose Iβ Samples for X-ray and Neutron Diffraction.

Yoshiharu Nishiyama[1], Paul Langan[2]* and Henri Chanzy[3]

[1] Department of Biomaterials Science, Graduate School of Agricultural and Life Sciences, The University of Tokyo, Tokyo 113-8657, Japan
[2] Biosciences Division, Los Alamos National Laboratory, Los Alamos, NM 87545, USA.
[3] Centre de Recherches sur les Macromolécules Végétales-CNRS, affiliated with the Joseph Fourier University of Grenoble, B.P. 53, 38041 Grenoble Cedex 9, France.

* Corresponding Author: M888 Biosciences Division, Los Alamos National Laboratory, Los Alamos, NM87545, USA. Tel: +1 505 665 8125; Fax: +1 505 665 3024; Email: langan_paul@lanl.gov

ABSTRACT

Methods are described for extracting crystalline cellulose Iβ microfibrils from the cellulosic mantles of tunicin (Halocynthia roretzi) and then reconstituting them into highly oriented films that diffract synchrotron X-rays and neutrons to atomic resolution.

INTRODUCTION

Cellulose is biosynthesized as nanometer thick crystalline microfibrils of *poly*(1-4)-β-D-glucan. These microfibrils consist of two crystal phases, namely Iα and Iβ [1]. Until recently, the accepted crystal structure for naturally occurring cellulose, cellulose I, was based on X-ray data collected from fibres containing both Iα and Iβ phases, without knowledge of this dimorphism [2,3]. In this report we describe advances in sample preparation and characterization methods that have allowed us to produce samples of pure Iβ phase that diffract X-rays and neutrons to atomic resolution.

The sea organism *Halocynthia roretzi*, commonly known as the 'sea squirt' or 'tunicate', because of the presence of a thick leathery mantle or tunic in their mature phase, was used as the source of cellulose. The mantles of tunicate consist of a composite structure of cellulose microfibrils organized in helical order and dispersed in a matrix of protein and acid mucopolysaccharide [4]. The cellulose from tunicate, called tunicin, is known from ^{13}C CP/MAS solid state NMR studies to consist of predominantly the Iβ phase [5,6]. Electron microscopy and diffraction studies have shown that the microfibrils are highly crystalline [7-10], each microfibril corresponding to a distinct single crystal approximately 10 nm in width [4, 9, 11]. Although these microfibrils have dimensions that are amenable to an electron diffraction study [10,11], they are too small for X-ray or neutron diffraction.

METHODS

Preliminary X-ray Measurements

The suitability of tunicate mantles for X-ray diffraction studies was assessed by collecting X-ray data from deproteinized mantles on a Philips 1720 X-ray generator equipped with a Wharus flat film X-ray camera, operated at 30kV and 20 mA with a Ni-filter and CuKα radiation. The resultant patterns contained at least 7 orders of diffraction and indicate that the crystalline cellulose microfibrils in the mantle diffract X-rays to high resolution, Figure 1. However, the smearing of these diffraction orders into powder rings indicates that the microfibrils have random orientation within the mantle. This is in agreement with the observation from electron microscopy studies that the microfibrils appear to be organized in liquid crystalline order [4]. In order to obtain fibre diffraction samples, the methods described below had to be devised for extracting the microfibrils from the mantle and re-orienting them in suitably sized assemblies.

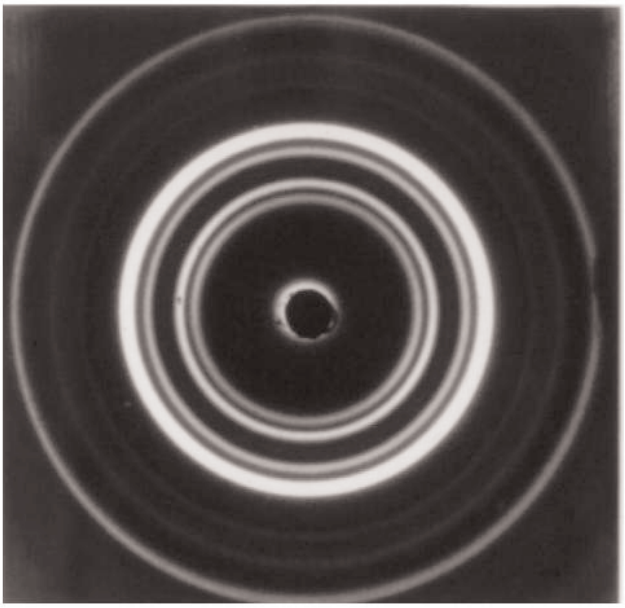

Figure 1. X-ray diffraction collected from the deproteinized mantle of tunicate (*Halocynthia roretzi*).

Extraction and Purification of Cellulose Microfibrils

Halocynthia roretzi were kindly supplied by Prof. Fumitaka Horii, Institute for Chemical Research, Kyoto University. The following procedure was arrived at as a means of extracting and purifying the cellulose without destroying the crystal quality of the microfibrils. The cellulosic mantles were separated from the rest of the organism and then partially hydrolyzed with sulphuric acid and soaked in 5% KOH solution. A white material was obtained after repeatedly treating the hydrolyzate with a 0.3% $NaClO_2$ solution buffered to about pH 4 at 70°C, and 5% KOH. The white material was cut into pieces of about 5 mm square while still wet. These sections were disintegrated using a double cylinder type homogenizer. The suspended cellulose fragments were collected by centrifugation. The solid content of the suspension was about 5%.

Two parts of 70 % sulphuric acid were added to one part of the wet cellulose sample and stirred rigorously with a Teflon coated propeller at 50°C overnight. The viscosity decreased drastically during this treatment. The resulting suspension was diluted about 5 times with distilled water and centrifuged at about 2000g. The transparent supernatant was removed by decantation and the cellulose-containing pellet was re-suspended in de-ionized water and centrifuged again. This process was repeated until the supernatant became turbid. At this stage the supernatant is a suspension of cellulose microcrystals stabilized by sulphate surface groups. The turbid supernatant was collected and the centrifugate was further washed with de-ionized water, each time harvesting the turbid supernatant, until only brownish impurities remained at the bottom of the tube. Finally the microcrystals in the turbid supernatant were collected by centrifugation at 16,000g and stored in a refrigerator at 4°C until further use.

Preparation of Films of Oriented Microfibrils

Films of oriented microfibrils were prepared using a variation of a previously described method [12]. The microcrystalline suspension described above was put into a glass vial and diluted to a solid content of about 1 %. Above a critical concentration, the particles in this colliodal dispersion organize spontaneously into a chiral nematic liquid crystalline phase. A suspension of these particles is shown in Figure 2.

Sulphuric acid was added to the suspension to about 1%. The suspension became very thick and more turbid when sulphuric acid, or for that matter any electrolyte, was added. After agitation with a Teflon coated magnetic stirrer, the viscosity dropped, athough it was still higher than in the electrolyte-free suspension. During stirring, an oriented gel formed on the surface of the vial. At this point the magnetic stirrer was removed from the vial and the gel was disintegrated by rigorous shaking of the vial. With the cap closed, the vial was attached horizontaly to a motor and spun at about 500 rpm around its centre axis. A smooth layer of jelly formed on the inner surface of the vial within an hour, which gradually thickened with time. This layer was removed and then dried, resulting in a film several centimeters long and a few microns thick, which when viewed under a polarizing microscope showed a strong birefringence (Fig. 3).

Assembly of Samples for Neutron and Fibre diffraction Studies

Samples large enough for X-ray or neutron diffraction studies were built by selecting films under a polarization microscope and then assembling these films into thick stacks as described previsouly [13]. Particular care had to be taken in deciding the dimensions of the neutron samples. On the one

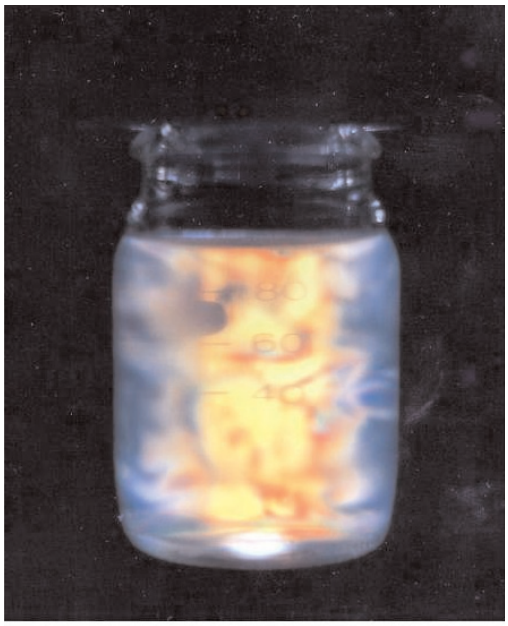

Figure 2. A 0.5% (w/v) supension of purified cellulose microfribrils from the mantle of tunicate (*Halocynthia roretzi*) observed in polarized light between crossed polarizers.

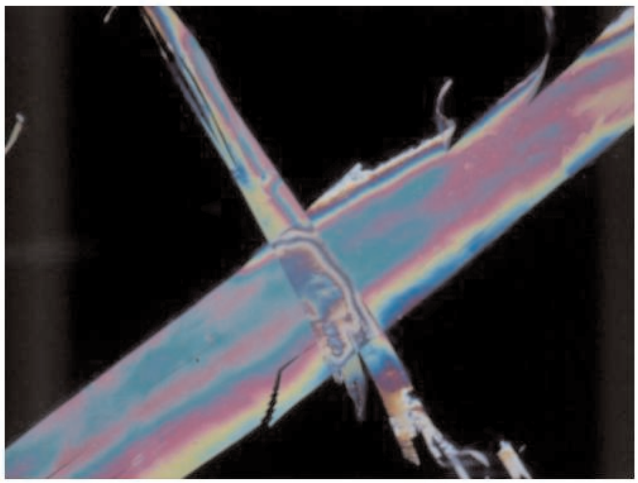

Figure 3. Films of oriented purified cellulose microfibrils extracted from tunicate (*Halocynthia roretzi*) viewed through a polarizing microscope with crossed polarizers (axes vertical and horizontal).

hand, neutron beams are relatively weak in flux so large sample sizes are desirable in order to maximise the number of diffracted neutrons. On the other hand, hydrogen in the sample has a large spin incoherent neutron scattering cross-section that effectively attenuates the diffracted neutron beams and also contributes to a large background signal. The final thickness of the neutron sample, τ , was therefore determined not by the amount of material avaible, but rather by a compromise between the above-mentioned two factors.

The optimum total reflected energy for a cuboid shaped sample occurs when $\mu\tau \sim 1$, where m is the effective linear absorption coefficient [14]. For cellulose Iβ, μ was calculated to be ~5.3cm-1 and therefore a sample with τ~2mm was used. The neutron experiments also involved collecting data from samples where all OH moeities had been replaced by OD [15]. In this case μ ~3cm^{-1} and a τ~3.5mm was used. For the X-ray experiments much smaller samples with τ~ 200mm were used in order to match the approximate size of the synchrotron X-ray beam. An example of some of the diffraction data recorded from these samples is shown in Figure 4.

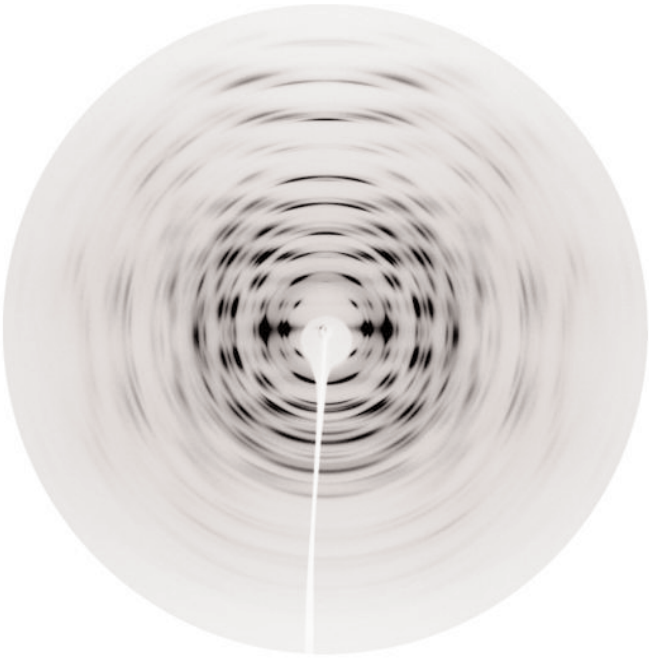

Figure 4. X-ray diffraction data collected from oriented purified cellulose microfibrils extracted from tunicate (*Halocynthia roretzi*). The data were collected using a wavelength of 0.72Å and a MAR image plate on station ID02A at the ESRF, Grenoble. The fibre axis is vertical. Diffraction features are present at scattering angles that correspond to **d**-spacing of less than 1Å.

DISCUSSION

A number of sea organisms contain cellulose microfibrils of high crystal quality but poor alignment. X-ray fibre diffraction patterns to ~2Å resolution were recorded in the 1970's from stretched algal (*Valonia ventricsa*) cell walls [2,3]. In contrast, electron diffraction patterns have been recorded to ~0.7Å resolution from minute fragments of oriented *Valonia ventricsa* cell wall [16]. This observation first suggested to us that if crystals of cellulose could be extracted and then reconstituted into highly oriented fibres it might be possible to

collect X-ray data of similar quality to the electron diffraction data.

The method presented here is derived from ongoing developments in the study of suspensions of colloidal cellulose microcrystals [17-19]. Our method is quite general, although there are usually variations in detail, and has been applied to other cellulose allomorphs. So far these samples have all diffracted synchrotron X-rays, and after hydrothermal deuteration [15], neutrons to atomic resolution (~1Å) [13,15,20,21]. The resolution of these data has allowed us to visualize individual atoms and to identify small variations in conformation. The ability to locate hydrogen atoms has allowed us to identify hydrogen patterns that can be related to the surface properties of cellulose microfibrils. These results have important implications for our understanding of the factors that influence the structure and properties of cellulose.

ACKNOWLEDGEMENT

Y.N. thanks the French Government and the Japanese Society for the Promotion of Science for financial support. P.L. thanks the office of Science and the Office of Biological and Environmental Research of the U.S. Department of Energy for financial support.

REFERENCES

[1] Atalla, R. & Van der Hart, D. L. (1984) Native Cellulose: a Composite of 2 Distinct Crystal Forms. *Science* **223**, 283-285.
[2] Gardner, K. H. & Blackwell, J. (1974) The Structure of Native Cellulose. *Biopolymers* **13**, 1975-2001.
[3] Sarko, A. & Muggli, R. (1974) Packing Analysis of Carbohydrate and Polysaccharides. III. Valonia Cellulose and Cellulose II. *Macromolecules* **7**, 486-494.
[4] VanDaele, Y., Revol, J-F., Gaill, F. & Goffinet, G. (1992) Characterization and Supramolecular Architecture of the Cellulose-protein Fibrils in the Tunic of the Sea Peach (Halocynthia papillosa, Ascidiacea, Urochirdata. *Biol. Cell*. **76**, 87-96.
[5] Belton, P. S., Tanner, S. F., Cartier, N. & Chanzy, H. (1989) High-Resolution Solid-State ^{13}C Nuclear Magnetic Resonance Spectroscopy of Tunicin, and Animal Cellulose. *Macromolecules* **22**, 1615-1617.
[6] Larsson, P. T., Westermark, U. & Iversen, T. (1995) Determination of the Cellulose Iα Allomorph Content in a Tunicate Cellulose by CP/MAS ^{13}C NMR spectroscopy. *Carbohydr. Res*. **278**, 339-343.
[7] Frey-Wyssling, A.& Frey, R. (1951) Tunicin im Elektronenmikroskop. *Protoplasma* **39**, 656-660.
[8] Rånby, B.G. (1952) Physicochemical Investigations on Animal Cellulose (Tunicin). *Ark. Kemi*. **4**, 241-248.
[9] Helbert, W., Nishiyama, Y., Okano, T. & Sugiyama, J. (1998) Molecular Imaging of Halocynthia Papillosa Cellulose. *J. Struct. Biol*.**124**, 42-50.
[10] Sugiyama, J., Persson, J. & Chanzy, H. (1991) Combined Infrared and Electron Diffraction Study of the Polymorphism of Native Cellulose. *Macromolecules* **24**, 2461-2466.
[11] Sugiyama, J., Chanzy, H. & Maret, G. (1992) Orientation of Cellulose Microcrystals by Strong Magnetic Fields. *Macromolecules* **25**, 4232-4234.
[12] Nishiyama, Y., Kuga, S., Wada, M. & Okanao, T. (1997) Cellulose Microcrystal Film of High Uniaxial Orientation. *Macromolecules* **30**, 6395-6397.
[13] Nishiyama, Y., Langan, P. & Chanzy, H. (2002) Crystal Structure and Hydrogen-Bonding System in Cellulose Iβ from Synchrotron X-ray and Neutron Fibre Diffraction. J. *Am. Chem. Soc*. **124**, 31, 9074-9082.
[14] Langan, P., Forsyth, V.T. & Mahendrasingam, A. (1995) Attenuation Corrections for X-ray and Neutron Fibre Diffraction Studies. *J. App. Cryst*. **28**, 49-52.
[15] Nishiyama, Y., Isogai, A., Okano, T., Muller, M. & Chanzy, H. (1999) Intracrystalline Deuteration of Native Cellulose. *Macromolecules* **32**, 2078-2081.
[16] Honjo, G. & Watanabe, M. (1958) Examination of Cellulose Fibre by the Low-temperature Specimen Method of Electron Diffraction and Electron Microscopy. *Nature* **181**, 326-328.
[17] Marchessault, R.H., Morehead, F.F. & Walter, N.M. (1959) Liquid Crystal Systems from Fibrillar Polysaccharides. *Nature* **184**, 632-633.
[18] Revol, J-F., Bradford, H., Giasson, J., Marchessault, R.H. & Gray, D.G. (1982) Helicoidal Self-ordering of Cellulose Microfibrils in Aqueous Suspension. Int. *J. Biol. Macromol*. **14**, 170-172.
[19] Dong, X. M., Kimura, T., Revol, J-F. & Gray, D. G. (1996) Effect of Ionic Strength on the Isotropic-chiral Nematic Phase Transition of Suspensions of Cellulose Crystallites. *Langmuir* **12**, 2076-2082.
[20] Nishiyama, Y., Okano, T., Langan, P. & Chanzy, H. (1999) High Resolution Neutron Diffraction Data on Hydrogenated and Deuterated Cellulose. Int. *J. Biol. Macromol*. **26**, 279-283.
[21] Nishiyama, Y., Chanzy, H., Wada, M., Sugiyama, J., Mazeau, K., Forsyth, V.T., Riekel, C., Mueller, M., Rasmussen, B. & Langan, P. (2002) Synchrotron X-ray and Neutron Fibre Diffraction Studies of Cellulose Polymorphs. Adv. in *X-ray Analysis.* **45**, 385-390.

Cross-beta structure of an amyloid-forming peptide studied by electron nano-crystallography

Ruben Diaz-Avalos*, Chris Long, Eric Fontano, Melinda Balbirnie, Robert Grothe, David Eisenberg and Donald L.D. Caspar

Institute of Molecular Biophysics, Florida State University, Tallahassee, Fl 32306.

*Corresponding Author: Ruben Diaz-Avalos,

ABSTRACT

The seven residue peptide GNNQQNY from the N-terminal region of the yeast prion protein Sup35, which forms both amyloid fibres and highly ordered microcrystals, provides a model system for characterizing the structure and stability of the elusive cross-beta amyloid conformation. Microcrystals of this peptide, which have largest dimension ~1μm in the cross-beta fibre axis direction, diffract electrons to ultra high resolution (<0.5Å spacing). The sharp 4.86Å layer-line spacing (with no trace of a 9.72Å spacing) establishes that the peptide chains form parallel β-sheets. The space group is $P2_12_12_1$ with cell dimensions ranging from $|\boldsymbol{a}|$ = 22.7-21.2, $|\boldsymbol{b}|$ = 39.9-39.3, $|\boldsymbol{c}|$ = 4.89-4.86Å for the wet to dried state. The relative intensities of the Bragg reflections determined from the electron diffraction data indicate that the backbones of the four peptides in the unit cell are aligned closely parallel to the a-axis, with the cross-beta sheets connected in two pairs related by the crystal 2-fold screw axes. Comparison of the cell volume with that calculated for the four peptides implies that water may occupy only 10-15% of the volume in the hydrated state. This nearly anhydrous packing can account for the insolubility of the crystalline aggregates of this hydrophilic peptide, since the activation energy for rehydration may be extremely high. Water excluding packing of paired cross-β peptide segments in thin protofilaments may be a general characteristic of the wide variety of anomalously stable pathological amyloid assemblies.

Introduction

The cross-β polypeptide conformation is characteristic of the pathological amyloid fibre aggregates associated with various neuro-degenerative diseases, including Alzheimer's, Huntington's and Parkinson's, as well as systemic amyloidoses. This fibrous protein folding, in which the β-strand direction is nearly perpendicular to the fibre axis, was first identified by X-ray diffraction from oriented specimens of denatured globular (Astbury, 1935) and fibrous (Rudall, 1952) proteins. In contrast to the familiar fibrous proteins consisting of extended α-helices (eg, keratin, myosin and fibrin), collagen triple helices or β-strands (e.g. silks), the cross-β conformation is rare among naturally occurring biological fibres (Fraser and MacRae, 1973). Cross-β appears to be a dead-end for protein folding. Exceptionally rare, protease-resistant, fibrous amyloid aggregates can be formed by proteins and peptides with uncorrelated amino-acid compositions and sequences by self-nucleated self-assembly. Beyond the evident regularly periodic cross-β sheet hydrogen bonding in the fibre axis direction, there is little experimental data regarding the atomic structure of amyloid aggregates that can account for their pathological stability and self propagating properties.

The cross-β structure was not fully characterized until the late 1960's, in the work of Eanes and Glenner (1968) and Bonnar *et al.* (1969) from X-ray patterns of partially-aligned specimens taken from human patients afflicted with amyloidosis. The characteristic signature of the cross-β fibre diffraction pattern is a sharp 4.7 - 4.9Å meridional maximum, accompanied by a ~10Å equatorial reflection, indicative of a β-sheet structure oriented with the polypeptide chains perpendicular to the fibre axis. The absence of a ~9.6Å layer-line spacing in the diffraction patterns of most amyloids indicates a tendency to a parallel β-sheet structure.

However, due to the disorder in these specimens, an anti-parallel structure cannot be excluded.

Synthetic peptides corresponding to some portions of amyloidogenic proteins assemble into fibres with all the amyloid characteristics (Kirschner *et al.*, 1987). In particular, peptides from the Alzheimer's amyloid Aβ-protein form cross-β fibrils, but different fragments have shown both parallel (Benzinger *et al.*, 1998) and anti-parallel β-sheet structure (Halverson *et al.*, 1990; Serpell and Smith, 2000). The presumption is then that the Ab amyloid fibrils may contain both parallel and anti-parallel β-sheets.

The best characterized cross-β structure is the egg-stalk of the green lace-wing fly, *Chrysopa flava*. The X-ray fibre pattern (Geddes *et al.*, 1968) clearly shows the 9.48Å spacing diagnostic of the anti-parallel β-sheet, but diffraction on this layer-line is weak compared to the 4.74Å layer-line marking the hydrogen-bonded chain separation. An atomic model for the peptide backbone was constructed, but unlike the detailed fibre patterns obtained from TMV and filamentous phage, the *Chrysopa* silk pattern does not provide sufficient information to define the atomic structure. It is evident that even with some simple amyloid-forming peptides, using a variety of biophysical tools, it is proving difficult to obtain detailed information about the cross-β atomic structure that can be related to biologically critical properties of amyloid.

The synthetic heptapeptide GNNQQNY from the prion determinant sequence of the yeast Sup35 protein forms a gel that shows all the characteristics of amyloid aggregates, and crystallizes spontaneously in aqueous solutions (Balbirnie *et al.*, 2001). No conditions have been found to dissolve these crystals in the presence of water.

Materials and Methods

Peptide synthesis and crystallization. The peptide (Gly-Asn-Asn-Gln-Gln-Asn-Tyr) has been synthesized at the Chemistry Department of Florida State University and at the Biopolymer Synthesis Center of the California Institute of Technology using F-moc and T-boc chemistry respectively. The peptide was then purified by reverse phase chromatography, dissolving the peptide in 8M Guanidine Hydrochloride, and eluting with a 0-70% acetonitrile gradient. The fractions containing the peptide were immediately dipped in liquid Nitrogen and lyophilized. The purity of the powder was assessed by mass spectrometry to be greater than 98%, and sequencing of the peptide showed it to have the correct amino-acid composition. A sample of the lyophilized peptide was put in an X-ray beam in order to make sure that aggregation had not occurred up to this point. Suspensions containing microcrystals were prepared as described in Balbirnie *et al.* (2001); solubilization of the peptide in water to a final concentration about 50mg/ml produced a thick gel which showed the characteristic green birefringence of an amyloid aggregate complexed with Congo red when viewed between crossed polarizers.

X-ray powder diffraction. Samples for X-ray powder diffraction were prepared under different solvent conditions by placing a small drop of crystal suspension on a quartz capillary, and centrifuging the capillary softly to sediment the crystals to the bottom. After collecting an X-ray pattern at room temperature, a cold nitrogen stream was used to lower the temperature of the sample to ~100K, and another diffraction pattern collected. The sample was then brought to room temperature and the excess water removed. Pure ethanol was then added to the capillary and the suspension stirred, after which the sample was centrifuged and the supernatant (ethanol) removed. The process was repeated once, and the sample placed in the X-ray beam to collect powder diffraction data at room and liquid nitrogen temperatures. The same process was repeated to replace the ethanol with acetone.

In order to test the effects of drying on the microcrystals, another sample of the crystalline suspension was placed in an evacuated dessicator containing P_2O_5 for three days in order to emulate the conditions found in the column of the electron microscope, and X-ray diffraction patterns were collected at room and liquid nitrogen temperatures. The X-ray powder patterns were collected with a Rigaku generator, using a copper anode and recorded with either an R-axisII image plate detector or a MAR research CCD detector.

Electron diffraction. A 4µl drop of sample (1:4 crystal suspension) was placed on a copper grid with a continuous carbon film for about two minutes. The excess solution was then blotted and a drop (4µl) of 1% (w/v) dextrose applied to the grid and blotted immediately. The grid was then left to dry for about 10 minutes before inserting into the microscope. In

order to have an internal calibration standard, we used evaporated gold on some samples. However, the inclusion of evaporated metals in the support film was somewhat disruptive for the data collection, with the least disruptive combination being a sandwich of gold between two carbon layers.

The samples were placed in a cryo-holder and inserted into the column of the microscope, where they were observed at liquid Nitrogen temperature. The crystals used for electron diffraction data collection were elongated, with dimensions the order of 1μm in length, and about 1000Å in width and thickness. The electron diffraction patterns were collected using a slightly convergent beam to confine the irradiated area to a region not much larger than the crystal, and the diffracted area was further reduced with a selected area aperture to ~1000Å in diameter. Once a crystal was found, a diffraction pattern was collected, and if this pattern was seen to arise from a single crystal with no obvious mosaic spread, a tilt series was collected from it, with the number of patterns recorded being constrained mainly by radiation damage. A diffraction pattern was collected at 0° at the end of the process, to assess the radiation damage inflicted on the sample. Some of the tilt series were collected using small angular increments in order to determine the shape of the Bragg reflections, as well as the mosaicity of the crystals.

The electron diffraction data was initially collected on Kodak SO163 film plates with a Philips CM30FEG microscope using an accelerating voltage of 300kV, and later on a JEOL 400 microscope fitted with a 2048 x 2048 pixel slow scan CCD camera (Gatan, Inc.) at the Lawrence-Berkeley laboratory, using an accelerating voltage of 400kV. The camera length values used for the data collection were between 1 and 2.5m.

Indexing of the electron diffraction data. The electron diffraction data was converted to R-axis format in order to use software readily available for X-ray crystallography, such as Denzo (Otwinowski and Minor, 1996) and MOSFLM (Leslie, 1999). However, the autoindexing algorithms of these programs do not take into account the finite size of the Bragg reflections and produced inconsistent results. We attempted then to index the data simulating the shape of the spots to be ellipsoidal (Dimmeler and Schroeder, 2000), but found the simulations to be unsatisfactory. The data were indexed by hand, using at first the unit cell dimensions determined from the X-ray powder patterns. The use of these values produced systematic deviations in the indexing that were easily corrected by modifying the unit cell parameters slightly to make all the data self-consistent. In some of the tilt series, the presence of either **a*** or **b*** was evident, allowing us to determine directly the ratio of either **a***/**c*** or **b***/**c*** for that series, and given that **c*** shows little variation between the wet and the dried state, we were able to find accurate values for **a*** and **b***.

Profile of the Bragg reflections. In order to determine the profile of the Bragg reflections, we needed to map the intensities of some reflections in the direction of the beam. To this end, it is necessary to determine the orientation of the reciprocal lattice with respect to the Ewald sphere. When successive frames of a tilt series differ by a sufficiently small angle, a given reflection appears in several frames. This permits an accurate estimation of the tilt angle that would give the maximum intensity of that reflection. Since the positions in reciprocal space of the reflections are known, we are able to determine the orientation with which the Ewald sphere samples reciprocal space in each frame.

Processing of the X-ray powder diffraction patterns The powder diffraction patterns were converted to raw images, and centred by minimizing the difference between the diffraction pattern with its own image, rotated by 180°. The centred pattern was then converted to polar coordinates and the image collapsed in the azimuthal direction to produce an average radial profile, which was corrected for the effects of the sphere of reflection in order to convert the data from detector to reciprocal space. The patterns were indexed on a 2-dimensional lattice using the reflections corresponding to spatial frequencies lower than ~5Å, which belong to the hk0 plane, and then adding the appropriate **c**-dimension to account for all the observed reflections.

Results

Crystal morphology The peptide micro-crystals imaged in the electron microscope do not have the smooth appearance of a single crystal, but they always have striations running along their long axis (Fig. 1). The long axis has the ~4.8Å periodicity

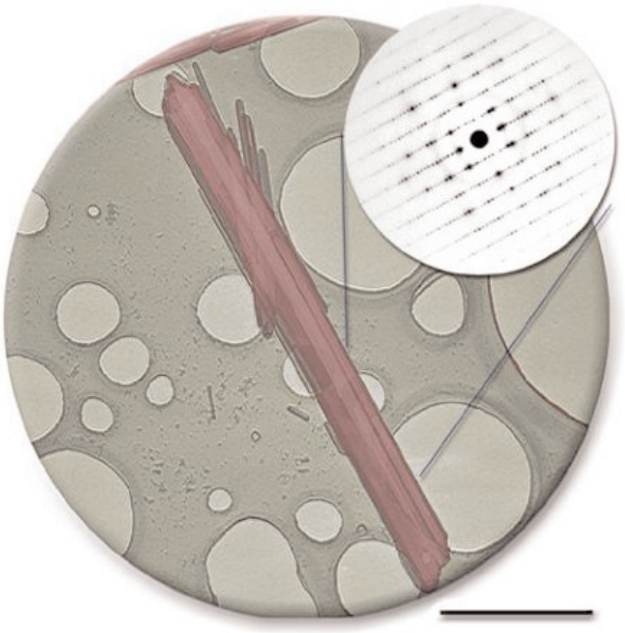

Figure 1. False colour electron micrograph of a peptide crystal, imaged over perforated carbon. The bar indicates 0.5μm. Some smaller crystals can be observed in the background. The long dimension of the crystal is the c-axis, which has a repeat distance of 4.86Å, corresponding to the hydrogen bonding between β-sheets. The inset shows the electron diffraction pattern of the indicated region.

typical of hydrogen bonding corresponding to a parallel β-sheet structure. The presence of Bragg reflections at high angles (corresponding to Bragg spacings of 1/(0.8Å) in Fig. 2A and (1/0.5Å) in Fig. 2D) indicates a high degree of order in the crystals. Smaller crystals with widths the order of 300Å can be easily found in the samples, which is consistent with the half-width measured from the reflections in the powder patterns collected at the synchrotron (Balbirnie *et al.*, 2001). On occasion, we have found crystals that yield diffraction patterns showing a continuous or nearly continuous intensity distribution along layer-lines, but with strong equatorial sampling (Fig.2C), suggestive of colloidal columnar crystalline ordering.

We collected in excess of 500 electron diffraction patterns from single crystals on film plates, and ten tilt series with the CCD camera at the Lawrence-Berkeley Laboratory, comprising a total of 280 diffraction patterns. Since the crystals lie on the grid with their long axes in the plane of the carbon film, but with these axes randomly oriented relative to the fixed tilt axis of the microscope, each tilt series samples a different region of the reciprocal lattice. Comparison of the diffraction patterns at the start and at the end of the tilt series shows the radiation damage to be noticeable after recording about 25-30 diffraction patterns, although we were able to collect up to ~45 patterns from a single crystal.

Unit cell dimensions The crystals always produced diffraction patterns (with X-rays and electrons) that can be indexed with an orthorhombic unit cell. From the X-ray powder patterns we found that the unit cell dimensions change slightly as a function of the solvent bathing the crystals, as summarized in Table 1. Axes **b** and **c** show little variability, while the a axis shows a variation the order of 1.4Å (~6%) at room temperature, and 0.92Å (~4%) at ~100K. The electron diffraction data show an even greater degree of variability. From the electron diffraction data collected at Berkeley, we measure |**a**| ~ 22.2Å. However, precise measurements that we have carried out with

Table 1. Unit cell values under different environmental conditions

Temperature (°K)	Solvent	a(Å)	b(Å)	c(Å)	V(Å^3)
300 X-rays	acetone	23.06	39.94	4.87	4490
	ethanol	22.98	39.88	4.89	4479
	water	22.93	39.95	4.89	4480
	dried	21.65	39.84	4.86	4192
100 X-rays	water + cryo-protectant†	22.6	39.4	4.88§	4345
	ethanol	21.97	39.95	4.88	4283
	water	22.69	39.68	4.87	4384
	dried	21.78	39.29	4.86	4159
EM	glucose (slow frozen)	21.2±0.2	39.4±0.24	4.87±0.02	4068±78
	glucose	21.8±0.3	39.4±0.3	4.87	4189
	glucose (fast frozen)	22.7±0.2	39.4±0.3	4.88±0.02	4353

§Indexing the strongest reflection as 021
†Balbirnie et al., 2001

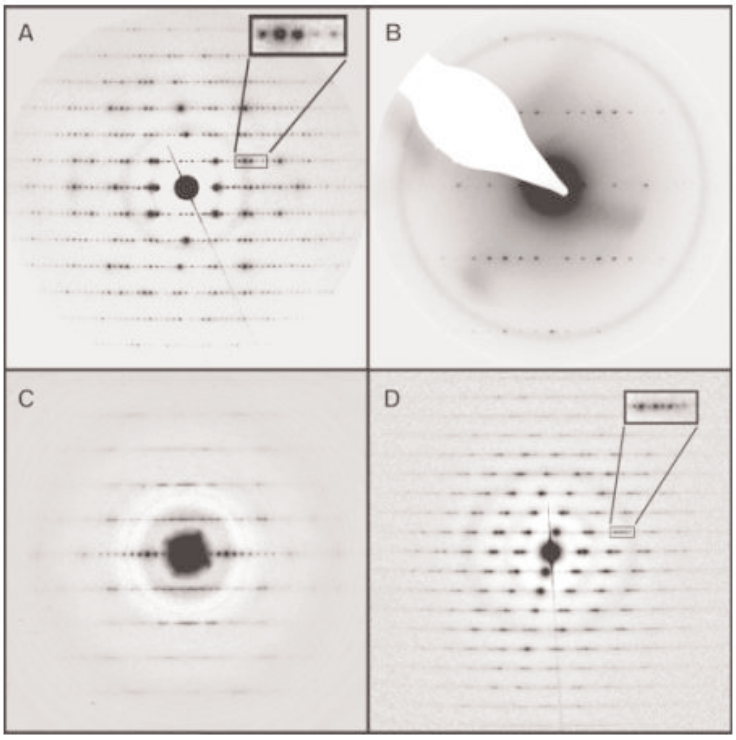

Figure 2. Gallery of electron diffraction patterns of the GNNQQNY peptide (the patterns are reproduced on different scales to illustrate particular features). The absence of any trace of a 9.4Å axial spacing unambiguosly rules out the possibility of an anti-parallel β-sheet structure in the crystals. **(A)** Typical electron diffraction pattern of a microcrystal. **(B)** Pattern of a crystal with the incident beam oriented very nearly along the **b**-axis, showing the systematic absence of reflections in the **a** and **c**-axes. The faint ring near the second layer-plane is due to evaporated gold, used as a calibration standard. **(C)** Pattern showing fibre-like (continuous transform) layer-lines. **(D)** ED pattern showing reflections extending to the 9th layer-line with ($1/0.53Å^{-1}$) Bragg spacing. The patterns shown in (A) and (D) were collected at the Lawrence-Berkeley Laboratory, while those shown in (B) and (C) were collected at FSU. The insets in (A) and (D) show the separation of the Bragg reflections.

evaporated gold included with the specimen have yielded values of |**a**| between 21.2 and 22.7Å. The difference in these measurements arises from the procedure followed for the data collection. The samples that gave the lower value for the **a** axis were inserted into the microscope column at room temperature, and cooled after they had been in the ultra high vacuum for a few minutes, whereas the samples that gave the larger value for the **a** axis were frozen to liquid Nitrogen temperature before being inserted into the microscope, and therefore retained more moisture. Thus the indication is that the spacing corresponding to the **a**-axis is related to the water activity.

Crystallographic space group The systematic absence of odd reflections in the h00, 0k0 and 00l directions (Fig. 2B) indicates that the crystals have $\mathbf{P2_12_12_1}$ symmetry. This implies that there are 4n monomers in the unit cell, and from volume and density considerations it is found that n=1 (Balbirnie *et al.*, 2001).

Shape of the Bragg reflections Analysis of the widths at half-maximum of the powder diffraction patterns collected at the synchrotron suggests a domain size the order of 300Å for the crystals that give rise to the pattern, consistent with the dimensions of the smaller crystals observed in electron micrographs. The determination of the width of the Bragg reflections in electron diffraction patterns is complicated by the fact that the relatively high energy of the 400 keV electrons produces a considerable amount of secondary electrons in the scintillator of the detector being used, blurring each Bragg reflection into several neighbouring pixels. However, the profile of the Bragg reflections in the direction of the beam was carefully determined for one series in which the angular step was small (1°), and we found it to be the order of $1/120\ Å^{-1}$. The fact that spots of comparable intensity (but different spacings) remain in reflecting position throughout the same number of frames indicates that the extent of the reflections increases as a function of the distance from the **c*** axis (Fig. 3).

Discussion

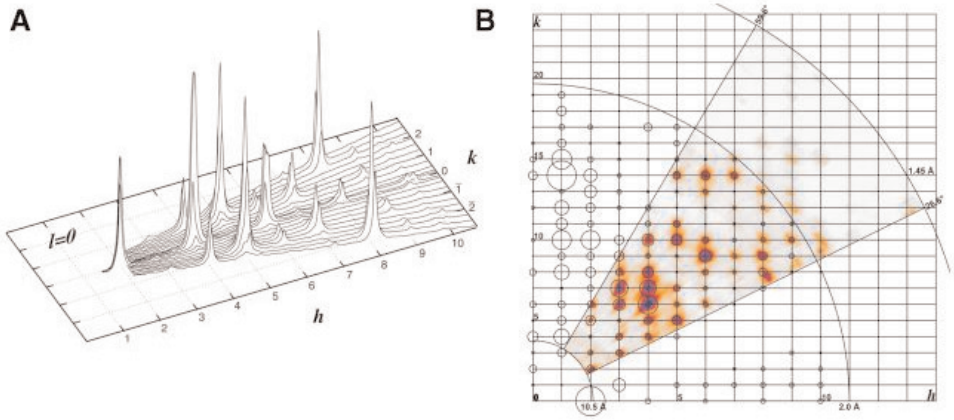

Figure 3. (A) Plot of the observed equatorial intensities throughout a tilt series that included the **a*** axis. The angular increment between frames was 1°, which amounted to ~0.73° in the equatorial plane. The spots show a considerable spread in reciprocal space. (B) Image of the intensities in a section of the HK0 plane, coloured according to the intensity. The circles at the reciprocal space locations have a diameter proportional to the intensity. This plot shows spots with an angular spread that increases with the distance from the origin.

Electron micrographs of the frozen hydrated suspension of crystals show that fibrils and thin sheets of peptide can coexist with the microcrystals (data not shown). The thin sheets have a variable width, and are long, with a morphology reminiscent of the larger microcrystals, only much thinner. Our attempts at collecting electron diffraction or high resolution images from these sheets have been unsuccessful so far. However, we have seen that these thin sheets tend to curl up or twist, giving the impression of fibrils that would have the characteristic signature of amyloids.

Some of the electron diffraction patterns show a colloidal crystalline character (Fig. 2C). The separation between the equatorial reflections in this pattern corresponds to a real space distance of 21.3Å, which is in the lower end of the length measured for the **a**-axis, but slightly larger than the width of a pair of β-sheets, which in the case of this peptide is ~19.7Å. This columnar crystalline pattern could arise from a regular lateral packing of protofilaments consisting of twisted paired cross-β sheets that are randomly rotated or axially translated relative to each other.

The presence of $\mathbf{P2_12_12_1}$ symmetry in the crystals imposes stringent constraints on the packing of the peptide in the unit cell. However, there is still some ambiguity to be resolved before producing a final atomic model for the crystal. At this point we favor a model that has four molecules per unit cell (Fig. 4), with the tyrosine rings face-to-face, related by a 2-fold screw axis. The peptide in this model has the backbone nearly along the **a**-axis, and the N-terminus located near the point (a/4, b/8, c/4). There must be a slight tilt of the backbone with respect to the **a**-axis (~7º), so as to weaken the intensities along the **b**-axis, while producing a strong (1,14,0) reflection. The side chains are nearly parallel to the **ab**-plane. The strong peak observed at 9.85Å in the X-ray powder patterns of the wet samples can be indexed as 220 and as 040. However, in the powder patterns of the dry samples the 040 and the 220 reflections are separated, and we can see that the 040 reflection contributes most of the intensity at that spacing (the 220 reflection occurs at a slightly smaller spacing in the dry samples). This suggests that the β-sheets are connected along the **b**-axis through side-chain contacts, spanning a distance of 9.85Å per monomer in the **b**-direction. There is little ambiguity about the nature of the peptide backbone structure viewed perpendicular to the **c**-axis, since it is the regularly hydrogen-bonded Pauling-Corey parallel β-sheet. The strongest reflection in both the electron diffraction and in the X-ray powder patterns occurs at 4.72Å. From the electron diffraction data, we identified this reflection as the 021. In our model, this reflection arises from the contacts made by the amide groups of the side-chains, which are forming ladders similar to those observed for polyglutamine specimens (Perutz, 1999). The arrangement of the peptide monomers in the unit cell is suggestive of a pair of protofilaments, in which a protofilament consists of one of the pairs of β-sheets, which would form a spiral with a pitch of 4.86Å, a width of ~30Å and a thickness ~20Å, resembling the packing of β-sheets

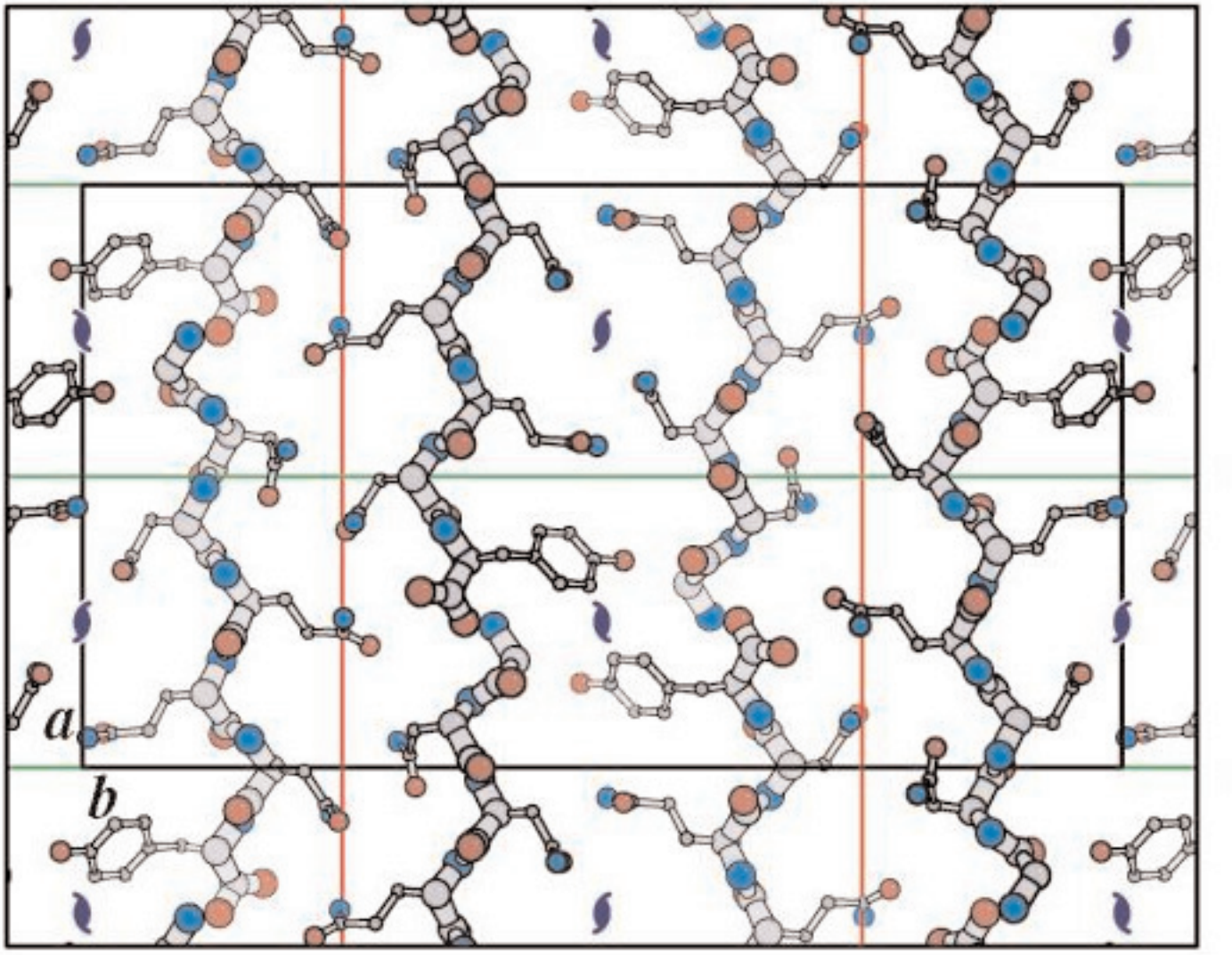

Figure 4. Schematic diagram of the packing of the peptide in the crystals, viewed along the **c**-axis. The presence of $\mathbf{P2_12_12_1}$ symmetry implies four peptide molecules per unit cell. The peptide backbone in this model is slightly tilted from the **a**-axis, and the tyrosine's are in close contact due to the presence of a 2-fold screw axis along **c**.

in pectate lyase (Yoder *et al.*, 1993).

The diffraction spots are slightly thinner in the meridional direction (~1/100Å) than in the equatorial (~1/80Å), indicating that the correlation length is larger in the **c**-direction than in the ab-plane. In the azimuthal direction we observe a half width ~1/140Å. The measurement in the azimuthal direction is independent of artifacts of the CCD detector used for the electrons. We found the width of the spots at half maximum to be variable and not clearly correlated with the intensity of the spot, or its corresponding spatial frequency. The shape of the spots might be perturbed by the presence of inelastic scattering (Spence, 1993).

One of the most interesting properties of this peptide, is the fact that it has eluded all efforts to produce large crystals suitable for single crystal X-ray crystallography. A tendency to form crystals of limited size might be an inherent property of the β-sheet packing, since β-sheets have a natural tendency to curve, and therefore being in an extended conformation might introduce a cumulative strain that hampers the growth of large crystals, as observed for the crystals of sickle cell hemoglobin (Mu *et al.*, 1998)

The use of electron scattering data for *ab initio* structure analysis has several potential pitfalls, such as dynamical scattering, secondary scattering and crystal bending (Dorset, 1995). However, all the information that we need to see the packing of the peptide in the crystal is contained in the hk0 reflections, since in the **c**-direction the structure connected in a predictable manner by hydrogen bonds. We have collected electron diffraction intensities that sample the hk0 plane to ~2Å, but

some of the reflections show non-trivial departures from Friedel's symmetry, indicating a perturbation on the data. Therefore more experiments are needed to ensure that the observed intensities are self-consistent.

Density measurements (Balbirnie *et al.*, 2001) show that the peptide occupies 93% of the volume in the unit cell, which translates to ~2.5 to 3.5 water molecules per peptide. However, calculations of the molecular volumes using the typically observed volumes for Gly, Asn, Gln and Tyr in protein crystals (Tsai *et al.*, 1999), give a peptide volume between 915 and 936Å [3], and consequently, between 4.5 and 5.5 water molecules per peptide in the unit cell. This discrepancy suggests that the side chains in the peptide are forming hydrogen bonds directly with the side chains from the neighboring peptide, largely excluding water in the process. A relatively large activation energy would be required to disrupt this network of hydrogen bonds, pointing to a possible explanation of the stability of the cross-β structures.

Acknowledgements

We would like to acknowledge the help from Drs. Ken Downing and Huilin Li for making the facilities at the LBL available to us, as well as for helpful discussions. This work was supported by NIH grant NS 42221 to D.L.D. Caspar.

References

[1] Adrian, M., Dubochet, J., Lepault, J. & McDowall, A.W. (1984). Cryo-electron microscopy of viruses. *Nature* **308**, 32-36.

[2] Astbury, W.T., Dickinson, S. & Bailey, K. (1935). The X-ray interpretation of denaturation of the seed globulins. *Biochem. J.* **29**, 2351-2360.

[3] Balbirnie, M., Grothe R. & Eisenberg, D.S. (2001). An amyloid-forming peptide from the yeast prion Sup35 reveals a dehydrated β-sheet structure for amyloid. *Proc. Natl. Acad. Sci.* **98**, 2375-2380.

[4] Benzinger, T.L.S., Gregory, D.M., Burkoth, T.S., Miller-Auer, H., Lynn, D.G., Botto, R.E. & Meredith, S.C. (1998). Propagating structure of Alzheimer's β-amyloid (10-35) is parallel β-sheet with residues in exact register. Proc. Natl. Acad. Sci. 95, 13407-13412.

[5] Bonnar, I., Cohen, A.S. & Skinner, M. (1969). Characterization of the amyloid fibril as a cross-β protein. Proc. Soc. Exp. Biol. Med. 131, 1373-1375.

[6] Dorset, D. (1995). Structural electron crystallography. Plenum Press, New York.

[7] Dimmeler, E. & Scroeder, R.R. (2000). Global least-squares determination of Eulerian angles from single electron diffraction patterns of tilted crystals. *J. Appl. Cryst.* **33**, 1088-1101.

[8] Eannes, E.D. & Glenner, G.G. (1968). X-ray diffraction studies on amyloid filaments, *J. Histochem. Cytochem.* **16**, 673-677.

[9] Geddes, A.J., Parker, K.D., Atkins, E.D.T. & Brighton, E. (1968). 'cross-β' conformation in proteins. *J. Mol. Biol.* **32**, 343-358.

[10]. Halverson, K., Fraser, P.E., Kirschner, D.A. & Lansbury, P.T. (1990). Molecular determinants of amyloid deposition in Alzheimer's disease. Conformational studies of synthetic beta-protein fragments. *Biochemistry* **29**, 2639-2644.

[11] Kirschner, D.A., Inouye, H., Duffy, L.K., Sinclair, A., Lind, M. & Selkoe, D.J. (1987). Synthetic peptide homologous to β-protein from Alzheimer's-disease forms amyloid-like fibrils *in vitro*. *Proc. Natl. Acad. Sci.* **84**, 6953-6957.

[12] Leslie, A.G.W. (1999). Integration of macromolecular diffraction data. *Acta Cryst*. **D55**, 1696-1702.

[13] Mu, X.-Q., Makowski, L. & Magdoff-Fairchild, B. (1998). Analysis of the stability of hemoglobin S double strands. *Biophys. J.* **74**, 655-668.

[14] Otwinowski, Z. & Minor, W. (1996). Processing of X-ray diffraction data collected in oscillation mode. *Methods in Enzymology* **276**, 307-326.

[15] Perutz, M. (1999). Glutamine repeats and neuro-degenerative diseases: molecular aspects. TIBS 24, 58-63.
Rudall, K.M. (1952). The proteins of the mammalian epidermis. *Adv. Prot. Chem.* **7**, 253-290.

[16] Serpell, L.C. & Smith, J.M. (2000). Direct visualisation of the β-sheet structure of synthetic Alzheimer's amyloid. *J. Mol. Biol.* **299**, 225-231.

[17] Spence, J.C.H. (1993). On the accurate measurement of structure-factor amplitudes and phases from electron diffraction. *Acta Cryst.* **A49**, 231-260.

[18] Tsai, J., Taylor, R., Chothia, C. & Gerstein, M. (1999). The packing density in proteins: standard radii and volumes, *J. Mol. Biol.* **290**, 253-266.

[19] Yoder, M.D., Keen, N.T. & Jurnak, F. (1993). New domain motif - the structure of pectate lyase-C, a secreted plant virulence factor. *Science* **260**, 1503-1507.

Type-4 bacterial pili: molecular models and their simulated diffraction patterns

D. A. Marvin[1]*, K. Nadassy[1], L. C. Welsh[1] and K. T. Forest[2]

[1] Department of Biochemistry, University of Cambridge, Cambridge CB2 1GA, UK
[2] Department of Bacteriology, University of Wisconsin, Madison WI 53706, USA

*Corresponding author: d.a.marvin@bioc.cam.ac.uk

ABSTRACT

Bacterial pili are long thin assemblies of pilin protein subunits, that extend outwards from the surface of bacteria and are involved in interaction of bacteria with their environment, notably attachment of pathogenic bacteria to their host and "twitching motility" of bacteria along surfaces. Pili are about one-third the diameter of bacterial flagella. Some types of pili are the adsorption sites of filamentous bacteriophage. X-ray fibre diffraction patterns of type-4 pili are classical α-helix patterns, with strong intensity in the equatorial direction at about 10 Å and in the meridional direction at about 5 Å. The crystal structure of the type-4 pilin subunit has a highly conserved ~50-residue N-terminal α-helix and a less conserved ~100-residue globular C-terminal domain, and this subunit structure has been used to construct models of type-4 pili in which the N-terminal α-helix of the pilin forms the central core of the pilus . We find that the calculated fibre diffraction patterns predicted for these models are less similar to the observed diffraction patterns than diffraction patterns predicted for models built from only the N-terminal α-helix portion of the subunit. Disorder in the globular domain may be one explanation for this effect, and the globular domain of pilin in pili may be "intrinsically unstructured" as found for binding regions of some globular proteins. Twitching motility and phage infection proceed by retraction of pili, probably involving dissolution of pilin at the base of the pili into the host cell membrane, reminiscent of the process of filamentous phage infection by disassembly of the phage subunits into the membrane.

Introduction

Pili are filamentous polymers of protein subunits extending from the surface of Gram-negative bacteria. They are about 50-100 Å in diameter, depending on the type of pili, significantly thinner than bacterial flagella. Many different types of pili have been identified. Pili of one type, type 4 pili (Tfp) have been extensively studied, especially because of their medical importance. Tfp interact with target mammalian cells in the first step of bacterial infection. They function in part by 'retraction': after the pilus attaches to the target, it withdraws into the bacterial cell, probably by depolymerization of the pilin subunits at the base of the pilus into the bacterial inner membrane, thereby drawing the bacterium to the attachment site. This retraction mechanism is also involved in 'twitching motility' of bacteria across surfaces, and in the infection mechanism of some filamentous bacteriophages. (For reviews see [1-5]).

X-ray fibre patterns of PAK and PAO Tfp from *Pseudomonas aeruginosa* bacteria show the strong 10 Å equatorial and 5 Å meridional intensity typical of a-helix assemblies [6]. These patterns also show orders of an apparent 41 Å layer-line periodicity. The determination of the crystal structure of the pilin subunit of MS11 Tfp from *Neisseria gonorrhoeae* bacteria [1,7,8] has opened the way for a major advance in the analysis of pili structure. The MS11 pilin has a ca. 50-residue a-helix at the N-terminus, a region that is highly conserved across different Tfp, and a ca. 100-residue globular four-stranded antiparallel β-sheet region at the C-terminus, a region that is less conserved. The structure of the globular region of Ps. *aeruginosa pilin* has been determined by x-ray crystallography for PAK pilin [9] and by NMR for K122-4 pilin [10], and has a largely β-sheet structure homologous to the corresponding region of MS11, but with some differences in the fold of the polypeptide chain. One would like to build the high resolution pilin structure into the symmetry determined from the lower resolution fibre patterns of pili, and thereby to determine how the pilin molecules are packed within the pilus filament. The proposal that the α-helix portions of pilin molecules pack together at the core of the pilus with the globular portion on the outside (7) is probably correct in general, but there are some

limitations to the current fibre diffraction data, and therefore there is some uncertainty about the details of the pilus helix parameters and even the hand of the pilus helix.

Materials and Methods

Experimental fibre diffraction. PAK pili were prepared and purified from *Pseudomonas aeruginosa* type K [6]. PAK fibre F28A was prepared by Dr. Waltraud Folkhard. A 3 µl drop of a 100 mg/ml gel of purified pili was suspended between the tips of two glass rods about 1.6 mm apart and dried under humidity control over 10 days; the fibre was stretched slightly several times during the first 5 days. The fibre was then stored for 20 years at room temperature and humidity. MS11 pili were prepared and purified as described [11], and fibres were prepared essentially as for PAK. Each fibre was dusted with Si powder to give a calibration ring at 3.136 Å, and diffraction patterns were obtained at the Synchrotron Radiation Source, Daresbury Laboratory on station 7.2 with a wavelength of 1.488 Å, at room temperature and humidity. See [12-15] for further details of our diffraction methods.

Building models and calculating simulated diffraction patterns. To generate coordinates of a reconstituted full PAK pilin molecule, we superimposed residues 30 to 51 of the truncated PAK model 1DZO [9] onto the corresponding residues of the MS11 model 2PIL [8], and added the coordinates of residues 1 to 30 of 2PIL to those of residues 31 to 144 of 1DZO. We then applied the matrix given for 2PIL [8] to move this model into the frame of reference of the pilus helix. We then applied integral multiples of the appropriate [unit twist, unit rise] (e.g., [72°, 8.2 Å] for a 5 units/turn right-handed helix) to generate a segment of pilus. When displaying the pilus models, we truncate at upper and lower axial (z) values, to give a representation of a slab sliced from a long pilus. For other types of model, we generated residues 1 to 50 as gently-curved α-helices with various orientations and shapes using the methods developed for filamentous phage [13]. We based some of our models on unpublished model-building studies of PAK carried out by Dr. Tania Watts at EMBL Heidelberg in 1981-1982; see also [6,16,17].

In the region of the diffraction pattern corresponding to spacings greater than about 10 Å, the reduced contrast between the solvent and the molecule reduces the observed diffracted intensity relative to that expected for a molecule in vacuum. We calculated the helix transform of the pilus including the solvent as described for filamentous bacteriophage [14]. We generated simulated fibre diffraction patterns from the calculated continuous molecular transform essentially as described [14], but using the program LSQINT (www.ccp13.ac.uk) to generate the simulated diffraction pattern to a reciprocal space radius of 0.32 $Å^{-1}$. We did not model the observed crystal lattice sampling in the inner equatorial region, so all our simulated patterns show strong J_0 transform in this region, which can be disregarded.

Fibre diffraction patterns generally show lines of intensity, the layer lines, and measuring the positions of these lines gives information about the helix parameters. On the PAK patterns, there is a clear layer line at 41 Å, with near-meridional intensity, and we take this as the helix pitch [6]. Better-aligned patterns would enable the distribution of continuous transform intensity along the layer lines to be measured and compared quantitatively with the intensity distribution predicted by models. If intensity changes due to heavy-atom derivatives can be measured, these intensity changes could give further information about the helix parameters.

There are various types of disorder that can smudge out layer lines. These include disorientation (not all filaments in the fibre lie parallel to one another) and limited coherence length (the regular helix extends for only a short distance along the filament). These two kinds of disorder can be modelled with the CCP13 program LSQINT, so given a hypothesis about the structure and about the nature of the disorder in the fibre pattern, one can model the predicted diffraction pattern and compare it with the observed diffraction pattern. After several trials for disorder in our simulated PAK diffraction patterns, we chose the width of the disorientation distribution (awid) as 13° and the coherence length (1/zwid) as 500 Å. There are other kinds of disorder that are not so easy to model, for instance the helix parameters may vary along the length of the pilus, so slightly different helix diffraction patterns are superimposed.

Units per turn. In order to build any detailed model, it is necessary to know the 'unit rise' of the helix; that is, the average distance from one subunit to the next along the helix axis. It is seldom possible to

determine this directly from the fibre diffraction data. Instead, one can determine, in separate experiments, the mass of the subunit and the mass per length of the helix. Then unit rise = (mass of subunit)/(mass per length of helix). The number of 'units per turn' (u/t) = (helix pitch)/(unit rise). Note that in principle u/t need not be integral, but a non-integral u/t will affect the pattern of layer lines, and the analysis of the PAK and PAO pili diffraction patterns [6] suggests that u/t is integral or near-integral. We take the helix pitch in this case as defined by the 41 Å near-meridional reflexion on the PAK fibre patterns. In 1981, neither the mass of the pilin subunit nor the mass per length of the pilus was known accurately. To determine the volume of the pilus repeat, the side *a* of the hexagonal unit cell in the fibre was measured as a function of water content of the fibre, and extrapolated to zero water content. These measurements are accurate to better than 1%, and have an internal control, a crystal powder on the fibre that gives a calibration ring of known spacing. Both PAK and PAO extrapolate to a = 52 Å at zero water content [6]. The cross-sectional area of a hexagonal unit cell with a = 52 Å is 2342 Å2. The volume of the pilin was estimated from the amino acid composition and estimates of amino acid volumes, as described for filamentous phage [12], and for 41 Å pitch, the calculation [6] gave u/t = 4. The molecular weight determined from the sequence [17] was found subsequently to be about 20 % smaller than previously estimated, so the estimate of u/t for PAK was increased from 4 to 5 [17]. This estimate was also used for molecular models of MS11 pili [7,8].

To get a better (but still poor) estimate of u/t for PAK, we have calculated the volume of a PAK pilin subunit reconstructed from the PAK globular portion and the MS11 α-helix portion, using VOIDOO [18] with a 0.4 Å probe radius (this radius, which is smaller than the 1.4 Å usually used in calculating water exclusion, was chosen by analogy with the value found for Pf1 filamentous phage [12]), giving 1.90×10^4 Å^3 for the volume of PAK pilin, so for a 41 Å pitch, u/t = 5.1. For MS11 we have not yet taken diffraction patterns at a series of water contents, but we used the value a = 55.9 Å from a pattern taken at low humidity. The cross-sectional area of the unit cell is then 2706 Å^2. Using VOIDOO we calculate 2.14×10^4 Å^3 for the volume of MS11 pilin, so for a 41 Å pitch, u/t = 5.2. We have tried both u/t = 4 and u/t = 5 in our model building, and left-handed as well as right-handed pilus helices. As found for filamentous phage, an integral change in the number of units per turn, or reversing the hand of the helix, makes little difference to the low resolution simulated diffraction pattern. If there are fewer units per turn the subunit will be at a smaller radius, to maintain the packing density, and contacts between overlapping subunits separated by one pitch length in the axial direction can be maintained by changing the slope of the α-helix [13].

Once one knows the helix symmetry, has well-resolved layer lines, and has measured the intensity distribution along the layer lines, one could use automatic refinement methods, as a kind of molecular replacement, to build the pilin molecule into the pilus symmetry. This would require fitting the molecular transform of the subunit to the observed fibre data, including stereochemical constraints with the possibility of some flexibility within the subunit, especially in the α-helix rod. This kind of automated refinement would require that the initial model be within the radius of convergence of the refinement method, and would work best when the helix parameters are known with certainty. We are not yet at this stage of the structure analysis, and our models must be considered as very preliminary.

A note on nomenclature: in fibre diffraction, the word 'fibre' refers to the macroscopic bundle of filaments that is put into the X-ray beam, analogous to 'crystal' in protein crystallography. Some authors have used 'fibre' to refer to the individual pilus, but this can lead to confusion, and it is better to use 'filament' or 'fibril' or indeed 'pilus' to refer to the individual pilus.

Results

Our fibre diffraction patterns of PAK and MS11 (Figure 1) are similar to those previously reported [6] for PAK and PAO pili. There is strong equatorial and near-equatorial intensity at about 10 Å, and strong meridional intensity at about 5 Å, suggesting a substantial fraction of α-helix oriented at a small angle to the fibre axis. There is meridional and near-meridional intensity that can be indexed as orders of a 41 Å layer-line spacing. (As pointed out [6], this spacing increases slightly with increased humidity, from about 39 Å to about 41 Å). But the MS11 pattern shows several interesting differences in detail from that of PAK. There is off-meridional intensity that cannot be indexed on the 41 Å layer-line spacing, suggesting the possibility of a pilus helix

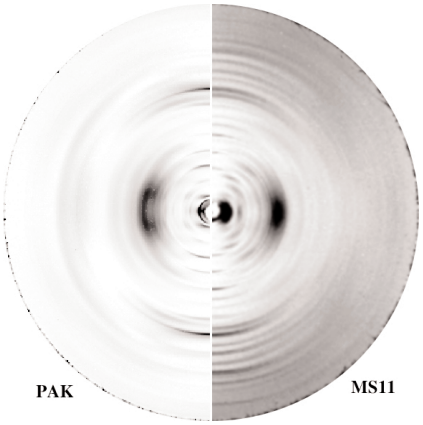

Figure 1. X-ray fibre patterns of type 4 pili. Left, PAK, fibre number F28A; right, MS11. Patterns are shown in detector space. Fibre axis is vertical. The outer radius of the patterns is about that of the calibration ring (about 3.1 Å).

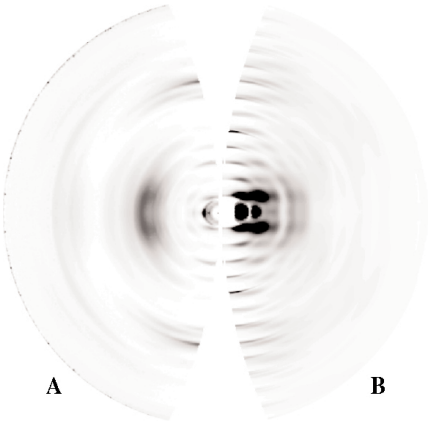

Figure 2. A. Observed diffraction pattern of PAK pili, transformed to reciprocal space. B. Simulated fibre diffraction pattern of a PAK model, residues 1 to 50 of 2PIL (MS11) combined with residues 51 to 144 of 1DZO (PAK) and transformed into the frame of reference of the pilus helix using the matrix and vector given in PDB entry 2PIL. Both the simulated and the observed patterns extend to about 3.1 Å.

with a non-integral number of units per turn in the 41 Å repeat. Moreover, the 10 Å equatorial region of PAK is stronger on $l = 1$ than on the equator ($l = 0$), whereas the corresponding region of MS11 seems strongest on $l = 0$. These differences in detail are reminiscent of differences between fibre patterns of class I and class II filamentous bacteriophage [12,14] that result from differences in packing of otherwise similar subunits within the bacteriophage helix [19]. The differences between the MS11 and PAK diffraction patterns suggest the possibility of interesting differences between the assembly of these otherwise similar proteins. However, in the absence of detailed data, we follow ref. [7] in applying the helix parameters of PAK to the preliminary analysis of MS11.

Modelling the pilus structure. At low resolution, the pilin can be considered as an α-helix rod with a globular portion at the C-terminal end. The position and orientation of the rod is fairly well defined by the 10 Å equatorial and near-equatorial intensity, and this will not be significantly affected by variation in the pilus helix parameters. There is little higher resolution off-meridional detail, suggesting that the globular portion does not contribute much to the diffraction pattern.

To test the validity of PAK models, we calculated simulated diffraction patterns to compare with the observed PAK diffraction pattern. As a first trial, we used the coordinates 1DZO of the PAK globular domain, spliced to the α-helix domain of the 2PIL MS11 model, and transformed into the position of a subunit in the MS11 helix using the matrix given in PDB entry 2PIL. The orientation of the globular domain with respect to the pilus axis is unchanged by this transformation, and in particular the hydrophobic residues still face inwards, and pack against the hydrophobic α-helix. The simulated diffraction pattern of this model has several flaws (Figure 2). There is little predicted intensity at the 10 Å equatorial position; and there is detailed predicted intensity on higher layer lines, even after applying corrections for disorder, whereas little detail is present in this region on observed patterns. Also the pattern of calculated intensity on the meridional series of reflexions is not the same as on the observed pattern. The absence of the 10 Å intensity suggests that the orientation and/or packing of the α-helix rod needs to be altered; and the calculated detail on higher layer lines suggests that further (not modelled) disorder may be present. The poor simulated pattern is not just a consequence of combining information from PAK and MS11 models, since we find that a simulated diffraction pattern of a pure MS11 model also is a poor fit to the observed MS11 pattern (calculation not shown).

The MS11 subunit α-helix domain is rather twisted, and in the MS11 pilus model the neighbouring α-helices are not in regular close contact along their length (see Figure 1 of ref. 1). The 10 Å equatorial region of an α-helix diffraction pattern arises from close packing of the 10 Å-diameter α-helices, and the curvature of the MS11 subunit prevents close packing. But an extended free-standing α-helix is relatively flexible and can be bent without distorting the internal stereochemistry. Thus we modelled the packing of the α-helix portion separately from the globular portion, and attached the globular portion

after the α-helix packing was established. We used the methods developed for building models of the filamentous phage subunit [13,19] to build a gently-curved α-helix domain with the sequence of PAK residues 1 to 50; the shape and orientation of the subunit in the pilus were chosen to give good local packing between α-helices. We added this to the globular domain, to generate a new model of the PAK pilus (Figure 3). The α-helices are close-packed in the 0-5 direction, that is, parallel to the pilus axis, beween subunits separated by one turn of the 41 Å pitch pilus helix, but they are not as close-packed in other directions. The simulated diffraction pattern of this model (Figure 4) has a stronger 10 Å equatorial region than that of Figure 2, but is still flawed in other ways, especially in predicting non-observed diffracted intensity.

We considered that the globular domain of the subunit might be substantially disordered, but we were unable to improve the simulated diffraction pattern by modelling this disorder, either by increasing the temperature factor of the atoms in residues 51 to 144 to B = 100 $Å^2$, or by replacing the globular domain by a low resolution diffuse electron density distribution. Fibre diffraction patterns of PAK pili studied as a function of water content over the range 0% to 98% relative humidity show an increase in unit cell volume of 50% but no appreciable increase in order [6], so the absence of order is unlikely to be due to distortion of the pilus surface as a result of close packing in dry fibres. We also tried models with u/t = 4 rather than u/t = 5, and left-handed rather than right-handed pilus helices, but these models also gave simulated diffraction patterns with low intensity in the 10 Å equatorial region where observed intensity is strong, and high

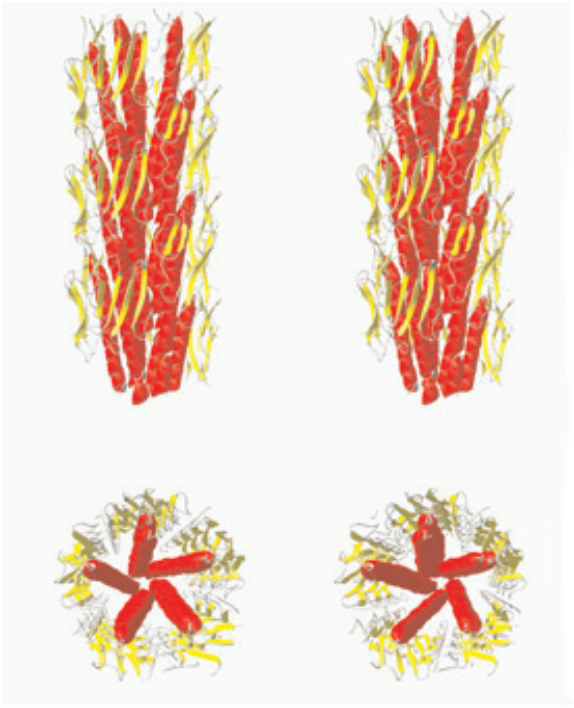

Figure 3. Model of PAK. Residues 1 to 50 of a gently-curved α-helix (with the MS11 sequence) were combined with residues 51 to 144 of 1DZO (PAK) and transformed into the frame of reference of the pilus helix using the matrix and vector given in PDB entry 2PIL. Ribbon representation. The α-helix is in red and the β-sheet in yellow. Slab 100 Å long in the axial direction. Stereo pairs. **Top**: view from the side of the pilus. **Bottom**: view down the axis of the pilus. This figure was prepared using Swiss-PdbViewer [26] (www.expasy.org/spdbv).

intensity in regions where observed diffraction is weak. Only one type of model gave a simulated diffraction pattern that looks similar to the observed: a model with the globular domain entirely removed, and the longer sidechains on the α-helix replaced by Ser, effectively assuming that everything except the α-helix backbone is so disordered that it blends into the solvent background (Figure 5). This type of

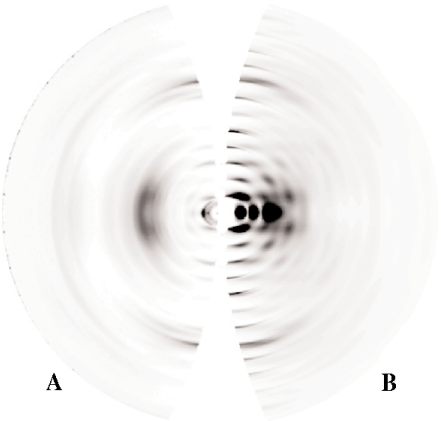

Figure 4. A. Observed diffraction pattern of PAK pili, transformed to reciprocal space. **B**. Simulated fibre diffraction pattern of the PAK model of Figure 3.

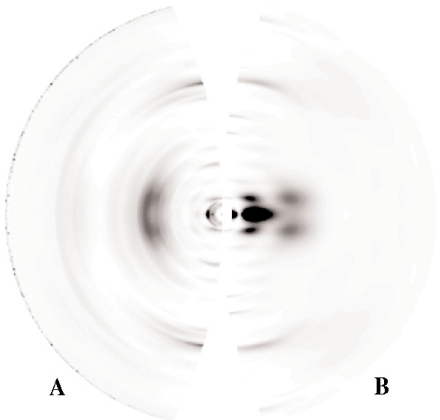

Figure 5. A. Observed diffraction pattern of PAK pili, transformed to reciprocal space. **B**. Simulated fibre diffraction pattern of the α-helix region only (residues 1 to 50) of the PAK model of Figure 3, with the larger sidechains replaced by Ser.

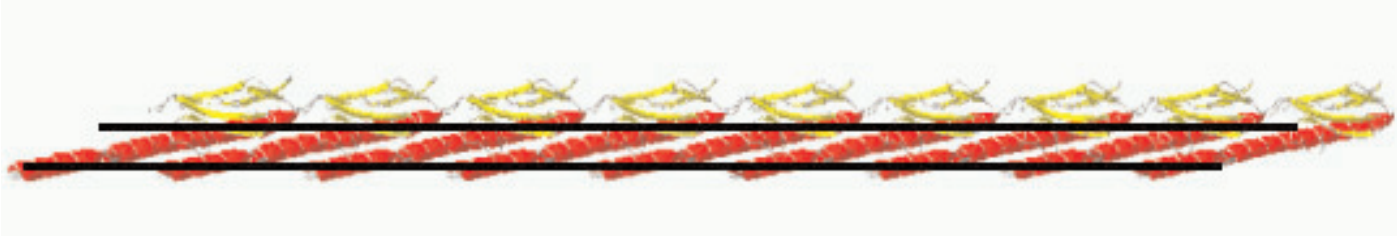

Figure 6. The subunits of a single 0 to 5 helicoid of the model of Figure 3 were generated by translating the subunit parallel to the pilus axis by integral multiples of 41 Å, and the assembly was rotated to represent a horizontal layer in the membrane. The thick black lines are about 25 Å apart, and represent the thickness of the hydrophobic region in the lipid bilayer. The globular C-terminal region at the top is in the periplasmic space, and the N-terminus of the α-helix region is in the cytoplasm [2].

model is reminiscent of "intrinsically disordered" regions in some globular proteins [20], although NMR solution studies of the globular domain of the K122-4 strain of Ps. *aeruginosa* Tfp pili do not suggest any unusual disorder [10]. In low-resolution single-crystal studies of globular proteins, the α-helix regions are often better defined than other regions.

From native fibre diffraction data alone one cannot determine the hand of the pilus helix, or the direction in which the α-helix wraps around the pilus helix axis. Models of different hands (but otherwise unchanged) are indistinguishable at low resolution. Moreover, instead of interpreting the 41 Å repeat as the pitch of a 5 units per turn helix, one could say that it corresponds to a group of 5 subunits related by a 5-fold rotation axis that coincides with the pilus axis. Such a model predicts meridional reflexions every 41 Å, which are not observed, although there could be special reasons for their absence. It is also conceivable that the asymmetric unit in the pilus helix is a pair of pilin subunits, related by a diad, as found for isolated pilin solubilised in octyl glucoside [17], and as found in the crystal structure [7], but this type of model would raise difficult questions about the mechanism of pilus assembly.

Discussion

Despite the imperfections in our model of pili, we can make some hypotheses about pili assembly and pili retraction. Possible mechanisms for pili retraction have been discussed [2-5,21]. Two separate questions arise: the nature of the retraction mechanism, presumed to occur at the base of the pilus; and the way in which the attachment of the pilus outer tip to the target transmits a signal to the base, to activate the retraction mechanism.

We propose a model for the assembly and retraction of pili that is based in part on the model for assembly of filamentous bacteriophage from α-helical subunits that reside in the bacterial inner membrane before assembly [22]. Assembly of filamentous bacteriophage and Tfp are both examples of the type II secretion system, involving assembly at the inner membrane followed by transport through a pore in the outer membrane [23]. Our model makes use of a fact from differential geometry, that a toroid can be deformed into a helicoid with no deformation of local geometry (for instance, see mathmuse.sci.ibaraki.ac.jp/deform/DeformationE.html). One can draw a set of helicoids through the α-helix axes of the pilin subunits in the Tfp model of Figure 3. One of these helicoids is illustrated in Figure 6. If the pilin subunits in the membrane pre-assemble side-by-side into ribbons in the membrane, then a set of these ribbons could twist out of the membrane into the pilus with little change in local contacts within

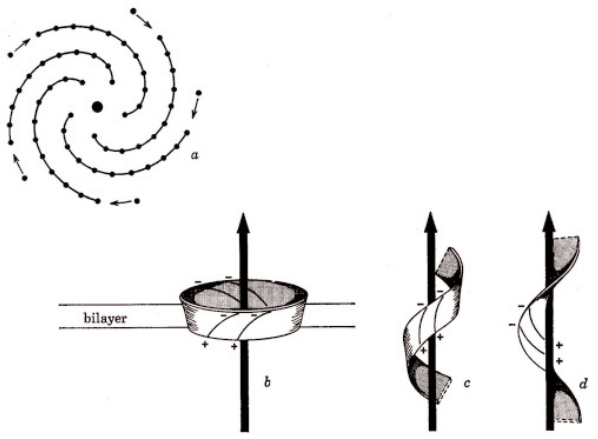

Figure 7. Schematic representation of how a set of ribbons in the membrane can be transformed into a set of helicoids in the pilus with minimal local distortion of the contacts between pilin subunits within the ribbon. (a) Top view of pilin in the membrane; dots represent individual pilin subunits, pre-assembled with contacts between α-helices within the membrane being the same as within the 0-5 ribbons of the pilus. (b-d) Transformation of a catenoid (b) to a helicoid (d). The catenoid, slit down one side and opened out, would correspond to one of the spirals in (a); the helicoids would correspond to one of the 0-5 ribbons in the pilus. The individual subunits are represented as curves on the ribbon; the (+) signs represent the N-terminus and the (-) signs represent the C-terminus. (After [22]).

the ribbon (Figure 7). For pilus retraction, the helicoids would convert back into ribbons in the membrane. The hydrophobic contacts between adjacent ribbons in the pilus would not be the same as the hydrophobic contacts between ribbons and lipids in the membrane, but they would be similar. A slight change in the helix parameters of the pilus, as a result of specific binding at the pilus tip, for instance like the transition caused by a slight temperature change of Pf1 filamentous phage [15], might change the contacts between ribbons in the pilus sufficiently to change the entropically favoured structure from 'ribbons in pili' to 'ribbons in membrane'. This mechanism could be classed as a 'Brownian ratchet' [5,21]. The random Brownian motion of the ribbons would be rectified in one direction or the other by the difference in entropy between the 'ribbons in the membrane' and the 'ribbons in pili'. This model for pili assembly and retraction does not depend on the details of our structural model for pili, but only on the general feature that α-helices are close-packed at the core of the pilus.

Conclusions

We need an accurate determination of mass/length, to combine with the known mass of the pilin subunit, to decide the number of units per turn in PAK and MS11 pili, to be able to build detailed models of pili. We need better quality fibre diffraction patterns of native and mutant pili of the various types, especially MS11 and PAK. The relatively poor quality of the fibre diffraction patterns suggests disorder, and the effects of various kinds of disorder can be analysed theoretically [24,25], but it is likely to be more productive to search for experimental methods to reduce this disorder. One needs to try many different conditions for making fibres: chemical (salt, pH, non-ionic detergents, in vitro reassembly); physical (temperature, shear, magnetic field, electric field); and biological (different natural strains; constructed mutants in the pilin sequence which might affect the alignment in the fibre, for instance mutants that form rigid pili, or pili that aggregate less readily; mutants that hyperproduce pili). In some ways surveying fibre formation is more difficult than surveying conditions for crystallizing a protein, because one usually gets a fibre no matter what the conditions, and one needs to take a diffraction pattern of every fibre to see its quality. Mutants of pili could be surveyed for altered morphology by electron microscopy in the first instance. Image reconstruction from electron micrographs of unstained samples imbedded in ice might be another approach to determine the relation between pilin molecules in the pili, but fibre diffraction has the potential to give higher resolution data than electron microscopy.

Acknowledgements

This research was funded in part by a grant from The Wellcome Trust to Professor R.N. Perham, and we thank Professor Perham for his support.

References

[1] Forest, K. T. & Tainer, J. A. (1997) Type-4 pilus-structure: outside to inside and top to bottom-a minireview. *Gene* **192**, 165-169.

[2] Wolfgang, M., van Putten, J. P. M., Hayes, S. F., Dorwald, D. & Koomey, M. (2000) Components and dynamics of fibre formation define a ubiquitous biogenesis pathway for bacterial pili. *EMBO J*. **19**, 6408-6418.

[3] Kaiser, D. (2000) Bacterial motility: How do pili pull? *Current Biology* **10**, R777-R780.

[4] Skerker, J. M. & Berg, H. C. (2001). Direct observation of extension and retraction of type IV pili. *Proc. Natl. Acad. Sci. USA* **98**, 6901-6904.

[5] Merz, A. J. & Forest, K. T. (2002) Bacterial surface motility: Slime trails, grappling hooks and nozzles. *Current Biology* **12**, R297-R303.

[6] Folkhard, W., Marvin, D. A., Watts, T. H. & Paranchych, W. (1981) Structure of polar pili from Pseudomonas aeruginosa strains K and O. *J. Mol. Biol.* **149**, 79-93.

[7] Parge, H. E., Forest, K. T., Hickey, M. J., Christensen, D. A., Getzoff, E. D. & Tainer, J. A. (1995). Structure of the fibre-forming protein pilin at 2.6 Å resolution. *Nature* **378**, 32-38.

[8] Forest, K. T., Dunham, S. A., Koomey, M. & Tainer, J. A. (1999) Crystallographic structure reveals phosphorylated pilin from Neisseria: phosphoserine sites modify type IV pilus surface chemistry and fibre morphology. *Molecular Microbiology* **31**, 743-752.

[9] Hazes, B., Sastry, P.A., Hayakawa, K., Read, R. J. & Irvin, R. T. (2000) Crystal structure of Pseudomonas aeruginosa PAK pilin suggests a main-chain-dominated mode of receptor binding. *J. Mol. Biol*. **299**, 1005-1017.

[10] Keizer, D. W., Slupsky, C. M., Kalisiak, M., Campbell, A. P., Crump, M. P., Sastry, P. A., Hazes, B., Irvin, R. T. & Sykes, B. D. (2001) Structure of a pilin monomer from Pseudomonas aeruginosa. *J. Biol. Chem*. **276**, 24186-24193.

[11] Forest, K. T., Bernstein, S. L., Getzoff, E. D., So, M., Tribbick, G., Geysen, H. M., Deal, C. D. & Tainer, J.A. (1996) Assembly and antigenicity of the Neisseria gonorrhoeae pilus mapped with antibodies. *Infect. Immun*. **64**, 644-652.

[12] Nave, C., Brown, R. S., Fowler, A. G., Ladner, J. E., Marvin, D. A., Provencher, S. W., Tsugita, A., Armstrong, J. & Perham, R. N. (1981). Pf1 filamentous bacterial virus. X-ray fibre diffraction analysis of two heavy-atom derivatives. *J. Mol. Biol.* **149**, 675-707.

[13] Marvin, D. A., Bryan, R. K. & Nave, C. (1987) Pf1 Inovirus. Electron density distribution calculated by a maximum entropy algorithm from native fibre diffraction data

to 3 Å resolution and single isomorphous replacement data to 5 Å resolution. *J. Mol. Biol.* **193**, 315-343.
[14] Marvin, D. A., Hale, R. D., Nave, C. & Helmer-Citterich, M. (1994) Molecular models and structural comparisons of native and mutant class I filamentous bacteriophages Ff (fd, f1, M13), If1 and Ike. *J. Mol. Biol.* **235**, 260-286.
[15] Welsh, L. C., Symmons, M. F. & Marvin, D. A. (2000) The molecular structure and structural transition of the α-helical capsid in filamentous bacteriophage Pf1. *Acta Crystallog. sect. D 56*, 137-150.
[16] Watts, T. H. (1983). Structure and Assembly of Pseudomonas Pili, Ph.D. Thesis, University of Alberta.
[17] Watts, T. H., Kay, C. M. & Paranchych, W. (1983) Spectral properties of three quaternary arrangements of Pseudomonas pilin. *Biochemistry* **22**, 3640-3646.
[18]. Kleywegt, G. J. & Jones, T. A. (1994). Detection, delineation, measurement and display of cavities in macromolecular structures. *Acta Crystallogr. sect. D* **50**, 178-185.
[19] Marvin, D.A. (1990) Model-building studies of Inovirus: genetic variations on a geometric theme. *Int. J. Biol. Macromol.* **12**, 125-138.
[20] Wright, P. E. & Dyson, H. J. (1999) Intrinsically unstructured proteins: Re-assessing the protein structure-function paradigm. *J. Mol. Biol.* **293**, 321-331.
[21] Mahadevan, L. & Matsudaira, P. (2000) Motility powered by supramolecular springs and ratchets. *Science* **288**, 95-99.
[22] Marvin, D. A. & Wachtel, E. J. (1976) Structure and assembly of filamentous bacterial viruses. *Phil. Trans. Roy. Soc. Ser. B* **276**, 81-98.
[23] Opalka, N., Beckmann, R., Boisset, N., Simon, M. N., Russel, M. & Darst, S. A. (2003) Structure of the filamentous phage pIV multimer by cryo-electron microscopy. *J. Mol. Biol.* **325**, 461-470.
[24] Vainshtein, B. K. (1966) *Diffraction of X-rays by Chain Molecules*, Elsevier, Amsterdam.
[25] Inouye, H. (1994) X-ray scattering from a discrete helix with cumulative angular and translational disorders. *Acta Crystallogr. sect. A* **50**, 644-646.
[26] Guex, N. & Peitsch, M. C. (1997) SWISS-MODEL and the Swiss-PdbViewer: An environment for comparative protein modelling. *Electrophoresis* **18**, 2714-2723.

Structural changes of α-crystallin during heating and comparisons with other small heat shock proteins

J. W. Regini[1] and J.G. Grossmann[2]

[1] The Biophysics Group, Department of Optometry and Vision Sciences, Cardiff University, Cardiff, CF10 3NB, UK
[2] CLRC Daresbury Laboratory, Synchrotron Radiation Department, Daresbury, Warrington WA4 4AD, UK

ABSTRACT

The small heat shock protein (sHSP) α-crystallin occurs in nearly all the major tissues of the body. It has two main functions; helping maintain transparency in the eye lens and as a molecular chaperone. We have investigated α-crystallin gels over a temperature range from 20 to 70ºC using wide and low angle X-ray scattering techniques. The low angle data show a moderate increase in both the spacing and intensity of the reflection from 20 to 45ºC. This was followed by a dramatic increase from 45 to 70ºC. Upon cooling, this effect was found to be irreversible over an eleven-hour period. Wide-angle scattering reflections from the α-crystallin gel arise from the secondary structure organisation, and can be characterized by inter-sheet (a ring at ~10 Å) and intra-sheet (a ring at 4.7 Å) interactions which appear to respond differently to increasing temperature. However, no indications of denaturation or unfolding are noticeable throughout the temperature range.

INTRODUCTION

The small heat shock protein (sHSP) α-crystallin occurs in nearly all the major tissues of the body. The highest concentration is to be found in the eye lens, where it occurs in very long fibre cells. It is the primary protein component and can approach 50% of the total dry weight of the lens [1]. One of its main functions here is the maintenance of short-range order in the lens cytoplasm, helping to achieve the refraction of light and to lens transparency in the visible spectrum [2]. Alpha-crystallin has two main isoforms, αA and αB, each with a molecular weight of about 20 kD. It is only in the lens that both isoforms are co-expressed. In other body tissues it is found at lower concentrations, with αB-crystallin by far the more prevalent [3,4]. In the lens however, the two isoforms co-aggregate into a heterogeneous population averaging a size of about 15 nm diameter and an overall mass of about 800 kD [5]. The α-crystallin subunit has unusual solution properties such that the aggregation process is propelled both by ionic and hydrophobic interactions. As a result the assemblages that are formed can vary considerably in number of subunits they contain. Recent studies of the aggregate structure of recombinant αB-crystallin using cryo-electron microscopy indicate that these assemblages share several structural features [6]. These include a spherical shell of about 3 nm thickness surrounding a hollow core of variable dimensions, and a dynamic region extending into the aqueous medium that appears to be quite flexible. The changeable structures of these assemblages has, so far, prevented crystal formation at the high concentrations of α-crystallin found in the lens *in vivo*. Thus the precise crystallographic structure of this protein is unknown. As α-crystallin is a member of the sHSP super-family, it exhibits chaperone-like activity and has been shown to prevent the superaggregation and/or precipitation of partially denatured target proteins at elevated temperatures [7]. Alpha crystallin is of great interest to medicine in general, as it is found at higher than normal concentrations in patients with ischemic heart [8]. It is also found at high levels in the brains of patients with Alzheimer's disease [9], multiple sclerosis [10] and other neurological diseases [11].

It has recently been shown that α-crystallin's chaperone-like activity at low and high temperatures is exhibited by very different populations of aggregates. At room and body temperatures, the size of the aggregate is typically around 15 nm. If the protein is heated, however, the aggregate size increases. A small gradual change in size can be observed between 20 and 50ºC, but by far the major changes occur above 50ºC, with aggregate size, shape, and mass fundamentally altered as indicated

by light scattering [12]; FPLC [13], non-denaturing gel electrophoresis, and transmission electron microscopy [14]. Such temperature-dependent structural changes are also observed for homopolymers of each α-crystallin isoform and for protein in the native isoform ratio that has been urea-denatured and then renatured [15]. There are also changes in the protein's secondary structure, as characterised by circular dichroism spectropolarimetry, which indicates alterations in β-sheet composition and/or stability in these samples after heating above 50ºC with subsequent cooling [14]. The mechanism by which this rearrangement occurs, and the organisation of sub-units in the resultant particles of each type remain the subject of much interest.

EXPERIMENTAL

α-crystallin was prepared from bovine calf lenses using a similar method of Thompson and Augusteyn (1983) [16], and concentrated by ultracentrifugation. Protein concentrations were determined spectrophotometrically, in serial dilutions using its extinction coefficient at 280 nm, or at 600 nm after reacting with Coomassie blue using bovine serum albumin as standard. The α-crystallin gel taken from the centrifuge precipitate was found to have a concentration of 296 mg/ml.

The α-crystallin gels were held in a temperature-controlled brass cell with a sample volume of 120µl, defined by a Teflon ring sandwiched by mica windows. For all specimens, 1min X-ray exposures were first taken at 20ºC. The temperature was then raised to 35ºC and left to equilibrate for a period of 10 minutes. The process was repeated in 5ºC steps until a temperature of 70ºC was reached.

The experiments were conducted on the low angle X-ray camera on station 2.1, and the wide angle diffraction station 14.1 at the Daresbury Synchrotron Radiation Source (SRS), UK. The X-ray patterns were recorded and analysed using BSL, OTOKO (Daresbury Laboratory, UK) and FIT2D [17] as well as Statistica (Statsoft, Tusla, USA) software packages. For most exposures, a vertical scan was taken through the centre of the pattern, resulting in a profile of the scattered intensity *I* versus radial position s. The intensity profiles were corrected for background scattering.

RESULTS

Low Angle Data

The scattering results for the α-crystallin gel (~300 mg/ml) are shown in Figure 1a). The X-ray intensity profiles are characterised by a strong peak, which with increasing temperature not only shifts its position to smaller scattering angles but also dramatically increases in intensity (by 67.3 % from 20ºC to 70ºC). The inset to Fig.1a) shows a weak secondary maximum , which disappears above 55ºC. At 20ºC the position of the main peak correlates with an average short-range distance between molecules of 138 Å. This result confirms the earlier work of Vérétout *et al* (1989) [18], who reported a broad reflection at room temperature of 14 nm at high concentrations, in the range about 100-300 mg ml^{-1}. The spacing of this reflection increases to 195 Å at 70ºC. This temperature-dependent change in spacing is highlighted in Fig.1b). The figure also emphasises that between 45ºC and 55ºC the gel undergoes a major transition, as both peak position and peak width change dramatically. Interestingly, both peak width and peak position correlate well above 55oC; however, in contrast to a fairly gradual increase in peak position between 20ºC and 50ºC, the corresponding peak width decreases steadily.

The sample measured at 70ºC was left overnight for a period of 11 hours to cool. Subsequently, a further X-ray scattering data set was taken at room temperature (19ºC) and compared with the curve measured at 70ºC (Fig.2). This shows that the effects of heating were essentially irreversible, as after cooling the peak position only increased a little correlating with a slightly lower spacing (i.e. from 195 Å at 70ºC to 192 Å at 19ºC). The intensity has increased at the peak position and decreased towards very low scattering angles, which indicates an improved X-ray scattering contrast. This change is most likely due to loss of water from the sample.

Wide Angle Data

The complementary wide-angle X-ray patterns of the native α-crystallin gel upon heating from 20ºC to 70ºC were also collected and studied. As the scattering is isotropic, the data were reduced to 1D scattering profiles in order to detect subtle changes (Figure 3). Within this scattering regime (0.075 $Å^{-1} \leq$

(a)

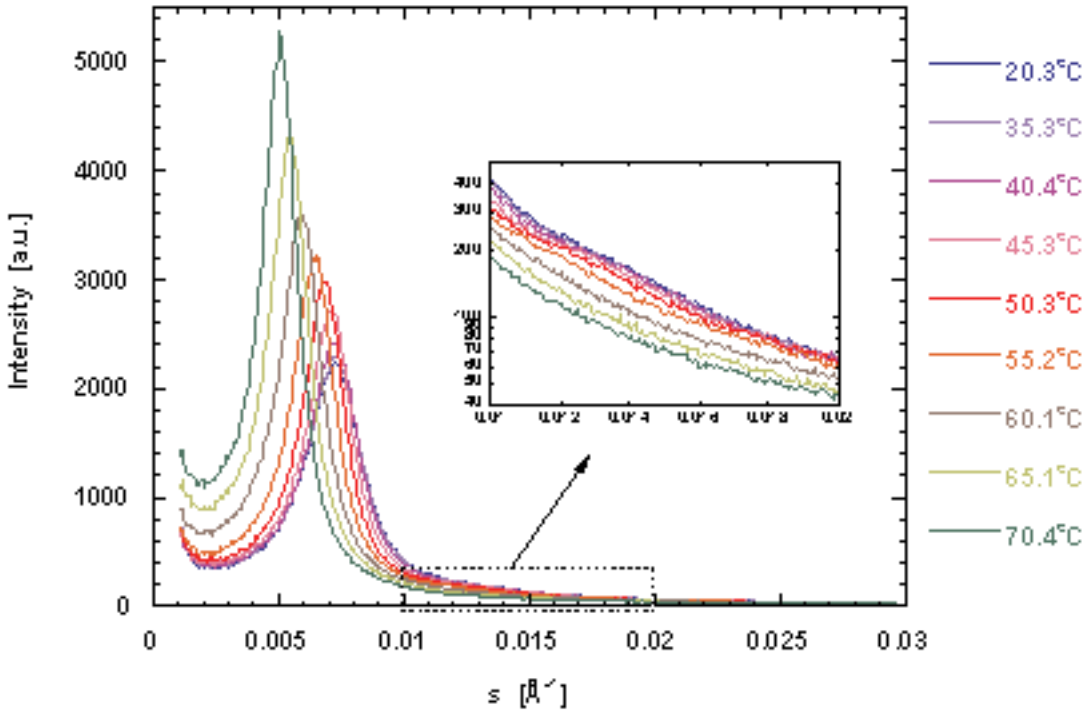

(b)

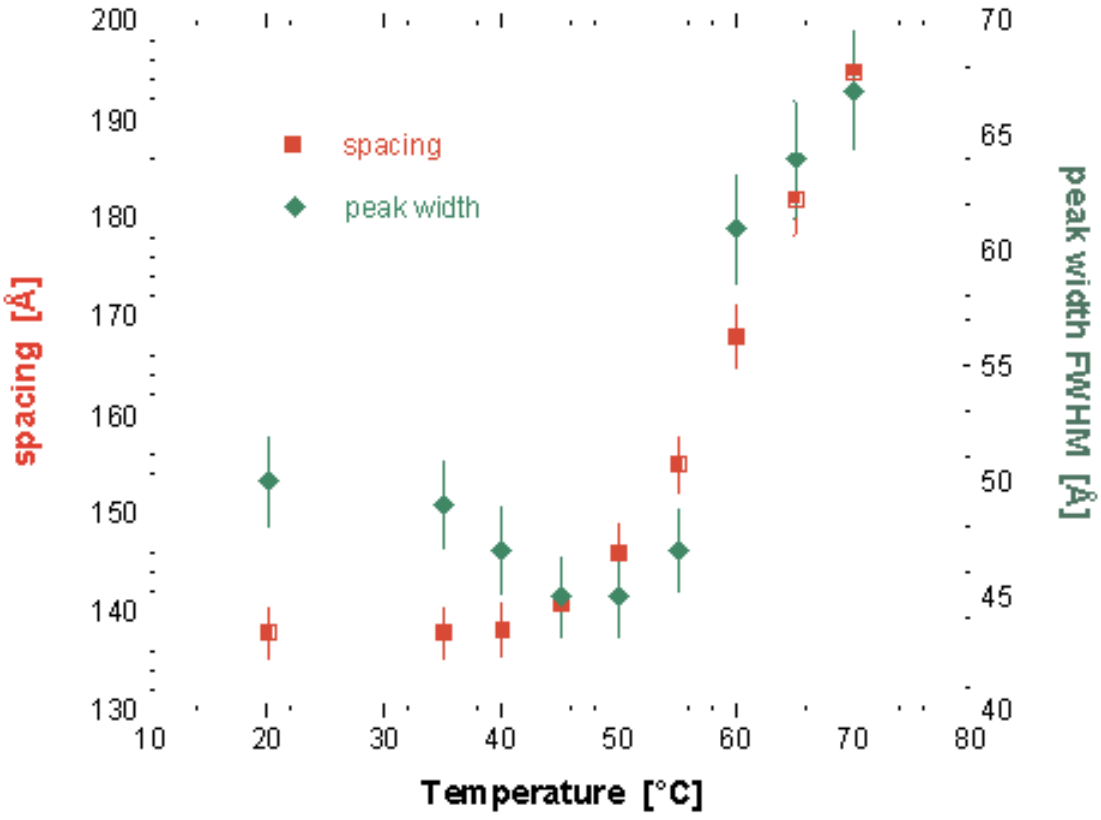

Figure 1 (a) X-ray intensity profiles of purified α-crystallin gel measured at temperatures between 20ºC and 70ºC showing the increase in both the spacing and intensity. The inset highlights the existence of a weak second-order peak at temperatures below 55ºC (note the use of a logarithmic scale). **(b)** The relationship between the position of the peak / the peak width (full length at half the maximum peak height) and increasing temperature.

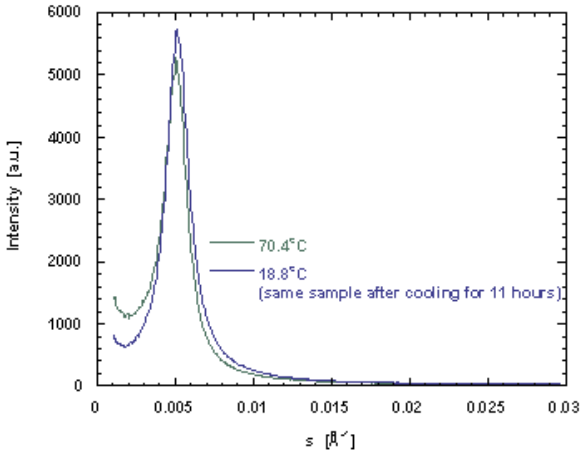

Figure 2 Comparison of intensity profiles measured for α-crystallin gel at 70ºC and after 11 hours when the sample was cooled down to room temperature (19ºC).

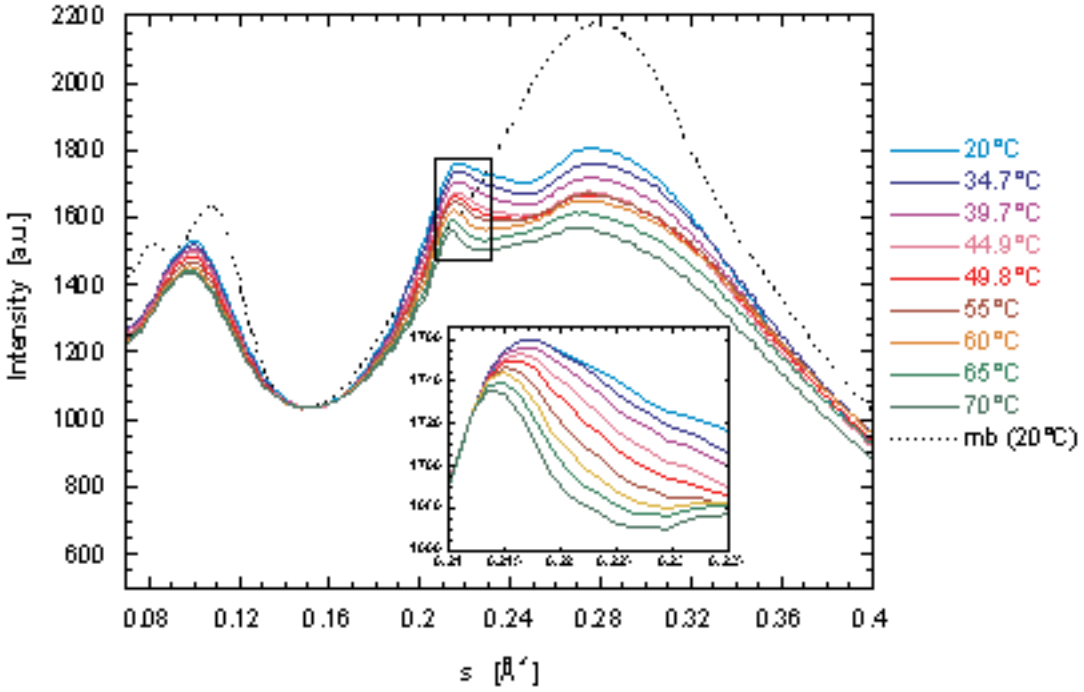

Figure 3 Reduced 1D wide-angle scattering data of native α-crystallin gel upon heating from 20ºC to 70ºC. The characteristic wide-angle features can be compared with a profile collected from a concentrated myglobin solution (~50mg/ml). Curves were normalized at s = 0.15 Å^{-1}. The insert shows the expanded region 0.21 Å^{-1} < s < 0.235 Å^{-1} highlighting the temperature-induced changes in the width of the peak corresponding to a Bragg spacing of 4.7 Å which is associated with the distance between β-strands. For the sake of clarity the curves in the inset were normalized at s = 0.212 Å^{-1}.

s ≤ 0.4 Å^{-1}) one can clearly see three major peaks around s = 0.1 Å^{-1}, s = 0.213 Å^{-1} and s = 0.275 Å^{-1}. The latter peak is relatively broad in comparison to the other two, and corresponds to a Bragg spacing of approximately 3.6 Å. It results from the diffuse scattering of water in the sample. However, the two other peaks, correlating to a Bragg spacing of 10 Å and 4.7 Å, respectively, are characteristic of β-sheets, and can be attributed to the high content of this secondary structure in α-crystallin. For comparison, Figure 3 also displays the wide angle scattering profile of a concentrated myglobin solution (i.e. a protein containing only helices as secondary structural elements) with peaks at around s = 0.083 Å^{-1} (12 Å) and s = 0.11 Å^{-1} (9 Å) corresponding to distances between helices. The 4.7 Å reflection in the α-crystallin pattern is diagnostic of the distance between neighbouring polypeptide chains in β-sheets (i.e. arises from the spacing between strands within a given sheet), while the 10 Å reflection is attributable to the separation of β-strands between sheets. It is the former peak in the isotropic wide-angle pattern of the α-crystallin gel that changes markedly during heating. With increasing temperature a reduction in

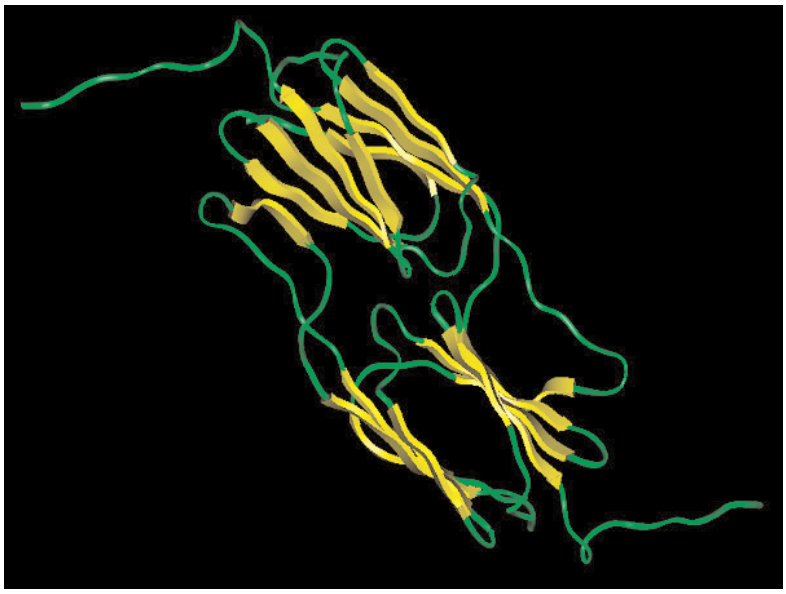

Figure 4. Ribbon model of a dimer taken from the structure of the 16.5kD small heat shock protein from *M. jannaschii* (pdb code 1shs), a structural relative of α-crystallin. Its secondary structure is dominated by β-strands (displayed in yellow) and the monomer-monomer interactions and dimensions of secondary structural units are shown.

peak width is clearly observable (see inset to Fig.3), indicating an increasing structural homogeneity and definition of this strand-strand interaction. This physical behaviour is in analogy to crystalline diffraction where a decrease in the peak width indicates an increase of the average size of perfectly crystalline regions. This improved structural uniformity of the strand-strand interaction at higher temperatures is in clear contrast to what one would expect if the protein had started to unfold or denature at elevated temperatures. Moreover, unlike the ring at 4.7 Å, the ring at around 10 Å remains effectively unchanged over the whole temperature range, indicating the conservation of the spacing between sheets with temperature.

DISCUSSION

The low angle studies of α-crystallin clearly show an increase in both the spacing and the scattered intensity. On increasing temperature the rise in scattered intensity indicates an increase in electron density of the aggregates. As the aggregates grow, so the average centre to centre distance between them also increases, which gives rise to the change in the spacing. Below 50°C, the rate of aggregate growth is low, while above 50°C, both the growth rate and the particle mass are higher. This is a striking phenomenon, which correlates well with an increase in functional efficiency that has been observed with increasing temperature for native α-crystallin [13, 19]. The presence of the secondary peak below 55°C (inset Figure 1) may indicate that below this temperature a weak long-range ordering of the α-crystallin molecules occurs in the gel state. Above this temperature the long-range ordering is lost completely due to thermal motion and the gel behaves similar to a dense liquid.

A focal point of the present study is the structural interpretation of the characteristic rings in the wide-angle scattering data. At protein concentrations as high as the concentration used here for the α-crystallin gel, the wide-angle scattering signal can provide valuable information on changes in the secondary structure. Over the temperature range considered herein, there is essentially no change in the spacing between the two β-sheets of the α-crystallin domain, nor is there a significant change in the spacing between β-strands. Nevertheless, the latter interaction becomes more uniform and homogeneous with increased temperature. These results differ from previous spectroscopic studies which show a loss of secondary structure with increasing temperature [13]. However we have to point out that our experiments were performed at much higher concentrations that are close to physiological conditions.

α-crystallin is a representative of the sHSP superfamily, varying in subunit size from 11-12 kD to 40 kD. They all share a common region which is referred to as the α-crystallin domain [20] spanning approximately 90-100 amino acids. The quaternary structure of sHSP superfamily members appears to be quite variable from one to another [21]. As

mentioned, α-crystallin aggregates are variable in size, shape, and mass, while other examples from the superfamily can show homogeneous aggregate sizes and symmetries. For instance sHSP 16.5 from *Methanococcus jannaschii*, assembles into a 24-subunit structure [22] which indicates that the region common to all superfamily members consists primarily of β-strands organized into two opposing sheets (see Figure 4). A loop within this region provides an additional short stretch of β-strand implicated in the formation of dimers, the basic structural unit for the aggregate. The C-terminal arms are involved in the formation of tetramers, with additional interactions leading eventually to the final closed-surface structure, while there is no structural information for the N-terminal region. In contrast, the wheat HSP 16.9 [23] exhibits very similar structural characteristics on the subunit level, but its quaternary structure (a dodecameric double disk) differs from the shell-type multimers seen in α-crystallin assemblies. This indicates that subunit interfaces and polypeptide extensions/deletions, which account for the high sequence variation in sHSP, correlate with the overall molecular shape of this protein family.

However, we would like to emphasize that recent studies [24-26] suggest that the exact dimer interactions of α-crystallin may differ greatly from other sHSP's. It has been shown that after deletion of the N-terminal domain of αB-crystallin no large oligomers are formed and that the C-terminal domain supports the assembly of a stable dimer which still retains chaperone-like activity [27]. Interestingly, it was observed by X-ray scattering that the αB-crystallin dimer in solution has a significantly different conformation compared to the dimer taken from the *M.jannaschii* sHSP crystal structure. Feil *et al.* [27] not only point out that this will result in different quaternary structures of the two proteins but also that the α-crystallin dimer interface is most likely very flexible. Given that the dimer appears to be a widespread building block in sHSP oligomer assembly [23], this flexibility is a crucial factor. It allows the overall quaternary structure of the α-crystallin oligomer to be variable and dynamic, since α-crystallins are shaped by a continuous exchange of subunits [28-30]. It is therefore conceivable that with rising temperature the α-crystallin aggregates become bigger as an increasing flexibility will facilitate association/dissociation events. Indeed Bova *et al.* [28] reported a 4.2 fold increase in the rate of subunit exchange by going from 37ºC to 42ºC. This dynamic structural behaviour would also explain the observed feature of the ring at 4.7 Å (associated with strand-strand interactions), which appears to be less well defined at temperatures below 50ºC. Considering physiological concentrations of around 300mg/ml and temperatures higher than 50ºC, the particle growth will eventually be limited by the interactions of relatively densely packed super-aggregates. As a result, subunit exchange reactions may become less frequent leading to a rather rigid and homogeneous shell structure. β-strand interactions (in particular those between neighbouring monomers) will become more stable and appear to be "locked" into position. This may explain why the width of the peak associated with a Bragg spacing of 4.7 Å becomes narrower at temperatures above 50ºC (Fig.3 inset). In contrast the 10 Å reflection, indicative of the distance between β-sheets, does not show any significant change over the temperature range. Consequently, it is tempting to suggest that this apparent change in secondary structure with heat is associated with the quaternary structural changes leading to larger and rather rigid aggregates which may be linked to a loss or decrease of chaperone-like activity above 50ºC.

In conclusion, we have shown that α-crystallin undergoes extensive structural changes with temperature with a major transition around 50ºC. Our findings confirm earlier observations at low concentrations of α-crystallin, which can now be confirmed at virtually physiological concentrations. The low angle results seem to apply both for low and high concentrations of α-crystallin. In contrast, investigating structural phenomena at almost physiological concentrations (as performed here on an α-crystallin gel) provided new insights into the secondary structure from wide-angle measurements. The study substantiates that α-crystallin function in the eye lens is closely associated with a highly dynamic oligomeric structure.

REFERENCES

[1] de Jong W.W. (1981). *Molecular and Cellular Biology of the Eye Lens*. New York

[2] Delaye, M. & Tardieu, A. (1983) Short-range order of crystallin proteins accounts for eye lens transparency. *Nature* **302**, 415-417.

[3] Bhat, S. P. & Nagineni, C. N. (1989) Alpha B subunit of lens-specific protein alpha-crystallin is present in other ocular and non-ocular tissues. *Biochem. Biophys. Res. Comm.* **158**, 319-325.

[4] Kato, K., Shinohara, H., Kurobe, N., Inaguma, Y., Shimizu, Y. & Oshima, K. (1991) Tissue distribution and developmental profiles of immunoreactive alpha B crystallin in the rat determined with a sensitive immunoassay system. *Biochim. Biophys. Acta* **1074**, 201-208.
[5] Harding, J. (1991). *Cataract*. Chapman and Hall, London.
[6] Haley, D. A., Horwitz, J. & Stuart, P. L. (1999) Image restrained modelling of alpha B-crystallin. *Exp. Eye Res*. **68**, 133-136.
[7] Horwitz, J. (1992) Alpha-crystallin can function as a molecular chaperone. *Proc. Natl. Acad. Sci. USA* **89**, 1449-1453.
[8] Chiesi, M., Longoni, S., & Limbrruno, U. (1990) Cardiac alpha-crystallin. III. Involvement during heart ischemia. *Mol. Cell. Biochem*. **97**, 129-136.
[9] Renkawek, K., Voorter, C.E., Bosman, G.J., van Workum, F.P. & de Jong, W.W., (1994) Expression of alpha B-crystallin in Alzheimer's disease. *Acta Neuropathol (Berl)* **87**, 155-160.
[10] van Noort, J.M., van Sechel, A.C., Bajramovic, J.J., el Ouagmiri, M., Polman, C.H., Lassmann, H. & Ravid, R. (1995) The small heat-shock protein alpha B-crystallin as candidate autoantigen in multiple sclerosis. *Nature* **375**, 798-801.
[11] Groenen, P.J., Smulders, R.H., Peters, R.F., Grootjans, J.J., van den Ijssel, P.R., Bloemendal, H. & de Jong, W.W. (1994). The amine-donor substrate specificity of tissue-type transglutaminase. Influence of amino acid residues flanking the amine-donor lysine residue. *Eur. J. Biochem*. **220**, 795-9.
[12] Thurston, G.M., Sun, T.X. & Liang, J.N. (1998) Relationship between molecular weight and hydrodynamic radius during heat-induced aggregation of human alphaA and alphaB crystallin. *Invest. Opthalmol. Vis. Sci. (ARVO Suppl)*. **40**, S2.
[13] Das, B.K., Liang, J.J. & Chakrabarti, B. (1997) Heat-induced conformational change and increased chaperone activity of lens alpha-crystallin. *Curr. Eye Res*. **16**, 303-309.
[14] Burgio, M. R., Kim, C. J., Dow, C. C. & Koretz, J. F. (2000) Correlation between the chaperone-like activity and aggregate size of alpha-crystallin with increasing temperature. *Biochem. Biophys. Res. Comm*. **268**, 426-432.
[15] Burgio, M.R., Bennett, P.M. & Koretz, J.F. (2001) Heat-induced quaternary transitions in hetero- and homo-polymers of alpha-crystallin. *Mol. Vis*. **7**, 228-233.
[16] Thompson, J.A. & Augusteyn, R.C. (1983) Alpha m-Crystallin: the native form of the protein? *Exp. Eye Res*. **37**, 367-377.
[17] Wess, T.J., Hammersley, A.P., Wess, L. & Miller, A. (1995) Type I collagen packing conformation of the triclinic unit cell. *J. Mol. Biol*. **248**, 487-493.
[18] Vérétout, F., Delaye, M. & Tardieu, A. (1989) Molecular basis of eye lens transparency. Osmotic pressure and X-ray analysis of α-crystallin solutions. *J. Mol. Biol*. **205**, 713-728.
[19] Raman, B. & Rao, Ch. M. (1997) Chaperone-like activity and temperature-induced structural changes of α-crystallin. *J. Biol. Chem*. **272**, 23559-23564.
[20] de Jong, W.W., Leunissen, J.A. & Voorter, C.E. (1993). Evolution of the alpha-crystallin/small heat-shock protein family. *Mol. Biol. Evol*. **10**, 103-126.
[21] Haley, D.A., Bova, M.P., Huang, Q.L., Mchaourab, H.S. & Stewart, P.L. (2000) Small heat-shock protein structures reveal a continuum from symmetric to variable assemblies. *J. Mol. Biol*. **298**, 261-272.
[22] Kim, K. K., Kim, R. & Kim, S. H. (1998) Crystal structure of a small heat-shock protein. *Nature*, **394**, 595-599.
[23] van Montfort, R. L., Basha, E., Friedrich, K. L., Slingsby, C. & Vierling, E. (2001) Crystal structure and assembly of a eukaryotic small heat shock protein. *Nat Struct. Biol*. **8**, 1025-1030.
[24] Salerno, J.C. & Koretz, J.F. (1999). Sequence, structure, and aggregation in small heat shock proteins. *Protein Sci.* **8 (Suppl. 1)**, 125.
[25] Eifert, C.L., Salerno, J.C. & Koretz, J.F. (2000). Characterization of an alpha-crystallin and HSP 16.5 chimera. . *Invest. Ophthalmol. Vis. Sci. (ARVO Suppl.)*, **41**, S582.
[26] Salerno J.C., Eifert, C. L., Salerno, K. M., & Koretz, J. F. (2003) Structural diversity in the small heat shock protein superfamily: control of aggregation by the N-terminal region. *Protein Engineering*, in press
[27] Feil, I.K., Malfois, M., Hendle, J., van der Zandt, H. & Svergun, D.I. (2001) A novel quaternary structure of the dimeric α-crystallin domain with chaperone-like activity. *J. Biol. Chem*. **276**, 12024-12029.
[28] Bova, M.P., Ding, L.-L., Horwitz, J. & Fung, B.K.-K. (1997) Subunit exchange of αA-crystallin. *J. Biol. Chem*. **272**, 29511-29517.
[29] Sun, T.-X. & Liang, J.J.-N. (1998) Intermolecular exchange and stabilization of recombinant human αA- and αB-crystallin. *J. Biol. Chem*. **273**, 286-290.
[30] Bova, M.P., Mchaourab, H.S., Han, Y. & Fung, B.K.-K. (2000) Subunit exchange of small heat shock proteins. *J. Biol. Chem*. *275*, 1035-1042.

X-ray fibre diffraction analysis of assemblies formed by prion-related peptides: Polymorphism of the heterodimer interface between PrP^{C} and PrP^{Sc}

Hideyo Inouye and Daniel A. Kirschner*

Biology Department, Boston College, Chestnut Hill, MA 02467-3811

Author for correspondence

ABSTRACT

The molecular mechanism in prion diseases involves structural alteration of the non-infectious cellular isoform (PrP^{C}) to the infectious, scrapie isoform (PrP^{Sc}). The structural transition is thought to involve a binding interface between the two isoforms in their N-terminal domains. Because prions and prion-related peptides can form amyloid-like fibrillar assemblies, we have used X-ray fibre diffraction to study the structure of the binding interface in synthetic peptides that have sequence similarity with the prion protein (PrP). Our previous studies show that the alanine-rich peptides PrP106-122 and PrP109-122 form slab-like structures that are stacked as one-dimensional lattices having cumulative disorder. The unit cell is a four-stranded β-sheet with the chains directed along the stacking direction. Neighboring β-sheets are quarter-staggered (like in β silk). Electron density projections indicate that the peptides form a reverse turn with the larger residues in the N-terminal domain distinguishable from the alanine-rich C-terminal domain. This reverse turn accounts for the 33 Å-length of β chains (or slab thickness) as measured from the low-angle scattering. In this report, we considered three different inter-molecular packings for the reverse turn molecules: i.e., anti-parallel, parallel, and staggered. The staggered arrangement gave the best agreement between the observed and calculated X-ray intensities. From the molecular model we suggest that the autocatalytic replication of prions may involve hydrogen-bonding between intermolecular antiparallel β chains of the alanine-rich domains at the binding interface between PrP^{C} and PrP^{Sc}.

Key words: Prion; amyloid; X-ray diffraction; reverse turn; beta-pleated sheet

Introduction

X-ray diffraction has been used to study the molecular organization of amyloid-like structures formed by the N-terminal domains of the prion protein (Figures 1 and 2)-including those of Syrian hamster (SHa; PrP27-30 or SHa90-231; SHa90-145; SHa106-122; "H1" or SHa109-122; "A8A" or SHa113-120); mouse (Mo; Mo89-143); and human Gerstmann-Sträussler-Scheinker or GSS type mutations expressed in mouse or Syrian hamster sequences (Mo89-143(P101L); SHa104-122(3A-V)) (Nguyen *et al.*, 1995; Inouye and Kirschner, 1997, 1998; Inouye *et al.*, 2000). As reported in these studies, X-ray fibre and powder diffraction (Figure 3) shows that the N-terminal domain in PrP is folded as a β-sheet which is the likely conformation for the PrP^{Sc} isoform (Pan *et al.*, 1993). On the other hand, solution NMR indicates an α helical-rich structure and an N-terminal domain (90-~125) that is "flexibly disordered" (Figure 2) (Riek *et al.*, 1996; James *et al.*, 1997; Donne *et al.*, 1997; Liu *et al.*, 1999; Lopez *et al.*, 2000; Zahn *et al.*, 2000). X-ray single crystal analysis gives a similar monomeric structure as shown by solution NMR, but does not resolve a structure for the N-terminal residues 90-119 (Knaus

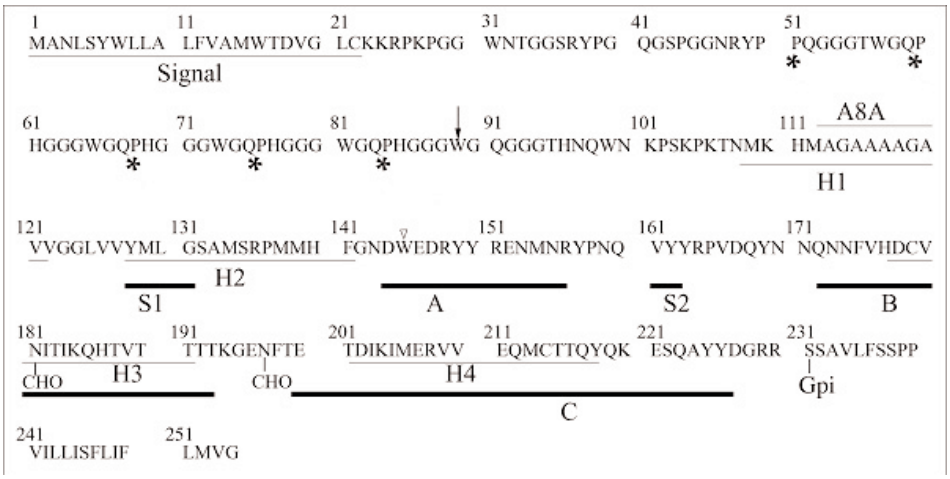

Figure 1. Primary structure of hamster prion protein (Stahl *et al*., 1993; Inouye and Kirschner, 1998). The first N-terminal 22 residues are the signal sequence. While PrP^{C} is completely digested by proteinase K, PrP^{Sc} is partially digested yielding PrP27-30 (Prusiner *et al*., 1983) which starts with residue 90 (black arrow). The glycosylation sites at residues 181 and 197 are indicated by -CHO, and the glycosylphosphatidylinositol anchor is shown at residue 231 by Gpi. A stop codon has been found for the human prion gene at 145 (open arrowhead) (Kitamoto *et al*., 1993). The N-terminal octarepeats (*) are likely Cu binding sites (Viles *et al*., 1999). The four predicted helices (H1,H2,H3 and H4) are shown, as are the helical domains A, B and C, and b chains S1 and S2 as determined by solution NMR (James *et al*., 1997). X-ray fibre diffraction studies on domains H1, A8A and SHa106-122 are discussed in this paper.

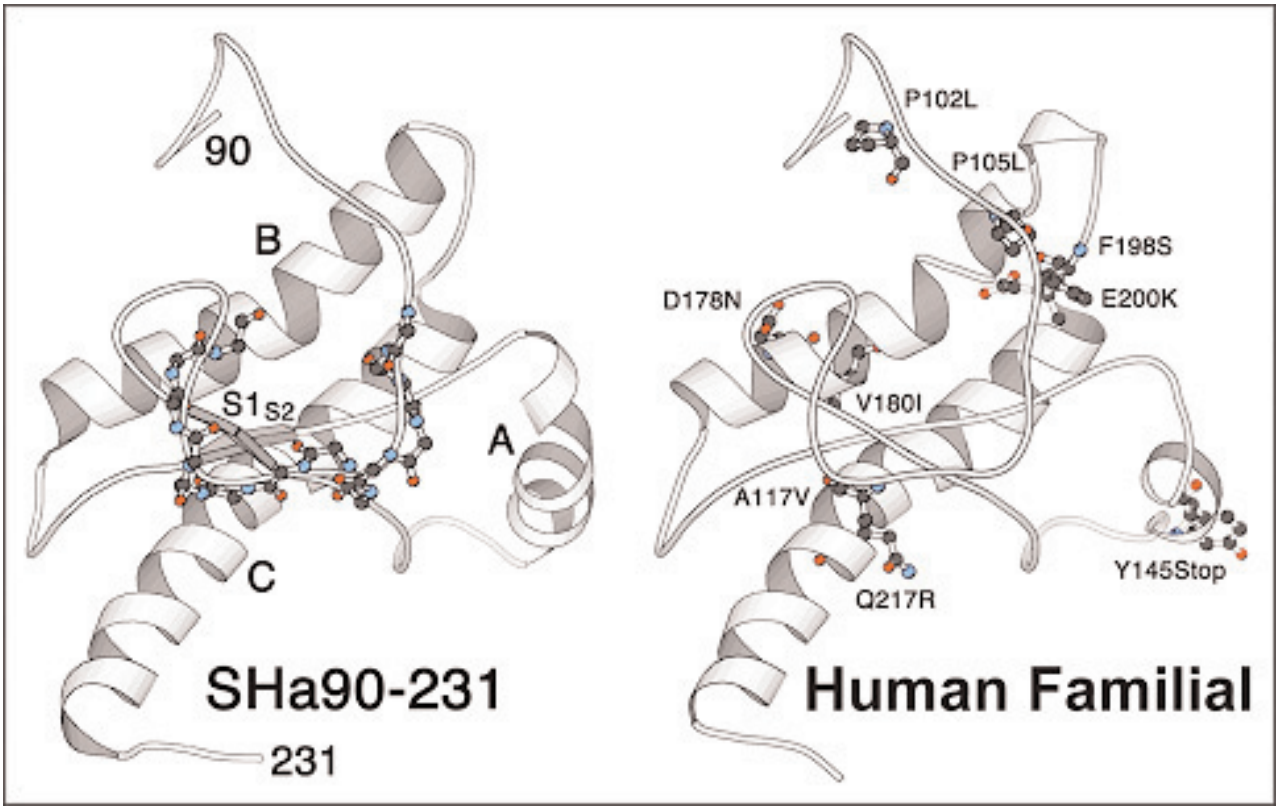

Figure 2. Molscript representation of PrP. (**Left**) Location of the peptide fragments in Syrian hamster 90-231 (SHa90-231). H1 domain (SHa109-122; shown as ball and stick model) as determined by solution NMR (James *et al*.,1997). The N-terminal domain is flexibly disordered, while the C-terminal domain contains three a helical domains (A, B, C), and two short β strands (S1, S2). The 3F4 epitope domain is at the N-terminal end of the ball and stick model, and alanine-rich A8A is at the C-terminal end. If A8A forms a β strand, then A8A, S1, and S2 are likely to be H-bonded together, forming a β sheet. (**Right**) The three-dimensional structure of human PrP as predicted by Swiss Modeler (Guex *et al*., 1999) using the NMR hamster PrP structure (left panel) as a template. The mutations in human familial prion disease including Gerstmann-Sträussler-Scheinker syndrome (GSS), familial Creutzfeldt-Jakob disease (CJD), and fatal familial insomnia (FFI) are indicated (Prusiner, 1991). Formation of a β sheet is likely facilitated by these mutations. X-ray fibre diffraction of peptides containing the GSS type P102L and A117V substitutions appears to confirm this (Inouye *et al*., 2000).

et al., 2001). The α helical structure may be present in the PrP^C isoform.

Peptide fragment SHa109-122 (designated H1), which is at the binding interface between PrP^C and PrP^{Sc}, shows two different diffraction patterns depending on the treatment or physical state of the sample, i.e., lyophilized or solubilized in 50% acetonitrile (AcN) solution followed by drying (Nguyen *et al.*, 1995). With the latter treatment, the N-terminal part of H1-i.e., the epitope region (residues 109-112: MKHM) for the 3F4 antibody-is likely to be folded as a β chain while in the former state the epitope is not in the b conformation and is probably exposed on the protein surface (Nguyen *et al.*, 1995; Inouye and Kirschner, 1998; Inouye *et al.*, 2000). The two conformations indicated by the X-ray diffraction and NMR data are consistent with the notion that PrP^{Sc} goes through a partial denaturation or unfolding when it interacts with PrP^C. The folding-unfolding transformation is evident in cell-free PrP replication, where treatment of PrP^{Sc} by guanidinium hydrochloride (GdnHCl) is required (Kocisko *et al.*, 1994) to expose the 3F4 epitope that is concealed in PrP^{Sc} (Safar *et al.*, 1998).

In this report we address the question of the folding of the H1 domain, which by harboring the 3F4 epitope is thought to be at or near the binding interface between the two PrP isoforms and therefore to play a crucial role in the $PrP^C \rightarrow PrP^{Sc}$ transition. We previously proposed three different molecular packings for H1 assemblies, i.e., anti-parallel, parallel, and staggered (Inouye *et al.*, 2000); however, atomic models were not tested against the observed X-ray intensity. Here, we first summarize our previous X-ray analysis and then extend it by fitting atomic models to the electron density map. Staggered inter-molecular packing of H1 monomers most closely fits the X-ray data, and suggests a role for hydrogen-bonding at the binding interface between PrP^C and PrP^{Sc}.

Materials and Methods

The experimental methods have been described in detail in our previous reports (Nguyen *et al.*, 1995; Inouye and Kirschner, 1997; Inouye *et al.*, 2000) and are given in brief here.

X-ray diffraction

Peptides and Samples. The sample peptides (sequences indicated Figure 1) were analyzed in the lyophilized state and after solubilization and drying, as previously described.

Data Collection and Analysis. X-ray diffraction patterns were recorded on film and digitized as described. The intensities were obtained from narrow strip scans along the equatorial, meridional or radial directions using the public domain NIH Image program on a Macintosh computer (developed at the U.S. National Institutes of Health and available on the Internet at http://rsb.info.nih.gov/nih-image/). The diffraction pattern showing slight orientation was treated as a powder pattern. The structure amplitudes are related to the observed intensity by Lorentz and polarization factors. The Lorentz factor L in powder diffraction, for example, is given by $\frac{\lambda}{4\sin\theta}$, where λ is X-ray wavelength and θ is half of the scattering angle (Cella *et al.*, 1970). As the spherically distributed intensity I_s is measured along the radial direction on flat film, the structure factor F is related to I_s by

$$I_s = \frac{F^2 LP}{2\pi R} = \frac{F^2 P}{4\pi R^2},$$

where

$$R = \frac{2\sin\theta}{\lambda}$$

and the polarization factor (Inouye *et al.*, 1993)

$$P = \frac{1+\cos^2 2\theta}{2}.$$

The lattice constants and indices were searched by comparing the observed and calculated spacings using different combinations of indices within a particular range of lattice constants and indices. The final values of lattice constants were determined by the linear least squares procedure.

Fourier synthesis iteration and molecular modelling

The Fourier procedure for fibre or powder diffractions has been described in detail (Inouye *et al.*, 1993; Inouye and Kirschner, 1995, 1997). In brief:

1. We first choose the initial phase model which defines the atomic fraction coordinates (x_j,y_j,z_j) for the *j*th atom in the unit cell, using initial phases derived from the Cα, Cβ, and peptide bonds of the β

silk backbone (Marsh *et al*., 1955).

2. Next, we calculate the structure factors $F_{calc}(hkl)$ within a given range of *h,k,l* and for the observed unit cell according to

$$F_{calc}(hkl) = \sum_j f_j \exp i2\pi(hx_j + ky_j + lz_j) \quad ,$$

where f_j is the atomic factor. We use space group P1 (which assumes no symmetry) and calculate the structure factors for both positive and negative indices. In this report, the orthogonal unit assigned to the peptides is not required by symmetry, but simply happens to be convenient.

3. We next combine the observed structure amplitudes $|F_{obs}(hkl)|$ and calculated phases $\phi_{calc}(hkl)$. For powder diffraction the observed intensity is given as the spherically distributed intensity $I_s(R)$ as a function of radial component of spherical reciprocal coordinates *R*. Since multiple indices may contribute to each peak in powder diffraction, the observed structure amplitudes for the specified indices are calculated by dividing the observed intensity in proportion to the calculated intensities from the model. The observed structure amplitudes are, therefore given by

$$\left|F_{obs}(hkl)\right|^2 = \frac{C(hkl)I_s(R)}{LP} \quad ,$$

where

$C(hkl) = \dfrac{\left|F_{calc}(hkl)\right|^2}{\sum\left|F_{calc}(hkl)\right|^2}$ and LP is the Lorentz-polarization factor (see above). The indices *hkl* for summation satisfies the condition $\left|R_{hkl}^{-1} - R^{-1}\right| < \Delta d$, where R_{hkl} is the radial component of the Bragg spacing in spherical coordinates, and Δd is a defined critical value between the observed and calculated Bragg spacings (usually 0.005 - 0.01 Å). The relative deviation between the observed and calculated structure amplitudes is given as

$$R_{obs-amp} = \frac{\sum\left|\left|F_{obs}\right| - \left|F_{calc}\right|\right|}{\sum\left|F_{obs}\right|} \quad .$$

4. Finally, we use the observed amplitudes and calculated phases to calculate the electron density map with XtalView (McRee, 1992), and we fit the density map with a molecular model built using Swiss-Modeler (Guex *et al*., 1999). In most cases, before building the molecular model, we optimized the phase from the β silk backbone in the Fourier iteration procedure by modifying the electron density distribution, i.e., setting the negative electron densities (on a relative scale) to zero (Nguyen *et al*., 1995; Inouye and Kirschner, 1997). The atomic model is then modified to fit the newly-derived electron density map. With the new atomic model, we then go back to Step (2), and iterate the process until the *R*-factor does not decrease further.

Molecular modelling

The three dimensional molecular model is displayed and manipulated with Molscript (Kraulis, 1991), XtalView (McRee, 1992), Rasmol (by Roger Sayle), Swiss-PDB Viewer (Guex, *et al*., 1999), and QUANTA (Accelrys, Inc., San Diego, CA, USA). The secondary structure is determined from the atomic coordinates using DSSP (Kabsch and Sander, 1983) and STRIDE (Frishman and Argos, 1995; http://www.embl-heidelberg.de/stride/stride_info.html).

Theory of one-dimensional disordered lattice

Some prion peptides assemble *in vitro* to form a slab-like structure. Stacking along the β chain direction of the slabs gives a strong reflection in the low-angle region, and subsequent broad intensity maxima. The former likely arises from the interference of the disordered lattice, and the latter arises from the Fourier transform of the unit structure. Since a single interference peak is observed-i.e., the interference curve rapidly approaches unity-the lattice is disordered. In the current report, correct measurement of the thickness of the slab gave a crucial constraint to the length of the extended β chain, indicating a reverse turn or hairpin. In the following we describe the Fourier transform of a one-dimensional lattice having cumulative or non-cumulative disorder. The formulation follows the case for a discrete helical array (Inouye, 1994). Here, the disorder parameter is included in the structure factor, whereas usually it is defined in the autocorrelation function. The advantage of this formulation is that the intensity function for a discrete helical array can be written in closed form (Inouye, 1994).

We first define a lattice-generating function with disorder, an auto-correlation function, and an intensity function for a one-dimensional lattice. The lattice position is defined by

$$r_j = jd + \delta_j \qquad (1)$$

where *d* is a distance between lattice points and δ_j is

a displacement from the ideal position. The lattice $\rho(r)$ is described as

$$\rho(r) = \sum_{j=0}^{N-1} \delta(r - r_j) \quad , \qquad (2)$$

where N is the number of lattice points. The autocorrelation function, using (1) is

$$\rho(r) * \rho(-r) = \sum_{j=0}^{N-1} \sum_{k=0}^{N-1} \delta\left[r - (j-k)d - (\delta_j' - \delta_k')\right] \quad . \qquad (3)$$

Fourier transform of (3) gives the intensity function as

$$I(R) = N + \sum_{\substack{j=0 \\ j \neq k}}^{N-1} \sum_{k=0}^{N-1} \exp\left[i2\pi(j-k)dR\right] \exp\left[i2\pi(\delta_j' - \delta_k')R\right] , \qquad (4)$$

where the summation in the second term is performed with $j \neq k$. Since the observed intensity refers to the intensity for a statistical average (denoted by < >) of the positional displacements, then

$$< I(R) >= N + \sum_{\substack{j=0 \\ i \neq k}}^{N-1} \sum_{k=0}^{N-1} \exp[i2\pi(j-k)dR] < \exp[i2\pi(\delta_j' - \delta_k')R] > \qquad (5)$$

To evaluate the averaged exponential term, we assume a probability distribution function for the positional displacements as shown below.

Perfect lattice. When there is no disorder, the intensity function is written as

$$I_0(R) = \sin^2(\pi N dR) / \sin^2(\pi dR) \qquad (6)$$

The intensity maxima N^2 occur periodically at $R=l/d$ where l is an integer and N/d is the integral peak area. The integral width of the reflection is thus $1/(Nd)$. When N is large, the intensity $I_o(R)$ is written using a delta function

$$I_0(R) = (N/d) \sum_{l=-\infty}^{\infty} \delta(R - l/d) \qquad (7)$$

according to the following relationship

$$\sum_{n=-\infty}^{\infty} \delta(x - n x_0) = (1/x_0) \sum_{m=-\infty}^{\infty} \exp(i2\pi m x / x_0) \qquad (8)$$

Non-cumulative disorder. Assuming that δ_j and δ_k are independent and the distribution of δ_j is Gaussian with zero mean and mean square displacement $<\delta^2>$(Barakat, 1987), the statistical average of the displacement in (5) is given by

$$< \exp[i2\pi(\delta_j' - \delta_k')R] >=< \exp(i2\pi\delta_j' R) > \quad \text{and}$$

$$< \exp(-i2\pi\delta_k' R) >= \exp(-2M) \quad , \qquad (9)$$

where $M = 2\pi^2 R^2 <\delta^2>$. The term (9) has been called a Debye-Waller factor for thermal disorder. From (5) the intensity is given as

$$< I(R) >= N + \exp(-2M) \sum_{\substack{j=0 \\ j \neq k}}^{N-1} \sum_{k=0}^{N-1} \exp[i2\pi(j-k)dR] \qquad (10)$$

Substituting j-k by m, and replacing the double sum by a single sum yields

$$< I(R) >= N + \exp(-2M) \sum_{m=1}^{N-1} (N-m)[\exp(i2\pi m dR) + \exp(-i2\pi m dR)] \qquad (11)$$

The intensity corresponds to an independent oscillator model of thermal disorder and to static disorder of the first kind. Including the intensity function of $I_o(R)$ for a perfect lattice, we rewrite (11) as

$$< I(R) >= I_0(R) \exp(-2M) + N[1 - \exp(-2M)] \quad . \qquad (12)$$

The first term indicates that the Bragg intensity of the perfect lattice is reduced, and the second term contributes to the diffuse scattering.

Cumulative disorder. When the displacements δ_j' and δ_k' are not independent, Egelman and DeRosier (1982) and Barakat (1987) assumed that the deviation at the jth position is cumulative, then the jth displacement is written in terms of the previous ones as

$$\delta_j' = \sum_{t=1}^{j} \delta_t \quad . \qquad (13)$$

Substituting this in (5) yields

$$< \exp[i2\pi(\delta_j' - \delta_k')R] >=< \exp[i2\pi R(\sum_{t=1}^{j} \delta_t - \sum_{t=1}^{k} \delta_t)] > , \qquad (14)$$

which becomes $< \exp(i2\pi R \sum_{t=j+1}^{k} \delta_t) >$ for $k > j$, and $< \exp(i2\pi R \sum_{t=k+1}^{j} \delta_t) >$ for $k < j$. According to the multivariate characteristic function for zero-mean uncorrelated Gaussian random variables,

$$< \exp(\pm ib \sum_{t=m_1}^{m_2} a_t \delta_t) >= \exp[-b^2 < \delta^2 > (\sum_{t=m_1}^{m_2} a_t^2)/2] \qquad (15)$$

where a_t and b are constants, δ_t is a random variable, and $<\delta^2>$ is the mean square displacement (Barakat, 1987). Averaging over the δ_t in (14) leads to

$$< \exp[i2\pi(\delta_j - \delta_k)R] >= \exp(-2\pi^2 R^2 |j-k| < \delta^2 >) \quad \text{for } j \neq k \qquad (16)$$

This statistical average is the same as the one for a paracrystalline disorder of the second kind (Hosemann and Bagchi, 1962; Vainshtein, 1966; Inouye *et al*., 1989). Using this representation of the statistical average in (5), the intensity is given by

$$< I(R) >= N + \sum_{\substack{j=0 \\ j\neq k}}^{N-1}\sum_{k=0}^{N-1} \exp[i2\pi(j-k)dR]\exp(-2\pi^2 R^2 |j-k| < \delta^2 >) \quad (17)$$

Replacing the double sum by a single sum with $j\text{-}k=m$ $(1 \le m \le N\text{-}1)$ yields

$$< I(R) >= N + \sum_{m=1}^{N-1}(N-m)[\exp(i2\pi mdR) + \exp(-i2\pi mdR)]\exp(-2\pi^2 R^2 m < \delta^2 >) \quad (18)$$

This gives a closed form for a finite number of N (Vainshtein, 1966),

$$< I(R) >= \mathrm{Re}[N(1+F)/(1-F)] - 2\,\mathrm{Re}[(F - F^{N+1})/(1-F)^2] \quad (19)$$

where

$$F = \exp(-2\pi^2 R^2 < \delta^2 >)\exp(i2\pi dR)$$

and R_e refers to the real part of the function. When N is large, the second term is negligible, and (19) reduces to

$$< I(R) >= \frac{N(1-[H(R)]^2)}{1+[H(R)]^2 - 2[H(R)]\cos(2\pi dR)} \quad (20)$$

$$\text{with } H(R) = \exp(-2\pi^2 < \delta^2 > R^2).$$

Results & Discussion

X-ray diffraction from assemblies formed by prion-related peptides

The X-ray diffraction patterns of SHa106-122, SHa109-122 ("H1") (Nguyen *et al*., 1995; Inouye *et al*., 2000), and SHa113-120 (A8A) have been reported (Figure 3 and Table 1). SHa106-122 (Fig. 3A) and SHa109-122 (Fig. 3B) dried from 50% acetonitrile (AcN) solution show slightly oriented diffraction patterns while the lyophilized H1 (Fig. 3C) and A8A (Fig. 3D) dried from 50% AcN show powder patterns. The wide-angle reflections were indexed by a two-dimensional orthogonal lattice with a=9.5-9.6 Å and c=10.2-15.9 Å, where a is the hydrogen-bonding direction in the β sheet, and c is the intersheet direction. In the oriented patterns, the *(h0l)* reflections were accentuated on the meridian, indicating that the rotation axis is in the *b*-direction (or on the equator). Therefore, macroscopically the sample is slab-like, with the slabs stacked in the direction of the *b*-axis.

A strong low-angle reflection is observed at 73 Å for SHa106-122 (Fig. 3A; and Fig. 2A in Inouye *et al*., 2000), and at 40 Å for AcN-treated H1 (Fig. 3B; Table 1). In the former, subsequent broad intensity maxima are observed at 23 Å and 13 Å Bragg spacings. The strong reflection likely arises from a one-dimensional interference function *Z(R)* for the stacking of the slab-like structures with period *d*, and the broad maxima is from the Fourier transform of the unit slab of thickness *a* (Inouye *et al*., 2000). Considering the interference function of *Z(R)* as the average intensity function of the one-dimensional lattice with cumulative disorder (see above) - i.e., $<I(R)>$ in equation (20)-and using $<\delta^2> = \Delta^2$, the intensity function can be written as $I(R) = |F(R)|^2 Z(R)$, where R is the reciprocal coordinate of the real coordinate r along the slab stacking direction and the Fourier transform of a slab with thickness a is given by $F(R)=a\sin c(\pi aR)$. The parameters a = 33.6 Å and Δ = 18.5 Å for SHa106-122 having d = 73 Å were determined by searching for the minimum residual between the observed and calculated intensities (Inouye *et al*., 2000). The thickness of 33 Å gives a crucial constraint to the length of the extended β chain.

In the wide-angle region of the diffraction patterns the (201) reflection is strong, whereas the (200) reflection at ~4.7 Å Bragg spacing for A8A and for lyophilized H1 is much weaker or nonexistent, or for SHa106-122 and solubilized./dried H1 nearly as strong as the (201) reflection. This intensity distribution and the large lattice constant c indicate that the unit cell contains four β chains, and that neighboring β sheets are quarter-staggered in the hydrogen bonding direction (Figure 4A-D, left panels) as in β silk (Marsh *et al*., 1955). The intersheet distance is ~8 Å for SHa106-122 and solubilized/dried H1, but ~5 Å for lyophilized H1 and A8A. With the β silk backbone as an initial phase model, the structure amplitudes from the model were calculated, and compared with the structure amplitudes extracted from the observed intensity (Table 1). The electron density maps from the observed structure amplitudes and phases from the silk model for SHa106-122 and solubilized/dried H1 (Figure 4A,B: centre panels) show electron density peaks other than the ones expected from the peptide backbone. For lyophilized H1 and A8A the β silk backbone fit well with the observed electron density map (Figure 4C,D: centre panels). At this stage the *R*-factors (i.e., $R_{obs\text{-}amp}$) were 0.61 and 0,64 for SHa106-122 and solubilized/dried H1, 0.45 for

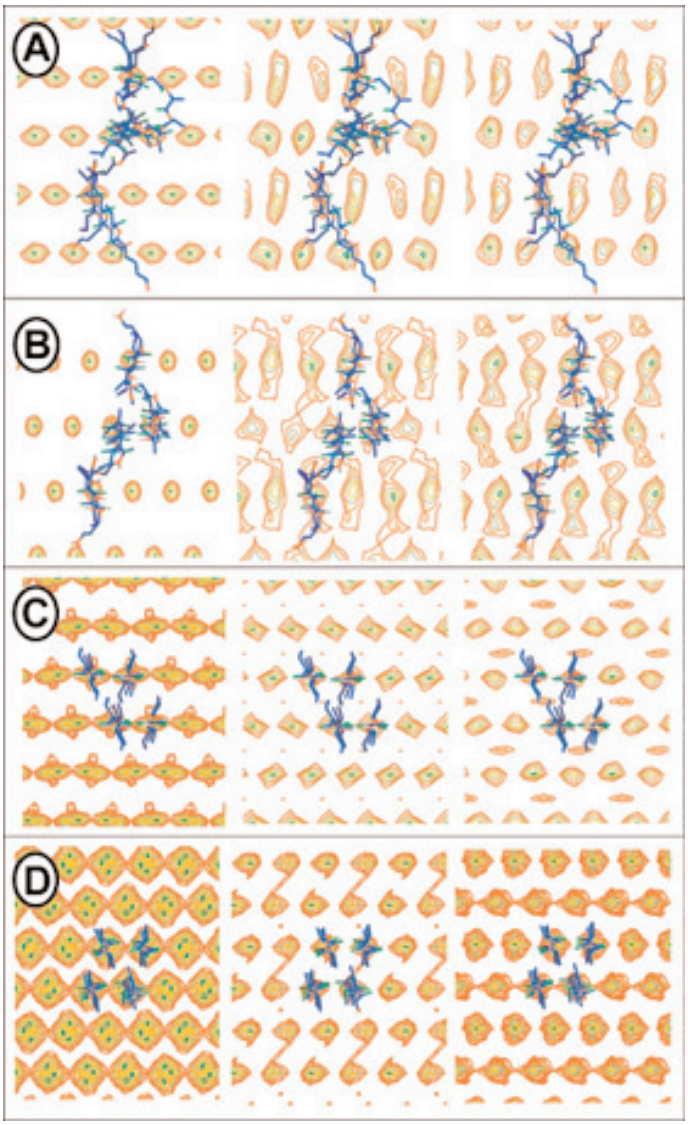

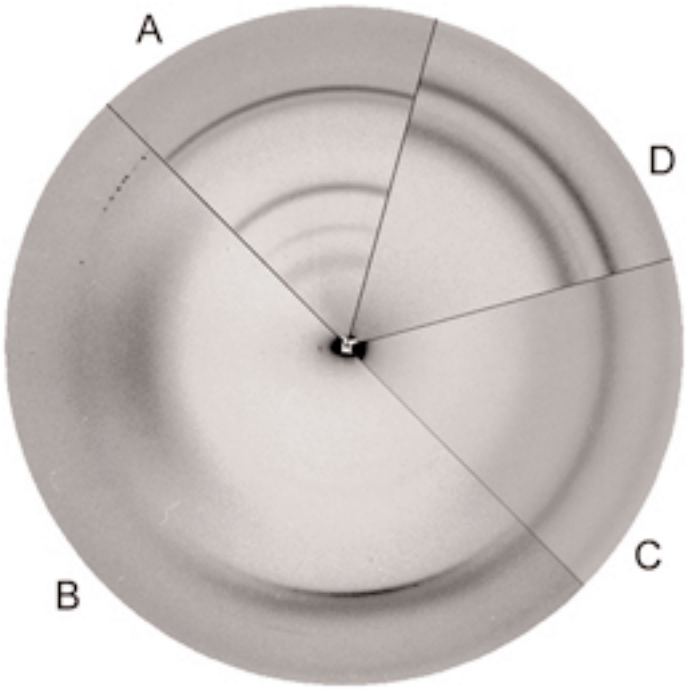

Figure 3. X-ray diffraction patterns of prion-related peptides. (A) SHa106-122 dried from 50% AcN. (A slight accentuation of the reflections was observed in the original diffraction pattern.); (B) H1 (SHa109-122) dried from 50% AcN; (C) lyophilized H1; and (D) A8A (SHa113-120) dried from 50% AcN. of SHa106-122 (Figure 2A in Inouye *et al*., 2000). Diffraction pattern (A) was previously reported by Inouye *et al*. (2000), and patterns (B)-(D) were reported by Nguyen *et al*. (1995). Note that the strongest reflection are: 4.56 Å (201) in (A); 4.77 Å (200) in (B); 4.44 Å (201) in (C); and 4.33 Å (201) in (D).

Figure 4. Electron density maps projected along the chain direction (*b*-axis) onto the plane defined by the H-bonding (*a*-axis; horizontal) and intersheet (*c*-axis; vertical) directions. (A) SHa106-122 dried from 50% AcN; (B) H1 domain dried from 50% AcN; (C) lyophilized H1; and (D) A8A. The unit cell projections in (A) and (B) contain two molecules, while the ones in (C) and (D) contain four molecules. The maps were calculated from: (*left*) amplitudes and phases from the initial model of β silk; (*center*) observed amplitudes and phases from β silk; and (*right*) observed amplitudes and phases from the prion model (shown as skeletal models for all maps). The contours show five levels of electron density; and the contour level steps were defined as one-tenth of the difference between the maximum and minimum electron densities, i.e., $\Delta\rho = (\rho_{max} - \rho_{main})/10$. The first contour level was given by $\rho_1 = \rho_{max} - \Delta\rho/2$, and subsequent ones were $\rho_2 = \rho_1 - \Delta\rho$, $\rho_3 = \rho_2 - \Delta\rho$, $\rho_4 = \rho_3 - \Delta\rho$, $\rho_5 = \rho_4 - \Delta\rho$. The *R*-factors for the initial silk model and the best prion model are indicated in Table 1.

lyophilized H1, and 0.33 for A8A (Table 1). The large R-factors for the first two peptides are probably due to not including in the initial model the side chains of the N-terminal domain. The molecular models of prion peptides including side chains were built and fit the electron density maps (Figure 4A-D, right panels).

Atomic models

In H1 (Figure 4B and 5A-C) the intra-chain turn creates two anti-parallel β-sheets, one that is constituted by the N-terminal larger residues, and the other by the alanine-rich region.. This structure agrees with the slab thickness as shown above and the larger and smaller electron density peaks. While three schematic molecular packings of H1 and SHa106-122 dried from AcN were suggested (Inouye *et al*., 2000), the structure amplitudes from the atomic models were not calculated in the past. We have now built the three models and rotated and translated the structures by XtalView to test them against the observed electron density maps (Figure 5A-C): in *Model 1*, the H1 molecules are registered, and the β chains are arranged anti-parallel (Figure 5A); in *Model 2* the H1 molecules are registered, and

Table 1. Summary of Bragg spacings (in Å) and *R*-factors from PrP-related peptides.

	Peptide			
	SHa106-122	H1 SHa109-122	H1 SHa109-122	A8A SHa113-120
Sample Preparation →	Dried from 50% AcN	Dried from 50% AcN	Lyophilized	Dried from 50% AcN
a (Å)	9.50	9.51	9.58	9.52
b (Å)	-	7.06	-	6.33
c (Å)	14.34	15.94	11.84	10.25
β (°)	90	88.41	90	90
$R_{obs\text{-}amp}$ (β-silk model)	0.61	0.64	0.45	0.33
$R_{obs\text{-}amp}$ (final)	0.34	0.24	0.36	0.36
	72.6 (Es)[a]	39.8 (Es)[a]	5.91 (Cw) (002)	31.9 (Cw)[a]
	23.2 (Ew)[b]	5.67 (Em) (110)	4.44 (Cs) (201)	5.13 (Cm) (002)
	12.8 (Ew)[b]	7.99 (Mw) (002)	3.73 (Cm) (202)	4.75 (Cw) (200)
	9,49 (Mw) (100)	4.77 (Ms) (200)	2.98 (Cvw) (004)	4.33 (Cs) (201)
	7.17 (Mm) (002)	4.57 (Mm) (201)		3.68 (Cw) (112)
	4.73 (Mm) (200)	3.94 (Mw) (004)		3.26 (Cvw)[c]
	4.56 (Ms) (201)	3.74 (Mm) (104)		2.82 (Cs)[c]
	3.19 (Cw) (300)	2.97 (Mw) (302)		
	2.86 (Cvw) (204)			

The Bragg spacings are cited in Inouye *et al*. (2000) for SHa106-122 dried from 50% AcN solution, and in Nguyen *et al*. (1995) for H1 (SHa109-122) lyophilized and dried from 50% AcN, and for A8A dried from 50% AcN. The unit cell lattice constants *a*, *b*, *c* and β are indicated, where *a*, *b* and *c* are in the H-bonding, β chain, and intersheet directions. The unit cell contains two β-chains in the H-bonding direction (along the *a*-axis) and two β-sheets in the intersheet direction (along the *c*-axis). (In Fig. 4, these correspond to the horizontal and vertical directions, respectively.) All the observed reflections in the oriented patterns of SHa106-122 and SHa109-122 (dried from 50% AcN) were indexed with the cylindrical (rotation) axis in the *b* direction. Because the meridional axis is defined to be in the direction of the ~4.7 Å H-bonding reflection, then the cylindrical axis in the oriented patterns is on the equator. The meridional location of the sharp (*h0l*) reflections indicates, therefore, that the scattering object is slab-like.

[a]These low-angle reflections likely arise from the interference between slab-like or fibrillar structures that are stacked.

[b]These broad intensity maxima likely arise from the Fourier transform of the slab-like unit.

[c]These reflections are likely from NaCl.

the N-terminal and C-terminal β chains are in a parallel β-sheet conformation (Figure 5B); and in *Model 3* the H1 molecules are staggered in the intersheet direction and the β chains are anti-parallel (Figure 4B, right, and 5C). The models were then used to calculate the structure factors for comparison with the observed amplitudes. The calculated *R*-factors ($R_{amp\text{-}obs}$) were found to be 0.46 for the anti-parallel registered arrangement, 0.37 for the parallel registered arrangement, and 0.24 for the staggered arrangement (Table 1). A similar staggered assembly of reverse-turn SHa106-122 molecules gave an R-factor of 0.34 (Figure 4A, right); and the atomic model for the N-terminal alanine-rich domain in lyophilized H1 (Figure 4C, right, and 5D) and for A8A gave similar R-factors of 0.36 (Figure 4D, right), which is nearly the same as the initial *R*-factor derived using the β silk backbone (Table 1).

Molecular interpretation

Lysine residues are spatially localized close to one another (as are histidine residues) in both the anti-parallel and parallel β chain models (Figure 5A,B); however, because of electrostatic repulsion, such arrangements may not be stable. In the staggered arrangement (Figure 5C), by contrast, the histidine and lysine residues are close together. If the positive-charged lysine residue is directed toward the aromatic ring of the histidine, the staggered arrangement may, in fact, be stabilized. In this arrangement His111 of one molecule is closely positioned to Lys110 of the neighboring molecule. The atomic model indicates that the neighboring residues of His111 are Ala113, Ala117, and Lys110. When a larger valine residue substitutes for Ala117 in the GSS mutation, His111 will interact with valine more strongly due to van der Waals contacts. Thus, in PrP having the GSS substitution the folded β sheet structure may be stabilized. The interaction between

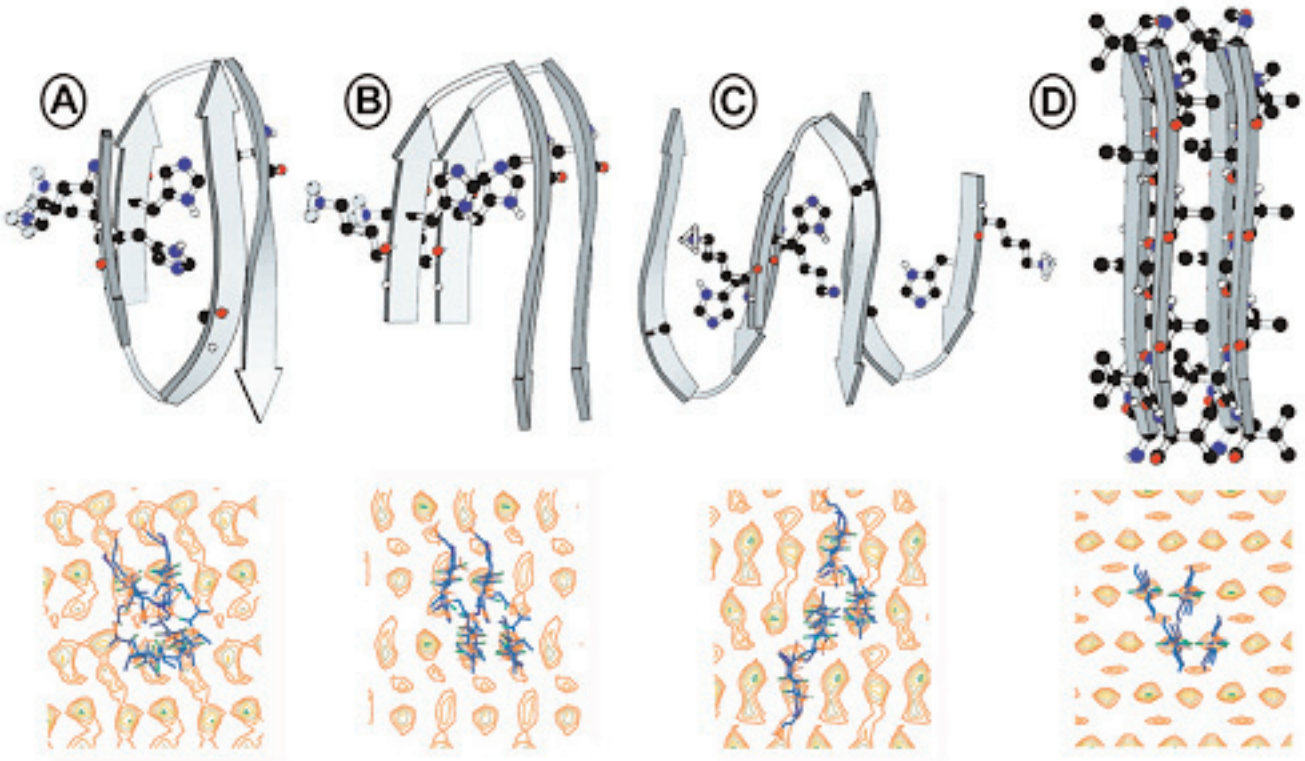

Figure 5. Molscript representations (*upper*) and electron density projections (*lower*) based on structural analysis of X-ray fibre diffraction patterns of H1 (SHa109-122). (A) anti-parallel, (B) parallel, and (C) staggered arrangement of H1 dried from 50% AcN; and (D) lyophilized H1. *Upper*: The molecular model which fits the observed electron density map shows two β chains, where Gly114-Ala115 are at the g inverse turn (as defined by STRIDE; Frishman and Argos, 1995). Lys110, His111 and Ala117 are indicated by the ball and stick models. Note that the Lys side chains (and those of His) are close together in the anti-parallel and parallel arrangements while Lys and His are adjacent to one another in the staggered arrangement (C). In the lyophilized sample (D), the alanine-rich domain as a β strand fits the electron density distribution, and the 3F4 domain is likely disordered (not shown). *Lower*: XtalView representations of skeletal models superposed on the electron density projection along the chain direction of H1. H-bonding is horizontal, and the intersheet direction is vertical.

histidine and lysine is not unprecedented. For example, the NMR structure of CD59 (which inhibits formation of the membrane attack complex) shows that lysine interacts with histidine, and forms a motif that marks this complement regulator as a potential glycation target (Fletcher *et al*., 1994; Acosta *et al*., 2000).

Comparison with previous models of binding interface

Arguments based on sequence differences and the species barrier to prion infectivity have led to the suggestion that the 3F4 antibody-specific epitope (residues 109-112) is at the binding interface for the PrP^{C}-PrP^{Sc} heterodimer (Schätzl *et al*., 1995; Warwicker, 1997). The binding interface was established by identifying peptides that can inhibit the cell-free replication of PrP^{Sc}. Such peptides likely interact at the heterodimer interface and block the binding of PrP^{C} to PrP^{Sc}. Horiuchi *et al*. (2001) found that peptides SHa119-136, SHa166-179 and SHa200-223 inhibit the binding, and Chabry *et al* (1998) identified SHa106-141 as having a similar effect. Since the 3F4 epitope in the PrP^{Sc} isoform is not reactive to the antibody (Peretz *et al*., 1997), the molecular conformation of this region most likely changes when heterodimerization occurs, such that the domain becomes exposed on the surface of the protein. Previous molecular modelling (Warwicker, 2000) suggested that the interface is Ala118-Ala133 and that the corresponding domains of the two molecules interact with each other. This domain was modeled as a reverse-turn anti-parallel b chain with the turn at Gly126-Gly127. The side chain interaction in the intersheet direction was via H-bonding between the S atom of Met129 and N-H in Gly124, and via van der Waals interactions between Val122 side chains. This model, however, agrees neither with our model which shows the turn in the H1 domain (residues 109-122; γ inverse turn as indicated by STRIDE; Nguyen *et al*., 1995; Inouye and Kirschner, 1998) nor with the crystallographic finding of an Ω turn that involves residues 104-113 near the 3F4 epitope (Kanyo *et al*., 1999). While neighboring β chains appear to be hydrogen-bonded

to one another in most proteins (as in the PrP dimer: Warwicker, 2000), there are examples (like in H1) where the two β chains are not H-bonded but interact across the intersheet space, e.g., the Ω turn for the Fab3F4 epitope in prion (Kanyo *et al*., 1999), and turn II (residues 7-20) of bovine myelin P0-glycoprotein (Shapiro *et al*., 1996). Molecular dynamics simulation (Levy *et al*., 2001) also shows a similar reverse-turn model with the two chains interacting across the intersheet space of PrP106-126.

Conclusion

From an analysis of X-ray fibre diffraction patterns of prion-related peptides, we observed structural polymorphism (two different conformations) for the H1 domain-one folded and the other unfolded. In the former the 3F4 epitope region is a β chain, while in the latter the epitope does not assume this conformation and is likely to be exposed on the protein surface. The folded structure is stabilized by an interaction between His111 and Ala117. Cell-free replication of PrP requires a partial denaturation of PrP^{Sc} which exposes the 3F4 epitope domain on the protein surface. The conformational transformation, termed template breathing (Caspi *et al*., 1998), therefore, involves the folding → unfolding of the H1 domain. The intermolecular packing characterized by our fibre diffraction analysis indicates that the alanine-rich domains are hydrogen-bonded together, which may be the major binding force driving the interaction of PrP^{C} and PrP^{Sc}.

Acknowledgements

For discussions and/or collaborations over the past eight years that have contributed to our application of fibre diffraction to understanding the organization of PrP, we gratefully acknowledge Mr. J.P. Bond and Drs. J.T. Nguyen, R.J. Fletterick, F.E. Cohen, M.A. Baldwin, H.L. Ball, and S.B. Prusiner. The research in our lab was supported by an Alzheimer's Association/T.L.L. Temple Discovery Award (D.A.K.), the Alzheimer's Disease Research Program of the American Health Assistance Foundation (D.A.K.), and institutional support from Boston College.

References

[1] Acosta, J., Hettinga, J., Fluckiger, R., Krumrei, N., Goldfine, A., Angarita, L., & Halperin, J. (2000) Molecular basis for a link between complement and the vascular complications of diabetes. *Proc. Natl. Acad. Sci. USA* **97**, 5450-5455.

[2] Barakat, R. (1987) X-ray scattering from helical structures possessing random variable twist. *Acta. Cryst*. **A43**, 45-49.

[3] Caspi, S., Halimi, M., Yanai, A., Sasson, S.B., Taraboulos, A. & Gabizon, R. (1998) The anti-prion activity of Congo red. *J. Biol. Chem*. **273**, 3484-3489.

[4] Cella, R.J., Lee, B. & Hughes, R.E. (1970) Lorentz and orientation factors in fibre X-ray diffraction analysis. *Acta Cryst.* **A26**, 118-124.

[5] Chabry, J., Caughey, B., & Chesebro, B. (1998) Specific inhibition of in vitro formation of protease-resistant prion protein by synthetic peptides. *J. Biol. Chem.* **273**, 13203-13207.

[6] Donne, D.G., Viles, J.H., Groth, D., Mehlhorn, I., Jamesm T.L., Cohen, F.E., Prusiner, S.B., Wright, P.E. & Dyson, H.J. (1997) Structure of the recombinant full-length prion protein PrP(29-231): The N terminus is highly flexible. *Proc. Natl. Acad. Sci. USA* **94**, 13452-13457.

[7] Egelman, E.H. & DeRosier, D.J. (1982) The Fourier transform of actin and other helical systems with cumulative random angular disorder. *Acta Cryst.* **A38**, 796-799.

[8] Fletcher, C.M., Harrison, R.A., Lachmann, P.J., & Neuhaus, D. (1994) Structure of a soluble, glycosylated form of the human complement regulatory protein CD59. *Structure*. **2**, 185-199.

[9] Frishman, D. & Argos, P. (1995) Knowledge-based protein secondary structure assignment. *Proteins*. **23**, 566-579.

[10] Guex, N., Diemand, A., & Peitsch, M.C. (1999) Protein modelling for all. *Trends Biochem. Sci*. **24**, 364-367.

[11] Horiuchi, M., Baron, G.S., Xiong, L.W., & Caughey, B. (2001) Inhibition of interactions and interconversions of prion protein isoforms by peptide fragments from the C-terminal folded domain. *J. Biol. Chem*. **276**, 15489-15497.

[12] Hosemann, R. & Bagchi, S.N. (1962) *Direct Analysis of Diffraction by Matter*, North-Holland Publishing Co., Amsterdam.

[13] Inouye, H. (1994) X-ray scattering from a discrete helix with cumulative angular and translational disorders. *Acta Cryst*. **A50**, 644-646.

[14] Inouye, H., Bond, J.P., Baldwin, M.A., Ball, H.L., Prusiner, S.B., & Kirschner, D.A. (2000) Structural changes in a hydrophobic domain of the prion protein induced by hydration and by Ala → Val and Pro → Leu substitutions. *J. Mol. Biol.* **300**, 1283-1296.

[15] Inouye, H., Fraser, P.E., & Kirschner, D.A. (1993) Structure of β-crystallite assemblies formed by Alzheimer β-amyloid protein analogues: Analysis by X-ray diffraction. *Biophys. J*. **64**, 502-519.

[16] Inouye, H., Karthigasan, J., & Kirschner, D.A. (1989) Membrane structure in isolated and intact myelins. *Biophys. J*. **56**, 129-137.

[17] Inouye, H. & Kirschner, D.A. (1996) Refined fibril structures: The hydrophobic core in Alzheimer's β-amyloid and prion as revealed by X-ray diffraction. *In: The Nature and Origin of Amyloid Fibrils*, Ciba Foundation Symposium No. 199, p. 22-39, John Wiley & Sons, Chichester, UK and New York, NY.

[18] Inouye, H. & Kirschner, D.A. (1997) X-ray diffraction analysis of scrapie prion: Intermediate and folded structures in a peptide containing two putative α-helices. *J. Mol. Biol*. **268**, 375-389.

[19] Inouye, H. & Kirschner, D.A. (1998) Polypeptide chain

folding in the hydrophobic core of hamster scrapie prion: Analysis by X-ray diffraction. *J. Struct. Biol*. **122**, 247-255.
[20] James, T.L., Liu, H., Ulyanov, N.B., Farr-Jones, S., Zhang, H., Donne, D.G., Kaneko, K., Groth, D., Mehlhorn, I., Prusiner, S.B., & Cohen, F.E. (1997) Solution structure of a 142-residue recombinant prion protein corresponding to the infectious fragment of the scrapie isoform. *Proc. Natl. Acad. Sci. USA* **94**, 10086-10091.
[21] Kabsch, W., & Sander, C. (1983) Dictionary of protein secondary structure: Pattern recognition of hydrogen-bonded and geometrical features. *Biopolymers* **22**, 2577-2637
[22] Kanyo, Z.F., Pan, K.M., Williamson, R.A., Burton, D.R., Prusiner, S.B., Fletterick, R.J. & Cohen, F.E. (1999) Antibody binding defines a structure for an epitope that participates in the $PrP^{C} \rightarrow PrP^{Sc}$ conformational change. *J. Mol. Biol*. **293**, 855-63.
[23] Kitamoto, T., Iizuka, R. & Tateishi, J. (1993) An amber mutation of prion protein in Gerstmann-Sträussler syndrome with mutant PrP plaques. Biochem. *Biophys. Res. Commun.* **192**, 525-531.
[24] Knaus, K.J., Morillas, M., Swietnicki, W., Malone, M., Surewicz, W.K. & Yee, V.C. (2001) Crystal structure of the human prion reveals a mechanism for oligomerization. *Nature Struct. Biol*. **8**, 770-774.
[25] Kocisko, D.A., Come, J.H., Priola, S.A., Chesebro, B., Raymond, G.J., Lansbury, P.T. & Caughey, B. (1994) Cell-free formation of protease-resistant prion protein. *Nature* **370**, 471-474.
[26] Kraulis, P.J. (1991) MOLSCRIPT: A program to produce both detailed and schematic plots of protein structures. *J. Appl. Crystallogr*. **24**, 946-950.
[27] Levy, Y., Hanan, E., Solomon, B. & Becker, O.M. (2001) Helix-coil transition of PrP106-126: Molecular dynamic study. *Proteins: Structure, Function and Genetics*. **45**, 382-396.
[28] Liu, H., Farr-Jones, S., Ulyanov, N.B., Llinas, M., Marqusee, S., Groth, D., Cohen, F.E., Prusiner, S.B. & James, T.L. (1999) Solution structure of Syrian hamster prion protein rPrP(90-231). *Biochemistry* **38**, 5362-5377.
[29] Lopez Garcia, F., Zahn, R., Riek, R. & Wüthrich, K. (2000) NMR structure of the bovine prion protein. *Proc. Natl. Acad. Sci. USA* **97**, 8334-8339.
[30] Makowski, L. (1988) Preparation of magnetically oriented specimens for diffraction experiments. In *Brookhaven Symposium - Synchrotron Radiation in Biology*. R.M. Sweet and A.D. Woodhead, Editors. New York, Plenum Press, pp. 341-347.
[31] Marsh, R.E., Corey, R.B. & Pauling, L. (1955) The structure of Tussah silk fibroin. *Acta Cryst*. **8**, 710-715.
[32] McRee, D.E. (1992) A visual protein crystallographic software system for X11/XView. *J. Mol. Graph*. **10**, 44-46.
[33] Nguyen, J.T., Inouye, H., Baldwin, M.A., Fletterick, R.J., Cohen, F.E., Prusiner, S.B. & Kirschner, D.A. (1995) X-ray diffraction of scrapie prion rods and PrP peptides. *J. Mol. Biol*. **252**, 412-422.
[34] Oldenbourgh, R. & Phillips, W.C. (1986) Small permanent magnet for field up to 2.6T. *Rev. Sci. Instrum*. **57**, 2362-2365.
[35] Pan, K-M., Baldwin, M., Nguyen, J., Gasset, M., Serban, A., Groth, D., Mehlhorn, I., Huang, Z., Fletterick, R.J., Cohen, F.E. & Prusiner, S.B. (1993) Conversion of α-helices into β-sheets features in the formation of the scrapie prion proteins. *Proc. Natl. Acad. Sci. USA*. **90**, 10962-10966.
[36] Peretz, D., Williamson, R.A., Matsunaga, Y., Serban, H., Pinilla, C., Bastidas, R.B., Rozenshteyn, R., James, T.L., Houghten, R.A., Cohen, F.E., Prusiner, S.B. & Burton, D.R. (1997) A conformational transition at the N-terminus of the prion protein features in formation of the scrapie isoform. *J. Mol. Biol*. **273**, 614-622.
[37] Prusiner, S.B. (1991) Molecular biology of prion diseases. *Science* **252**,1515-1522.
[38] Prusiner, S.B., McKinley, M.P., Bowman, K.A., Bolton, D.C., Bendheim, P.E., Groth, D.F. & Glenner, G.G. (1983) Scrapie prions aggregate to form amyloid-like birefringent rods. **Cell 35**, 349-358.
[39] Riek, R., Hornemann, S., Wider, G., Billeter, M., Glockshuber, R. & Wüthrich, K. (1996) NMR structure of the mouse prion protein domain PrP(121-231). *Nature* **382**, 180-182.
[40] Safar, J., Wille, H., Itri, V., Groth, D., Serban, H., Torchi, M., Cohen, F.E. & Prusiner, S.B. (1998) Eight prion strains have PrP^{Sc} molecules with different conformations. *Nature Med*. **4**, 1157-1165.
[41] Schätzl, H.M., DaCosta, M., Taylor, L., Cohen, F.E., & Prusiner, S.B. (1995) Prion protein gene variation among primates. *J. Mol. Biol*. **245**, 362-374.
[42] Stahl, N., Baldwin, M.A., Teplow, D.B., Hood, L., Gibson, B.W., Burlingame, A.L. & Prusiner, S.B. (1993) Structural analysis of the scrapie prion protein using mass spectroscopy and amino acid sequencing. *Biochemistry* **32**, 1991-2002.
[43] Vainshtein, B.K. (1966) *Diffraction of X-rays by Chain Molecules*. Amsterdam: Elsevier.
[44] Viles, J.H., Cohen, F.E., Prusiner, S.B., Goodin, D.B., Wright, P.E. & Dyson, H.J. (1999) Copper binding to the prion protein: Structural implications of four identical cooperative binding sites. *Proc. Natl. Acad. Sci. USA* **96**, 2042-2047
[45] Warwicker, J. (1997) Species barriers in a model for specific prion protein dimerization. Biochem. *Biophys. Res. Commun*. **232**, 508-512.
[46] Warwicker, J. (2000) Modelling a prion protein dimer: Predictions for fibril formation. Biochem. *Biophys. Res. Commun*. **278**, 646-652.
[46] Zahn, R., Liu, A.Z., Luhrs, T., Riek, R., von Schroetter, C., Garcia, F.L., Billeter, M., Calzolai, L., Wider, G. & Wüthrich, K. (2000) NMR solution structure of the human prion protein. *Proc. Natl. Acad. Sci. U.S.A.* **97**, 145-150.

Structure - Property Relationships for Polyisocyanurates with Varied Modulus

A-L. Abbott, M.L. Turner, A.J. Ryan

The Department of Chemistry, University of Sheffield, S3 7HF, U.K.

Introduction.

Vibrations in mechanical parts create unwanted noise and cause wear. Viscoelastic materials act as good damping agents due to their ability to absorb vibrational energy. The construction of elastomers with a range of glass transition temperatures, T_g, has been predicted to give the optimum performance when these materials are used as damping coatings[1]. A polyisocyanurate system was employed to achieve controlled variation in the density of cross-links and therefore T_g. Both static and dynamic Nanoindentation have been used in conjunction with Small Angle X-Ray Scattering (SAXS) to investigate how the mechanical properties of these materials are affected by microphase separation.

Experimental Procedure

Polyisocyanurates were prepared via a two-stage reaction pathway [2]. Various lengths of polyether were end-capped by the reaction between methylenediphenyldiisocyanate and poly-propyleneoxide forming a urethane bond. The trimerisation of the isocyanate end groups was then undertaken using a heat activated catalyst, enabling processing of the liquid 'prepolymer' before network formation. Thus a range of materials, with polyether molecular weights varying from 192 to 8200, and hard segment (isocyanurate and excess diisocyanate) content from 15 to 80% have been prepared. The length of polyether chain used and the density of cross-links determined the modulus of the resultant material.

Mechanical Properties - Nanoindentation

Mechanical measurements were made using a Triboscope® Nanomechanical test system made by Hysitron Inc. This is an adapted Scanning Probe Microscope with the SPM head (cantilever and detector) replaced with a Hysitron transducer, giving accurate numerical data from precise nanoindents and *in situ*, high resolution, surface imaging [3,4].

Figure 1 shows indents made in a 425 54% sample from static nanoindentation and figure 2 shows values of reduced modulus obtained from a number of polyether M_w and hard segment contents. A consistent value is obtained after overcoming surface effects by applying higher loads.

The nanoindentor has been fitted with a heating stage to allow a much larger range of dynamic mechanical data to be collected. A set load was applied and the tip oscillated ±5% of this load. Figure 3 shows the results of time - temperature - superposition for 725 40% after performing frequency sweeps of 10 - 110 Hz at temperatures ranging from 15 to 60 °C. The maximum in tan δ, seen at 35 - 40°C corresponds to the T_g for this material as obtained by Differential Scanning Calorimetry.

Structure Development - Small Angle X-Ray Scattering

SAXS measurements were carried out on Beamlines 8.2 of the SRS, Daresbury Laboratory, Warrington, U.K., details of which have previously been recorded [5]. Static measurements were taken by mounting the polyisocyanurate sample in the X-Ray beam. Time-resolved measurements monitoring the curing of the prepolymer were taken by loading DSC pans fitted with mica windows with prepolymer and trimerisation catalyst. Samples were heated from 25°C to 120 °C at 50 °C minute^{-1} and held there until no further change was seen. Data were collected in 6 second frames.

Figures 4a and 4b show Lorentz corrected SAXS patterns from a range of 2200 and 4200 M_w polyether segment polyisocyanurates with varying hard segment contents. As indicated by the maximum peak height occurring at lower q, domain spacing increases with hard segment content and

with polyether segment length. The development of phase separation in 2200 M_w polyether segment with increasing amounts of hard segment content can be see in Figures 5a, 5b and 5c.

Relating Structure to Mechanical Properties

For each prepolymer length, as the hard segment content increases, the modulus increases. However, whilst the d-spacing increases with polyether length, the modulus decreases. Highest modulus polyisocyanurates are not phase separated. The highest tan δ values are seen from phase separated materials with larger polyether length and smaller d-spacings.

References

[1] Sperling, L.H., (1990), 'Sound and vibration damping with polymers - basic viscoelastic definitions and concepts' *American Chemical Society Symposium Series*, **424**, 5 - 22.

[2] Wang, C.L., Klempner, D. and Frisch, K.C., (1985), 'Morphology of polyurethane isocyanurate elastomers' *Journal of Applied Polymer Science*, **30**, 4337 - 4344.

[3] VanLandingham, M.R., Villarrubia, J.S., Guthrie, W.F., and Meyers, G.F., (2001), 'Nanoindentation of Polymers: An overview' *Macromolecular Symposia*, **167**, 15 - 43.

[4] Oliver, W.C. and Pharr, G.M., (1992), 'An improved technique for determining hardness and elastic modulus using load and displacement sensing indentation experiments' *Journal of Materials Research*, **7**, 1564 - 1583.

[5] Bras, W., Derbyshire, G.E., Ryan, A.J., Mant, G.R., Felton, A., Lewis, R.A., Hall, C.J. and Greaves, G.N., (1993), 'Simultaneous time resolved SAXS and WAXS experiments using synchrotron radiation' Nuclear Instruments and Methods in *Physics Research A*, **326**, 587 - 591.

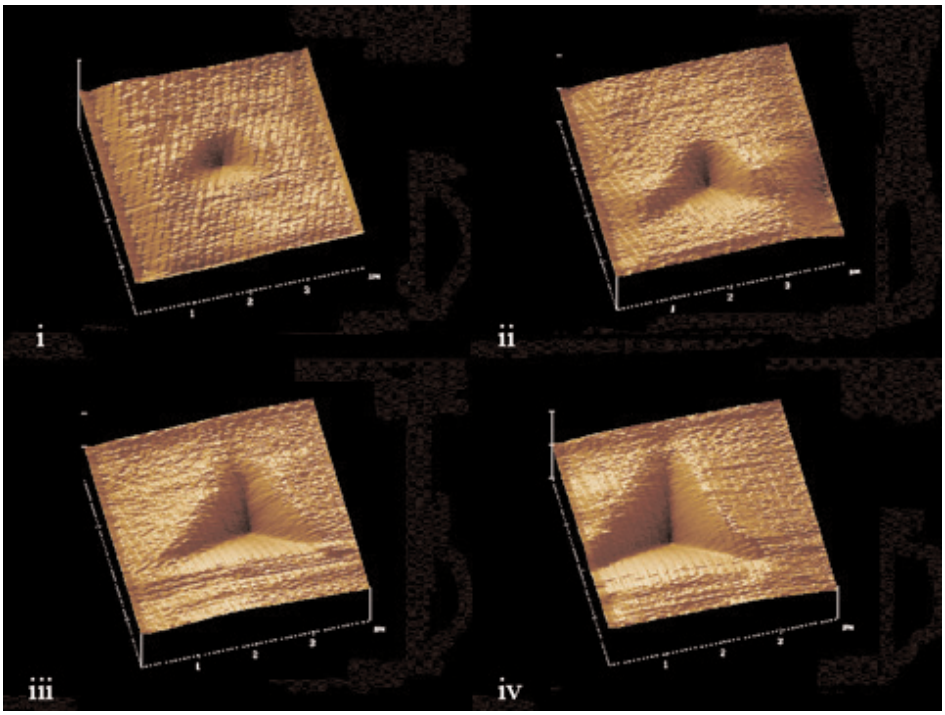

Figure 1: Images obtained after indentation with loads of **(i)** 50, **(ii)** 100, **(iii)** 150 and **(iv)** 200 μN .

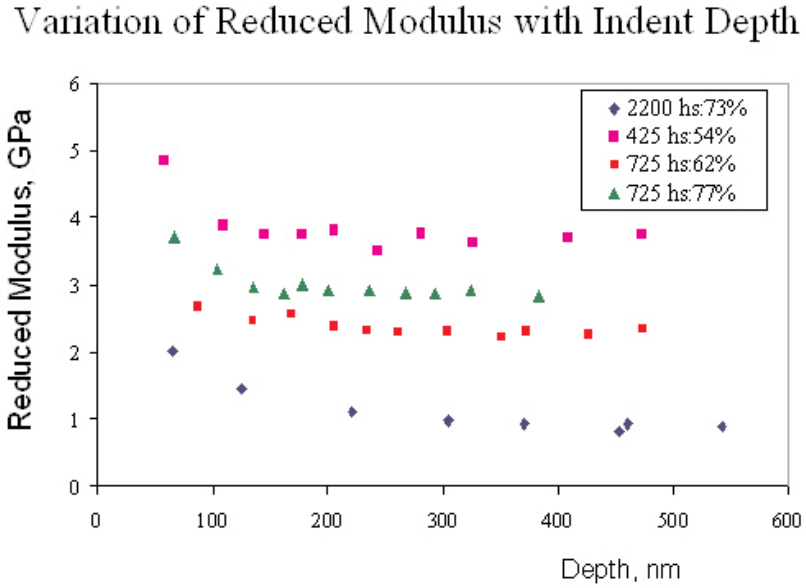

Figure 2: The variation in obtained modulus with indent load for 4 polyisocyanurates with varying polyether segment length and hard segment content.

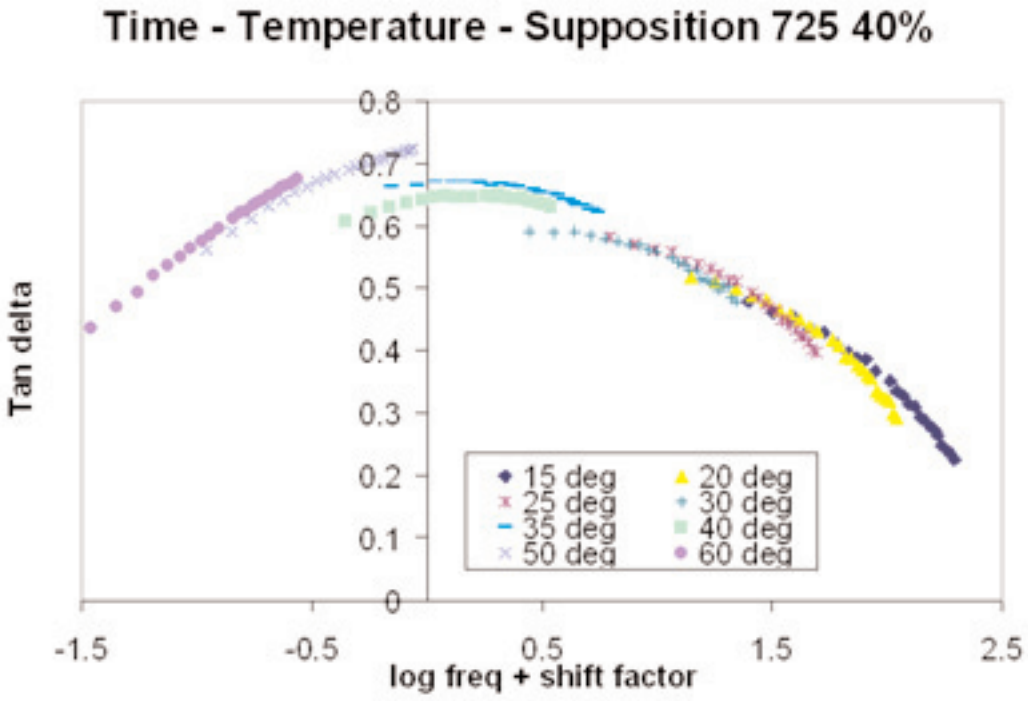

Figure 3: Time-Temperature-Superposition according to the WLF equation for sample 725 M_w polyether with 40% hard segment content

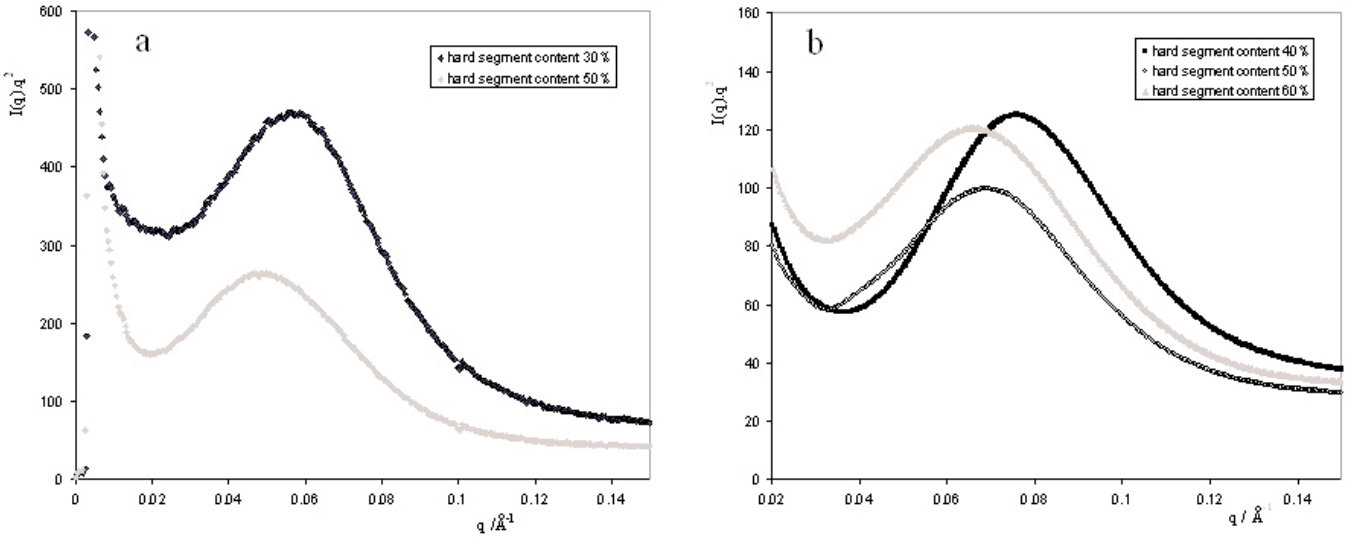

Figure 4: Lorentz corrected SAXS patterns for 2 different prepolymer lengths with varying amounts of hard segment content - **a)** 2200 M_w prepolymer, d-spacing for 40% - 81 Å, 50% - 90 Å, 60% - 97 Å and **b)** 4400 Mw prepolymer, d-spacing for 30% - 108 Å and 50% - 128 Å

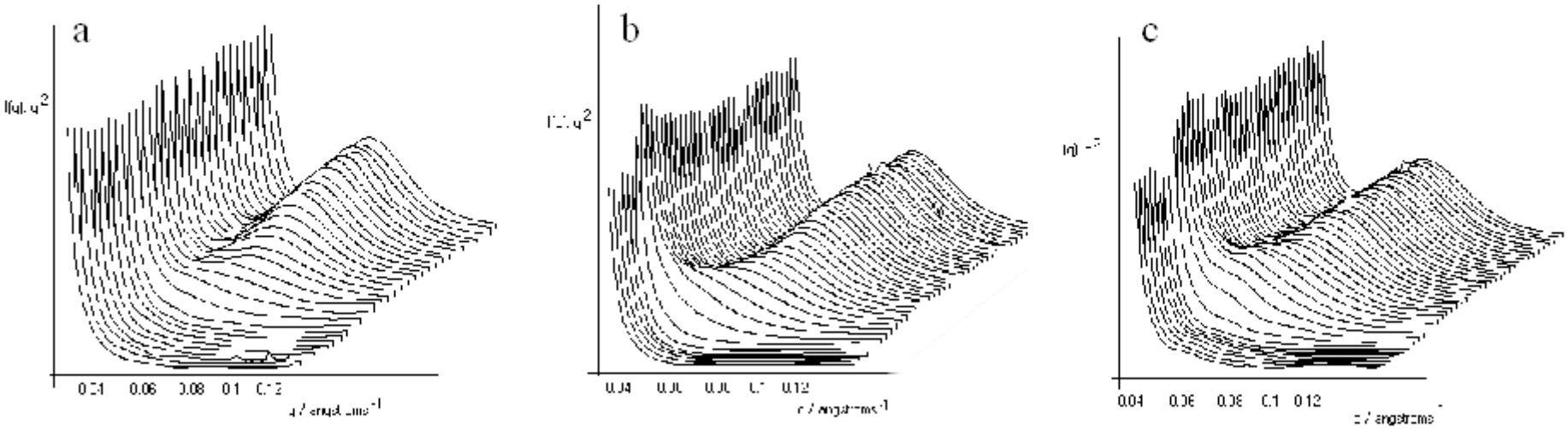

Figure 5: Lorentz corrected SAXS patterns showing the development of phase separation in 2200 M_w polyether segment with a) 40%, b) 50% and c) 60% hard segment content.

Analysis of collagen structure in parchment by Small angle X-ray diffraction

C.J. Kennedy[1], K. Nielsen[2], L. Ramsay[3] and T.J. Wess[1].

[1] Centre for Extracellular Matrix Biology, Department of Biological Sciences, University of Stirling, Stirling, FK9 4LA
[2] Department of Chemistry, Technical University Denmark, 2800, Lyngby, Denmark
[3] National Archives for Scotland, Thomas Thomson House, 99 Bankhead Crossway North, Edinburgh, EH11 4DX

Parchment has the characteristic molecular packing associated with other collagen rich structures, particularly skin. A wealth of information is available about the structure of collagen and its hierarchical arrangements from the molecular structure to the organisation of fibres in a tissue. X-ray diffraction of collagen has provided information about the molecular organisation of individual collagen molecules and the way that they pack together to form fibrils.

The main consideration with understanding the structure of parchment at the molecular level is that the collagen within parchment has undergone deterioration due to external factors. It is important to assess this deterioration for the conservation of historically important documents. Collagen deterioration at the molecular level corresponds to the breakage of covalent bonds and a subsequent increase in molecular disorder. With increasing molecular disorder the hierarchical organisation of collagen, from the molecular to the mesoscopic levels (Figure 1), is compromised.

Small angle X-ray diffraction provides a means of monitoring changes in the physical organisation of the collagen within the parchment sample. With increasing disorder, the characteristic pattern of collagen from parchment changes and displays less of an organised structure.

Principal Components Analysis (PCA) is a statistical technique that is capable of describing the nature and degree of variance in a data set. PCA of linear profiles of X-ray diffraction patterns (Figure 2) is capable of describing changes in the linear traces such as variations in the levels of diffuse scatter, the presence or absence of collagen or lipids, the crystallinity of the samples and changes in the periodicity of the collagen arrangement. This allows for a more detailed and quantifiable analysis of discrete changes occurring within parchment that can be detected by X-ray diffraction (Figure 3).

By using X-ray diffraction and PCA, subtle changes brought about in parchment, for instance gelatinisation and alterations in the structural organisation of collagen, can be analysed. External factors that may contribute to parchment deterioration include short-term factors such as fire, flood or conservation techniques and longer-term factors such as humidity and pollution levels. The effect of these factors can subsequently be stated in terms of damage assessment of parchment.

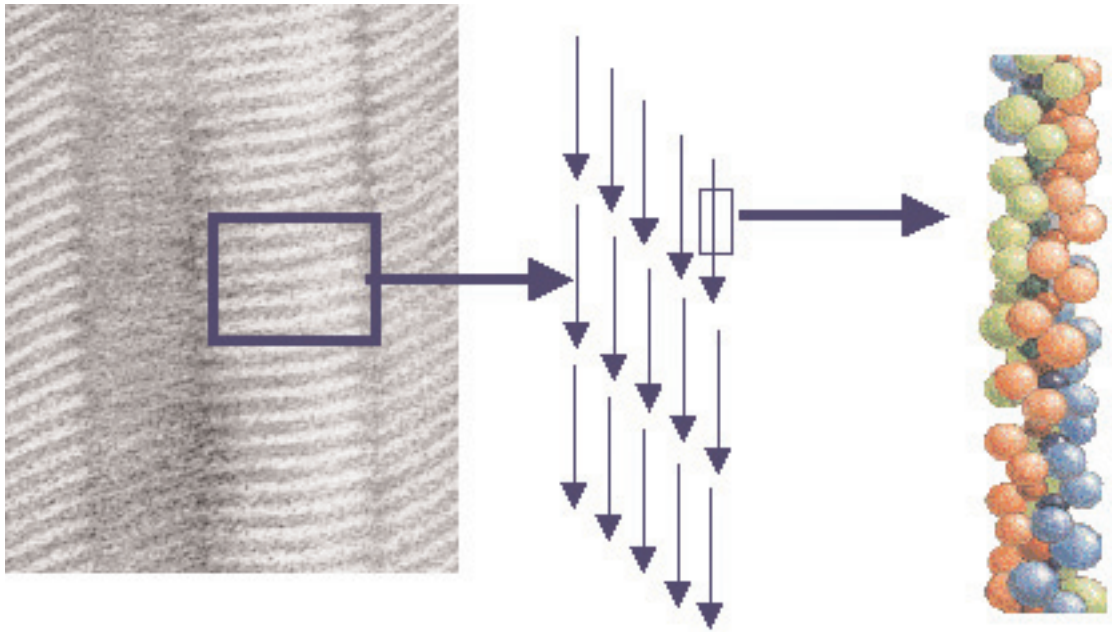

Figure 1. The hierarchical arrangement of collagen from parchment. (a)Transmission Electron Microscope image of collagen. The banding pattern is characteristic of the repeating gap/overlap function of collagen, which has a 67 nm axial repeat or D-period. This exists at the mesoscopic level. (b) Representation of the quarter-staggered arrangement of collagen molecules within a fibril at the nanoscopic level. (c) Diagram of the collagen triple helix; this exists at the molecular level, where the sidegroups of individual amino acids are shown as spheres..

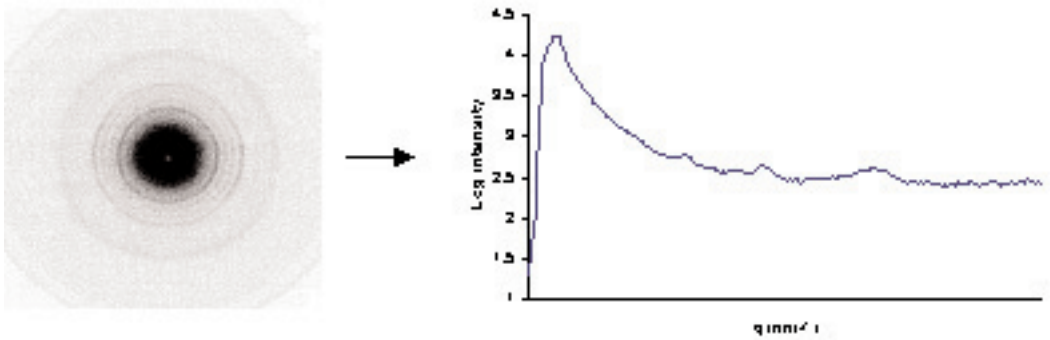

Figure 2. Small angle X-ray diffraction pattern from parchment sample USH01 and the linear profile of its radial integration. Discernible are the 6th, 7th, 8th and 9th orders of the collagen D-period and also the lipid ring.

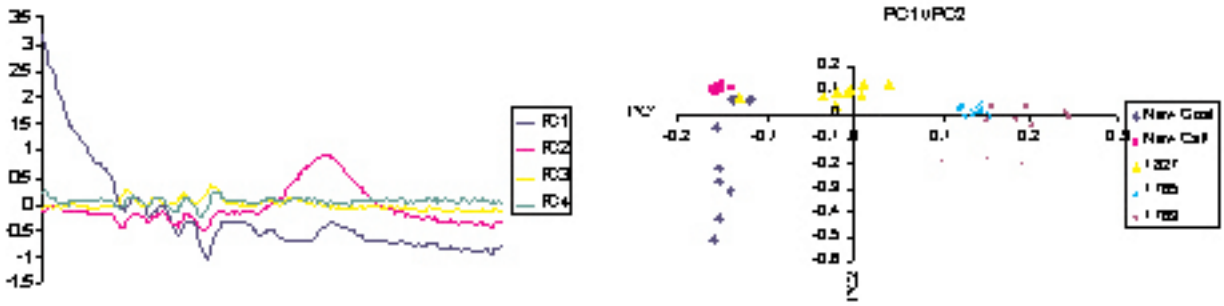

Figure 3. Principal components analysis results from a data set of forty linear traces from five different parchment samples. (a) The principal components. These four components account for over 97% of the variance in the data set. PC1 can be interpreted as variations in the diffuse scatter in the samples. PC2 accounts for the lipid ring. PC3 and PC4 display minor changes in the collagen D-period. (b) The correlation coefficients of the original data to the principal components 1 and 2. If the original data shows positive correlations to the principal components then the features of the principal components are present; if the correlation is zero then the feature is not present; if the correlation is negative then the feature is the reverse of the component. There is a clear grouping of the samples in the correlation coefficient scatter plot.

X-ray diffraction of rat tail tendon at ambient and cryo-cooled temperatures - a comparison

J. H. Laing, J.P.R.O. Orgel, J. Dubochet; A. Al-Amoudi; T. J. Wess, G. J. Cameron, C. Laurie

Biophysics Group, Dept. of Optometry and Vision Sciences, Cardiff University, Redwood Building, King Edward VII Avenue, Cardiff CF10 3NB, Wales UK.

Introduction

Rat-tail tendon is primarily composed of type I collagen fibres in which the collagen molecules are axially packed according to the quarter-stagger model (Hodge and Petruska (1963). This arrangement produces the characteristic meridional series of reflections in the X-ray diffraction pattern of this tissue. Crystalline-like lateral packing interactions produce a series of discrete but often overlapping Bragg reflections arranged as rowlines in the equatorial plane of the X-ray diffraction pattern. Analysis of the equatorial reflections reveals that the collagen molecules are packed on a non-standard quasi-hexagonal lattice, where the unit cell is triclinic (Fraser *et al*.,1983; 1987; Wess *et al*., 1995; 1998; Orgel *et al*., 2001). The equatorial row-lines are overlaid by a continuous layer of diffuse scatter, thought to arise from liquid-like molecular disorder, particularly in the gap region (Hulmes *et al*., 1995). Some of the diffuse scatter is removed on cryo-cooling the sample to 90-100 Kelvin during data collection and some non-physically by mathematical means (Wess *et al*., 1998). Analysis of the component underlying Bragg peaks and of the distribution and intensity of the diffuse scatter at different temperatures will help to further clarify the positions, mobilities and paths of the molecular segments within the gap and overlap regions of the triclinic unit cell.

Materials and Methods

Medium angle X-ray diffraction of whole rat tail tendon in the cryo-cooled and ambient states was performed at stations 7.2 and 14.1, at the SRS Laboratory in Daresbury (UK). Whole tendons were mounted and decrimped in a customised cell and cryo-cooled in a liquid nitrogen gas shroud (Oxford Glycosystems™) to between 97.5 and 100 Kelvin (-176 to -173 °C; cooling rate set to experimental maximum), using 20 percent (v/v) glycerol in PBS, pH 7.4 as cryoprotectant. Some of the background diffuse scatter remaining after cryo-cooling was removed using in-house (CEMB) software. In this routine, a window of user-defined size roved across the image, ranking intensities and plotting the median as a background function, which was then subtracted from the original data. The background and subtracted original datasets were scaled and analysed using Fit2d (Hammersley, 1993) and Excel. TEM cryosections were prepared by colleagues at the University of Lausanne, Switzerland. For fibrils, rat tail tendon was crushed under liquid nitrogen and suspended in PBS (pH 7.4). A suspension of fibrillar collagen prepared in this way was flash-frozen to 133 Kelvin (-140°C) using 20 percent (w/v) dextrose as cryoprotectant and sectioned to 50 nm thickness. Images were analysed using Fit2d (Hammersley, 1993) and one-dimensional electron density line profiles were averaged and outputted using Excel. Fourier analyses to the 12th order were performed on each averaged line profile using in-house software.

Results and Discussion

(a) Cryocooling

Cryo-cooling the tendon prior to and during data collection altered the profile of the diffuse scatter in the near equatorial region of the diffraction pattern (Figures 1 and 2). This effect was possible without dehydration, and therefore without structural modification, of the sample. Cryo-cooling effectively produces an *in situ* "snap-shot" of the molecular position; therefore, it may represent a range of tilts of different direction and magnitude within and between gap regions and fibrils. These molecular configurations are likely to be influenced by the cooling rate.

Overall, the ambient samples have a higher relative intensity than the cryo-cooled samples, but the profiles of the diffuse scatter and the Bragg peaks

both indicate that the biggest change lies in the low angle (near equatorial) region (Figure 3). Electron density contrasts between the four segments in the gap region are known to contribute significantly to the diffraction intensities in this region (Fraser *et al*., 1987; Hulmes *et al*., 1995). Thus, it is shown here that cryo-cooling probably reduces or restricts the thermal lateral and rotational mobility of molecular segments particularly in the gap region, where there is a lower molecular packing density and a reduced frequency of stabilising amino acid triplet sequences (Fraser *et al*., 1983). There may also be an effect on the mobility of the telopeptides, which are also thought to contribute significantly to the low angle intensities (Fraser *et al*., 1987). Any diffuse scatter remaining after cryo-cooling may be largely attributed to static (positional) molecular disorder within the unit cells.

(b) Cryo-TEM

To investigate the presence of sub-fibrillar structures, and to monitor the effect of freezing on sample preservation, fibrillar preparations of rat tail tendon collagen were analysed by cryo-TEM. Unlike most TEM preparations of stained collagen fibrils, the banding profile in the cryo-TEM images (Figure 4) is not a product of dye interactions. Rather, it is due to the inherent electron density distribution along the fibrils: the electron-dense overlap region appearing dark and the electron-lucent gap region appearing pale. Cryo-TEM thus affords a closer approximation to the near native structure of fibrils (providing the freezing process is rapid enough to prevent ice formation and thus structural damage). The average electron density profile from seven gap-overlap repeats of the TEM cryo-section is shown in Figure 5. The N and C-termini peaks are clearly visible at either end of the overlap region on the left of the profile, with the less intense gap region on the right. There is only moderate agreement between the Fourier analyses of the cryo-TEM sections and those of simulated (model) data for orders one to six, and poor agreement for the higher orders (Figures 6 and 7). This is important as the cryo-TEM images are from unstained samples.

Acknowledgements

Dr. M. McDonald and Dr. Rob Kehoe at station 14.1, Daresbury Laboratories, UK

References

[1] Fraser R. D. B., MacRae, T.P., Miller, A. & Suzuki, E. (1983) Molecular conformation and packing in collagen fibrils. *J. Mol. Biol.* **167**, 497-512.

[2] Fraser R. D. B., MacRae, T.P. & Miller, A. (1987) Molecular packing in type I collagen fibrils. *J. Mol. Biol.* **193**, 115-125.

[3] Hammersley, A.P. (1993) Fit2D: a scientific data analysis program. ESRF Internal Report EXP/AH/93 - 02.

[4] Hodge, A. J. & Petruska, J. A. (1963) Recent studies with the electron microscope on ordered aggregates of the tropocollagen molecule. In, *Aspects of Protein Structure* (Ramachandran, G. N., ed.) 289-300 Academic Press, London.

[5] Hulmes, D. J. S., Wess, T.J., Prockop, D.J. & Fratzl, P. (1995) Radial packing, order and disorder in collagen fibrils. *Biophys. J.* **68**, 1661-1670.

[6] Orgel, J.P.R.O., Miller, A., Irving, T.C., Fischetti, R.F., Hammersley, A.P. & Wess, T.J. (2001) The in situ supermolecular structure of type I collagen. *Structure* **9**, 1061-1069.

[7] Wess, T. J., Hammersley, A., Wess, L. & Miller, A. (1995) Type I collagen packing and conformation of the triclinic unit cell. *J. Mol. Biol.* **248**, 487-493.

[8] Wess T. J., Hammersley, A., Wess, L. & Miller, A. (1998). *J. Mol. Biol.* **275**, 255-267.

Ambient **Cryo-cooled**

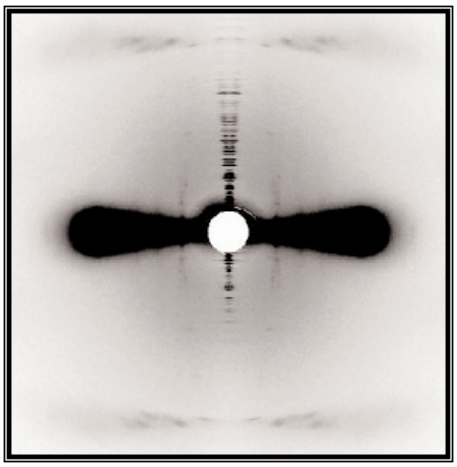

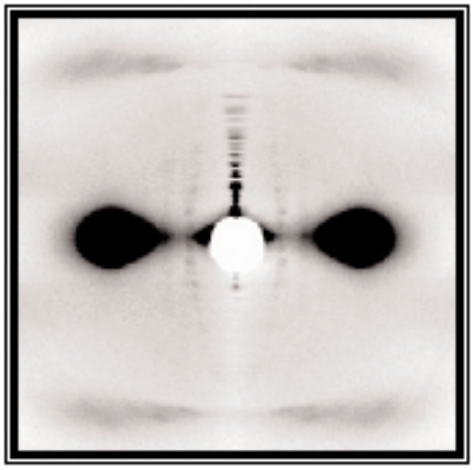

Figures 1 & 2: X-ray diffraction patterns of whole rat tail tendon at (Fig 1: left) ambient (294K; 21°C) and (Fig. 2: right) near liquid nitrogen (97.5K; -176°C) temperatures. Coherent X-ray scatter in the meridional plane arises from the characteristic 67nm (D-periodic) gap-overlap step function of collagen molecules packed axially according to the quarter-stagger model (Hodge and Petruska, 1963). Bragg peaks overlaid with diffuse scatter are observed along the equator and these arise from lateral molecular packing interactions. The resolution of the diffraction data extends to approximately 1.0 nm along the equator and 0.54 nm parallel to the meridian. Note the different equatorial profiles of diffuse scatter at the different temperatures

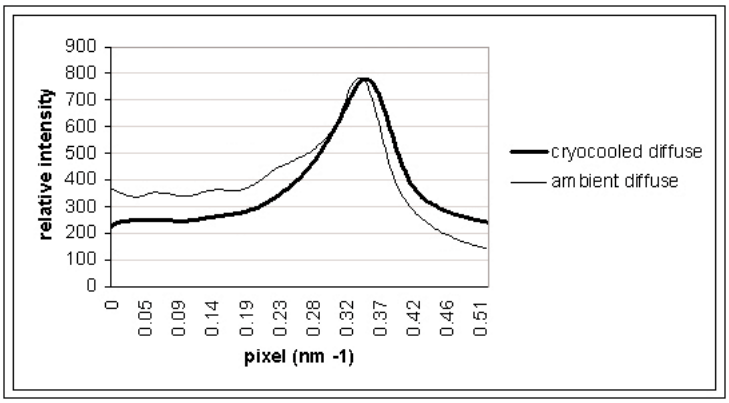

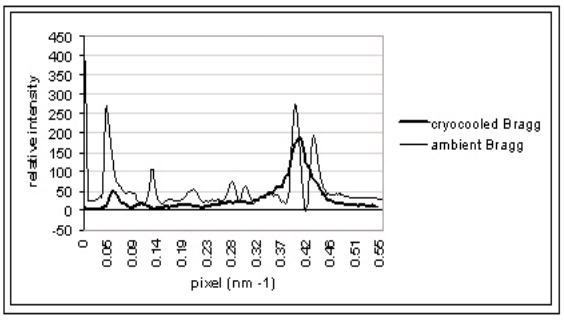

Figure 3: Equatorial profiles of diffuse (left) and Bragg (right) scatter from X-ray diffraction of whole tendon in the cryo-cooled and ambient states.

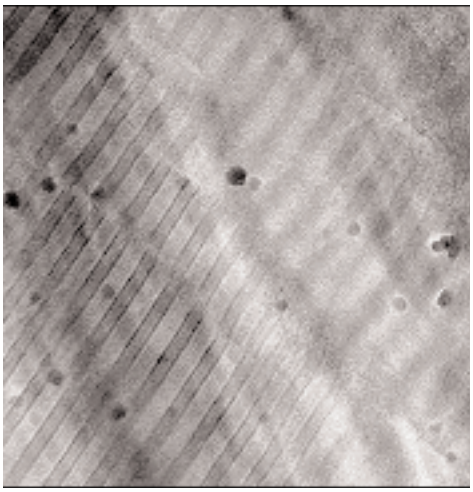

Figure 4: Transmission electron micrograph of unstained cryosectioned rat-tail tendon collagen fibrils (x 440,000). The N- and C-termini of the molecules appear as narrow (~4 nm) bands of electron dense material at either end of the overlap region. Finer (<2 nm) bands of electron dense material are also present throughout the gap region.

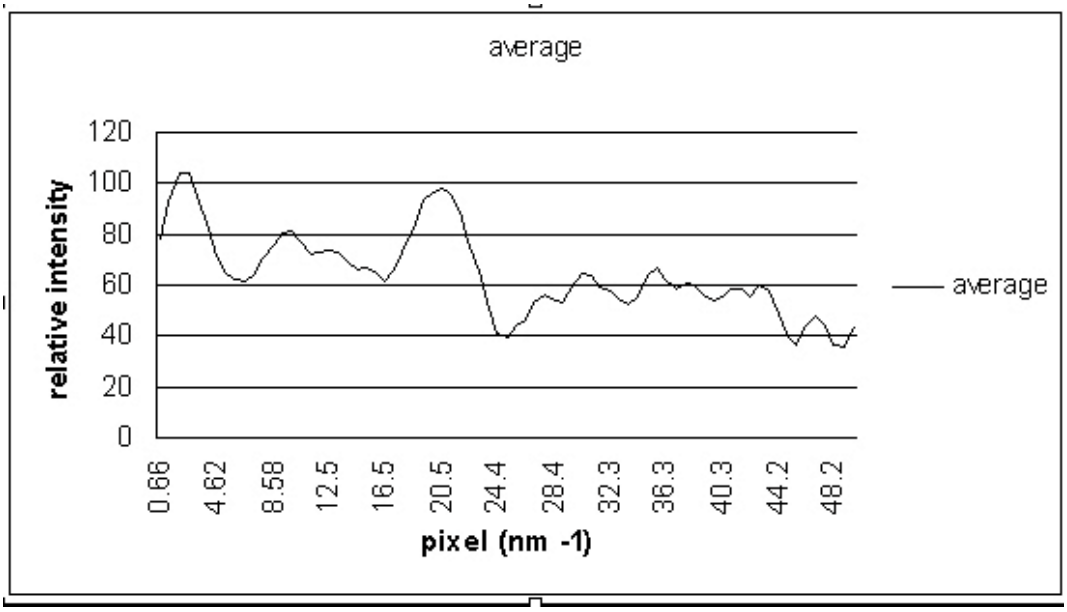

Figure 5: Average electron density profile taken from seven gap/overlap repeats shown in Figure 4.

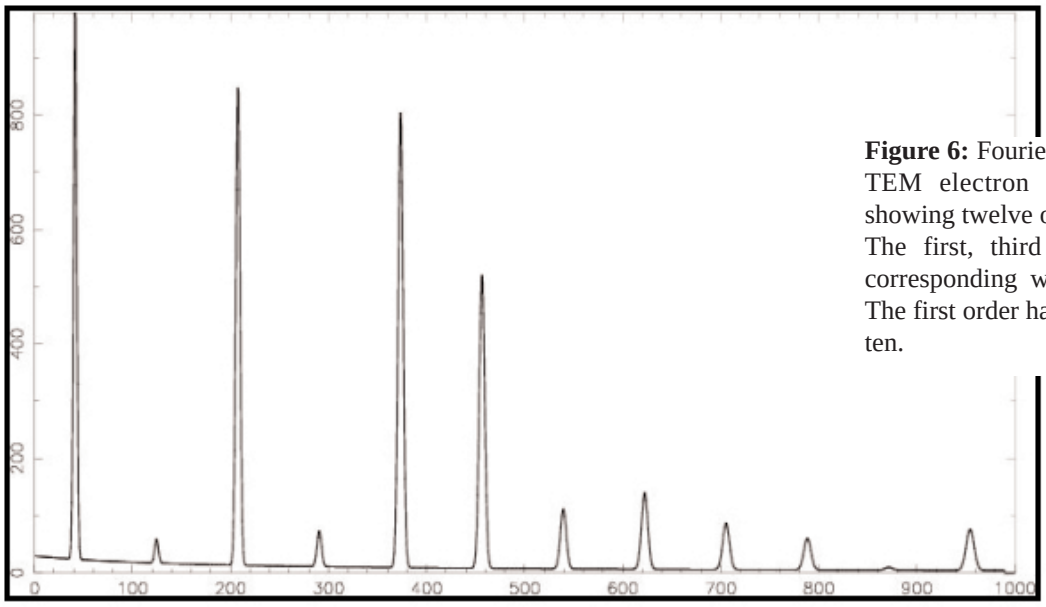

Figure 6: Fourier analysis of the averaged cryo-TEM electron density profile in Figure 5, showing twelve orders of intensity (left to right). The first, third and fifth orders are strong, corresponding with simulated data (Figure 7). The first order has been attenuated by a factor of ten.

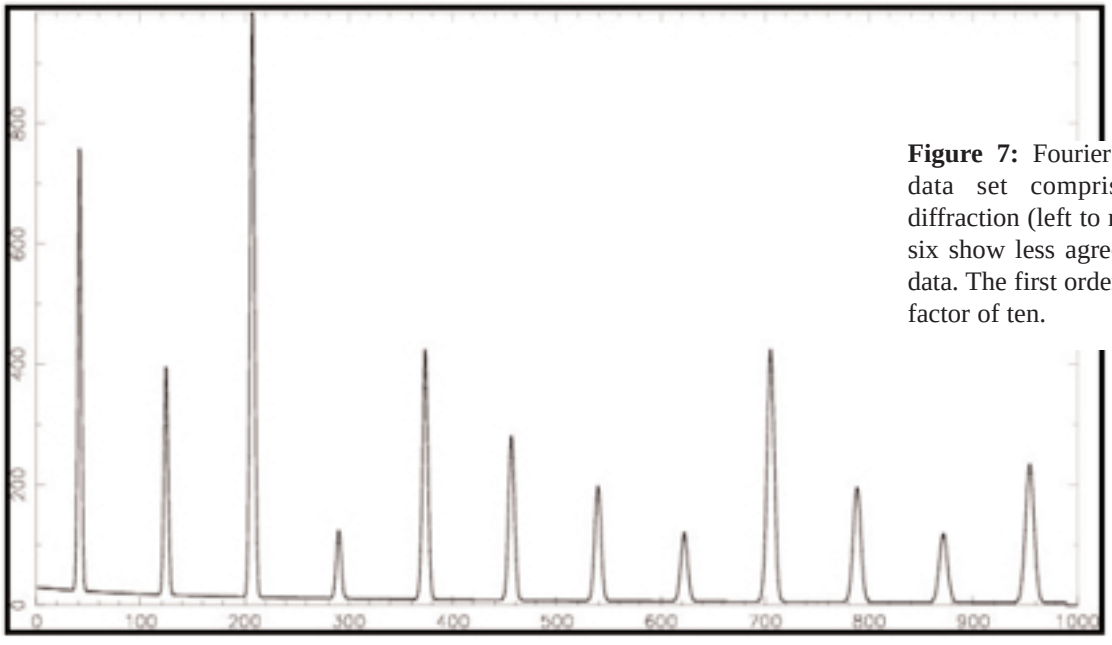

Figure 7: Fourier analysis of a simulated data set comprising twelve orders of diffraction (left to right). Orders greater than six show less agreement with the cryoTEM data. The first order has been attenuated by a factor of ten.

A Wide-Angle X-ray Diffraction Study of the Developing Embryonic Chicken Cornea

C. Boote, V. Siegler, K. M. Meek and A. J. Quantock

Biophysics Group, Dept. of Optometry and Vision Sciences, Cardiff University, Redwood Building, King Edward VII Avenue, Cardiff CF10 3NB, Wales UK.

ABSTRACT

In terrestrial vertebrates the cornea is the main refractive component of the eye. Its remarkable mechanical toughness and almost 100% light-transparency are largely a consequence of the unique collagenous architecture of the corneal stroma. We have used WAXS methods to investigate stromal remodelling in the embryonic chicken cornea in the latter stages of development. Collagen organisation at day 13-15 of embryogenesis is dominated by a four-fold orthogonal arrangement of fibrils. Thereafter this preferential alignment recedes, seemingly because further collagen is deposited in a more isotropic manner, masking the initial orthogonal template. In contrast, the mean lateral spacing of fibril-forming collagen molecules remains unaltered over this developmental period. Our observations have important implications for the biomechanical strength and shape of the cornea.

Introduction

The cornea is the tough, transparent window at the front of the eye. It serves as a physical barrier to mechanical trauma and infection, and provides around two-thirds of the eye's total focussing power. Instrumental to the cornea's function is the unique fibrous structure of the stroma, which constitutes the vast majority of the corneal thickness and is bounded on either side by thin epithelial and endothelial cell layers [1]. The bulk of the stroma comprises collagen fibrils that lie in layers, or "lamellae", in the plane of the cornea [2]. Fibrils within a single lamella lie parallel to each other, but are rotated with respect to fibrils in adjacent lamellae. The fibrils themselves are composed of rod-like Types I and V collagen molecules that run approximately parallel to the fibril axis and are spaced at regular ~1.5 nm intervals. Collagen fibrils are strongest axially, and directions of preferred fibril orientation therefore closely associate with directions of increased tissue strength [3]. Tissue strength is paramount to the cornea's refractive function because of the need for the corneal surface to maintain its normal curvature under intraocular pressure.

Wide-angle equatorial diffraction from corneal stroma derives from interference between X-rays scattered from individual fibril-forming collagen molecules [4]. Because the molecules lie near-axially within fibrils, we can use the azimuthal (i.e. circumferential) intensity distribution in a corneal WAXS pattern to determine the relative number of fibrils oriented in any given direction (see Figure 1). Consider an X-ray beam of wavelength l incident on an isolated collagen fibril. We may represent the amplitude and phase of scattered X-rays by F(**K**), where **K** is related to the scattering angle 2θ, by,

$$|\mathbf{K}| = (4\pi/\lambda) \sin\theta \qquad (1)$$

The resultant scattered intensity for an array of *N* identical fibrils is given by:

$$I(\mathbf{K}) = \sum_{j=1}^{N} F_j(\mathbf{K})\, F^*_j(\mathbf{K}) + \sum\sum_{j\neq k} F_j(\mathbf{K})\, F^*_k(\mathbf{K}) \exp\left[-i(\mathbf{r}_j - \mathbf{r}_k).\mathbf{K}\right] \qquad (2)$$

where $\mathbf{r}_j$ defines the position of the jth fibril and F* denotes a complex conjugate. The second term in Equation (2) represents interference between fibrils. However corneal collagen fibrils are arranged such that, $|\mathbf{r}_j - \mathbf{r}_k| \approx 60$ nm[4] , so that resulting diffraction fringes would be expected to appear for values of |**K**| of the order of $(2\pi/60)$ nm^{-1}. For our typical WAXS set-up, encompassing a ~20 cm camera length, these fringes would (from Equation (1)) have a spacing at the detector of ~ 5 μm. Such fringes do not make a significant contribution to the WAXS pattern when using a typical 200-500 μm diameter X-ray beam. Thus wide-angle diffraction from an array of corneal collagen fibrils may be simply represented by the sum of intensities from individual fibrils, and

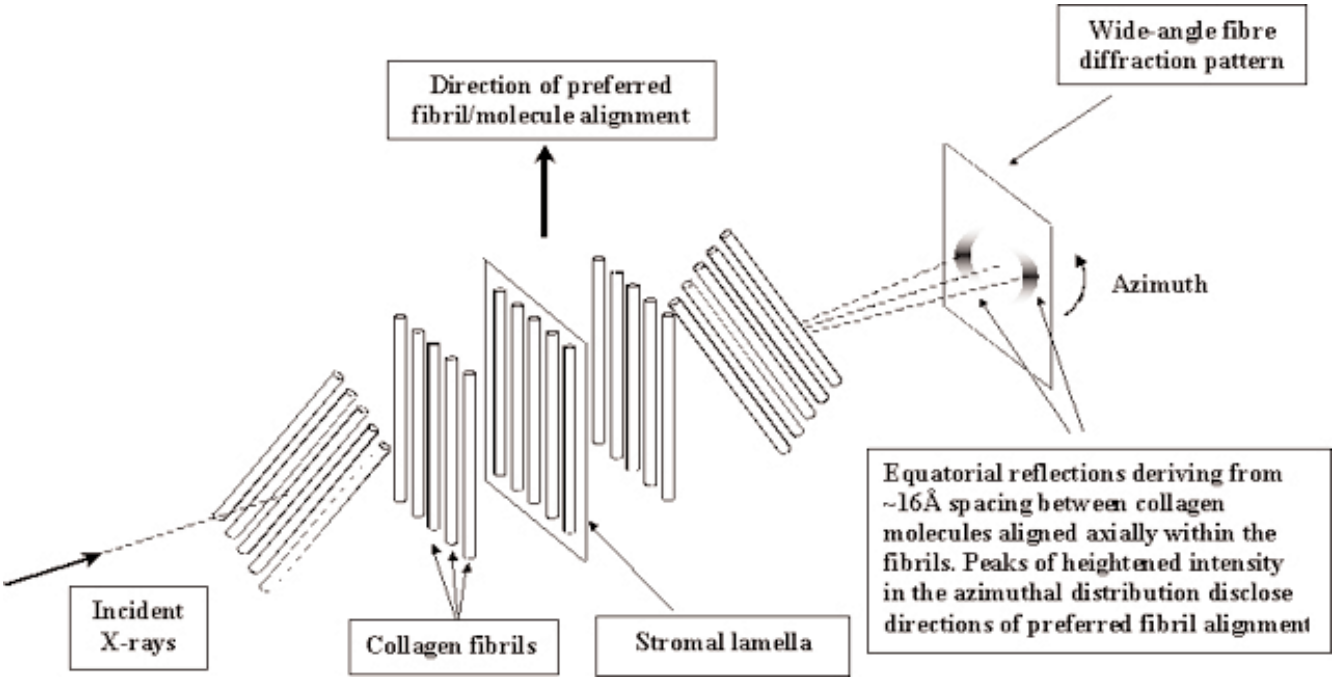

Figure 1: Wide-angle X-ray diffraction from corneal stroma.

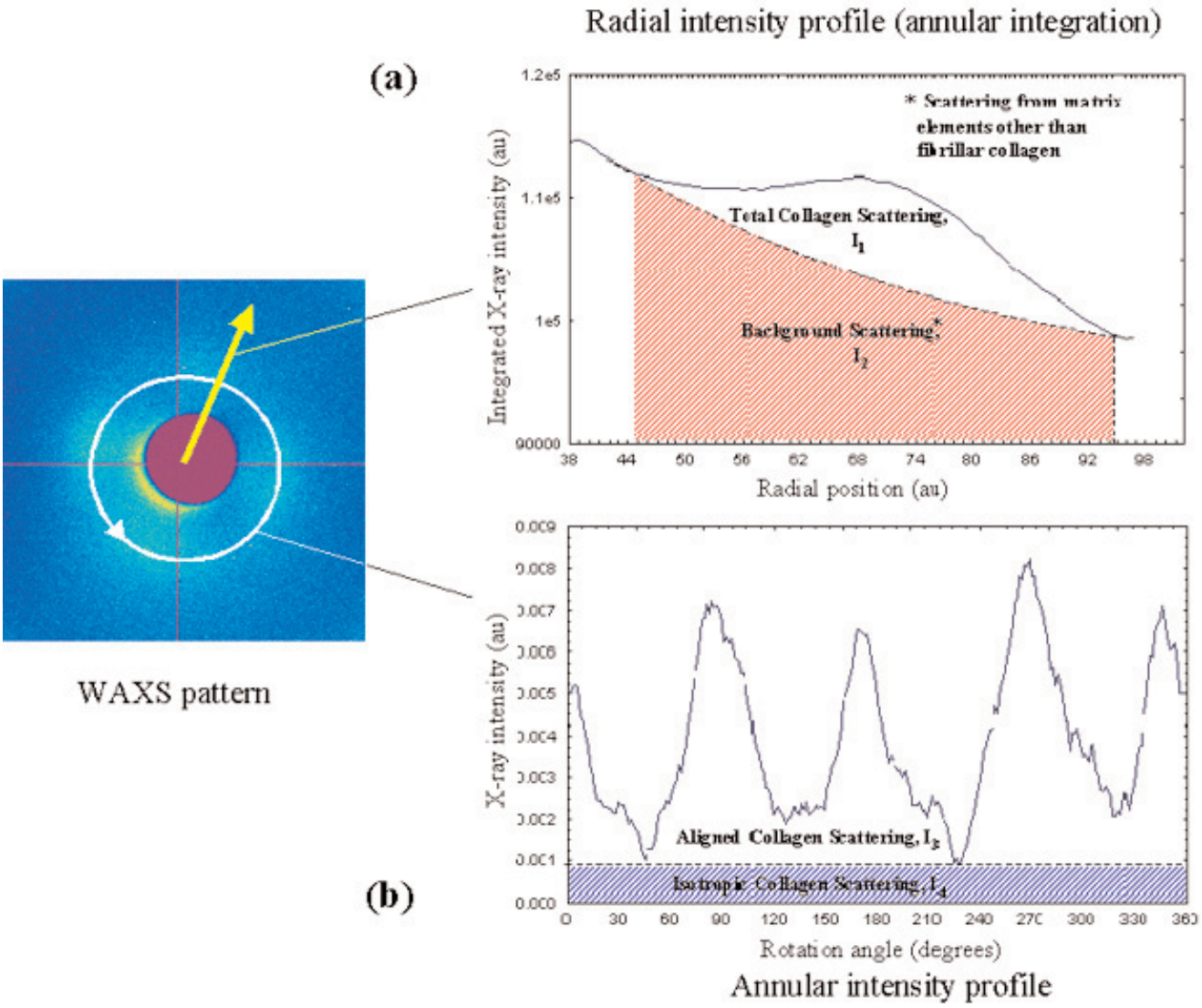

Figure 2: Analysis of WAXS patterns from corneal stroma. **(a)** A radial intensity distribution allows the total fibrillar collagen to be expressed as the ratio of fibrillar collagen scattering to the total scattering from the stromal matrix i.e. $I_1 / (I_1 + I_2)$. **(b)** An azimuthal intensity distribution allows the proportion of preferentially aligned collagen to be expressed as the ratio of scattering from aligned fibrils to scattering from all fibrillar collagen i.e. $I_3 / (I_3 + I_4)$.

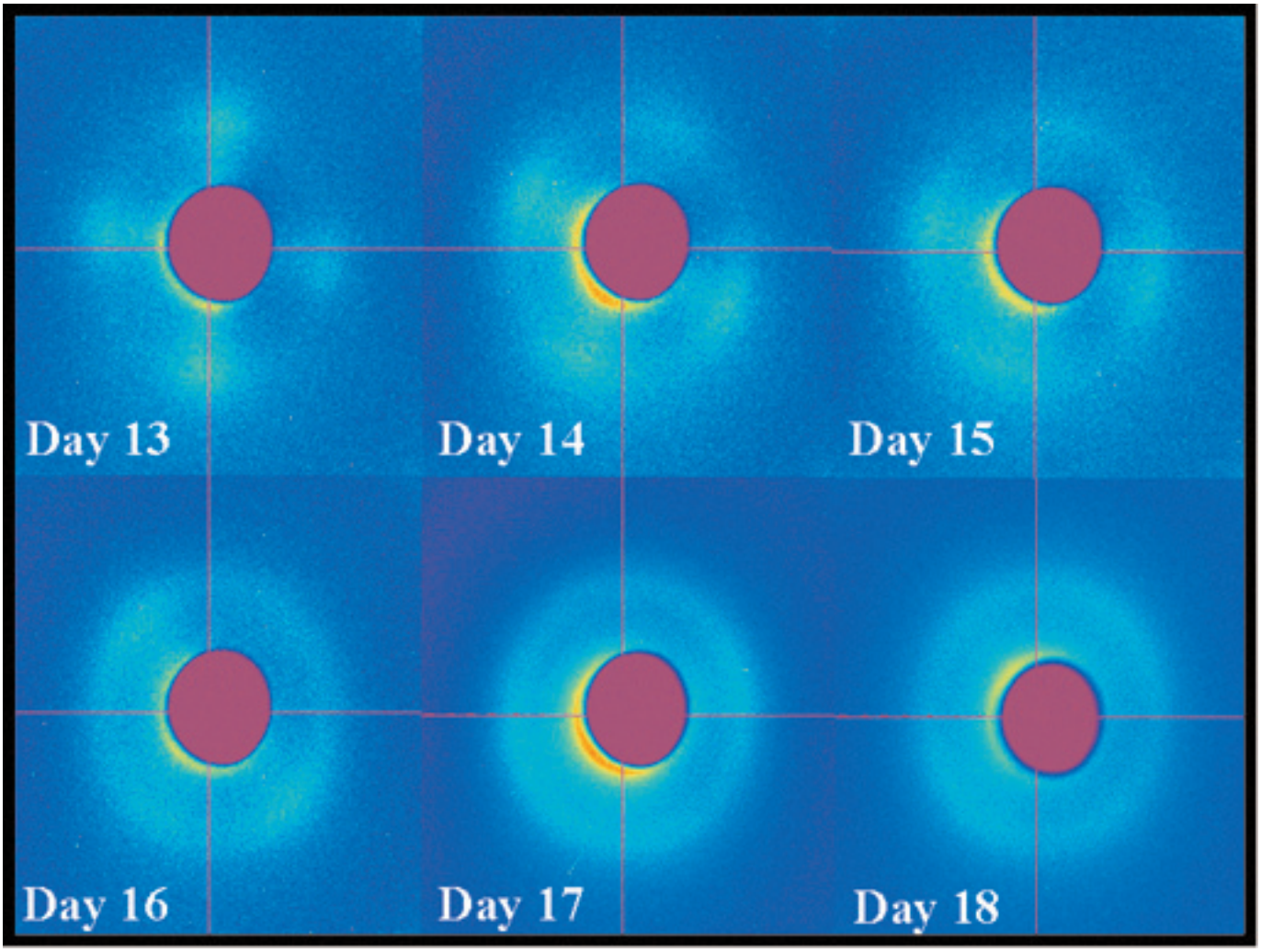

Figure 3: WAXS patterns from the centre of embryonic chicken corneas at developmental days 13-18. Reproduced from Quantock *et al*. (2002) [24], with permission of the copyright holder, the Association for Research in Vision and Ophthalmology.

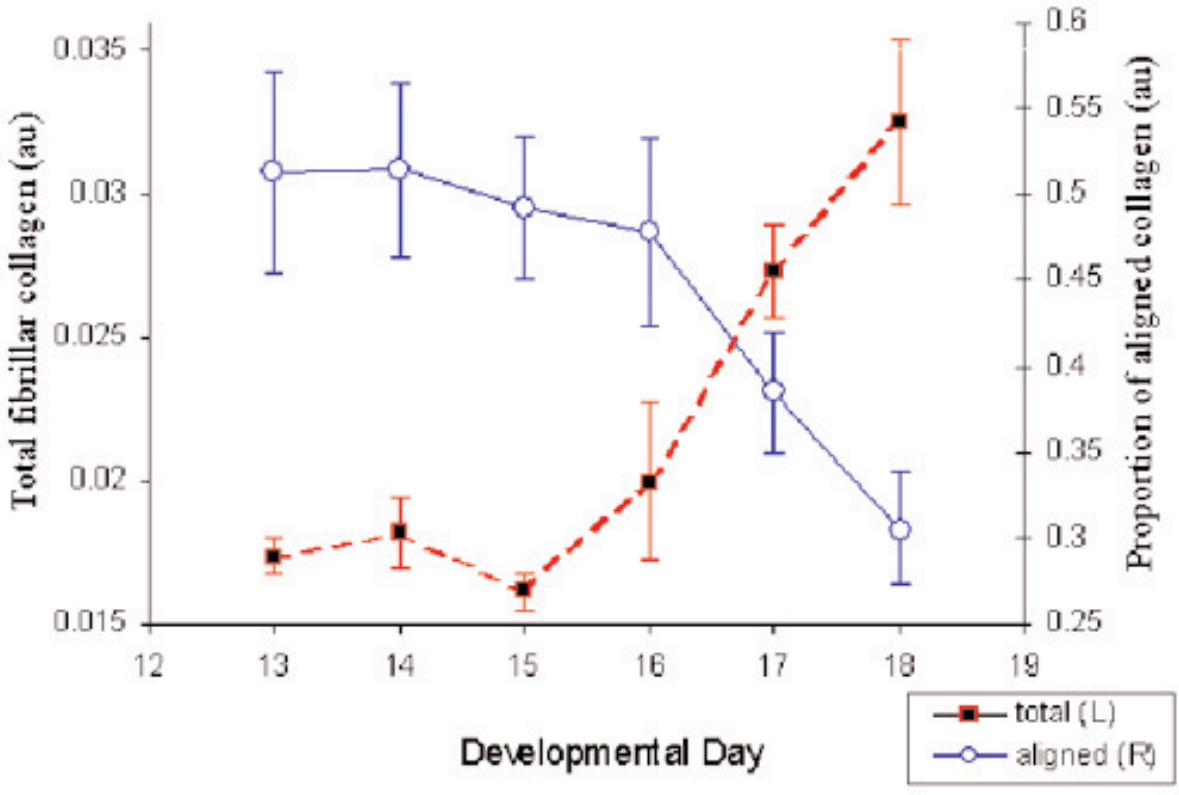

Figure 4: Variation in the total fibrillar collagen and proportion of aligned fibrillar collagen in embryonic chicken cornea at developmental days 13-18.

interference between fibrils may be ignored, i.e.,

$$I(\mathbf{K}) \approx \sum_{j=1}^{N} F_j(\mathbf{K})\, F^*_j(\mathbf{K}) \qquad (3)$$

By extension, the X-ray intensity is (to a first approximation) proportional to the number of aligned fibrils, and we define the azimuthal fibril distribution B(ϕ) as,

$$B(\phi) \approx I(\phi') \qquad (4)$$

where ϕ and ϕ' are the azimuthal angles at the sample and detector respectively, and are related by $\phi' = \phi + 90^o$. That is to say the scattering is equatorial, as shown in Figure 1. This approach to the analysis of WAXS data has been used previously to determine fibril orientations in other collagenous connective tissues [5,6].

In the chicken, formation of the corneal stroma occurs as a sequence of distinct events initiated early in the 21-day incubation period, and beginning with the formation of the corneal epithelium [7]. The epithelial cells synthesise collagen fibrils that are secreted into the space between the corneal epithelial basement membrane and that of the lens directly posterior to this, so that by day 3 a loose 2-3 μm thick network of collagen fibrils is formed known as the primary corneal stroma. On day 5 of embryogenesis the primary stroma is invaded by presumptive fibroblasts that continue to deposit collagen as the cornea matures into what is usually termed the secondary stroma.

Development of the secondary stroma from day 9 of embryogenesis until hatching at day 21 is of particular interest, because during this time period major remodelling of the stroma takes place that governs corneal function. Structural changes to both collagenous [8-11] and non-collagenous [12,13] stromal matrix components occur that are instrumental to the formation of a fully functional mature cornea. Most notable amongst these is a two-stage fibril compaction in the stromal extracellular matrix, observed previously using SAXS techniques, that occurs during the latter stages of secondary corneal development [8,10]. Given that theories of corneal transparency require a degree of fibrillar order for light transmission [14], a link between fibril re-organisation and the acquisition of corneal transparency appears likely. However, the volume of literature describing the latter stages (i.e. after ~14 days) of secondary corneal development remains limited. In order to appreciate any reorganisation that might occur in the lateral spacing of fibril-forming collagen molecules and in the orientation of the corneal fibrils themselves during this important period of embryogenesis, we initiated a WAXS study.

Experimental

We collected fertilised hen eggs from a commercial hatchery and dissected out the corneas after 13, 14, 15, 16, 17 and 18 days of incubation. Excised corneas were immediately snap-frozen via immersion in liquid nitrogen-cooled isopentane, wrapped in Clingfilm to limit evaporation, and stored at -80^{o}C prior to the diffraction experiments.

Station 14.1 at the Daresbury SRS was used to collect WAXS patterns from a total of 47 corneas (n = 7 or 8 at each developmental day). Each cornea was allowed to thaw within an airtight Perspex specimen chamber with Mylar entrance and exit windows. An X-ray beam of wavelength 0.1244 nm was passed through the centre of each cornea parallel to the optical axis. The beam dimensions at the sample measured 0.3mm x 0.3mm and the exposure time was 2 minutes.

The experimental set-up was calibrated using the 0.304 nm X-ray reflection from powdered calcite. This achieved, we were able to determine the mean separation of fibril-forming collagen molecules in a central 300 micron zone of each cornea from the radial co-ordinate of the intermolecular X-ray reflection. In addition, the total intensity of this reflection provides a measure of the relative amount of fibrillar collagen present in the volume of tissue through which the X-ray passes. In order to generate a numerical index of this quantity, we generated radial distribution plots of scattered X-ray intensity, in which each point represented an integration through 360^o at that particular radius (see Figure 2(a)). The analysis protocol loosely followed that documented previously by Daxer and Fratzl [15]. A power law background function (representing scattering from stromal matrix elements other than fibrillar collagen) was fitted to and subtracted from the radial plots (Figure 2(a)), and the relative proportion of fibrillar collagen presented as the ratio of integrated intensity above background to the total integrated intensity (including background). This is equivalent to $I_1 / (I_1 + I_2)$ in Figure 2(a).

As previously mentioned, the azimuthal distribution of X-ray intensity in the intermolecular reflection discloses the spread of fibril orientations present in the portion of tissue traversed by the X-ray beam. We produced azimuthal intensity plots for all 47 corneas studied, integrating radially over the intermolecular reflection. A numerical index of the relative amount of fibril alignment was computed as the ratio of X-ray scatter from preferentially oriented fibrils to total scatter from all fibrillar collagen. This is denoted by $I_3 / (I_3 + I_4)$ in Figure 2(b).

Results

Figure 3 shows a representative selection of WAXS patterns from corneas excised at developmental days 13 through 18. At days 13-15 the intermolecular reflection clearly displayed predominant four-fold symmetry, indicating the presence of a largely orthogonal fibrillar array. However, WAXS patterns from days 16-18 disclose a progressive recession in this arrangement, in favour of a more isotropic fibril array. A numerical index of the amount of preferentially aligned/orthogonal collagen was computed for all 47 corneas, and the mean values at each developmental time point are plotted in Figure 4. To more fully appreciate the structural remodelling at play here, we computed an index of the total fibrillar collagen present for each cornea and determined the mean value for each time point (Figure 4). The results disclose a significant increase in the deposition of fibrillar collagen, initiated at day 16, which accompanies the loss of orthogonality.

Developmental Day	Mean Intermolecular Bragg Spacing, nm (S.D.)
13	1.42 (0.03)
14	1.43 (0.03)
15	1.42 (0.02)
16	1.45 (0.02)
17	1.41 (0.02)
18	1.45 (0.01)

Table 1: Mean intermolecular Bragg spacings for secondary embryonic chicken cornea at developmental days 13-18.

Analysis of the radial position of the intermolecular reflection provides a measure of the mean lateral separation of fibril-forming collagen molecules. The exact manner in which corneal collagen molecules pack into fibrils is still unknown, although studies of tendon have pointed to a possible quasi-hexagonal type packing arrangement [16]. Hence, the figures we present in Table 1 represent the mean intermolecular Bragg spacing for each developmental day. Conversion to centre-to-centre spacing requires multiplication by a packing factor, in the case of quasi-hexagonal packing this has been calculated to be 1.11 [17]. Our data reveal that the mean collagen intermolecular Bragg spacing remains unchanged at around 1.43 nm throughout the latter stages of secondary corneal development.

Discussion

As shown in Table 1, the mean separation of fibril-forming Type I/V collagen molecules does not change appreciably between days 13 and 18 of embryogenesis. The average value of 1.43 nm that we obtained is in the normal range and comparable to the mature avian cornea [18]. The result may at first appear surprising in light of the tissue dehydration that takes place during the same period [10], and which has been linked with the aforementioned fibril compaction. However, *in vitro* studies of the dehydration of bovine cornea [19,20] reveal that, at the tissue hydration levels encountered in our study, water is removed almost exclusively from the interfibrillar space. Any intermolecular compaction would require water to be removed from within the fibrils themselves, a situation that only seems to occur at much lower tissue hydration.

Figure 4 shows that proportionally less collagen fibrils are aligned orthogonally as the embryonic cornea develops between days 13 and 18 of incubation. We believe that, rather than pointing to any degradation in the orthogonal matrix, this observation simply reflects the increased synthesis of collagen initiated at day 16. The data provide evidence that the proportions of aligned and total fibrillar collagen respectively decrease/increase in a concomitant fashion (Figure 4). Based on current evidence it seems that, at day 16, additional collagen is deposited isotropically so as to obscure the overall orthogonality of existing fibrils.

Let us consider how our observations can be reconciled with the established picture of the developing embryonic chicken cornea, gained mainly from light and electron microscopy observations. It has long been established that the primary corneal stroma at day 5 comprises an exclusively orthogonal array of fibrillar collagen

synthesised by the epithelium [21]. Invading fibroblasts deposit collagen in register with the existing lamellae, thus preserving the orthogonality into the early stages of secondary corneal development. Consequently, the primary stroma is often considered the scaffold or template for the secondary cornea [21,22].

Concurrently, the epithelium continues to synthesise collagen and deposit it anterior to the invaded stroma. This population of collagen, however, is deposited in lamellae that are successively rotated by about 3-6^o clockwise, as viewed from the endothelial side and traversing the cornea from its endothelial to epithelial surfaces [21]. As embryogenesis progresses, invasion of the expanding stroma by fibroblasts continues, with the fibroblasts continuing to lay down collagen in register with existing fibrils. Of course, because of the continuing deposition of rotated lamellae by the epithelium, the new collagen laid down by the fibroblasts is also rotated.

As a consequence of this dual mechanism of collagen deposition, by day 14 the secondary stroma has been shown to comprise a posterior 50 μm layer containing mainly orthogonally arranged fibrils, with the remaining 150 μm of anterior stroma being made up of progressively rotated lamellae exhibiting a net total angular displacement of ~ 210^o [21]. If we assume that rotation between successive lamellae is fairly constant, a total net rotation of 180^o (or any multiple thereof) would represent a fully isotropic fibril distribution. Our contention is that the net rotation of 210^o estimated by Trelstad and Coulombre [21] at day 14 is close enough to 180^o to give rise to a fully homogeneous X-ray reflection. Of course, since X-ray measurements represent an average through the full-thickness tissue, we expect the almost exclusively orthogonal posterior fibrils to produce a four-fold reflection, which would superimpose on the homogeneous reflection from the anterior stroma. This appears to be what we are observing at days 13-15 of development.

At day 16 there is clearly a swing towards a more isotropic fibril arrangement overall. While our data point to increased collagen deposition, rather than re-organisation or degradation of the posterior collagen template (Figure 4), it cannot, of course, tell us at which depth in the stroma this deposition might be occurring. However, in light of our data, it is interesting that immunofluorescence studies have revealed a dual layer of stable collagen in the anterior stroma that develops gradually between days 14 and 19, and which appears to form a physical link between the scleral ossicles (bony plates circumscribing the avian eye) [23]. It is possible that the collagen which we argue is deposited after day 16, and acts to obscure the orthogonality in the posterior cornea, is associated with these two stable collagen bands. Furthermore, if, as has been suggested, the presence of the bands were required to stabilise the shape of the cornea [23], a totally isotropic arrangement of fibrils would clearly be an advantage biomechanically.

Acknowledgements

We would like to thank Mike MacDonald, Rob Kehoe and Mike Bailey for help at the SRS, Daresbury. This work was funded by a grant from the MRC (Programme Grant: 60001033) and the TFC Frost Charitable Trust.

References

[1] Forrester, J.V., Dick, A.D., McMenamin, P. & Lee, W.R. (1996) The structure of the eye. In: The Eye.(Saunders, London).

[2] Maurice, D.M. (1957) The structure and transparency of the corneal stroma. *J. Physiol.* **136**, 263-286.

[3] Hukins, D.W.L. (1996) Collagen fibril orientations in tissues and their relationship to mechanical properties. *Fibre Diffraction Review* **5**, 14-16.

[4] Meek, K.M. & Quantock, A.J. (2001) The Use of X-ray Scattering Techniques to Determine Corneal Ultrastructure. *Prog. Ret. Eye Res.* **20**, 95-137.

[5] Boote, C., Sturrock, E.J., Attenburrow, G.E. & Meek, K.M. (2002) Psuedo-affine behaviour of collagen fibres during the uniaxial deformation of leather. *J. Mat. Sci.* **37**, 3651-3656.

[6] Aspden, R.M. & Hukins, D.W.L. (1979) Determination of the Direction of Preferred Orientation and the Orientation Distribution Function of Collagen Fibrils in Connective Tissues from High-Angle X-ray Diffraction Patterns. *J. Appl. Cryst.* **12**, 306-311.

[7] Linsenmayer, T.F., Fitch, J.M., Gordon, M.K. *et al.* (1998) Development and roles of collagenous matrices in the embryonic avian cornea. *Prog. Ret. Eye Res.* **17**, 231-265.

[8] Quantock, A.J., Kinoshita, S., Capel, M.C. & Schanzlin, D.J. (1998) A synchrotron X-ray diffraction study of developing chick corneas. *Biophys. J.* **74**, 995-998.

[9] Hirsch, M., Noske, W., Prenant, G. & Renard, G. (1999) Fine structure of the developing avian corneal stroma as revealed by quick-freeze, deep-etch electron microscopy. *Exp. Eye Res.* **69**, 267-277.

[10] Siegler, V. & Quantock, A.J. (2002) Two stage compaction of the secondary avian cornea during development. *Exp. Eye Res.* **74**, 427-431.

[11] Birk, D.E., Fitch, J.M. & Linsenmayer, T.F. (1986) Organisation of collagen types I and V in the embryonic chicken cornea. *Inv. Ophthalmol. Vis. Sci.* **27**, 1470-1477.

[12] Cai, C.X., Gibney, E.P., Gordon, M.K., Marchant, J.K., Birk, D.E. & Linsenmayer, T.F. (1996) Characterization and developmental regulation of avian corneal β-1,4-galactosyltransferase mRNA. *Exp. Eye. Res.* **63**, 193-200.
[13] Dunleavy, J.R., Beales, M.P., Berryhill, B.L., Cornuet, P.K. & Hassell, J.R. (2000) Expression of the keratan sulfate proteoglycans lumican, keratocan and osteoglycin/mimecan during chick corneal development. *Exp. Eye Res.* **70**, 349-362.
[14] Farrell, R.A. (1994) Corneal transparency. In: Albert D.M. and Jacobiec S.A. (eds.) *Principles and Practice of Ophthalmology*. (Saunders, Philadelphia).
[15] Daxer, A. & Fratzl, P. (1997) Collagen fibril orientation in the human corneal stroma and its implications in keratoconus. *Inv. Ophthalmol. Vis. Sci.* **38**, 121-129.
[16] Fraser, R.D.B., MacRae, T.P., Miller, A. & Suzuki, E. (1983) Molecular conformation and packing in collagen fibrils. *J. Mol. Biol.* **167**, 497-521.
[17] Maroudas, A., Wachtel, E., Grushko, G., Katz, E.P. & Weinberg, P. (1991) The effect of osmotic and mechanical pressures on water partitioning in articular cartilage. *Biochim. Biophys. Acta.* **1073**, 285-294.
[18] Meek, K.M. & Leonard, D.W. (1993) The ultrastructure of the corneal stroma: a comparative study. *Biophys. J.* **64**, 273-280.
[19] Meek, K.M., Fullwood, N.J., Cooke, P.H., *et al*. (1991) Sychrotron X-ray diffraction studies of the cornea with implications for stromal hydration. *Biophys. J.* **60**, 467-474.
[20] Fratzl, P. & Daxer, A. (1993) Structural transformation of collagen fibrils in corneal stroma during drying. *Biophys. J.* **64**, 1210-1214.
[21] Trelstad, R.L. & Coulombre, A.J. (1971) Morphogenesis of the collagenous stroma in the chick cornea. *J. Cell Biol.* **50**, 840-858.
[22] Coulombre, J. & Coulombre, A. (1975) Treatment of five-day-old embryos of domestic fowl with 6-Diazo-5-oxy-L-norleucine (DON). *Dev. Biol.* **45**, 291-303.
[23] Linsenmayer, T.F., Gibney, E. & Fitch, J.M. (1986) Embryonic avian cornea contains layers of collagen with greater than average stability. *J. Cell. Biol.* **103**, 1587-1593.
[24] Quantock, A.J., Boote, C., Siegler, V. & Meek, K.M. (2003) Collagen Organisation in the Secondary Chick Cornea During Development. *Inv. Ophthalmol. Vis. Sci.* (in press).

Collagen Orientation During Development of the Embryonic Avian Cornea.

Craig Boote, Veronique Siegler, Keith M. Meek, Andrew J. Quantock.

Biophysics Group, Department of Optometry & Vision Sciences, Cardiff University, Cardiff, U.K.

Purpose: During the latter stages of development, the secondary chick corneal stroma undergoes significant structural and compositional changes. The current study was designed to provide information about the orientation of collagen molecules (and thus fibrils) as the cornea matures before hatching. Collagen orientation is an important biomechanical parameter given that collagen lamallae consisting of parallel fibrils are thought to be strongest axially. Methods: Forty-eight corneas were obtained from fertilised chick embryos at developmental days 13 through 18 (n8 at each timepoint), stored frozen and later examined at the Synchrotron Radiation Source, Cheshire UK, where high-angle X-ray diffraction patterns were obtained. From the X-ray patterns the amount of X-ray scatter from aligned versus non-aligned (i.e. isotropic) collagen molecules was measured. Given that collagen molecules run approximately axially within fibrils, molecular orientation was taken to represent fibrillar orientation. Results: X-ray scatter from fibrillar stromal collagen (aligned and isotropic) as a proportion of X-ray scatter from all matrix elements measured 0.018 (day 13), 0.018 (day 14), 0.018 (day 15), 0.020 (day 16), 0.027 (day 17), and 0.033 (day 18). The increase after day 16 is indicative of increased deposition of fibrillar collagen. The amount of X-ray scatter from aligned fibrillar collagen as a proportion of scatter from all matrix elements (including aligned and isotropic collagen) measured 0.51 (day 13), 0.51 (day 14), 0.50 (day 15), 0.48 (day 16), 0.39 (day 17) and 0.30 (day 18). The decrease after day 16 points to lower levels proportionally of aligned collagen. Conclusions: The stromal matrix of the secondary chick cornea at day 13-16 of development contains a sizeable proportion of collagen fibrils that are preferentially aligned, often in a four-fold, orthogonal manner. Thereafter, this preferential alignment recedes, presumably because new collagen fibrils are being deposited in an non-orthogonal array, thereby masking the initial orthogonal template.

A Wide Angle Fibre Diffraction Camera for station 14.1 of The SRS

R. Kehoe

Daresbury Laboratory, Daresbury, Warrington. Ches. WA44AD

Collecting the best possible data from a wide variety of samples on a single synchrotron station can be difficult to achieve. Requirements include easy optimisation of the X-ray beam size, optimisation of intensity, accommodating sample mounts varying in size and shape, easy sample alignment, providing a variety of sample environment conditions, providing both transitional and rotational degrees of freedom to sample movement. A wide angle diffraction camera designed to meet these demanding requirements is being used on station 14.1 of The SRS at Daresbury Laboratory.

Changes in cellulose crystal structure under tensile stress

K. Koelln[1], H. Schober[3], W. Press[1], C. Riekel[4], S. Funari[2], M. Mueller[1,4]

[1] Institut für Experimentelle und Angewandte Physik, Leibnizstraße 19, 24098 Kiel, Germany.
[2] HASYLAB, Notkestr. 85, 22607 Hamburg, Germany
[3] ILL, 6, rue Jules Horowitz, 38000 Grenoble, France
[4] ESRF, 6, rue Jules Horowitz, 38000 Grenoble, France

Cellulose is the most abundant structural biopolymer found on earth. It is organised as a fibrous composite material made up of small crystals (microfibrils) and disordered regions. The crystalline structure of the cellulose microfibrils itself is well-known [1]. On the contrary, there are still open questions about the morphology and the tensile properties of cellulose as composite material. As a first step in understanding this material a determination of the mechanical properties of the individual microfibrils is required. We investigated the tensile properties of flax cellulose fibres using microfocus wide-angle X-ray diffraction (WAXS) at the ESRF (ID13) and standard WAXS at HASYLAB (A2). Single flax fibres (at ID13) and small bundles of flax and ramie fibres (at A2) were mounted in a stretching device. Tensile load was applied along the fibre direction. The

measurement of the displacement of the jaws and the force onto the fibre direction yielded a stress--strain curve of the fibre as a whole. In addition, the stress--strain relationship for the microfibrils could be monitored by the change in lattice spacing using the recorded WAXS pattern. Assuming an isotropic distribution of the stress within the composite material, Young's modulus can then be calculated for the entire fibre as well as for the microfibrils. Furthermore parameters such as microfibril angle, crystallinity, and defects of the crystals could be deduced, thus, leading to a better understanding of the morphology of cellulose. An unexpected increase of the lattice spacing perpendicular to the applied force was also observed. This can be explained by radiation damage to the intermolecular hydrogen bonds, leading to an increase of the chain-chain distance of the cellulose chains within the crystals. This effect has already been observed for electron radiation [2].

References

[1] A. C. O'Sullivan; *Cellulose* **4**, 173 (1997)
[2] J. F. Revol; *J. Mater. Sci. Lett*. **4**, 1347 (1985)

Structure of native wood cellulose

Martin Müller[1], Manfred Burghammer[2], Junji Sugiyama[3]

[1] Institut für Experimentelle und Angewandte Physik der Universität Kiel, Leibnizstr. 19, D-24098 Kiel, Germany
[2] European Synchrotron Radiation Facility, B. P. 220, F-38043 Grenoble Cedex, France
[3] Wood Research Institute, Kyoto University, Uji, Kyoto 611-0011, Japan

The models for the crystal structure of native cellulose (cellulose I) are more than 25 years old [1,2]. Since cellulose single crystals are not available, fibre diffraction is the only access to the structure. Cellulose nanocrystals (microfibrils) are long (about 100 nm) but very thin (2.5 to 25 nm, depending on the origin). We investigated the highly oriented cellulose poplar tension wood fibres. In order to profit from the high orientation, single wood fibres (2 mm long, 30 microns wide) were investigated with an X-ray microbeam (ID13, ESRF). The fibre was cooled to 100 K and thus stable in the intense beam for several minutes. Fibre diffraction data with a resolution of about 0.11 nm were obtained as a basis for structure determination.

Structural changes of alpha-crystallin during heating observed with small and wide angle X-ray scattering

J. W. Regini, J.G. Grossmann

Cardiff University, Daresbury Lab

Whole eye lens and alpha-crystallin gels and solutions were investigated using X-ray scattering techniques at temperatures ranging from 20 to 70ºC. In whole lens the spacing of the single X-ray reflection seen with small angle scattering was constant from 20 to 45ºC, increasing at 50ºC to 165 Å. These results indicate that in whole lens alpha-crystallin is capable of protecting other lens proteins against superaggregation up to 50ºC. In alpha-crystallin gels a moderate increase in both the spacing and intensity of the reflection was observed from 20 to 45ºC, followed by a dramatic increase from 45 to 70ºC. Upon cooling, this effect was found to be irreversible over an eleven-hour period. Qualitatively similar results were observed for alpha-crystallin solutions at a variety of concentrations. Wide angle scattering reflections from the alpha-crystallin gel arise primarily from the beta-sheet organization of the alpha-core, and appear to be essentially preserved throughout the temperature range. These results confirm earlier observations at low concentrations of alpha-crystallin in vitro of a major temperature transition around 50 ºC, and can be extrapolated to physiological concentrations.

Quantitative interpretation of the 2D X-ray diffraction patterns from skeletal muscle using direct modelling

N. Koubassova[1], S.Y. Bershitsky[2], M.A. Ferenczi[3], A.K. Tsaturyan[1].

[1] Institute of Mechanics, Lomonosov Moscow State University, Vorobjovy Gory, Moscow 119899 Russia;
[2] Institute of Ecology and Genetics of Micro-Organisms, Ural Branch of the Russian Academy of Sciences, 91 Pervomayskaya str., Yekaterinburg 620219 Russia;
[3] Imperial College of Science, Technology and Medicine, London SW7 2AZ UK

A 3D structural model of the actin-myosin super-lattice based on available atomic structures of F-actin, myosin subfragment-1 and their complex was developed. To reduce the number of parameters in

the model, a principle of 'minimal elastic distortion energy' was employed. According to this principle, a myosin head chooses that actin monomer on one of six surrounding thin filaments for which binding requires the least elastic distortion energy. In our model binding of up to 270 myosin heads to actin in a unit cell is determined by two parameters only: fraction of stereo-specifically attached myosin heads, n, and the ratio of the axial and transversal cross-bridge stiffness, l. Calculated 2D X-ray diffraction patterns were compared with the low angle X-ray diffraction data from skeletal muscle. The model provides good fit of the diffraction pattern from rabbit muscle fibres in rigor without a global parameter search. The stiffness ratio, l, and parameters of disorder in the actin-myosin lattice can be estimated separately from individual layer lines. The total off-meridional intensity of the 1-st actin layer line, A1, was found to be independent of lattice sampling and tilting of the light chain domain of the myosin head. Radial distribution of the intensity along the A6 and A7 actin layer lines appeared to be very sensitive to the shape of bound heads. We also tested how azimuthal disorder of attached myosin heads affects the intensity of the actin layer lines. The A6 and A7 layer lines were found to be almost insensitive to such disorder, while the intensity of A1 significantly decreases when the disorder increases. The fraction of stereo-specifically bound heads, n, during isometric muscle contraction at different temperatures was estimated from the time-resolved X-ray diffraction data obtained in T-jump experiments with small (3-5 fibres) bundles from rabbit muscle. The T-jumps from ~6ºC to ~36ºC induced 2.6-fold tension rise. Estimated n increased nearly proportionally to tension: from ~18% at ~6ºC to ~45% at ~36ºC. X-ray diffraction data was collected with RAPID 2D gas-filled detector on beamline 16.1, SRS, Daresbury Laboratory. Supported by grants from INTAS, HHMI and RFBR and by MRC and Daresbury Laboratory, UK.

BS - 2D X-ray diffraction data processing program

N. Koubassova

Institute of Mechanics, Lomonosov Moscow State University, Vorobjovy Gory, Moscow 119992 Russia

A program was written for the treatment of 2D low angle X-ray diffraction data as MS Windows version of BSL. It is currently used for the analysis of the X-ray diffraction patterns from skeletal muscle, but like BSL can deal with any fibre diffraction data. Windows interface makes the program user friendly and open codes provide greater flexibility to adopt to the ever changing requirements. Colour graphics and export to standard graphic formats (BMP, TIFF) is implemented. Mouse selection of integration limits is available for horizontal, vertical and 2D integration. 1D plots can be displayed in a separate window and saved in ASCII format. A set of mirroring functions contains horizontal and vertical mirroring as well as standard four quadrants mirroring operation, the centre of the pattern can be defined with a half pixel precision. A scrpit with the set of instructions can be written as the text file. The program is available at http://www.imec.msu.ru/~natalia/bs_form.htm. Supported by grants from INTAS, HHMI and RFBR.

Fibre Diffraction Studies of Potato Virus X on the BioCAT Beamline at the Advanced Photon Source.

Gerald Stubbs[1], Amy Kendall[1], Kelly Lynch[1], Lauren Parker[1], and Nicholas Taraska[2], Elena Kondrashkina[2], and T. Irving[2]

[1] Department of Biological Sciences and *Department of Chemistry, Vanderbilt University, Nashville, TN 37235, USA.
[2] BioCAT,Dept. BCPS., Illinois Institute of Technology, Chicago Il 60616.USA.

Fibre diffraction from flexible filamentous viruses has been limited by disorientation in the fibres, and by the close spacing of the layer lines in the diffraction patterns. Potato virus X (PVX) is the most important member of a major group of filamentous viruses, the potexviruses, and has great potential significance for basic virology, agriculture, and biotechnology. There have been reports of fibre diffraction from potexviruses for many years, but the diffraction patterns have been highly disordered. We have adapted methods originally developed for bacterial flagella by Namba's group to orient sols of PVX as fibre diffraction specimens. A combination of centrifugation in glass capillaries to form liquid crystals and exposure to strong magnetic fields (up to 18 Tesla) has produced greatly improved specimens. We hae constructed a camera for high resolution fibre diffraction on the BioCAT beamline at the APS,

Argonne, Il, USA allowing small (35 x 60 micron), high intensity (~2 x 10^{12} photons/s) X-ray beams to examine small ordered domains in the sols. Data so obtained have enabled us to determine accurately the symmetry of the helical virus, and to demonstrate the presence of deep intersecting helical grooves running longitudinally and azimuthally in the surface of the virus. Detailed structure determination will depend on further development of the specimen preparation methods, and will probably require high-resolution crystallographic structure determination of the isolated coat protein. Supported by grants MCB-9809879, DBI-9604789, and INT-9602486 from the National Science Foundation, and by Vanderbilt University. Use of the Advanced Photon Source was supported by the U.S. Department of Energy, Basic Energy Sciences, Office of Science, under contract No. W-31-109- ENG-38. BioCAT is a National Institutes of Health-supported Research Center RR-08630.

Type-4 bacterial pili: molecular models and their simulated diffraction patterns

D. A. Marvin, K. Nadassy, L. C. Welsh and R.N. Perham

Department of Biochemistry, University of Cambridge, Cambridge CB2 1GA, UK

Bacterial pili are long thin assemblies of pilin protein subunits, that extend outwards from the surface of bacteria and are involved in interaction of bacteria with their environment, notably attachment of pathogenic bacteria to their host and "twitching motility" of bacteria along surfaces. Pili are about one-third the diameter of bacterial flagella. Some types of pili are the adsorption sites of filamentous bacteriophage. X-ray fibre diffraction patterns of type-4 pili are classical alpha-helix patterns, with strong intensity in the equatorial direction at about 10 Å and in the meridional direction at about 5 Å [1]. The crystal structure of the type-4 pilin subunit has a highly conserved ~50-residue N-terminal alpha-helix and a less conserved ~100-residue globular C-terminal domain, and this subunit structure has been used to construct models of type-4 pili in which the N-terminal alpha-helix of the pilin forms the central core of the pilus [2-4]. We find that the calculated fibre diffraction patterns predicted for these models are less similar to the observed diffraction patterns than diffraction patterns predicted for models built from only the N-terminal alpha-helix portion of the subunit. Disorder in the globular domain may be one explanation for this effect, and the globular domain of pilin in pili may be "intrinsically unstructured" as found for binding regions of some globular proteins [5]. Twitching motility and phage infection proceed by retraction of pili [6], probably involving dissolution of pilin at the base of the pili into the host cell membrane, reminiscent of the process of filamentous phage infection by disassembly of the phage subunits into the membrane.

References

[1] Folkhard *et al*. (1981). *J. Mol. Biol*. **149**, 79.
[2] Parge *et al*. (1995). *Nature*, 378, 32;
[3] Hazes *et al*. (2000). *J. Mol. Biol*. **299**, 1005;
[4] Keizer *et al*. (2001). *J. Biol. Chem*. **276**, 24186.
[5] Wright & Dyson (1999). *J. Mol. Biol*. **293,** 321.
[6] Skerker & Berg (2001). *Proc. Nat. Acad. Sci*. **98**, 6901.

MYOSIN CROSSBRIDGE DYNAMICS IN FISH MUSCLE

C. Knupp, N-S. Mok, J.J. Harford, and J.M. Squire

Biological Structure & Function Section, Biomedical Sciences Division, Faculty of Medicine, Imperial College, London, SW7 2AZ, UK.

The crossbridge power stroke on actin appears to involve a change in angle between the actin-attached motor domain and the neck region of the myosin heads. Fast (1ms) time-resolved low-angle X-ray diffraction from contracting fish muscle during the rising phase of an isometric tetanus has been used to study the kinetics of the crossbridge cycle. Fish muscle is particularly advantageous for such studies because of its high degree of 3D order (Harford and Squire, 1986; Harford and Squire 1993; Hudson *et al*, 1997; Squire 2000). The data recorded at Daresbury (line 16.1) using the rapid detector are explained by five different kinetic states and three different structural states for the myosin heads: A resting state (structurally indistinguishable from an "off" and "reset" state), a weakly bound state and a strongly bound state. Weak and strong binding states are presumably related by a change in angle between myosin neck and motor domain. The myosin head starts the cycle in the resting state (solved by Hudson *et al*, 1997) and becomes mobile on activation going through an "off" state to a "weak" initial binding state on actin. The power stroke (weak to strong binding states) occurs, the head then resets and restarts the contractile cycle again in the "off" position. Time-resolved X-ray diffraction is proving effective in providing reasonable values for the kinetic constants and in separating the weak and strong crossbridge states in the contractile cycle.

References

[1] Harford JJ & Squire JM (1986)"Crystalline" myosin cross-bridge array in relaxed bony fish muscle. Low-angle X-ray diffraction from plaice fin muscle and its interpretation. *Biophys J*.; **50(1)**:145-55.
[2] Harford JJ & Squire JM (1993) Time-resolved studies of crossbridge movement: why use X-rays Why use fish muscle *Adv Exp Med Biol*. **332**:435-48;
[3] Hudson, L., Harford, J.J., Denny, R.J. & Squire, J.M. (1997) "Myosin head configurations in relaxed fish muscle: resting state myosin heads swing axially by 150Å or turn upside down to reach rigor". *J. Mol. Biol*. **273**, 440-455.
[4] Squire, J.M. (2000) "Fibre and Muscle Diffraction" in '*Structure and Dynamics of Biomolecules*' (E. Fanchon, E. Geissler, L-L. Hodeau, J-R. Regnard & P. Timmins, Eds), pp. 272-301. Oxford University Press, Oxford, UK.

MPW 6.2 - A station dedicated to investigating Materials for the Third Millenium

N.J. Terrill*, AJ.Dent, G. Bushnell-Wye, G.P. Diakun, C.C. Tang

Daresbury Laboratory, Warrington, WA4 4AD, UK

Station 6.2 has entered its commissioning phase haven taken 'first light' in December 2001. The station brings together three techniques optimised for materials processing. The beamline's optics comprise a vertically focussing collimating mirror followed by a double crystal sagittal bent monochromator and then a plane focusing mirror. It is designed for very rapid, tuneable, combined SAXS/WAXS experiments, X-ray diffraction and XAS (X-ray absorption spectroscopy). The station is equipped with state of the art detectors constructed along similar lines to the RAPID 2D detector for station 16.1. These will enable count rates of ca 10 MHz for both 1D small and wide angle experiments exceeding the existing capabilities of the detectors on station 8.2 by ca. 40 and 500 respectively. This has huge advantages as in many experiments it is necessary to attenuate the X-ray beam to avoid overloading the detectors. In addition because of the variable wavelength it will also be possible to carry out anomalous scattering experiments, something which is new to the repertoire of facilities offered to the non-crystalline community.

MYOSIN HEAD DISPOSITION MODELLED FROM LOW-ANGLE X-RAY DIFFRACTION OF RELAXED LETHOCERUS INSECT FLIGHT MUSCLE

Hind A. AL-Khayat[1], Liam Hudson[1], Michael K Reedy[2], Bruce Baumann[3], Thomas C Irving[4] & John M. Squire[1]

[1] Biological Structure and Function Section, Biomedical Sciences Division, Imperial College of Science, Technology & Medicine, London SW7 2AZ, UK,
[2] Department of Cell Biology, Duke University, Durham, NC 27710, USA,
[3] Florida State University, Tallahassee, FL, USA,
[4] Illinois Institute of Technology, Chicago, IL 60616, USA

Superbly ordered sarcomere structures in fibrillar insect flight muscle (IFM) and bony fish skeletal muscle favor detailed structural studies. We seek to picture the 3D molecular structures and actions of actin and myosin filaments in IFM by computer-modeling of low-angle X-ray patterns. Initially we are modeling IFM myosin head disposition to 5 nm resolution using the 1.43 nm resolution versions of both Rayment and Dominguez myosin heads crystal structures, and using 105 myosin reflections from MgATP-relaxed fibres of glycerinated IFM. We use the simulated annealing and local refinement approaches shown by Hudson *et al*. (J. Mol. Biol. 273: 440, 1997) to yield a 3% R-factor in their final best-fit-to-X-rays model of myosin head disposition on relaxed fish thick filaments. Our IFM model so far, based on layer lines 10, 16, 22, 26 and 32 (orders of 232 nm) has all crowns alike, all 8 [Rayment-type] heads per crown projecting at ~90° in a square shelf of density that rotates 33.75° for every 14.5 nm axial repeat. R-factor is 11.96%. Polarity re: Z- vs. M-band is clear from a unique fit to negative stained IFM thick filaments (Morris *et al*., J. Struct. Biol. 107: 237, 1991). Later, we propose to model the full unit cell, including thin filaments, against X-rays from relaxed, rigor and active IFM, ultimately to 1 nm resolution and study the interactions between the different proteins in the different muscle states.

MPW 6.2 - A station dedicated to investigating Materials for the Third Millennium

N. J. Terrill[1], G.P. Diakun[1], C.C. Tang[1], G. Bushnell-Wye[1], A.J. Dent[1], R.J Cernik[1], P. Barnes[2], G.N. Greaves[3], T. Rayment[4], A.J. Ryan[5]

[1] CLRC Daresbury Laboratory, Warrington, Cheshire WA4 4AD, UK
[2] Dept. of Crystallography, Birkbeck College, University of London, UK,
[3] Dept. of Physics, University of Wales, Aberystwyth, UK.
[4] Dept. of Chemistry, University of Cambridge, UK
[5] Dept. of Chemistry, University of Sheffield, UK

A new X-ray instrument, MPW6.2 is being commissioned for the study of non-crystalline and polycrystalline materials at the SRS, Daresbury Laboratory. The beamline is optimised to receive synchrotron X-rays of 5-18 keV from a multi-pole (x11) wiggler (B2 tesla). The optics - two mirrors and a Daresbury sagittal monochromator - have been arranged to focus the beam vertically and horizontally respectively to deliver an estimated flux of 1011-10^12 photons/mm2/s/0.01% onto the sample under investigation, at least 100 times more intense than any other XRD source on the SRS. At the heart of this development are two state-of-the-art detectors. The first of these is a new wide-angle curved position-sensitive detector to be mounted on a heavy-duty two-circle diffractometer (theta, 2theta). This high angular resolution (0.06degrees) detector system is based on the novel micro-gap multi-wire (RAPID) technology for fast data acquisition [1], and will allow an entire X-ray diffraction pattern (XRD) to be recorded in a very short time (microseconds to seconds). Utilising the same technology, a quadrant style detector will also be installed for small angle X-ray scattering (SAXS). Together, these two installations constitute an exceptionally powerful instrument for combined small/wide-angle scattering (SAXS/WAXS). Additionally, X-ray absorption apparatus will be provided for combining these techniques with parallel spectroscopy measurements (EXAFS). Purposely designed for kinetic studies, to follow structural changes in solid and liquid state reactions and materials processing, the combination of tuneable wavelength, high flux and rapid data collection make this new beamline a world-class facility for carrying out simultaneous measurements by researchers in the field of materials science.

References

[1]. Lewis RA, Berry A, Hall CJ, Helsby WI, Parker BT, *NUCL INSTRUM METH A* **454 (1)**: 165-172 NOV 1 2000

Ultrastructural Changes in Keratoconic-like Mice Corneas

S. Dennis[1], Adachi W[2], Y. Matsushima[3], M. Tachibana[3], C. Boote[1], K. Meek[1], S. kinoshita[1] and A. Quantock[1]

[1] Dept of optometry and vision sciences, Cardiff University
[2] Dept of ophthalmology, Kyoto Prefectural University of Medicine, Japan
[3] Saitama Cancer Centre, Saitama, Japan Austrian Academy of Sciences

Purpose: Corneas from transgenic mice showing a form of keratoconus (conical cornea) were investigated by X-ray fibre diffraction to see if structural collagen alterations were responsible for the misshapen tissue. Methods: Low-angle (station 2.1) fibre diffraction was used to measure collagen interfibrillar spacing and fibril diameter in normal and keratoconus corneas. Also, the intermolecular spacing and the degree of preferred collagen fibril orientation was measured at 200 micron intervals across four keratoconus (two males and two females) and two normal mice corneas (one male and one female) using high-angle X-ray diffraction on station 14.1. Results: Collagen interfibrillar spacing and fibril diameter was greater in male (n8) and female (n6) keratoconus than in normal (n8) mice corneas. Variation in the amount of preferred collagen fibril orientation across mice corneas is similar to that seen in humans, with strong alignment occurring at both edges of the cornea suggesting the presence of an annulus at the limbus. Differences were observed between normal and keratoconus mice in the amount of preferred collagen fibril orientation across the cornea, with the differences being most marked in one of the male keratoconus mice which showed no evidence of an annulus. Conclusion: Changes in the corneal fibrillar array are possibly responsible for biomechanical and shape changes in mice corneas with a form of the human disease keratoconus.

The modelling of strain induced molecular changes in type I collagen in rat tail tendon

Craig Laurie[1], Tim Wess[1], Ivo Zizak[2], Peter Fratzl[3]

[1] University of Stirling
[2] Hahn-Meitner-Institut
[3] Erich Schmid Institute of Materials Science

Type I collagen is one of the most important stress bearing proteins in vertebrates, being predominant in tendon, skin and bone. Tendon is composed of almost 100 percent type I collagen, and displays outstanding mechanical properties which have been extensively studied. However, as yet, no satisfactory explanation has been proposed to describe the changes in conformation at the molecular level. These changes are evident in the diffraction pattern of tendon revealed during mechanical testing, collected in a time-resolved manner utilising synchrotron radiation. This work shows the attempts made to explain the changes in the profile of the meridional diffraction pattern of rat tail tendon which occur when the tissue is stretched. When observing the diffraction pattern of stretched tendon the changes in the intensity profile can be summarised as: 1)The attenuation of the higher orders in the diffraction series, 2)The modulation of the lower order diffraction terms apparent in the change in the ratio of the even to odd orders, most apparent in the 2nd and 3rd orders, The attenuation of the higher orders were interpreted as incoherence in the structure produced through a microfibrilar shearing process. The modulation in the even to odd orders was modelled as molecular slippage causing a change in the electron density profile. This has produced the most satisfactory models as yet proposed to describe these events.

Challenges Facing DNA Fibre Crystallography

Clive Delmonte

Associate Lecturer, Open University, Clarendon Park, Nottingham NG5 1AH

Initial theoretical studies of alternative helical DNA structural models have been published recently and matched against fibre diffraction patterns [1,2]. These models arise from the wide range of kinetic, mechanistic and other experimental results for duplex DNA which have accumulated since 1950 [3,4,5]. Variety in DNA structure remains a topic of great interest [6]. Apart from a rare, exceptional polynucleotide fibre diffraction pattern of poly(d(AT)) at very high resolution derived from an yet unreported atomic structure [7], DNA fibre diffraction has too low a resolution to allow certain competing helical structures to be distinguished from each other without taking cognisance of results from other fields. Results from studies of oligodeoxynucleotide diffraction from true crystals are compromised by a convention that imposes algorithmic constraints, thus ensuring that there is only a restricted range of permitted structural solutions [8].

References

[1]. Lucas, A. A.; *Proceedings of SANIBEL Conference, Florida, USA,* **Feb. 2002**
[2]. Lucas, A. A.; *J Quant. Chem.* (in press, 2002)
[3]. *Towards a New Structural Molecular Biology*; C. Delmonte; ISBN 0 9512276 0 2 (1991)
[4]. Advances in AFM & STM *Applied to the Nucleic Acids*; C. Delmonte; ISBN 0 9512276 2 9 (1997)
[5]. *DNA Structure Puzzles*; C. Delmonte; ISBN 0 9512276 3 7 (2000)
[6]. Delmonte, C. & Mann, L. R. B.; *Current Science* (in prep. 2002)
[7]. Garner, C. D. & Helliwell, J. R.; *Chemistry in Britain* (1986) 835 - 840
[8]. Dickerson, R. E.; J Mol. Biol. 205 (1989) 787 - 791 or *Nucl. Acids Res.* **17** (1989) 1797 - 1803

The three dimensional packing of type I collagen molecules in rat tail tendon

Laing, J. H.; Wess, T.J.W.; Alberts, I.L.A.

University of Stirling, Scotland, FK9 4LA

The axial packing of type I collagen molecules is well described, but the lateral or three-dimensional packing topology is less clear. It is generally accepted that the molecules pack on a triclinic lattice in a microfibrillar manner; however, the precise long- and short-range packing interactions remain unclear. This work aims to define these through a combination of X-ray diffraction analysis and computer modelling. Lateral packing interactions between type I collagen molecules in rat tail tendon give rise to a series of Bragg peaks overlain with diffuse scatter in the equatorial region of the X-ray diffraction pattern. The diffuse scatter may partly arise from thermal molecular disorder and we show that it is possible to reduce the degree of diffuse scatter, and thus facilitate analysis of the underlying Bragg intensities, by cryo-cooling the sample to 90-100 Kelvin during data collection. We also report on various methods used to distinguish the Bragg peaks from the diffuse scatter in XRD patterns collected from cryo-cooled and ambient samples. We describe

a computer model that simulates the lateral packing of type I collagen molecules. In this model, a unit cell slice of five molecular segments with triclinic lattice coordinates is energy minimised to a global minimum using the discriminatory procedure of simulated annealing which finds the optimal, lowest energy, three dimensional packing conformation. For the first time, this model incorporates amino acid interactions such as charge and Van der Vaal radii and accounts for interactions in the gap, overlap and telopeptide regions.

The Conjugative Pili of The RP4 Plasmid

Samantha J Holland, Don A Marvin, Richard N Perham.

University of Cambridge, Department of Biochemistry

Conjugative pili are long filaments, consisting of multiple copies of a single pilin subunit. The pili protrude from the surface of bacteria and are involved in DNA transfer. They are also the sites of attachment of many filamentous bacteriophages. The RP4 plasmid codes for the conjugative RP4 pilus, which is the initial attachment site for filamentous bacteriophage Pf3. This pilus is involved in the transfer of RP4 plasmid DNA between Gram-negative bacteria and to a wide range of organisms such as Gram-positive bacteria and even yeasts. The RP4 pilin subunit, TrbC, has a molecular weight of 8 kDa and in contrast to the pilin of most other conjugative pili, is circular, with N- and C- termini joined by a peptide bond. We are studying Pf3 bacteriophage / RP4 pilus interaction and fibre diffraction studies of RP4 pilus structure are in progress.

A Bayesian approach to phase extension

D. S. Sivia

ISIS Facility, Rutherford Appleton Laboratory

A Bayesian approach to the heavy-atom method for solving crystal will be presented. It will be shown that, in contrast to conventional procedures, probability theory makes full use of the information inherent in a known fragment since both the related phase and amplitude play a central role. This property is particularly important for powder data, where peak overlap makes it difficult to infer the intensities of individual reflections reliably. A covariance matrix is also shown to be essential, in the latter case, for capturing the constraints imposed by the diffraction measurements in the space of the structure factors. Prior knowledge about the positivity of the underlying electron density, at least for X-ray diffraction, can be encoded through the use of an entropic prior, which further enhances the quality of the results.

Photonic Structures from Amphiphilic Block Copolymers

Laurence Corvazier, Loic Messé, Corinne L.O. Salou, Ronald N. Young, J. Patrick A. Fairclough and Anthony J. Ryan

The Polymer Centre, Department of Chemistry, University of Sheffield, S3 7HF Sheffield, UK

The order-disorder transition (ODT), microdomain structures and the phase diagram for ternary blends of low molecular weight PS, PI and PS-PI have been determined by a combination of X-ray scattering and transmission electron microscopy. The distribution of the homopolymer within the layers of a related PS/PB/PS-PB system has also been determined by a combination of X-ray and neutron reflectivity. A series of nearly symmetric, ternary blends of polystyrene (PS), polyisoprene (PI) and polystyrene-block-polyisoprene (PS-PI) have been studied by small angle X-ray scattering, static light scattering and transmission electron microscopy. The molecular weight of the homopolymers and block copolymer were in the ratio NH / NBCP 0.19, which gave a block copolymer ODT and a homopolymer blend TC that were similar (TC / TODT ~ 1.1). The block copolymer and its blends showed a weakly first-order transition from a lamellar phase to a fluctuating disordered phase in the volume fraction range FH 0.77. A bicontinuous microemulsion was found between FH 0.79 and FH 0.93, and for FH 0.93 macrophase separation was observed. In a similar PS, polybutadiene (PB) and polystyrene-block-polybutadiene (PS-PI) system the distribution of the homopolymer diluent was studied by X-ray and neutron reflectivity with deuterium labelled PS. The initial microstructure formed on spin coating had a dry-brush structure with the homopolymer concentrated in the centre of the domains and on subsequent annealing a wet-brush morphology was observed with the homopolymers uniformly distributed. The potential applications of self-assembled block copolymers as photonic structures will be highlighted.

The Preparation and Characterisation of Polyisocyanurates with Graded Modulus.

Abbott, A.L. Turner, M.L. Ryan, A.J.

Department of Chemistry, University of Sheffield, Brook Hill, Sheffield. S3 7HF

The preparation of polyisocyanurate elastomers for use as damping coatings on mechanical parts, with a range of glass transition temperature, Tg, through the depth of the sample has been achieved. This was accomplished by varying the density of cross-links in the sample. Material properties were characterised using a variety of techniques including FT-IR Microscopy, Laser Ablation Mass Spectroscopy, Small Angle X-ray Scattering and Nano-indentaion. SAXS was used to monitor the phase separation of the material under different processing conditions. Phase separation was seen in all materials made from polyisocyanurates with polyether segments with Mw greater than 2200, regardless of the proportion of diisocyanate used. The degree of microphase separation, obtained from SAXS results is important in the determination of the mechanical properties of the elastomer. The kinetics of phase separation could be studied by performing the curing in the X-ray beam. FT-IR Microscopy and Laser Ablation Mass Spectroscopy were used to characterise the changing chemical structure through the depth of the material. This was possible due to the chemical difference between the isocyanurate cross-linking units and the polyether soft segments. The Nano-indentor proved to be a powerful tool for investigating the mechanical properties of the material, as it makes use of dynamic and static indentation under thermally controlled conditions. These elastomers were also used to aid the understanding of the nano-indentation technique for 'soft' materials.

Structural Changes in Muscle Correlated with ATP Hydrolysis

Leepo C. Yu[1], Sengen Xu[1], Gerald Offer[1], Jin Gu[1] and Howard White[2]

[1] National Institutes of Health, USA

[2] East Virginia Medical School, USA.

Two dimensional X-ray diffraction was obtained from skinned rabbit psoas muscle fibres. The goal is to correlate structures of the cross-bridge population with various intermediate states in the ATP hydrolysis cycle. By systematically using analogs, or variations in temperature and ionic strength, the distribution and disposition of myosin heads in eight of the intermediate states have been characterized. Some highlights of the findings: in the state of A.M.ATP, before ATP is hydrolyzed, the binding of myosin to actin is characterized by random orientations, and the binding site on actin differs from that for rigor binding. When myosin is not bound to actin, only the state with the hydrolysis products ADP.Pi bound at the active site (i.e. M.ADP.Pi) exhibits an ordered helical arrangement on the myosin filament. Myosins in other states (M.ATP, A.ADP, M) are disordered. Recently, Malnasi-Csizmadia, *et al*. (Biochemistry (2000), 39:16135-16146; and (2001) 40:12727-12737) studied the effects of temperature and ligands on the open - closed conformational transition in Dictyostelium myosin. The enthalpy change for the open - closed transition is identical for the disorder - order transition found in the myosin filament by X-ray diffraction. The close correlation strongly suggests that the open - closed conformational change and the disorder - order transition are the same process. It also suggests that helical order may be used as a signature for the closed conformation of myosin in relaxed muscle.

SAXS studies of sheared nanophase separated copolymers

I.W.Hamley, V.Castelletto

University of Leeds

Recent work in our group has focussed on the effect of shear on nanophase separated block copolymers in solution, melt and crystalline states. The main focus of this talk will be synchrotron SAXS studies of shear-induced alignment of poly(oxyethyelene)-poly(oxybutylene) diblock copolymers in solution [1]. The orientation of twinned face-centred and body-centred cubic crystals has been studied following steady shear in a Couette cell, or oscillatory shear using a modified Rheometrics rheometer. The latter has recently been modified to allow WAXS as well as SAXS with simultaneous rheology - a powerful combination to examine the effect of shear on crystallization in polymers. Preliminary results from experiments on

crystallization in block copolymers containing a semicrystalline PEO block will be presented [2]. We have also constructed a small goniometer stage to fit inside the rheometer oven, and this allows "mesoscopic crystallography" experiments to be performed, where samples are first sheare and then mounted on the goniometer which is rotated with respect to the shear axis, allowing the 3-dimensional diffraction pattern of shear-aligned copolymer mesophases to be mapped out. Time (and results) permitting, SAXS studies of shear-induced orientation of cross-linked gels formed by hydrophobically-modified poly (N-isopropy-lacryalmide) in water will also be discussed. ([1] Work done in collaboration with group of C.Booth (Dept of Chemistry, University of Manchester). [2] Work done in collaboration with Prof G. Floudas (University of Ioannina, Greece), and Dr F.Schipper (FORTH-IESL, Crete, Greece))

The Liquid-Solid Transition in a Micellar Solution of a Diblock Copolymer in Water

V. Castelletto[1], C. Caillet, J. Fundin, I. W. Hamley, Z. Yang, A. Kelarakis

[1] Department of Chemistry, University of Leeds, Leeds LS2 9JT, UK
[2] Department of Chemistry, University of Manchester, Manchester M13 9PL, UK
[3] National and Kapodistrian University of Athens, Department of Chemistry, Physical Chemistry Laboratory, Panepistimiopolis 157 71 Athens, Greece

The structure of a diblock copolymer solution in the vicinity of the transition between micellar liquid and solid phases was investigated using small-angle X-ray scattering. An amphiphilic poly(oxyethylene)-poly(oxybutylene) diblock was studied in water. Static and dynamic light scattering techniques were used to provide an independent measure of micelle dimensions and aggregation numbers. Dynamic shear rheometry and mobility measurements were used to locate phase transitions. A micellar liquid phase was identified at low concentration and a cubic micellar phase at higher concentration, the transition between the two occuring at higher temperature as the concentration increased. The cubic micellar phase behaves rheologically as a solid and SAXS confirmed a face-centered cubic structure. Intermediate between these two phases, a viscoelastic solft solid was observed, with finite yield stress but with a much lower dynamic modulus than the crystalline solid. Several distinct suggestions have been put forward for the structure of the solution in this region. In a poly(oxyethylene)-poly(oxypropylene)-poly(oxyethylene) Pluronic triblock, small-angle neutron scattering and rheology provided evidence for a percolation transition between micellar liquid and solid phases [L.Lobry *et al.*, Phys Rev E 1999, 60, 7076], indicating a fractal structure of micelles aggregated due to attractive interactions. Alternatively, a defective solid phase has been proposed. We analysed the structure of solutions of our diblock copolymer via detailed model fits to the SAXS data for concentrations spanning the liquid- solid transition. The micellar form factor was modelled as a homogeneous micellar core with attached Gaussian chains; and the intermicellar structure factor could be described using the hard sphere model. Thus there is no evidence for percolation induced by effective attractive interactions between micelles in our system. In contrast SAXS data indicates there is a coexistence region between hard sphere fluid and solid crystal phases, in which small grains of close-packed crystal coexist with fluid. It is apparent that block copolymer micelles act as model colloidal systems in which it is possible to investigate the influence of attractive and repusive interactions between spherical particles by varying the copolymer composition.

The crystal structures and hydrogen bonding in cellulose polymorphs

Yoshiharu Nishiyama[1], Henri Chanzy[2], Masahisa Wada[1], Junji Sugiyama[3], Karim Mazeau[2], Trevor Forsyth[4,5], Christian Riekel[6], Martin Muller[6], B.Rasmussen[6] and Paul Langan[7]

[1] Department of Biomaterials Science, Graduate School of Agriculture and Life Sciences, The University of Tokyo, Tokyo 113-8657, Japan.
[2] Centre de Researches sur les Macromolecules Vegetale, CNRS, BP53, 30841, Grenoble, France.
[3] Wood Research Institute, Kyoto University, Kyoto 611-0011, Japan.
[4] Institut Laue Langevin, 156X 38042, Grenoble Cedex 9, France.
[5] Physics Dept., Keele University, Staffs ST5 5BG, UK.
[6] European Synchrotron Radiation Facility, BP 220, 38042 Grenoble Cedex, France.
[7] M888 Biosciences Division, Los Alamos National Laboratory, Los Alamos, NM 87545, USA 2. University of Manchester

Although the crystalline nature of cellulose has been one of the most studied problems in polymer science there remain many open questions. We are determining the precise crystal structures and hydrogen-bonding systems of cellulose polymorphs by fibre diffraction. X-rays are used to determine the positions of carbon and oxygen atoms. Neutrons, in combination with isotopic substitution of labile hydrogen atoms in the fibres by deuterium, are used to determine the positions of hydrogen atoms involved in hydrogen bonding. Methods have been developed for obtaining oriented polycrystalline fibres that diffraction X-rays and neutrons to atomic resolution [1,2]. For the first time data have been collected from natural occurring pure cellulose I-alpha isolated from Glaucocystis and from pure cellulose I-beta isolated from Tunicate. We have also collected data from the polymorphs resulting from cellulose processing; II(both mercerized and regenerated), III(I) and III(II). Our initial results on regenerated cellulose II, mercerized cellulose II[3,4] and cellulose I-beta[5], have lead to new crystal structures, direct identification of hydrogen bonding systems, and new insights into the factors that determine the structure and properties of cellulose.

References

[1] Nishiyama, Y.; Kuga, S.; Wada, M.; Okano, T. *Macromolecules* 1997, **30**, 6395.
[2] Nishiyama, Y.; Okano, T., Langan, P.; Chanzy, H. *Int. J. Macromolecules*, 1999, **26**, 279.
[3] Langan, P.; Nishiyama, Y.; Chanzy, H. *J. Am. Chem. Soc.*, 1999, **121**, 9940.
[4] Langan, P.; Nishiyama, Y.; Chanzy, H. *Biomacromolecules*, 2001, **2**, 410.
[5] Nishiyama, Y.; Langan, P.; Chanzy, H. *J. Am. Chem. Soc.*, submitted Jan 2002.

Transthyretin Amyloid Fibres

L. Gales[1,2], I. Cardoso[1,3], M.J. Saraiva[1,3], A.M. Damas[1,2]

[1] ICBAS, Instituto de Ciências Biomédicas Abel Salazar, Universidade do Porto, Largo Prof. Abel Salazar nº2, 4099-003 Porto, Portugal.
[2] Grupo de Estrutura Molecular, Instituto de Biologia Molecular e Celular, Universidade do Porto, rua do Campo Alegre nº 823, 4150 Porto, Portugal.
[3] Grupo de Amilóide, Instituto de Biologia Molecular e Celular, Universidade do Porto, rua do Campo Alegre nº 823, 4150 Porto, Portugal.

Familial Amyloidotic Polyneuropathy (FAP) is characterized by deposits of insoluble amyloid fibres in which transthyretin (TTR) is the major protein component. TTR is a tetramer with identical 127 aminoacid sub-units and an extensive β-sheet structure. How this structure is related to the molecular organization of the FAP amyloid fibre is one of the major questions in understanding the pathophysiology of the disease. The mechanism by which the soluble protein converts to insoluble fibre can only be conveniently established when the structure of the fibres is elucidated. Amyloid fibres constitute a high molecular weight, insoluble material and therefore the atomic structure cannot be investigated by conventional X-ray crystallography or nuclear magnetic resonance (NMR). However, information about the fibrillar structure can be obtained by X-ray fibre diffraction from very well oriented samples. Using this approach it was shown that they exhibit a cross β-sheet structure [1] and are formed by a continuous β-sheet helix [2] or an association of units with a structure close to the TTR monomer [3]. Aiming at improving our knowledge about the molecular structure of amyloid fibrils, new X-ray experiments were performed at European Synchrotron Radiation Facility (ESRF), beam line ID13. The fibrillar Leu55Pro TTR samples were drawn up into siliconized glass capillary tubes, sealed at the top, then placed into a 2-T magnet and allowed to dry at ambient conditions. X-ray diffraction patterns from these samples indicated the presence of the cross-b pattern, characterized by a meridional reflection at 4.65 Å and a broad equatorial reflection at 10.3 Å. Interpretation of the data shows that the protofilament building blocks are monomers composed of a pair of β-sheets with an intersheet distance of 10 Å. End-to-end association of four monomers in the fibre direction and related by some kind of axial rotation constitute a repeating unit of 116 Å. The estimated protofilament diameter is 42 Å and the calculated mass-per-length is 0.47 kDa / Å. These values are in good agreement with results obtained by scanning transmission electron microscopy (STEM) [4]. Future work concerning the alignment of the amyloid fibres and their interaction with fibre disrupters will be performed.

References

[1] Damas, A., Sebastião, M.P., Domingues, F.S., Costa, P.P., Saraiva, M.J. (1995) Amyloid *Int. J. Exp. Clin. Invest.* **2**, 173-178.
[2] Blake, C., Serpell, L. (1996) *Structure* **4**, 989-998.
[3] Inouye, H., Domingues, F.S., Damas, A.M., Saraiva,

M.J., Lundgren, E., Sandgren, O., Kirschner, D. (1998) Amyloid *Int. J. Exp. Clin. Invest*. **5,** 163-174.
[4] Cardoso, I., Goldsbury, C.S., Muller, S.A., Olivieri, V., Wirtz, S., Damas, A.M., Aebi, U., Saraiva, M.J. (2002) *J. Mol. Biol.* **317**, 683-695.

The Compaction and Delivery of DNA.

A.J.Colclough, A.M.Voice, T.A.Waigh

Department of Physics and Astronomy, University of Leeds, Leeds, LS2 9JT.

The medical profession increasingly desires the ability to deliver treatment, by a drug, to a specific organ or area of the body. Examples include the targeting of anti-tumour drugs for the treatment of cancer, or genetic material for gene therapy. One particularly effective strategy is to use a carrier particle to house the drug while in vivo. Viruses have been investigated for this purpose, but this can provoke an immune response. Therefore bio-compatible polymers are being designed to circumvent these problems. We investigate a simplification of the drug molecule - carrier particle relationship by examining the association between a charged spherical particle (representing a polyelectrolyte micelle) and an oppositely charged polyelectrolyte, in this case DNA. Dynamic light scattering, Raman spectroscopy and small-angle X-ray scattering are used to examine the conformational behaviour of the complexes.

A solution structural model of human IgA2

P.W.Whitty[1], A. Robertson[2], P.B. Furtado[2], J.T. Eaton[2], M.A.Kerr[1], J.M.Woof[1] and S.J.Perkins[2]

[1] Department of Molecular and Cellular Pathology, University of Dundee, Ninewells Hospital, Dundee DD1 9SY, UK

[2] Department of Biochemistry, University College London, Gower Street, London WC1E 6BT, UK

There are two subclasses of human immunoglobulin A, IgA1 and IgA2. Human IgA2 has a short hinge region of 8 amino acids linking the Fab arms and the Fc region, while IgA1 possesses a much more extended hinge of 23 residues. X-ray and neutron scattering analysis of recombinant monomeric IgA2 (of IgA2m(1) allotype) revealed a radius of gyration RG of 5.1 nm, which is significantly smaller than that of IgA1 at 6.1-6.2 nm. For IgA2, the distance distribution function P(r) comprised a single peak and a maximum dimension of 17 nm, while IgA1 gave two peaks and a 21 nm maximum dimension. An automated curve fit search analysis of a homology model for IgA2 was conducted, in which random IgA2 hinge structures connect the Fab and Fc fragments in any orientation. Around 50 out of 10,000 models fitted the scattering and ultracentrifugation data. This approach produced an IgA2 structure that is significantly more compact than that of IgA1. The IgA2 Fab and Fc arrangement resembles that in the crystal structure of the hinge-deleted human IgG1 Mcg, which shares the characteristic of an inter-light chain disulphide bond.

Synchrotron studies of exotic smectic liquid crystals.

H F Gleeson

Department of Physics and Astronomy, Manchester University, Manchester M13 9PL UK

Liquid crystals are ordered fluids that are well-known for their use in display devices. One family of these materials, the smectic phases, have the potential to exhibit ferroelectricity, antiferroelectricity and ferrielectricity through subtle variations in their structure. All such liquid crystals have titled molecules that pack in layers with an overlying helicoidal structure. They differ in the interlayer periodicity. Ferroelectric liquid crystals change little from one layer to the next, antiferroelectrics alternate in tilt direction (so have a two-layer periodicity), while the structures of the intermediate phases have proven to be a considerable challenge to solve, but are known with both 3- and 4-layer periodicities. As well as deducing the structures that these materials adopt, it is also important to understand the structural modifications that occur within devices both with and without the application of electric fields. This paper describes the structures and properties of this novel class of fluids in devices. Static and time-resolved small angle X-ray scattering have been used to probe ferroelectric switching, while resonant X-ray scattering experiments have provided unique information on the layer structures of the antiferroelectric and intermediate phases, and their modification using switching fields. The experiments and results are summarised.

A-DNA before, during and after Watson Fuller's PhD thesis

Struther Arnott

Biomedical Sciences Division, Imperial College of Science, Technology and Medicine, Exhibition Road, London SW7 2AZ, England.

With retrospective wisdom we can allocate some of the confusion in interpreting the earliest (1930s) fibre diffraction patterns of DNA to the fact that the specimens were mixtures of the two commonest allomorphs of the DNA duplex. These were labelled A and B only after uncontaminated patterns of each were obtained by Maurice Wilkins and his associates in the early 1950s. From the beginning of their studies they found that all of their A-DNA specimens were not only uniaxially oriented but also polycrystalline. Despite this presumed advantage which attracted much of Rosalind Franklin's analytical effort, more attention came to be focussed on the apparently more hydrated B allomorph that was expected to be the more relevant biological form especially after oriented and polycrystalline specimens were obtained for it also. The A-DNA duplex has 2 111 symmetry with the pitch of its helical chains 2.86nm. The duplexes are packed in a C-face-centered monoclinic (space group C2) unit cell (a 2.17, b 3.99, and c 2.80nm, b 96.80) which approximates to the close packing of cylinders of about 2.25nm diameter. One consequence of this is that although there are many Bragg reflexions on each layer line they are often in partially overlapping clumps. Even today a convincingly scrupulous extraction of structure factors from such a complicated fibre diffraction pattern would be non-trivial. In the late 1950s the task was herculean and had to be followed by equally meticulous rounds of manual model-building and repeated Fourier transform calculations. It is to Watson Fuller's great credit that his efforts and 1960 conclusions about this structure and its details have not been improved upon significantly since its belated publication in 1965 (Fuller *et al*. J. Mol. Biol. 12, 60). What revived interest in A-DNA itself was the discovery that ribonuclease-resistant ribosomal RNA fragments and the lengthier nucleic acid components of certain RNA viruses consisted of Watson-Crick base-paired duplexes with A-DNA-like secondary structures. Subsequent studies of DNA-RNA hybrid helices, and of the Watson-Crick base-paired duplex regions in t-RNA and other RNAs with complex tertiary structures, and even of polynucleotide duplexes and triplexes with non-Watson-Crick base-pairings have confirmed the importance of A-DNA-like secondary structures whose C3'-endo furanose ring conformations are associated with a morphology quite different from that in double helices like the B form where all the furanoses have C2'-endo puckering. More surprising has been the discovery that some helical duplexes with purine-purine or pyrimide-pyrimidine base-pairs have structures in which the the polynucleotide chains are not just similar to those of A-DNA but identical with them. To understand why this DNA chain conformation is so special as to persist with no modification in so many environments one has to look to the geometry of the water molecules that are associated with this unique polynucleotide fold. Crystal structures of oligonucleotides have provide the needed insight but it would not be surprising if Watson Fuller's good data could not be persuaded to confirm this directly for the eponymous structure itself.

An Investigation into the Phase Behaviour of Block Copolymers in Solution - Phases Formed and their Transition Kinetics

Alex Norman, Patrick Fairclough, Shaomin Mai, Yuan Deng and Anthony Ryan

Department of Chemistry, University of Sheffield, Brook Hill, Sheffield, S3 7HF Building, Sheffield, S3 7HF

Various block copolymers in aqueous solution have been studied to show how the chain architecture effects the phase behaviour and the kinetics of the phase transitions. This has many biological applications such as artificial lung surfactants in premature babies(1). The block copolymers under investigation are diblock PEO-PI copolymers, triblock PEO-PBO-PEO copolymers, and triblock PBO-PEO-PBO copolymers. Micelles are formed when the concentration of polymer in water reaches a critical value known as the CMC. As the concentration is increased further the micelles pack together to form ordered arrays of specific geometry such as Cubic, Hexagonal or Lamella structures. PI-PEO and PEO-PBO-PEO block copolymers form spherical micelles rather than "flower like" micelles (PBO-PEO-PBO) due to the positioning of the hydrophobic component within the polymer. These stuctures have been deduced by Simultaneous SAXS/WAXS/DSC on Beamline 8.2 of the CCLRC

Daresbury Laboratory, Warrington, U.K and at the CRG BM26 at the European Synchrotron Radiation Facility, (ESRF), Grenoble, France. The positioning of the SAXS peak-to-peak ratio is indicative of the structure formed. The samples are heated and the structure changes due to a change in the peak ratio. This can be monitored by using the CCP13 Program XFIT. From this we can deduce the whereabouts of the phase transition, and consequently map the phase morphologies. The kinetic parameters of the phase transition can be studied by performing SAXS/WAXS/DSC. The sample is heated to a point in the phase diagram where it displays a certain structure. It is then rapidly quenched to another point in the phase diagram of a different structure. Here a peak can be seen to grow. This will give us information on the kinetics of the phase transition. These experiments have been performed at various quench depths. In addition, Polarised Optical Microscopy experiments have been performed in a similar way. Here the number of coloured pixels emerging from an image are counted. Howver this technique only works from an isotropic phase (Cubic or Disorder) to an Anistropic phase (Hexagonal or Lamellae). Avrami kinetics are performed on the SAXS and Microscopy data to achieve values for the rate consatnt and the Avrami exponent, which tells us information abut the mechanism of the phase transition. (1)- W. R. Perkins, R. B. Dause, R. A. Pareante, S. R. Minchey, K. C. Neuman, S. M. Gruner, T. F. Taraschi, A. S. Janoff.; Science, 273, 1996, 330.

The Structrue of type I and type III collagen heterotypic fibrils: An X-ray diffreaction study

G.J.Cameron, I.L.Alberts, J.H.Laing, T.J.Wess

Centre for Extracellular Matrix Biology Department of Biological Sciences University of Stirling Stirling FK9 4LA

The molecular packing arrangement within collagen fibrils has a significant effect on the tensile properties of tissues. To date, most studies have focused on homotypic fibrils composed of type I collagen. This study investigates the packing of type I/III collagen molecules in heterotypic fibrils of colonic submucosa using a combination of X-ray diffraction data, molecular model building and simulated X-ray diffraction fibre diagrams. A model comprising a 70 nm diameter D-(~65nm) axial periodic structure containing type I and type III collagen chains was constructed from amino acid scattering factors organised in a liquid-like lateral packing arrangement simulated using a classical Lennard-Jones potential. The models that gave the most accurate correspondence with diffraction data revealed that the structure of the fibril involves liquid-like lateral packing combined with a constant helical inclination angle for molecules throughout the fibril. Combinations of type I:type III scattering factors in a ratio of 4:1 gave a reasonable correspondence with the meridional diffraction series. The attenuation of the meridional intensities may be explained by a blurring of the electron density profile of the D period caused by non-specific or random interactions between collagen types I and III in the heterotypic fibril.

Effect of Chain Architecture on the Crystallisation of Polyolefins

Ariana Morgovan

The University of Sheffield Department of Chemistry Dainton Building Brook Hill Sheffield S3 7HF

Advances in understanding and predicting relationships between polymer properties (such as their rheology) and their structure require the availability of macromolecules with well-defined architectures and narrow molecular weight distributions. Polybutadiene with controlled molecular weight and polidispersity close to 1.0 was synthesised using high vacuum techniques. It was then hydrogenated using the diimine method, which is the most direct route to obtain near-monodisperse linear low-density polyethylene. These and some industrial polyethylenes were subjected to simultaneous Small Angle X-Ray Scattering (SAXS)/ Wide Angle X-Ray Scattering (WAXS) / Differential Scanning Calorimetry (DSC) experiments performed at SRS CLRC Daresbury Laboratory, UK and at ESRF, Grenoble, France to analyse their crystallisation kinetics. Rheology (arm retraction mechanisms) were also investigated.

Small Angle X-ray Scattering Analysis of Historic Parchment

Craig J. Kennedy[1], Tim Wess[1], Linda Ramsay[2]

[1] University of Stirling
[2] National Archives of Scotland

Small Angle X-ray Scattering (SAXS) is a powerful yet non-destructive technique that is capable of providing information about the level of deterioration of collagen fibres within historic parchment. A great deal of cultural heritage is stored on historic parchment throughout the world. Over time and subject to the conditions that the parchment is stored in, the parchment deteriorates. This can be brought about by the effects of pollution, humidity, chemical modification and conservation techniques. As the parchment deteriorates the long-range order of the collagen fibres is degraded. SAXS reveals the level of this degradation. SAXS can provide data concerning the molecular detail of the deterioration of historic parchment in a non-destructive fashion that can be utilised in a conservation context.

Using SAXS/WAXS to follow Shear-Induced Crystallization

E.L. Heeley[1], A.C. Morgovan[1], W. Bras[2], I. P. Dolbnya[2], C.M. Fernyhough[1], A.J. Gleeson[3], & A.J. Ryan[1]

[1] Department of Chemistry, University of Sheffield, Sheffield, S3 7HF, UK
[2] ESRF,156 rue des Martyrs, B.P. 220, F-38043 Grenoble Cedex, France
[3] Daresbury laboratory, Daresbury, Warrington, Cheshire, WA4 4AD, UK

Investigations of shear-induced crystallization have been performed on several commercial and laboratory synthesized polyethylene (PE) samples. A Linkam CSS450 shear cell has been used to shear PE samples providing a pulse of shear at shallow under-coolings from the melt where, quiescent crystallization would normally take several hours. Small- and Wide- Angle X-ray Scattering (SAXS/WAXS) has been used to follow the crystallization kinetics: SAXS giving long range structural ordering, WAXS giving atomic ordering. Time resolved simultaneous SAXS was recorded at the Dubble station ESRF, France and SAXS/WAXS at station 16.1 Daresbury SRS, UK. From the data obtained molecular orientation from a pulse of pre-shear, increases crystallization kinetics up to two orders of magnitude greater than that compared with quiescent crystallization at the same temperature. The SAXS shows that crystalline lamellae structures grow perpendicular to the initial flow direction giving oriented meridional scattering peaks. The WAXS shows similar development of Bragg peaks with some orientation being concentrated in the equatorial direction. During pre-sheared crystallization, the formation of a stacked lamella structure is said to follow a route in which oriented molecular chains act as 'orientation-inducted nuclei'. These then facilitate crystalline lamellae to grow outwards from these sites perpendicular to the direction of flow and the stacked lamellae structure. This is termed as the 'shish-kebab' morphology (the 'shish' being the oriented molecular chains (nuclei) and the 'kebabs' the overgrowth of lamellae). The formation of shear induced nuclei, depends greatly on the molecular weigh, polydispersity and molecular architecture of the sample along with temperature. Critical shear rates are also required to provide oriented chains to form the nuclei. From the experimental investigation, the high molecular weigh chains are seen to give shear-induced nuclei however, low molecular weight chains (and high polydispersity) do not give such well defined oriented lamella morphologies.

An Investigation into the phase behaviour of block copolymers in solution - phases formed and their transition kinetics

A. I. Norman, J. P. A. Fairclough, Y. Deng, S. Mai and A. J. Ryan

University of Sheffield Sheffield S3 7HF

Various block copolymers in aqueous solution have been studied to show how the chain architecture effects the phase behaviour and the kinetics of the phase transitions. This has many biological applications such as artificial lung surfactants in premature babies(1). The block copolymers under investigation are diblock PEO-PI copolymers, triblock PEO-PBO-PEO copolymers, and triblock PBO-PEO-PBO copolymers. Micelles are formed when the concentration of polymer in water reaches a critical value known as the CMC. As the concentration is increased further the micelles pack together to form ordered arrays of specific geometry such as Cubic, Hexagonal or Lamella structures. The structure is deduced from simultaneous SAXS/WAXS/DSC experiments performed on beamlines 8.2 of the SRS Daresbury Laboratory and CRG DUBBLE at the European Synchrotron Radiation Facility (ESRF), Grenoble. Slow heating ramps are employed whilst SAXS/WAXS is collected. The postions of the peak-to-peak ratios determined the geometry that the micellar array adopts. Such experiments are repeated for different block copolymer concentration in order to map the morphology. From the phase diagrams the position of the Order-Order and Order-Disorder Transitions are located. These positions can be located more accurately by monitoring the intensity of the various reflectiojs from the SAXS pattern. This is done using the CCP13 program XFIT. The kinetics of the phase transitions has initially been studied using Polarised Light Microscopy. The sample has been heated to a point where the structure is disordered, and isotropic. Under crossed polars we observe a black image. The sample is rapidly quenched using a temperature jump apparatus to a point where the sample will form a hexagonal or lamellae structure. Coloured images are formed at this point, since the sample is becoming more and more birefringent, thus visible under crossed polars. The degree of birefringence is monitored with time, and Avrami kinetic theory(2) is employed to determine the exponent, which gives us information on the mechanism of the transforamtion, and the rate constant for the phase transition. Simliar experiments have been carried out with SAXS/WAXS techniques. In this case the evolution of a peak is monitored with time.

References

[1]. W. R. Perkins, R. B. Dause, R. A. Parente, S. R. Minchey, K. C. Neuman, S. M. Gruner, T. F. Tarashi, A. S. Janoff, Science, 273, 1996, (330).
[2]. M. Avrami, J. Chem. Phys., 7, 1939, (1103).

Polymers : SAXS/WAXS techniques at DUBBLE(CRG-ESRF)

D. Detollenaere , I. Dolbnya , S. Hoffmann, J. Jacobs, M. Malfois , S. Nikitenko, B. Zawilski, W. Bras

DUBBLE CRG - ESRF F-38043 Grenoble Cedex

The Dutch-Belgian beamline (DUBBLE) is a collaborative research group (CRG) beamline at the European Synchrotron Radiation Facility (ESRF). 30% of its time is available to ESRF users. The SAXS/WAXS station has been operational since January 2000. Most of the research is concentrated in the soft condensed matter area for which the beamline was designed, but it is also possible to perform biological molecule solution scattering experiments. Up to now a considerable range of sample environments has been implemented and made available to the users in order to accommodate the requirements for their specific projects. Complicated sample environments are available like magnets, high temperature heating cell (1500ºC)… and the users can combine their SAXS/WAXS experiments with others techniques (FTIR, Raman…). Results obtained on polymers with different sample environments will be shown.

Simultaneous SAXS and WAXS study of the precipitation of calcium carbonate

C. K. Poh R. I. Ristic M. J. Hounslow A. J. Ryan J. P. A. Fairclough

University of Sheffield

In this work, we report the study of crystallization of calcium carbonate from aqueous solutions of calcium nitrate and sodium carbonate using simultaneous Wide Angle X-ray Scattering (WAXS) and Small Angle X-ray Scattering (SAXS) techniques. By means of a novel flow cell, in-situ monitoring of the crystallization processes as a function of initial supersaturations has been made on a time-resolved basis. The WAXS results show that the precipitation under the condition of high initial supersaturations proceeds by the production of an amorphous phase, and is then followed by the transformation of this phase to a crystalline phase of which calcite is predominant. The use of the Scherrer Formula and the Full Width at Half Maximum (FWHM) of the Gaussian symmetrical profile function fitted to the calcite (104) Bragg peak has yielded results showing the change in crystallite size with time. The change in integrated intensity of the (104) peak is used to follow the change in mass fraction of crystals in solution with time. The SAXS results show a corresponding change with time. This work has significant relevance to the industry particularly because the on-line observation of the crystallization phenomena has been done using an experimental set-up that mimics industrial crystallizers. It has been shown that WAXS and SAXS techniques are informative, in-situ experimental methods that allow simultaneous observations of time-resolved processes such as those taking place in real, industrial processes.

CRYDAM - From atomic coordinates of macromolecules to scattering intensity

M. Malfois[1,3] and D. I. Svergun[1,2]

[1] European Molecular Biology Laboratory, Hamburg Outstation, c/o DESY, Notkestrasse 85,D-22603 Hamburg, Germany

[2] Institute of Crystallography, Russian Academy of Sciences, Leninsky prospekt 59, 117333 Moscow, Russia

[3] CRG-DUBBLE, ESRF, BP 220, 38043 Grenoble Cedex, France

Computation of scattering patterns from atomic models of macromolecules permits one to validate theoretical models, to analyse similarities between the quaternary structure in the crystal and in solution and to perform rigid body refinement. A program for evaluating the X-ray or neutron scattering intensity from proteins and/or nucleic acids with known atomic structure (e.g. from the Protein Data Bank) is presented. The program is a further development of the programs CRYSOL [1] and CRYSON [2] but uses a more robust way to compute the scattering from its excluded volume and its hydration shell. A grid of densely packed dummy solvent atoms with the radius 0.15 nm is built enclosing the particle. The excluded volume is built from the dummy atoms contacting an atom in the particle. Subsequently, the dummy atoms contacting the excluded volume atoms are considered as potentially belonging to the hydration shell. The program can either predict theoretical scattering intensity or fit experimental curves by varying two parameters, the excluded volume and the contrast of the hydration layer. The program runs on IBM PCs and on the major UNIX platforms.

References

[1]. Svergun, D.I., Barberato, C. & Koch, M.H.J. (1995). *J. Appl. Crystallogr*. **28**, 768-773.

[2]. Svergun, D.I., Richards, S., Koch, M.H.J., Sayers, Z., Kuprin, S. & Zaccai, G. (1998). *Proc. Natl. Acad. Sci. USA*, **95**, 2267-2272.

Fibre Diffraction Review: Instructions to Authors

Submitted original papers, technical reports, Reviews, comments/letters and meeting reports for inclusion in Fibre Diffraction Review are welcome.

Technical Reports:
These include presentations of the latest developments in CCP13 and other fibre diffraction/ non-crystalline diffraction software and their scientific justification and also, for example, reports on developments at synchrotron beamlines used for fibre diffraction and non-crystalline diffraction studies.

Reviews:
These include summary presentations of the 'state of the art' in the structural analysis of particular fibrous or non-crystalline systems.

Original Papers:
These present previously unpublished results from fibre diffraction or small-angle scattering experiments using either X-ray, neutron or electron diffraction.

Expanded Poster-Prize Abstracts:
At each of the CCP13/ NCD Annual Workshops cash prizes are presented to the best poster presentations. The judges are always senior scientists in the field and are often from overseas. Winners of the Poster Prizes are invited to expand their abstracts into short papers for inclusion in Fibre Diffraction Review.

Refereeing:
All papers, of whatever category above, will be refereed by at least two people (from the CCP13 Committee or their nominated referees) and may be either (a) accepted as they stand, (b) returned for rapid revision, or (c) rejected. As well as their scientific content, papers will be judged on their clarity of presentation and the quality of their figures.

Meeting Reports:
Fibre Diffraction Review includes reports on relevant meetings and conferences which include an element of fibre diffraction or small-angle scattering and which will be of general interest to our readers. Such reports will often be solicited by the Editor from known meeting participants. Other potential contributors to this part of the Journal should contact the Editor prior to writing their report.

Comments/Letters:
Feedback from readers about CCP13, about the NCD community and about the Journal itself are welcome. These could be in the form of comments or letters to the Editor. Suitable contributions will be published in the Journal.

Advertisements:
Industrial/commercial adverts of interest to our readers are welcome. Potential advertisers should contact the Editor for details of current rates.

Submission:
Contributions should be sent to the Editor before the annual deadline (November 30th) for each issue. Contributions submitted after this date may be held over for the following issue.

Colour illustrations are welcome and are included without charge. Contributions should be submitted both in hardcopy (ONE complete copy) and in electronic format to the Editor (j.squire@ic.ac.uk).

Text should be in Word 6 format and illustrations should be submitted as separate files at high resolution in TIFF or JPG format.

References should be in the format specified for *J. Molecular Biology*, and should be complete with title. Please find more details from our website.

Reprints:
It is not economic for us to produce reprints of articles. However, in future, papers will be made available on the CCP13 website in downloadable pdf format.

Those wishing to purchase extra copies of the whole Journal should contact the Editor to find out costs.

Editor's Address:
Professor John M. Squire,
Head, Biological Structure and Function Section,
Biomedical Sciences Division,
Imperial College of Science, Technology & Medicine,
London SW7 2AZ, UK.

Editor 'Fibre Diffraction Review' (ISSN 1463-8401).

Useful World Wide Web addresses (URL)

Fibre Diffraction Review	**http://www.fibrediffractionreview.org**
CCP13	**http://www.ccp13.ac.uk**
	http://www.ccp13.org
	http://www.bio.aps.anl.gov/biocat/mirror/www.ccp13.ac.uk/
	http://www.ill.fr/ccp13
NCD	**http://www.srs.dl.ac.uk/NCD**
SRS	**http://www.srs.ac.uk/SRS**

ISSN 1463-8401